POLITECNICO DI TORINO
Repository ISTITUZIONALE

Current trends in electron beam and laser powder bed fusion additive manufacturing of copper alloys: Composition, defects, properties, and challenges

Original
Current trends in electron beam and laser powder bed fusion additive manufacturing of copper alloys: Composition, defects, properties, and challenges / Bhatt, B., Martucci, A., Biamino, S., Ugues, D., Bondioli, F., Montanaro, L., Lombardi, M., Fino, P.. - In: MATERIALS & DESIGN. - ISSN 0264-1275. - 253:(2025). [10.1016/j.matdes.2025.113742]

Availability:
This version is available at: 11583/3004443 since: 2025-10-24T13:22:26Z

Publisher:
Elsevier

Published
DOI:10.1016/j.matdes.2025.113742

Terms of use:

This article is made available under terms and conditions as specified in the corresponding bibliographic description in the repository

Publisher copyright

(Article begins on next page)

18 November 2026

Materials & Design 253 (2025) 113742

Contents lists available at ScienceDirect

Materials & Design

journal homepage: www.elsevier.com/locate/matdes

Current trends in electron beam and laser powder bed fusion additive manufacturing of copper alloys: Composition, defects, properties, and challenges

Bhaskaranand Bhatt [a,*], Alessandra Martucci [a], Sara Biamino [a,b], Daniele Ugues [a,b], Federica Bondioli [a,b], Laura Montanaro [a,b], Mariangela Lombardi [a,b,*], Paolo Fino [a,b]

[a] Department of Applied Science and Technology (DISAT), Politecnico Di Torino, Corso Duca degli Abruzzi 24, Torino 10129, Italy
[b] Center of Integrated Additive Manufacturing (IAM), Politecnico di Torino, Corso Castelfidardo, 51, 10138 Torino, Italy

ARTICLE INFO

Keywords:
Additive manufacturing review
Process parameters
Powder bed fusion
Copper alloys
Defects
Post processing heat treatments
Microstructures

ABSTRACT

Currently, laser and electron beam powder bed fusion (L/E-PBF) are prevalent in metal additive manufacturing (AM), demonstrating exceptional potential for producing copper (Cu) alloy components indispensable for numerous aerospace, automotive, energy, and marine applications. However, despite groundbreaking advances in metal AM, Cu alloys remain underdeveloped. This comprehensive review highlights the unremitting efforts to develop superior and bespoke L/E-PBF Cu alloy parts. Initially, roadblocks to Cu alloy printability are identified, along with solutions to surmount them, followed by feedstock development in the context of L/E-PBF. An extensive process-induced defect analysis is presented to assess the impact of powder feedstock characteristics, process parameters, and heat treatments. Furthermore, the mechanical, electrical, corrosion, and tribological properties of L/E-PBF-fabricated Cu alloy parts are elaborated to elucidate the nexus among material-microstructure-performance. In addition, this review delves into various strengthening mechanisms, the significance of post-processing heat treatment in stabilising non-equilibrium microstructures, and its influence on the material-property space. The discussion then extends to the importance of modelling for comprehending complex melt pool dynamics. Finally, the review uncovers lacunas and presents critical future research aspects to boost the technological readiness of L/E-PBF Cu alloys/composites for accelerated adoption.

1. Introduction

As we scroll through history, we see that copper is one of the oldest metals found and used by mankind. Evidence indicates copper was used as early as 10,000 BC, making it a cornerstone material for the emergence of human civilisation from the Stone Age [1]. Beyond the advent of bronze (Cu–Sn) and brass (Cu–Zn), Cu-based alloys/composites continue to pervade our daily lives, providing numerous capabilities across a wide array of modern applications. Cu alloys are fully integrated into our daily lives, from aerospace, marine, and automotive components to electrical and consumer items, owing to their optimal amalgamation of essential mechanical and electrical properties, hydrogen compatibility, resistance to corrosion, biofouling, wear, explosion, oxidation, etc. [2]. These diverse material properties have positioned copper as the second most consumed alloy family, following aluminium [3]. However, the traditional manufacturing processes of Cu alloys/composites face two significant challenges: material and process limitations. Process limitations include a narrow window for microstructure manipulation, restrictions on component size, geometry constraints, etc., while material limitations include limited composition flexibility, macro-segregation, solubility limits, phase separation—particularly for immiscible alloys ($\Delta H_{mix} > 0$) due to equilibrium conditions, etc. As a consequence of these limitations, the design freedom for parts and compositions, topology optimisation, and integrated functionality of current and next-generation engineering components that employ Cu alloys/composites are restricted, thus limiting the potential applications of Cu alloys/composites. At present, the advent of additive manufacturing (AM), a bottom-up technique that possesses a distinctive combination of solidification rate and temperature gradients, has facilitated the overcoming of the pressing challenge of materials and process limitations in conventional processes, thereby enabling the fabrication

* Corresponding authors at: Department of Applied Science and Technology (DISAT), Politecnico Di Torino, Corso Duca degli Abruzzi 24, Torino 10129, Italy (M. Lombardi).
E-mail addresses: bhaskaranand.bhatt@polito.it (B. Bhatt), mariangela.lombardi@polito.it (M. Lombardi).

https://doi.org/10.1016/j.matdes.2025.113742
Received 11 December 2024; Received in revised form 15 February 2025; Accepted 18 February 2025
Available online 19 February 2025
0264-1275/© 2025 The Authors. Published by Elsevier Ltd. This is an open access article under the CC BY license (http://creativecommons.org/licenses/by/4.0/).

Nomenclature

3D	3 Dimensional
%EL	Plastic Strain
μm	Micron
AB	As-built
Ag	Silver
AGA	Argon Gas Atomization
Al	Aluminum
AM	Additive Manufacturing
APT	Atom-Probe Tomography
ASTM	American Society for Testing and Materials
BD	Build Direction
BJ	Binder Jetting
BMG	Bulk Metallic Glasses
BCC	Body Centred Cubic
C63000	Cu-Al-Fe-Ni-Si
C95800	Cu-Al-Fe-Ni-Mn
CAD	Computer-Aided Design
CDPM	Cool Down Phase Model
CET	Columnar-to-Equiaxed Transition
CFD	Computational Fluid Dynamics
CHS	Concentrated Heat Source
CNT	Carbon Nanotube
CNP	Carbon Nanoparticles
Co	Cobalt
Cr	Chromium
Cr_2O_3	Chromium Oxide
CT	Computed Tomography
CTE	Coefficients of Thermal Expansion
Cu	Copper
CSAM	Cold Spray Additive Manufacturing
DA	Direct Aging
DED	Directed Energy Deposition
DEM	Discrete Element Modelling
DIN	Deutsches Institut für Normung
DMLM	Direct Metal Laser Melting
DP	Discontinuous Precipitation
DS	Dislocation Strengthening
E-PBF	Electron Beam Powder Bed Fusion
EBM	Electron Beam Melting
EBSD	Electron Backscatter Diffraction
EDM	Electrical Discharge Machining
EDS	Energy Dispersive X-ray
EIS	Electrochemical Impedance Spectroscopy
EM	Elastic Modulus
EPMA	Electron Probe Microanalysis
FCC	Face Centred Cubic
FEM	Finite Element Model
FGM	Functionally Graded Material
Fe	Iron
FWHM	Full–Width at Half–Maximum
G	Local Temperature Gradient
GA	Gas Atomization
GB/T	Guóbiāo Tuījiàn
GBS	Grain Boundary Strengthening
GND	Geometrically Necessary Dislocation
GO	Graphene Oxide
GRCop-42	Glenn Research Copper 42
GRCop-84	Glenn Research Copper 84
h	Hour
HAADF-STEM	High-Angle Annular Dark-Field Scanning Transmission Electron Microscopy
HAGB	High-Angle Grain Boundaries
HCF	High Cycle Fatigue
HDI	Heterogeneous Deformation-Induced Strengthening
HND	Heterogeneous Nanoprecipitate Dislocation
HEA	High Entropy Alloys
HIP	Hot Isostatic Pressing
HS	Hatch Spacing
HSHC	High Strength High Conductivity
HSMC	High Strength Medium Conductivity
HT	Heat Treatment
IACS	International Annealed Cu Standard
IEA	International Energy Agency
IHT	Intrinsic Heat Treatment Process
ISO	International Organisation for Standardisation
KAM	Kernel Average Misorientation
LaB_6	Lanthanum Hexaboride
LAGB	Low-Angle Grain Boundaries
LCF	Low Cycle Fatigue
LED	Linear Energy Density
LoF	Lack of Fusion
LP-DED	Laser Powder Directed Energy Deposition
L-PBF	Laser Powder Bed Fusion
LT	Layer Thickness
LTS	Load Transfer Strengthening
Mg	Magnesium
ML	Machine Learning
Mn	Manganese
MMC	Metal Matrix Composite
MM	Mechanical Mixing
MPB	Melt Pool Boundary
M-S	Mott–Schottky Analysis
MSHC	Medium Strength High Conductivity
MSMC	Medium Strength Medium Conductivity
NAB	Nickel–Aluminum-Bronze Alloys
Nb	Niobium
NIR	Near Infrared
Ni	Nickel
OM	Optical Microscopy
OPS	Orowan Precipitation Strengthening
P	Phosphorus
pH	Potential of Hydrogen
PA	Pre-Alloyed Powder
PP	Potentiodynamic Polarization
PSD	Particle Size Distribution
PSE	Plastic Strain Energy
PREP	Plasma Rotating Electrode Process
R	Solid-Liquid Interface Migration Velocity or Solidification Rate
R_a	Average Surface Roughness
RD	Relative Density
RMS	Root Mean Square
RS	Residual Stress
RT	Ray-Tracing Method
R_{CT}	Charge Transfer Resistance
S_a	Surface Arithmetic Average Roughness
SAT	Solution Aging Treatment
SAED	Selected Area Electron Diffraction
ST	Solution Treatment
SEBM	Selective Electron Beam Melting
SEPSE	Statistical Estimation of Plastic Strain Energy
SF	Schmid Factor
SHS	Scattered Heat Source
SSD	Statistically Stored Dislocations
SLM	Selective Laser Melting
SLS	Selective Laser Sintering
SSS	Solid Solution Strengthening
Si	Silicon

SMA	Shape Memory Alloys
Sn	Tin
TC	Thermal conductivity
TEM	Transmission Electron Microscopy
Ti	Titanium
TiB_2	Titanium Boride
TiC	Titanium Carbide
TGM	Temperature Gradient Mechanism
TRL	Technology Readiness Level
UAM	Ultrasonic Additive Manufacturing
UTS	Ultimate Tensile Strength
UV	Ultraviolet
VED	Volumetric Energy Density
VHCF	Very High Cycle Fatigue
VOF	Volume of Fluid
WAAM	Wire Arc Additive Manufacturing
W	Tungsten
XPS	X-Ray Photoelectron Spectroscopy
XRD	X-Ray Diffraction
YS	Yield Strength
Y_2O_3	Yttrium Oxide
Zn	Zinc
Zr	Zirconium
τ	Shear Strength
σ_{GBS}	Grain Boundary Strength
k	Hall-Petch Constant
d or D	Average Grain Size
V_f	Volume Fraction of Fine Grain
V_c	Volume Fraction of Columnar Grain
d_f	Mean Grain Size of Fine Grains
d_c	Mean Grain Size of Columnar Grains
σ_{ss}	Solid Solution Strength
M	Taylor Factor
ε_{ss}	Cu Lattice Distortion-Induced Strain
c	Solute Concentration
μ	Poisson Ratio
b	Burgers Vector
E	Elastic Modulus
a	Lattice Parameter
ε_g	Shear Modulus Coefficient
ε_b	Lattice Mismatch Coefficient
r_c	Dislocation Core Radius
τ_p	Precipitate Shear Stress
σ_{OPS}	Orowan Precipitation Strength
σ_{DS}	Dislocation Strength
ρ	Geometrically Necessary Dislocation Density
r_{mp}	Average Circular Radius in Random Plane for Spherical Precipitate
δ	Inter-Precipitate Spacing
r_p	Mean Precipitate Radius
φ	Geometrical Constant
β_{hkl}	FWHM
θ	Diffraction Angle
k_d	Dislocations Strengthening Constant
λ	Wavelength of Radiation
ε	Internal Strain
σ_{load}	Load Transfer Strength
σ_{cu}	Copper Yield Strength
f_{vol}	Hard Particles/Phases Volume Fraction
A	Aspect Ratio
σ_{HDI}	Heterogeneous Deformation-Induced Strength
σ_{UL}	Unloaded Yield Stress
σ_{RL}	Reloaded Yield Stress
σ_o	Lattice Friction Stress
σ_{cal}	Estimated Yield Stress

of bespoke Cu alloys/composites for advanced engineering applications. Fig. 1 illustrates the four-generation evolution of the AM Cu family, highlighting their increasing potential, beginning with the inception of the first generation (pure Cu) and advancing to the second (micro-alloyed) and third (macro-alloyed) generations. The fourth generation encompasses advanced Cu alloy/composite-based materials such as bulk metallic glass (BMG), functionally graded materials (FGM), shape memory alloys (SMA), etc., which broaden the range of future applications.

In recent years, L/E-PBF has demonstrated the potential to fabricate complex and high-performance Cu alloys/composite printed parts. Using laser powder bed fusion (L-PBF), Zheng et al. [4] printed Cu alloy metamaterial with multifunctional idiosyncratic properties of zero Poisson's ratio and superelasticity, which could be used for exciting energy absorption and vibration isolation applications. Moreover, the utilisation of L-PBF to combine Cu alloy with other alloys, including Ni, Ti, and Fe alloys, presents an opportunity to satisfy distinctive design requirements for functional materials, thereby expanding the scope of Cu alloy applications [5–7]. Additionally, the high-temperature stability and resistance to coarsening of Cr_2Nb precipitates endow the L-PBF Glenn Research Copper–84 (GRCop–84) alloy with enhanced properties, enabling its use in fusion reactor components and combustion chambers of rocket engines [8,9]. Moreover, the Cu–Ni–Si–Cr alloy, using L-PBF, shows promise for future electrical machine windings due to its tailored properties [10]. The antibacterial properties of copper were examined by utilising L-PBF Cu–W–Ag alloys for antiviral mask filters, revealing the promise of Cu alloys in healthcare devices to align with the intended clinical need [11]. The recent use of high-conductivity (307 W/mK) Cu–Cr–Zr alloys in L-PBF paves the way for the fabrication of complex fins for superior-performance heat sinks in future technologies [12,13]. The rapid cooling rate of L-PBF ($\sim 10^4$-10^8 K/s) surpasses the critical cooling rate (10^2-10^4 K/s), facilitating the formation of an utterly amorphous microstructure, which proves promising for Cu-based BMGs while also overcoming the size and geometrical limitations of conventional processes, paving the way for new engineering applications [14–17]. Furthermore, combined with AM, Cu–Cr alloy is explored for intricate EDM electrodes with micro-holes for improved fluid flow and electrical contacts [18,19]. The integration of Cu–Sn alloy into L-PBF, which is recognised for its ductility, low friction, and superior corrosion resistance, will enable the manufacture of components such as bearings, worm wheels, ship parts, and electrical connectors for future applications [20–22]. The utilisation of L/E-PBF in conjunction with NAB alloys (which possess superior corrosion resistance and strength) renders them suitable for complex parts for niche applications in maritime components [23]. Recent findings indicate that the high cooling rate ($\sim 10^4$-10^8 K/s) of L-PBF mitigated brittle phase formation in Cu-based (Cu–Al–Ni) SMA, which obstructs the shape memory effect, while its ability to fabricate complex structures (porous/lattice) opens new avenues for integrating SMA into next-generation components [24,25]. Moreover, controlling the alloying and phase separation behaviour of Cu-based immiscible alloys (Cu–Fe, Cu–Co, etc.) using L-PBF lays the groundwork for Cu alloys in progressive engineering applications [26–29]. This underscores the potential of the emerging L/E-PBF technique for printing Cu alloys/composites as a coin with two bright sides: on the one hand, it enables the fabrication of intricate parts with otherwise impossible geometries to circumvent process limitations, while on the other hand, the rapid cooling rate can overcome material limitations.

Despite the remarkable capabilities of L/E-PBF, Cu alloys/composites have yet to reach their full potential due to constraints in intrinsic thermophysical characteristics associated with Cu alloys/composites

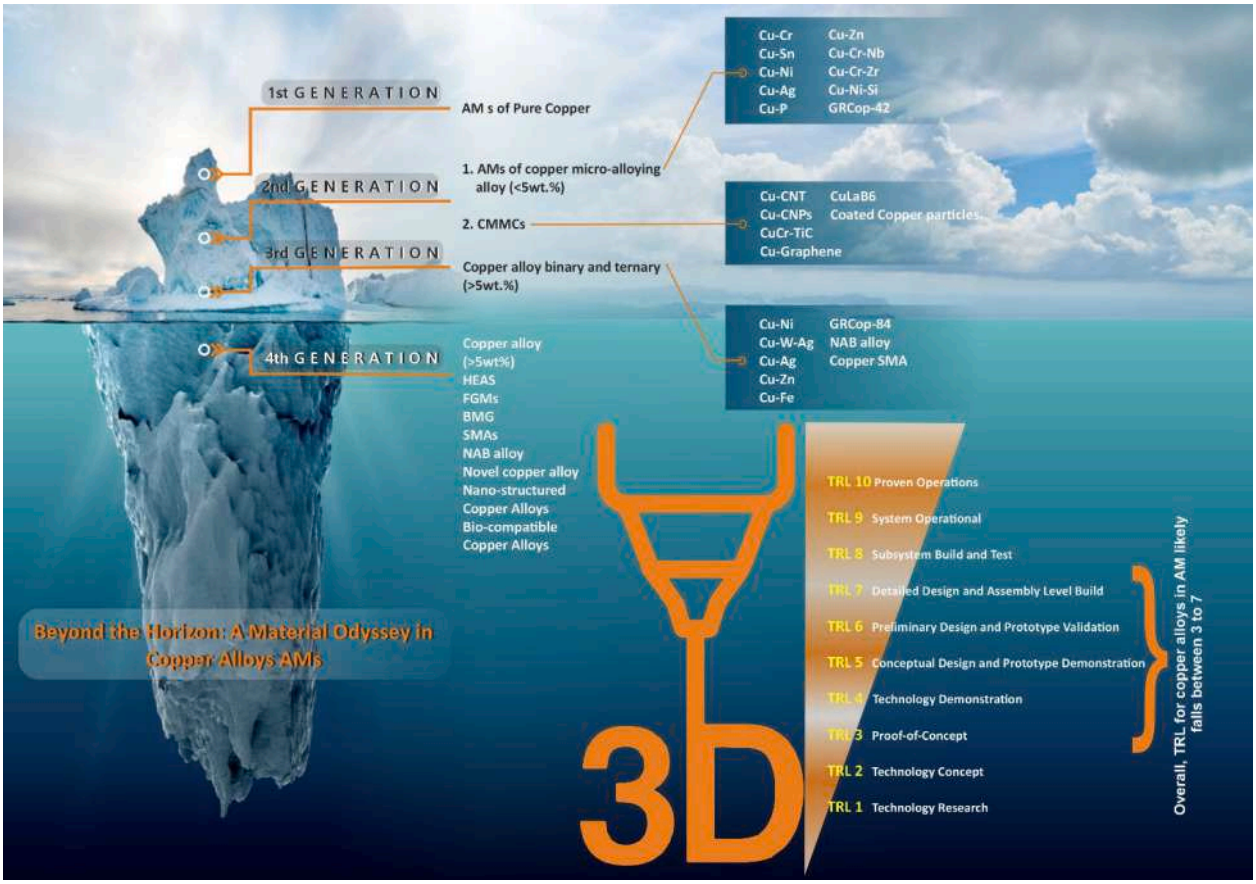


Fig. 1. Evolution of copper alloys for additive manufacturing and their overall technology readiness levels (TRL). (CMMC: Copper metal matrix composite; HEA: High entropy alloys; FGM: Functionally graded material; BMG: Bulk metallic glasses; SMA: Shape memory alloys; NAB: Nickel–Aluminum–Bronze alloys).

powder feedstocks and in-process challenges. On one side, Cu-based powder feedstocks (alloys/composites) are not readily printable with near-infrared (NIR: 1070 $\pm$ 10 nm) fiber laser irradiation due to their high reflectivity (95% at room temperature), and their higher thermal conductivity dissipates heat faster, leading to fusion and solidification instability. On the other hand, the complex dynamics of the melt pool, localised solidification conditions, and multiple process parameters in the L/E-PBF lead to non-equilibrium microstructures. These often exhibit micro-chemical segregation, heterogeneous grain morphologies, defects, etc., which significantly impact the mechanical, thermal, electrical, corrosion, and functional performance etc. of AM Cu alloys/composites. Thus, there is a pressing need to address the challenges that Cu alloys and composites pose to mitigate printability concerns and design components with bespoke performance. Hereby, the questions arise:

- How can Cu-based feedstock absorptivity be enhanced to improve part quality, consistency, and performance?
- Why is it crucial to tune the process parameters when analysing the relationships between material, microstructure, and performance in L/E-PBF Cu alloys/composites?
- If any trade-offs are observed in the mechanical and electrical properties of L/E-PBF Cu alloys/composites, can they be minimised? How?
- What triggers defects, and how do they influence L/E-PBF Cu alloy/composite performance? How may Cu-based powder feedstock characteristics and process parameters be optimised to reduce defects?
- How do post-printing heat treatments modulate solidification microstructure and affect the mechanical, electrical, corrosion, and tribological performance?
- How can the anisotropy in the mechanical behaviour, corrosion behaviour, etc., of Cu alloy/composite-based AM components be mitigated?
- How does the contribution of strengthening mechanisms vary from printing to post-printing heat treatments, and how does this impact the spectrum of printed part material properties?
- Is it possible to fathom the intricacy of powder bed dynamics and laser-material interaction through simulation to meet the industrial high-quality demands for printed products and process repeatability?

The following sections of this review article address the aforementioned questions to provide a comprehensive understanding of the current state of L/E-PBF Cu alloys/composites.

2. Scope of the review

This review concentrates on L-PBF and electron beam powder bed fusion (E-PBF) techniques for processing Cu alloys/composites. While other techniques, such as binder jetting (BJ) and directed energy deposition (DED), including wire arc additive manufacturing (WAAM), are also capable of printing Cu alloys, they are not covered within the scope of this article. Firstly, an introduction section is presented to outline the various processing methods utilised in AM for Cu alloys, as well as the challenges faced during ongoing investigations on the printing of Cu alloy/composite components. This is followed by a brief introduction to two well-known powder bed fusion techniques, L-PBF

Table 1
List of reviews on L/E-PBF Cu-based alloys/composites in the last five years.

Processes	Feedstocks	Research objects	Year	Ref.
BJ, UAM, DED, L-PBF, E-PBF	Pure Cu and Cu alloys	Composition and mechanical properties	2020	[30]
L-PBF	GRcop–84, GRcop–42	Development, processing, and contemporary microstructure-property	2021	[31]
E-PBF	Pure Cu and some Cu alloys	Microstructure and mechanical properties	2022	[32]
Casting to AM	Cu–Ni–Sn spinodal alloys	Material properties of different processing methods	2022	[33]
L-PBF	Cu–Cr–Zr and Cu–Cr–Nb alloys	Microstructure, mechanical, and thermal properties	2022	[34]
AM and conventional manufacturing	Cu–Ni–Sn alloys	Wear and corrosion behaviour	2023	[35]
L-PBF, LP-DED, E-PBF, CSAM	GRCop, GlidCop, and Cu–Cr–Zr alloys	Effects of post-processing and feedstock properties	2024	[36]
L-PBF, E-PBF	Cu-based alloys/composites	Feedstocks, process defects, material properties, strengthening mechanism, heat treatment, and modelling	2025	Present review

BJ: Binder jetting; UAM: Ultrasonic additive manufacturing; DED: Directed energy deposition; LP-DED: Laser powder directed energy deposition; CSAM: Cold spray additive manufacturing.

and E-PBF, as well as the effect of process parameters on Cu alloy/composite AM components and the selection of Cu alloy/composite powder feedstocks for L-PBF and E-PBF. Subsequently, defects commonly encountered during L/E-PBF processing of Cu alloys/composites are identified, along with potential remedies to mitigate the defects for enhanced performance of additively manufactured (AMed) Cu parts. Later, the article discusses how Cu powder feedstock characteristics (bulk and particulate properties such as composition, morphologies, O_2 content, rheology, etc.), process parameters (laser/electron beam), post-printing heat treatments, and testing conditions of material properties affect the mechanical (tensile, compressive, hardness, creep, fatigue, and tribological properties), electrical, thermal performance, and corrosion behaviour of L/E-PBF Cu alloy/composite. The article also examines post-printing heat treatments of printed parts, as well as the relevance of simulation and modelling in understanding the complexity and physics of melt pools, identifying optimal process parameters, etc. Finally, the review concludes by outlining promising future directions for research in L/E-PBF Cu alloys/composites to augment Cu alloys/composites additive manufacturing technology readiness level (TRL) for next-generation applications.

Table 1 summarises reviews on Cu alloys AM published from 2020 to 2024, highlighting the used methodologies, feedstock composition, research objects, and publication year. Notably, existing review articles primarily focus on specific Cu alloys and their properties. However, none have addressed process defects—the most significant impediment to the widespread use of L/E-PBF—or the material-microstructure-performance relationships, which are critical for advancing L/E-PBF Cu alloys/composites for novel engineering applications. Given the inherent anisotropy of L/E-PBF-fabricated Cu alloys/composites parts, post-processing heat treatments are critical for enhancing and reducing the scattering of material properties, but this has not been discussed in any articles. Additionally, the trade-off between strength-ductility and strength-conductivity in L/E-PBF Cu alloy/composites remains an unexplored frontier in the ongoing research landscape. To comprehend the material-microstructure-performance nexus for the development of Cu alloy/composite AM, an in-depth analysis of the design of Cu alloy/composite powder feedstock, the mechanism and mitigation strategies of process defects, the process parameters-material properties link, the strengthening mechanisms, post-AM heat treatments, and modelling is required. Thus, this review unifies the entire spectrum of knowledge on Cu alloys/composites in L/E-PBF under one comprehensive umbrella.

3. Additive manufacturing

The ISO/ASTM 52900:2021 terminology standard defines AM as the "process of joining materials to make objects from 3D model data, usually layer upon layer, as opposed to subtractive manufacturing methodologies" [37]. It encompasses seven principal categories, each distinguished by the type of initial feedstocks (solid or liquid) and the energy source employed (laser, electron beam, UV lamp, etc.): BJ, DED, material extrusion, material jetting, powder bed fusion, sheet lamination, and vat photopolymerisation [37]. These AM techniques continue to garner significant interest due to their unparalleled benefits, including ease of fabricating complex shapes with features like internal channels and lattice structures, the elimination of tooling costs, on-demand customisation and localised manufacturing, multi-material capabilities, design flexibility and consolidation, functional integration, maximum material utilisation, exclusive microstructure, and bespoke performance under one umbrella. Consequently, AM has emerged as a transformative fabrication tool across diverse industries, including automotive, medicine, electronics, fashion, sculpture, wearable technology, aerospace, energy sectors, etc., ushering in a revolution in both manufacturing and design. In recent years, AM has demonstrated its capacity to excel in challenging circumstances by devising a variety of medical components during the COVID-19 pandemic and constructing schools in war zones [38,39]. Recognising the revolutionary potential of AM, governments worldwide are increasingly investing in AM technologies, exemplified by initiatives such as the U.S. AM Forward Fund ($42 billion), to drive innovation, workforce development, and economic growth [40]. Furthermore, projections by IDTechEx indicate that AM is poised to disrupt manufacturing, propelling the market to a remarkable $49 billion by 2034 at a sustained rate of an 11% CAGR, emphasising the increasing potential of AM in the industry [41]. Briefly, AM is a cutting-edge technology with the potential to play a transformative role in the advancement of Industry 5.0 in the future.

The selection of AM processes for Cu alloys/composites is contingent upon feedstock characteristics and specific application criteria, including design intricacy, dimensional precision, etc. For instance, DED offers enhanced flexibility in part dimensions compared to other AM processes, albeit with potentially reduced part resolution. According to the reviewed literature, several AM techniques have been explored for printing pure copper and Cu alloys/composites, as illustrated in Fig. 2 [42–45]. These techniques primarily include L/E-PBF, DED, and BJ. Although all processes build Cu alloys/composite components in a layer-by-layer fashion, they differ in the feedstock characteristics, build environment, size, process parameters, and post-processing, which result in different microstructures and material properties in AMed components. The distinct thermal characteristics experienced by Cu alloys/composites during specific processing or post-printing heat treatments determine their microstructure (crystallographic texture, grain morphology, etc.). For example, L-PBF has a smaller melt pool than DED due to a smaller (one-order) laser spot size, leading to a faster solidification rate and significant microstructural alterations. Consequently, printed parts exhibit distinct properties. Aside from that, the energy input varies between processes, influencing the defect propensity, distribution, and, ultimately, the overall performance of printed parts. Therefore, a thorough assessment of the material-process-microstructure-property nexus is essential to determine the optimal process parameters for a specific Cu alloy feedstock, ensuring superior performance with minimal scatter in the material properties of defect-

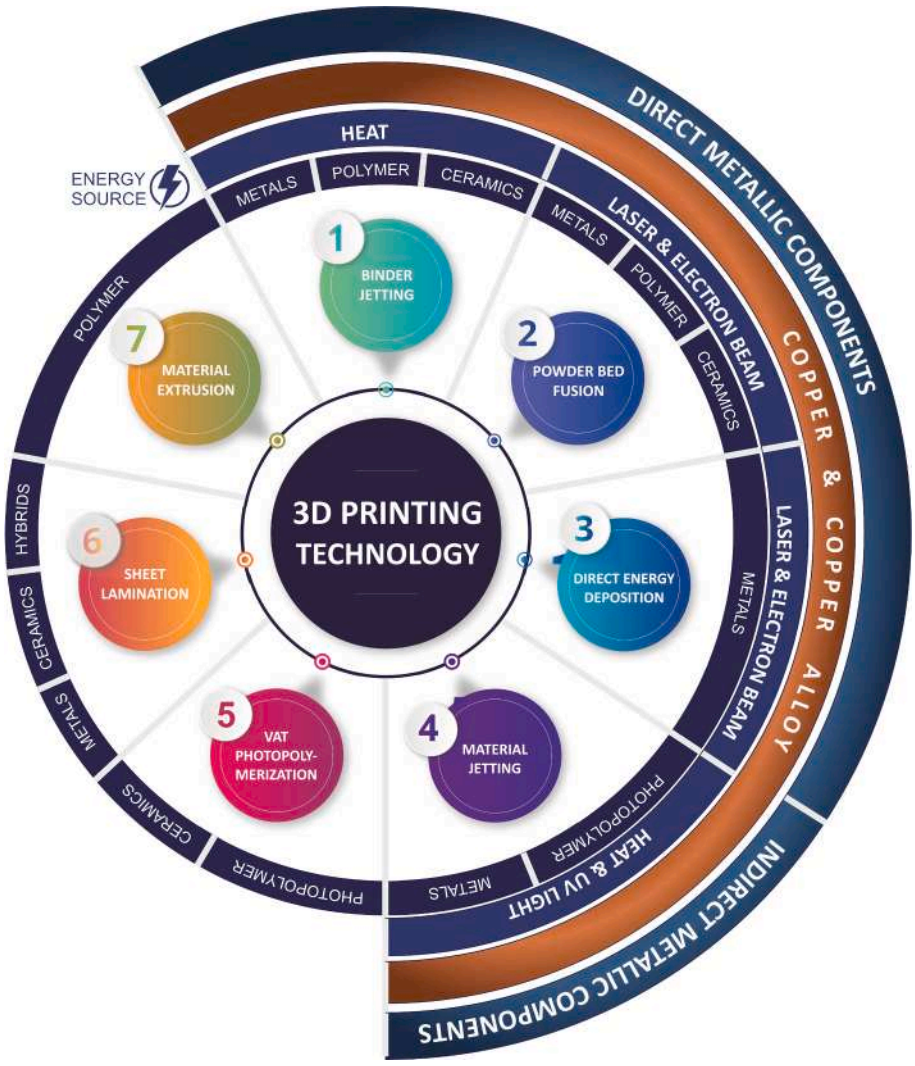


Fig. 2. Schematic of AM processes for copper and Cu alloys/composites.

free AMed Cu alloy/composite parts. For the copper family, the high thermal conductivity (pure Cu: 398 W/m.K and Cu-based alloys: 160–340 W/m.K) and reflectivity at fiber laser wavelengths require meticulous control and optimisation of process parameters, with variations in processes from L-PBF to E-PBF to modify energy density to ensure optimal performance and minimise process defects (metal evaporation: low-boiling point elements (Zn, $T_{boiling}$ = 907 °C) correspond to a pressure of 1×10^5 P, pores, etc.) [46–50]. Thus, there are two main challenges associated with printing Cu alloys/composites: material and processing challenges. The former includes the limited number of available Cu alloys and composites, intrinsic thermophysical characteristics of powder feedstocks, powder bed dynamics, etc., while the latter concerns laser/electron beam-powder interaction, melt pool dynamics, etc. Notably, researchers have employed two strategies to address the printability of Cu alloy/composite: process parameter modifications and material modifications [51–53]. The term "material modification" refers to alloying (avoiding low-boiling elements) or surface modification/functionalisation, which involves the addition of components (metallic/ceramic/carbon-based materials) that enhance Cu feedstock laser absorption to ensure complete fusion, thereby lowering process defect probabilities and improving performance [47,52–55]. In contrast, modifications to process parameters include energy source selection (red, green, blue lasers, or electron beams) [29,56–58], thermal management strategies [59], optimisation of laser or electron beam parameters [59–63], elimination of support structure design using BJ [64], atmosphere control (vacuum, argon), re-melting strategies [65,66], etc. The subsequent section of this review article provides a comprehensive discussion of material modifications and process parameter modifications for L/E-PBF powder bed fusion techniques.

4. Laser powder bed fusion of copper alloys/composites

L-PBF, also known as selective laser melting (SLM) or direct metal laser melting (DMLM), is an AM technique that utilises a high-powered laser beam (70-2000 W) in conjunction with tightly focused (spot sizes ~25-200 μm) lasers to melt metallic powder under controlled ambience (argon, nitrogen, helium) as shown in Fig. 3. This computer-controlled laser beam selectively melts specific regions of a thin metal powder layer (20 to 100 μm) at scanning speeds (~100-1600 mm/s), following the sliced data from a 3D computer-aided design (CAD) model. Upon completion of a layer (composed of particles with a PSD of 20–60 μm), the build platform is translated downward; this precise movement, facilitated by a motorised stage, establishes a predetermined gap for depositing the new powder layer using a recoater blade or roller system. This iterative layer-by-layer deposition process, characterised by rapid local melting and solidification, continues until three-dimensional structures (solid or hollow) are fully formed. After the L-PBF process, unused powder in the chamber can be reused. However, powder reuse depends on several factors, including Cu alloy type, surface chemical

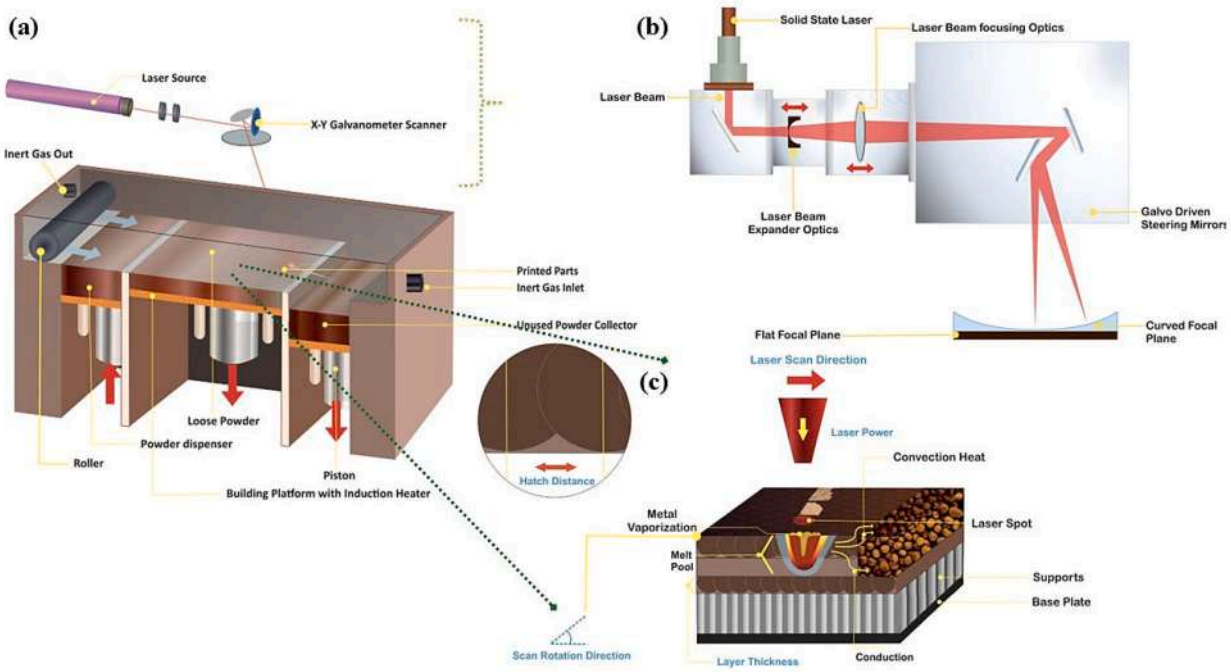


Fig. 3. (a) Schematic layout of L-PBF process; (b) Magnified view of the optical setup; (c) Heat transfer and process variables.

alterations, powder flowability, particle size distribution (PSD), etc. Repeated exposure to elevated temperatures during the L-PBF melting cycle may progressively degrade the virgin feedstocks, ultimately limiting their viability for subsequent printing operations. Fig. 4 depicts various digitally designed Cu alloys/composite parts fabricated using L-PBF technology, primarily for aerospace, automotive, and heat sink applications—components that cannot be manufactured efficiently using conventional methods. The amalgamation of superior mechanical and electrical properties, etc., of Cu-based alloys/composites makes them a prime choice for AMed parts, driving innovation and paving the way for advanced applications.

Cu, the second most reflective material after gold, exhibits reduced absorptivity for fiber lasers (usually below 5% in solid state and 15% in liquid state) in the NIR spectrum (1070 ± 10 nm) due to its electronic band structure [67]. This inherent higher reflectivity in pure Cu is also present in its alloys and composites, albeit to a lesser extent. It remains the primary impediment to defect-free and fully dense L-PBF Cu alloys/composite parts. Researchers have explored the alloying approach to augment absorptivity and curtail the reflectivity of Cu powder feedstocks (alloys/composites) towards NIR lasers. This method entails the use of ceramic particles (TiB_2, Cr_2O_3, LaB_6, etc.), metallic elements (Sn, Zr, Cr, Nb, W, etc.), and carbon-based materials (CNT, graphene oxides, etc.) [52,68–73]. Jadhav et al. [69] investigated the effect of incorporating 0.1 wt.% carbon nanoparticles into pure Cu powder. This functionalisation significantly enhanced the laser absorption rate of the Cu powder feedstock, increasing it from 29% to 67% while also improving flowability. The amalgamation of these enhancements led to an increased RD (>98%) in the final L-PBF parts, highlighting the critical role of surface and bulk composition in determining the printability of Cu alloys for L-PBF. Moreover, alloying elements in copper enable the tailoring of their properties to meet specific application requirements; however, trade-offs exist among electrical conductivity, strength (UTS/YS), ductility, corrosion resistance, etc. Nevertheless, careful selection of alloying elements can achieve the desired balance [81]. Additionally, specific alloying strategies can enhance the printability of Cu alloys for AM processes. In the L-PBF Cu–Cr–Nb alloys studied by Dai et al. [82], adding 1 at.% Cr and 0.5 at.% Nb to Cu powder significantly reduced NIR fiber laser reflectivity by 35% compared to pure Cu (Fig. 5). Overall, the incorporation of alloying elements—whether as discrete particles or surface coatings, in macro or nano form, and in varying proportions—has a substantial impact on the reflectivity reduction (%). Following the alloying process, the reflectivity of Cu powder feedstocks ranged between 30 to 70%. In micro-alloying, reflectivity was higher than that of alloys such as Fe, Al, Ti, and Ni (< 40%), whereas, in macro-alloying, reflectivity was similar to alloys such as Fe, Al, Ti, and Ni, though the target material properties of AMed Cu parts also influence the final outcome [82,83]. However, the fabrication challenges of L-PBF are further exacerbated by the higher thermal conductivity of Cu feedstocks (pure Cu ~398 W/m.K and Cu-based alloys: 160–340 W/m.K). This results in rapid heat dissipation from the melt pool, preventing proper melting and potentially introducing process defects. In order to circumvent this challenge, high-power NIR (200-2000 W) or higher VED (> 150-1000 J/mm^3, which is higher than the steel, Al, Ti, and Ni alloys family (< 150 J/mm^3)) is employed, facilitating efficient melting during L-PBF and achieving RD > 99% [50,63,84–86]. However, a key concern when using high-power fibre lasers for printing Cu feedstocks is the increased risk of laser optics damage. This risk stems from back reflection, where a portion of the laser beam reflects towards the source, potentially leading to the peeling of the dielectric coating, reducing the lifespan of the machine and techniques, and increasing operational costs. Jadhav et al. [46] noted dielectric coating flaking off the optics system within 12 h at 1 kW (Fig. 6). Although this was observed for pure Cu, comparable optical damage may occur in Cu alloys in the long run, as their reflectivity decreases by 20-40% compared to pure Cu. This can be validated by additional research for Cu alloys/composites in the future. Beyond optical damage, higher laser power/higher energy density also heightens the risk of printing defects due to melt pool instabilities caused by metal evaporation and the ablation of alloying elements during NIR laser processing of Cu alloys/composites [52]. Simulations have confirmed that such process-induced defects, including closed pore formation, arise from evaporation-driven instability influenced by surface tension and recoil pressure levels [87]. Similarly, L-PBF Cu–Zn alloys exhibit potential loss of alloying elements, particularly Zn, due to the high-power density used (typically 10^5–10^7



Fig. 4. Potential engineering applications of Cu alloys/composites via additive manufacturing [74–80].

W/cm^{-2}). This evaporation of Zn alters the final chemical composition of the printed part compared to the intended alloys. Such variations in composition influence microstructure evolution and compromise the array of properties in the L-PBF Cu alloy/composite parts [47]. An alternative approach to addressing the high reflectivity of Cu feedstocks is to utilise alternative laser sources with shorter wavelengths, such as blue (400–500 nm) and green lasers (500–550 nm) [56,57,88,89]. According to the well-known relationship between wavelength (λ) and energy (E), expressed as $E = hc/\lambda$ (where h is Planck's constant and c is the speed of light), blue and green lasers inherently deliver higher energy per photon. This results in significantly increased absorption (11 to 13 times) and reduced back reflection [90] (Fig. 7). Blue lasers have demonstrated potential in overcoming the limitations of NIR lasers for pure Cu, as Liu et al. [56] reported, with a high relative density of 99.6% achieved using a blue laser. In the future, it would be valuable to investigate the application of blue laser for Cu alloys/composites and explore hybrid laser strategies to address reflectivity challenges and achieve fully dense printed parts. However, their current high cost and potential limitations in beam quality necessitate careful consideration.

Aside from the high reflectivity of feedstock to NIR fibre lasers and the thermal conductivity of Cu powder feedstocks (alloy/composite), powder feedstock characteristics (PSD, composition, physicochemical rheology, O_2 levels, optical properties, etc.) are key to manufacturing fully dense components via L-PBF. These powder feedstock characteristics influence powder-spreading dynamics, laser-powder bed interaction, melt-pool dynamics, etc., resulting in distinct thermal histories and corresponding microstructure, defect formation (powder-related and processing-related), and properties. For Cu–xSn alloys (x = 5, 10, and 15 wt.% Sn), flowability (Hall flow rate: 1.51 s/50 g to 1.29 s/50 g) decreased with increasing Sn content from 5 to 15 wt.%, yet the apparent density increased (3.99 to 4.58 g/cm^3), while maintaining a constant D_{50} (38 μm). This indicates that chemical composition is a critical factor in achieving the optimal powder characteristic, which in turn affects layer consistency and powder bed density [91]. Feedstock characteristics are crucial not only for powder-spreading dynamics but also for attaining fully dense printed parts and superior material

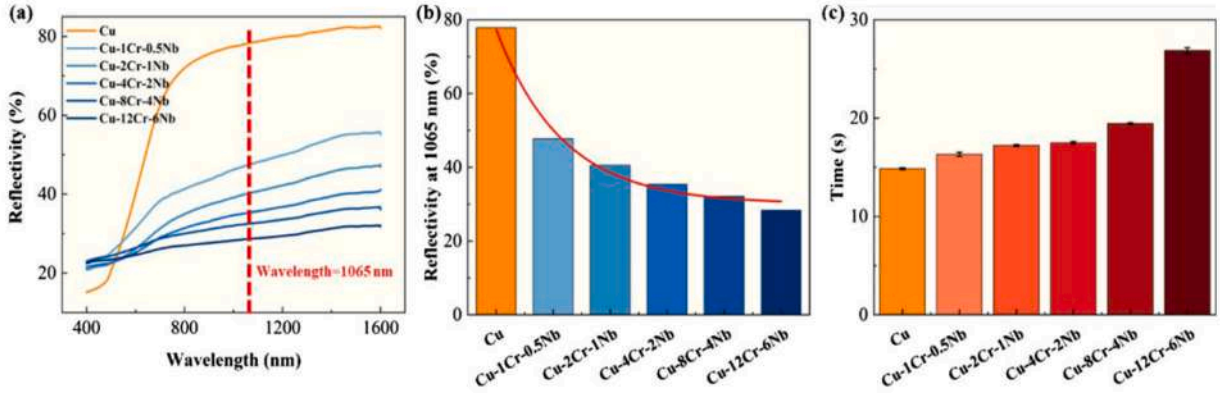


Fig. 5. (a) Variations in the reflectivity (%) of Cu alloys over a range of wavelengths; (b) Variation in reflectivity (%) for NIR fiber laser; (c) Hall flow rate variation with Cu alloys composition [82].

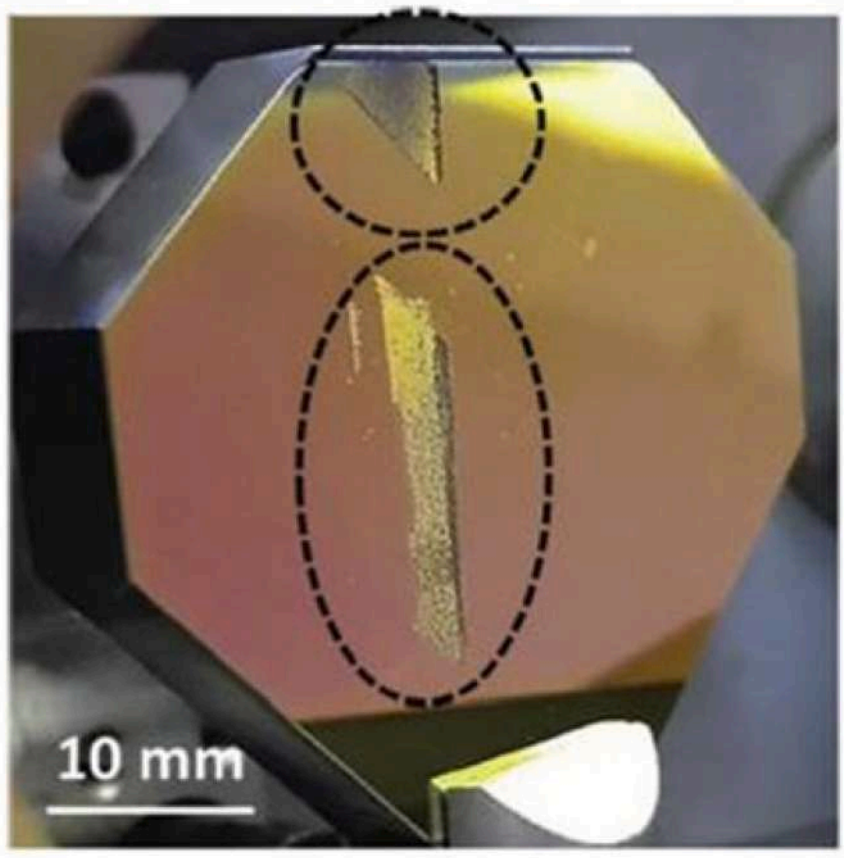


Fig. 6. Damage to optics in L-PBF using a high-power fiber laser (1000 W for 12 h) for copper [46].

properties. Bonesso et al. [92] observed a critical finding: even with the same energy density (514 J/mm^3) applied to different Cu feedstocks (Powders A (19-41 μm), B (8-36 μm), and C (13-28 μm) with varying PSD), the resulting mechanical properties differed. PSD affects not only mechanical properties but also surface quality and RD of parts [92]. Thus, PSD should be incorporated into the optimisation process (process parameters and compositions) to tailor Cu alloys/composites. Additionally, the high specific surface areas of particulate feedstocks, the susceptibility of Cu alloy constituents to oxygen, residual oxygen in the process chamber, and the high temperatures during L-PBF all contribute to an ideal situation for oxidation. This may result in defects and negatively impact the performance of the final product. Ma et al. [93] reported the presence of oxidised spatter particles during L-PBF of Cu–Cr–Zr alloys. The material properties of the L-PBF were compromised by these oxidised spatters, which negatively impacted their wettability, powder reusability, and surface roughness [94]. However, these effects have not been documented in the existing literature for L-PBF Cu alloy, which is crucial for comprehending the role of oxidation. Oxidation can have a deleterious impact on interlayer bonding, as reported for pure Cu, despite having 99% RD, because it acts as a barrier to

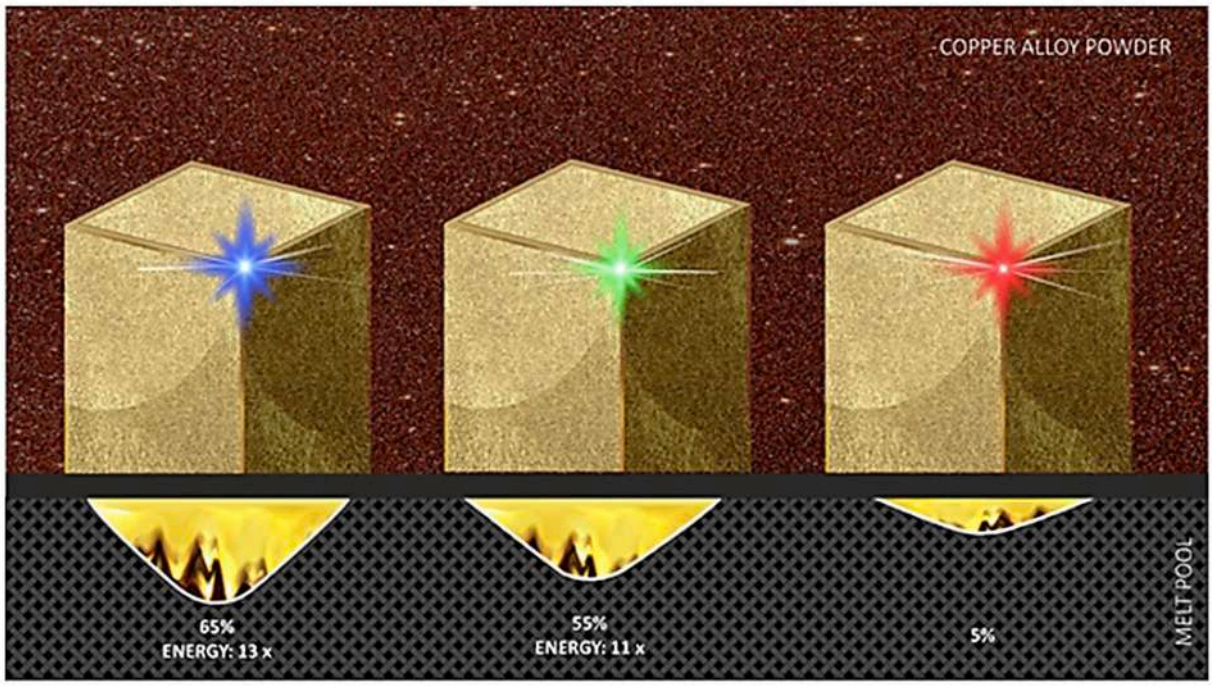


Fig. 7. Effect of laser energy with different wavelengths (blue, green, and red lasers) on the geometry of the melt pool.

wetting [95]. Moreover, spent Cu tracks following L-PBF revealed surface pores caused by gassing the oxide-rich surface layer and intergranular solidification cracking [94]. Future research should explore the critical oxygen levels in L-PBF Cu alloys that could disrupt bonding, induce process defects, and impair material properties. Recent findings suggest that 6000 ppm O_2 in Cu feedstock may be beneficial for both

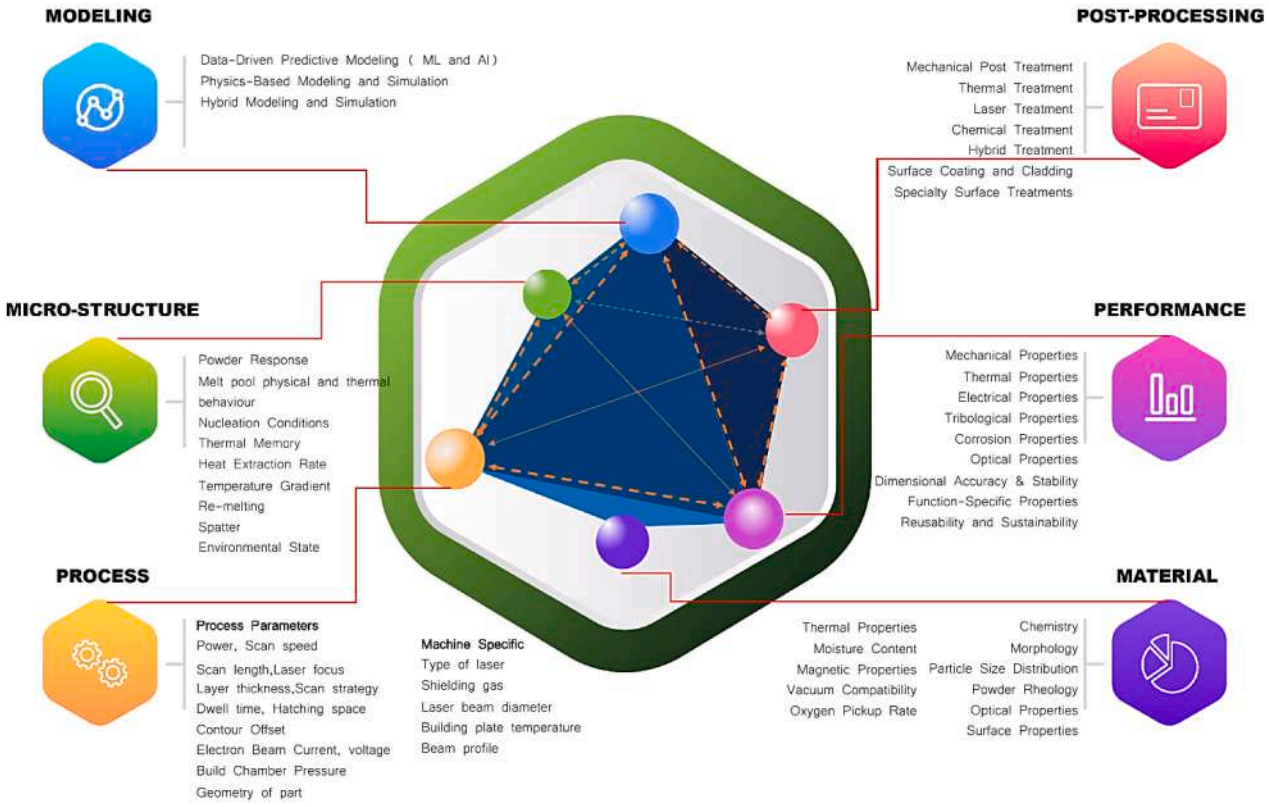


Fig. 8. Mapping the material science octahedron for L/E-PBF Cu alloys/composites: exploring the interplay of composition, process, microstructure, post-processing, performance, and modelling.

mechanical and electrical properties. Additionally, the reusability of Cu powder feedstocks is limited by oxidation, as spent Cu feedstocks exhibited higher reflectivity than virgin feedstocks. However, etching restored the original state [96]. Furthermore, the long-term storage (1 year) of Cu feedstock resulted in increased oxygen levels in Cu–Cr feedstocks (2200 ppm), which could alter flowability and melt pool stability [54]. This highlights the need for further research into the long-term effects of powder storage on powder-spreading dynamics, melt pool stability, etc., as well as the development of viable methods for reusing L-PBF Cu alloy powder feedstock to reduce feedstock costs, given the high expense of atomised feedstock. High-temperature preheating during L-PBF for pure Cu oxidised unfused powder at 400°C resulted in agglomerates, unfused powder oxidation, and oxide layers (1–3 μm thick) with a significantly higher oxygen content (10,000–14,000 ppm) compared to virgin powder (4600 ppm) [95]. This should be considered in future studies when printing Cu alloy components using high preheating temperatures via L-PBF (> 200 °C). On the other hand, limited oxygen (max. < 6000 ppm) enhanced laser absorptivity while maintaining flowability (oxide film undermines cohesive forces). Laser absorptivity and flowability (AoR reduced from 44.6° to ~51.5°) were enhanced by the Zr oxide layer as the Zr content increased (0.01 to 0.19 wt.%) in the Cu–Cr–Zr feedstock, as observed by Zhou et al. [97]. Additionally, the limited oxygen solubility of approximately 0.0002 wt.% in Cu is conducive to the expulsion of excess oxygen from the supersaturated solid solution and the formation of nanoprecipitate, as noticed for L-PBF Cu–O alloys (6000 ppm) [98]. Although oxidation did not significantly affect flowability and processability for L-PBF Cu–Cr–Zr and Cu–O alloys, further research is necessary to understand the impact of oxygen on the processability and flowability of other novel copper feedstocks, Cu–Ag, Cu–Zn, Cu–Sn (other oxide formations beyond CuO and Cu_2O, the free energy of the formation of oxides such as ZrO_2, SnO_2, etc. are lower, as evidenced by the Ellingham diagram [99]), etc. Overall, it is imperative to comprehend the behaviour of Cu powder feedstocks, driven by their characteristics, to address the performance and reproducibility challenges of defect-free L-PBF Cu alloy/composite parts.

A further challenge in printing Cu alloy/composite parts with L-PBF is optimising process parameters; otherwise, the presence of process defects can significantly deteriorate the array of properties in the printed parts. The complex melt pool dynamics, high susceptibility to back reflection, and potential for element evaporation during L-PBF limit the processing window for Cu alloys/composites. This necessitates the careful optimisation of laser power, scanning speed, and other process parameters to achieve successful melting, minimise defects, and ensure denser parts. The accompanying 'materials science octahedron' (Fig. 8) illustrates the role of process parameters in conjunction with other variables. The process, microstructure, performance, and post-processing are all supported by the material at the base of the 'materials science octahedron,' which indicates the relationship of material-process-microstructure-performance. However, several factors significantly impact the L-PBF of Cu alloys/composites for producing fully dense parts with tailored performance and functionalities. Laser power directly controls melting depth and melt pool size. Scanning speed balances complete melting with well interlayer bonding by adjusting dwell time. Hatch spacing, the gap between scan lines, influences interlayer bonding, defect formation, and density. Layer thickness affects resolution and surface finish. Finally, an inert atmosphere, such as argon, helps control oxidation to avert modifications in printability. Zhang et al. [48] observed a trade-off between energy density and RD for Cu–Al–Ni alloy. The lower energy density (low power/high hatch spacing/low exposure time) resulted in a lack of fusion (LoF) defects and ~95% RD. In comparison, high energy density (high power/low hatch spacing/high exposure time) caused keyhole porosity with ~98% RD and thermal cracks. Conversely, using high laser power (> 350 W) with a high scanning speed (1.25 m/s) led to balling defects and a discontinuous melt pool [48]. Corona et al. [100] investigated layer thickness between 10 and 40 μm for L-PBF Cu alloys but did not prioritise optimising layer thickness. They selected a 10 μm layer thickness with 175 W power based on the assumption that lower layer thickness and higher power would lead to higher energy density during L-PBF [101]. However, their results showed 91% RD in parts. This suggests that optimising both laser scanning speed and hatch spacing, in conjunction with layer thickness, is likely crucial for attaining the highest possible RD in Cu alloy/composite parts via L-PBF. Moreover, increasing layer thickness in L-PBF Cu–Ni–Si alloy led to higher porosity levels, regardless of the specific PSD and composition. Conversely, for a constant layer thickness (20 μm) with a similar PSD (10-45 μm), the alloy composition became the dominant factor influencing porosity levels [102]. This is further supported by the observation that alloying pure Cu significantly reduces porosity. Studies reported a decrease from 25.4% porosity in pure Cu to 6.6% porosity in the Cu–1.5Ni–Si alloy and 5.5% porosity in the Cu–3Ni–Si alloy (with a wider freezing range and lower Gibbs energy of melting), all fabricated with identical process parameters (layer thickness of 20 μm, PSD of 10-45 μm, hatch distance of 36 μm, laser power of 95 W, and laser speed of 200 mm/s). Apart from printing dense components, the meticulous selection of process parameters is crucial for tailoring the microstructure of L-PBF Cu alloys/composites. The type of scanning strategy, scanning parameters (power, speed, etc.), build direction (BD), and base plate temperature also influence the anisotropy of L-PBF Cu alloys [103–105]. This directional dependence arises from crystallographic texture, where specific grain orientations become preferential during solidification. Jóźwik et al. [103] demonstrated significant microstructural variations in the Cu–3Ni–1Si alloy processed with different deposition strategies, even at a constant energy density (83 J/mm^3). These variations occurred due to the influence of scanning speed, power combination, and distinct scanning strategies (320 W, 1067 mm/sec, and 340 W, 1133 mm/sec) on the solidification direction and temperature gradients inside the melt pool. Zhang et al. [48] noted crystallographic texture in L-PBF Cu–10Zn alloys, where the α-Cu phase formed elongated columnar grains. These grains were much more prominent along the build direction (e.g., vertical) than in other directions (e.g., horizontal). The root cause lies in the distinct thermal histories experienced by different build orientations during printing. Components built parallel (horizontal) or perpendicular (vertical) to the substrate undergo distinct heating and cooling cycles. These thermal variations influence ultimate microstructures, resulting in anisotropy in mechanical and electrical properties, etc., in the printed parts. Thus, the first strides towards bespoke performance of L-PBF Cu alloy with lower anisotropy lie in the optimisation of process parameters. Nevertheless, optimising these process parameters remains an intricate challenge for Cu alloy/composite L-PBF due to the enormous number of potential combinations (2000 possible combinations for 5 laser power, 10 speeds, 10 hatch spacings, and 4-layer thicknesses). Researchers have investigated numerous statistical techniques for the design of experiments (DOE) approaches [57], including response surface methodology (RSM) [91,93], full factorial design [106], central composite design (CCD) [93], and Taguchi design methods [107] to optimise process parameters of L-PBF Cu alloys/composites and minimise the number of fabrications/experiments. In addition to the statistical approach, empirical methods, such as trial and error, heuristic techniques, etc., are also employed to optimise process parameters for copper alloys. However, the statistical and empirical approaches are not always consistent due to the limited number of parameters and the complex in-process dynamics that are often not accounted for in the analysis. Thus, in the future, machine learning methods (Gaussian process regression (GPR), Bayesian optimisation (BO), etc.) combined with advanced characterisation tools (defects at an early stage) and numerical modelling approaches can be employed to optimise the process parameters of L-PBF Cu alloy/composite.

Printing L-PBF Cu alloys/composites presents a unique set of challenges. One such challenge is regulating the relative volume fraction of equiaxed to columnar grains from the interior of the melt pool to its

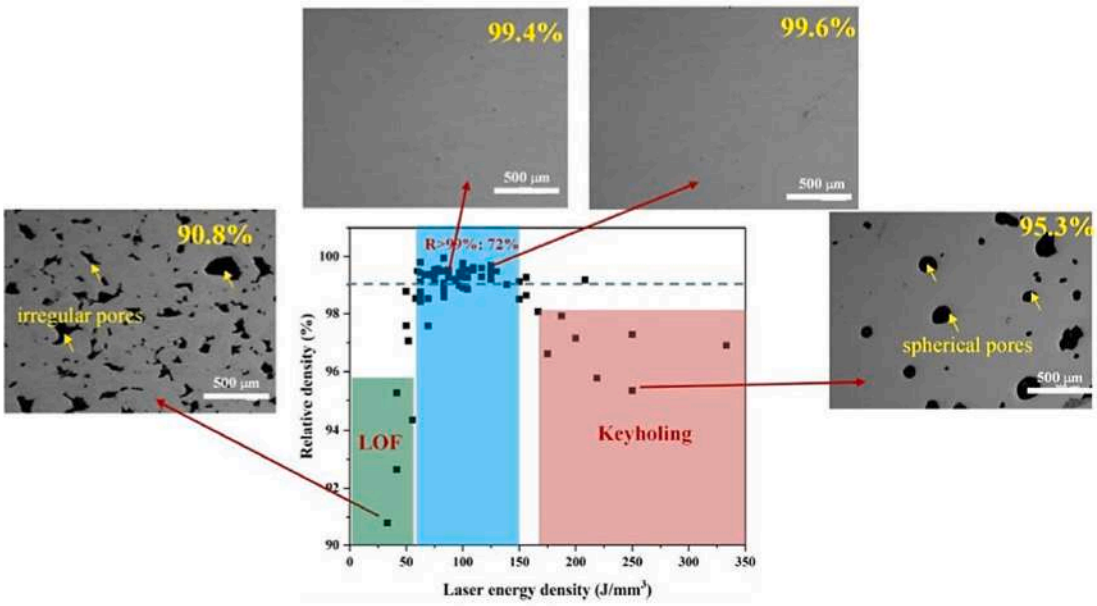


Fig. 9. The trade-off between volumetric energy density and relative density in Cu alloys L-PBF [111].

boundaries, as well as their spatial distribution. This regulation is crucial for achieving the envisioned microstructures for engineering applications, ensuring site-specific properties and superior performance. The process of localised laser-metal powder feedstock interactions during L-PBF Cu alloys/composites is marked by complex and dynamic multi-physics phenomena, including heat transfer, fluid dynamics, and phase transitions from melting to solidification. Upon solidification, the multi-scale microstructures (macro-, meso-, micro-, and nano-scale) form in L-PBF Cu alloys/composites, which in turn induce varying degrees of anisotropy. These microstructure characteristics range from dendritic, non-dendritic columnar grains to equiaxed grains with nano precipitate and dislocation cell walls, etc., along the build direction, leading to anisotropy in material properties of L-PBF Cu alloys/composite components [108,109]. This microstructure evolution is primarily governed by the local temperature gradient (G), the solid-liquid interface migration velocity (R), and interface undercooling, which promote the columnar to equiaxed transition (CET). These parameters can be altered by modifying process parameters and composition. For instance, L-PBF Cu–Co revealed morphological transitions with changes in composition (Co: 2 to 8 wt.%) while maintaining optimal process parameters (power of 375 W, speed of 400 mm/s, layer thickness of 30 μm) for all compositions. Columnar grains (20–160 μm in width and 180–560 μm in length) and an overall average grain size ranging from 23 to 25 μm were observed, attributed to epitaxial growth analogous to L-PBF Cu–Ni–Sn, Cu–Ni–Si, Cu–Cr–Nb, and Cu–Cr alloys, with 2 and 4 wt.% Co. In contrast, 6 and 8 wt.% Co exhibited a higher fraction of equiaxed grains in the solidified microstructure, with an average grain size below 2 μm, due to the higher heterogeneous nucleation rate induced by in-situ formed cobalt oxides, ultimately resulting in superior mechanical properties [29]. A similar transition was observed for L-PBF Cu–Cr–Zr + Y_2O_3, where the ex-situ addition of Y_2O_3 particles (as opposed to in-situ incorporation) promoted equiaxed grains, reduced grain size (from 28.9 μm to 13.1 μm), and improved HAGBs (from 36.9% to 42.3%), resulting in a strength-ductility synergy [110]. Consequently, it is imperative to regulate the volume fraction of columnar to equiaxed grains in order to manage the microstructural anisotropy of L-PBF Cu alloy/composite components, improving performance by addressing the strength-ductility, strength-conductivity trade-off and minimising anisotropy in material properties of printed Cu alloy parts.

As previously noted, printing defect-free L-PBF Cu alloy/composite components remains challenging due to a narrow processing window for specific Cu alloy compositions, which is contingent upon feedstock characteristics and process parameters. Fig. 9 demonstrates that LoF occurs in printed parts at low energy density (below 60 J/mm^3), resulting in a reduction of the RD to 90.8%. In contrast, at higher energy densities (above 150 J/mm^3), keyhole defects develop, further reducing the RD to 95%. The optimal energy density for the L-PBF Cu alloy achieves over 99% RD, emphasising the necessity for stringent control of process parameters to ensure defect-free parts, as evidenced by the inverted V-shaped fluctuation in RD. This highlights the narrow window available for printing defect-free parts. Therefore, it is essential to develop new Cu alloy/composite compositions with a broader processing window in the future for defect-free printed components, even though process optimisation and ML/modelling techniques have been explored to overcome this challenge.

The reheating and remelting of pre-deposited layers in L-PBF Cu alloy/composite at a high cooling rate ($> 10^4$ K/s) result in an inhomogeneous microstructure and alterations in material properties due to supersaturated solid solutions, variation of phase fractions, residual stress, etc., resulting in trade-offs between strength-ductility and strength-conductivity, along with anisotropic properties in AB L-PBF Cu alloy/composite components. Consequently, post-printing heat treatment is often required, particularly for heat-treatable Cu alloys, to disrupt the strength-ductility trade-off and strength-electrical conductivity trade-off and diminish component anisotropy [112]. However, achieving bespoke performance directly after L-PBF Cu alloy printing is formidable. To address post-printing limitations, researchers have explored accelerated in-situ precipitation to tailor the performance of as-printed Cu alloys. Yang et al. [113] reported a high UTS of 444 MPa and ductility of 22% in the as-built state of the Cu–Cr–Nb–2Fe alloy, attributed to the Nb(FeCr) core-shell nanostructure, which induces a significant precipitation effect. In the future, eliminating post-processing procedures, particularly heat treatment, should be prioritised to develop high-performance printed parts, reducing the development cycle and enabling the direct deployment of L-PBF printed Cu alloy/composite components. Finally, the size limitation of L-PBF Cu alloy/composite components—primarily constrained to dimensions below 200 mm × 200 mm × 300 mm—poses a barrier to the realisation of larger copper alloy/composite parts, necessitating further advancements in the field.

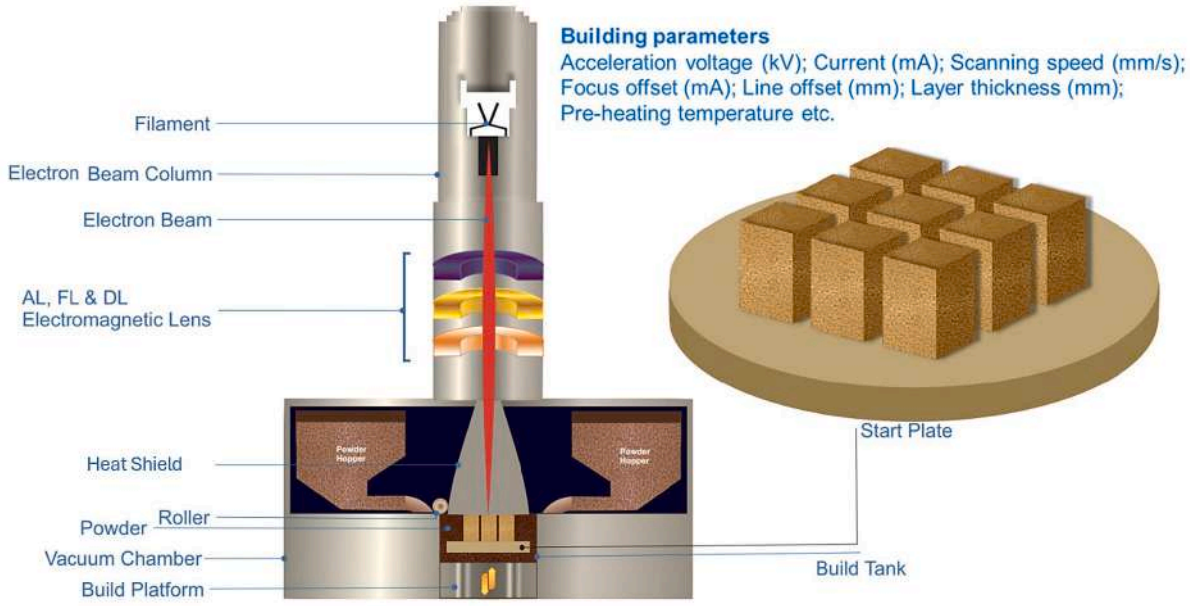


Fig. 10. Schematic of E-PBF with build variables (AL, FL, DL: astigmatism lens, focus lens, and deflection lens, respectively).

In a nutshell, the successful fabrication of Cu alloys/composites via L-PBF necessitates a delicate interplay between process parameters and feedstock characteristics. The primary challenges in developing fully dense Cu alloy parts include the reflectivity/thermal conductivity of Cu-based feedstock, process parameter optimisation, the formation of stochastic process defects, microstructural and material properties anisotropy, trade-offs in material properties, the necessity for post-processing heat treatment, and limitations in the size of printed parts. However, by carefully selecting Cu alloy/composite feedstocks and optimising process parameters, these challenges can be mitigated, enabling the fabrication of bespoke Cu alloy/composite components using L-PBF. Furthermore, despite the promise of L-PBF, AMed Cu alloys and composites exhibiting a combination of higher UTS (> 700 MPa), ductility (> 40%), and electrical conductivity (> 70%International Annealed Copper Standard (IACS)) have yet to be realised. By strategically employing alloying strategies, optimising process parameters, and implementing post-printing heat treatments in the future, L-PBF technology holds the potential to produce fully dense Cu alloy/composite parts with a wider spectrum of tailored properties and enhanced performance.

5. Electron beam powder bed fusion of copper alloys/composites

E-PBF, also known as electron beam melting (EBM) or selective electron beam melting (SEBM), utilises a focused high-energy electron beam (1 kW for the Cu system) to melt metal powder in a vacuum environment (Fig. 10). This technology, initially commercialised by Arcam AB, offers over 80% absorption for Cu alloys and composites, resulting in complete melting compared to L-PBF, which favours high-density Cu alloy printed parts [61,114]. Firstly, the metal powder (20-110 μm) is spread evenly across the build plate, with layer thickness typically ranging from 40 to 200 μm [114]. The defocused beam, operating at a high scanning speed (5 to 20 m/s) and beam current (10 to 50 mA) with a larger diameter, allows for preheating to reach the desired temperature of the build platform (from 400 to 600 °C), which varies depending on the Cu feedstock characteristics [115]. The preheating reduces smoking, increases powder bed conductivity, alleviates thermal stress, improves microstructure control, and provides in-situ heat treatment and defect reduction, although it negatively impacts the manufacturing time of the printed component. Following the preheating, a focused electron beam selectively melts the powder layer, with a varying range of process parameters, including scanning speed (0.5 to 3.5 m/s), beam current (4–17 mA), focus offset (5 to 15 mA), etc. Finally, a new layer of powder feedstock is then applied on top of the previously solidified layer for the next melt cycle until the 3D geometry of the component is formed. Moreover, the vacuum condition during processing reduces powder oxidation and contamination hazards, although it also leads to the evaporation of volatile constituents in alloys, which future research may validate for the Cu system [115]. Overall, E-PBF with copper alloys/composites offers advantages over L-PBF, including the absence of reflectivity concerns associated with copper alloys, no/less residual stress (high temperatures throughout the printing), improved microstructure control, etc.

Analogous to L-PBF, optimised process parameters are essential for achieving fully dense and preferred microstructures, as well as defect-free Cu alloy components. In the E-PBF of Cu alloys/composites, denser specimens (RD > 99%) were produced by using higher beam currents (9 and 12 mA), whereas specimens with RD > 97% were produced by using a lower beam current (6 mA). This indicates that higher beam currents, when matched with optimised power, can improve the RD and, potentially, the material properties of the E-PBF parts [59]. Additionally, higher beam current (and heat input) promoted the formation of zigzagged columnar grains within the material, reducing the presence of equiaxed grains [116]. Moreover, the relative density of the E-PBF Cu–Cr–Zr alloy parts initially increased and subsequently decreased as the scanning speed increased (with optimised heat input) [57]. However, the overall material properties were compromised by insufficient heat input resulting from high scanning speed and low power, which caused voids and weak spots. Conversely, slow scanning speed with high power led to excessive melting [57,58]. On the other hand, the scanning speed also influenced elemental distribution. Cr elements were more evenly distributed at slower rates, forming more prominent and homogeneous Cr spheres in the melt pools for E-PBF Cu–Cr alloy. Higher scanning speeds, however, produced a more random distribution of smaller Cr spheres, demonstrating that melting and solidification rates affect grain size and homogeneity [117]. Furthermore, simulation results suggested that the amount of heat input determines the degree of melting and the defectiveness of growing crystals, conditioning the final grain structure [118]. Adjusting the focus

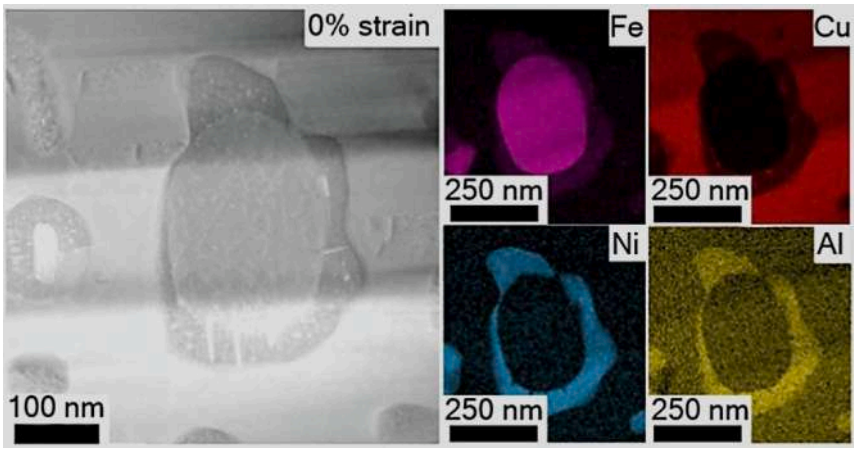


Fig. 11. HAADF-STEM micrograph demonstrates a peculiar iron core enveloped by a Ni shell for the precipitate (size: 440 ± 78 nm) in the Cu matrix of E-PBF [23].

offset during the E-PBF process also impacted the density of the produced samples. A narrower focus offset resulted in higher densities, suggesting its importance in producing defect-free, high-density parts [61]. Lu et al. [23] emphasised the importance of powder feedstock characteristics in achieving the dense part, as the RDs (%) of small (45-63 μm), medium (63-75 μm), large (75-105 μm), and mixed (45-105 μm) powders were 95.8, 99.7, 99.6, and 99.7, respectively. This underscores the necessity of meticulous tuning of process parameters and feedstock characteristics during E-PBF of Cu alloy/composite for process stability, enabling the production of defects-free with customised microstructures. In the future, this challenge may be resolved by utilising real-time feedback control of the process with AI to optimise process parameters.

The control of microstructure remains a daunting challenge responsible for the anisotropy of printed parts. However, E-PBF has shown potential in minimising this issue, in contrast to L-PBF Cu alloy/composite. The E-PBF NAB alloy demonstrated a 6.7% variation in YS, a 1.6% variation in UTS, and a -6.5% change in ductility between horizontal and vertical orientations [23]. E-PBF not only reduces microstructural anisotropy but also enables the printing of components in an as-built state with excellent mechanical properties. In the AB state, the UTS of the NAB alloy printed using L-PBF was 1123 MPa, with ductility of 2.7%, in contrast to the E-PBF printed part, which exhibited a higher ductility of 35% and a UTS of 1023 MPa [23,119]. Thus, E-PBF has shown the potential to address the strength-ductility trade-off in printed parts. Furthermore, E-PBF offers distinct advantages over L-PBF in terms of cooling rate and high substrate temperature, which enhance microstructural control and ultimately influence phase fraction, grain morphology, etc., in E-PBF fabricated parts. For instance, Lu et al. [23] identified a unique core-shell precipitate morphology (iron-rich core with a NiAl shell) in the E-PBF processed NAB alloy, which was not observed in the L-PBF NAB alloy, as shown in Fig. 11, which disrupted the strength-ductility trade-off in the AB state. Li et al. [120] observed in-situ precipitation due to the elevated build temperature (400 °C–600 °C), which yielded an exceptional amalgamation of mechanical and electrical properties in the E-PBF Cu–Cr–Zr alloy, with a UTS of 250 MPa and electrical conductivity of 70% IACS in the AB state, not reported for the L-PBF Cu–Cr–Zr alloy, demonstrating the potential to disrupt the strength-conductivity trade-off of AMed Cu alloy/composite parts. In conclusion, E-PBF holds the potential to print Cu alloy/composite parts with minimal anisotropy, offering superior material properties such as strength-ductility and strength-conductivity synergy.

Process-induced defects also present challenges in E-PBF Cu alloys due to the characteristics of feedstocks and improperly calibrated process parameters. The reduced LED (300 J/m) for copper alloy indicated the presence of pores, leading to reduced RD (< 99%) of printed Cu alloy components and negatively impacting the material properties [120]. For E-PBF Cu–50Cr alloy, higher energy density established a stirring effect in the molten pool, resulting in many tiny pores due to gas trapping, while lower energy density (<51 J/mm^3) caused warping [121]. Aside from process parameters, as the electron beam scans the powder bed, electrons may accumulate on the powder particle, leading to smoking. This results in powder spatter and beam obstruction, influencing defect formation and part performance. To mitigate this, the vacuum chamber is filled with inert helium gas at 10^{-1} Pa during melting and preheating to neutralise powder electrical charges and reduce smoking [23]. The exact cause of powder smoking during E-PBF remains under debate; however, some research suggested that residual water, momentum transfer, etc., may contribute to smoking [122]. Although no studies have documented smoking during the E-PBF printing of Cu alloy parts, future investigations should examine the oxidation threshold, particularly for reusable Cu alloy feedstock in E-PBF, beyond which smoking commences.

The necessity for post-printing heat treatment is not a major concern in E-PBF; however, further enhancement in E-PBF Cu alloys has been observed due to in-situ heat treatment resulting from the elevated build temperature. Following heat treatment, the Cu–Cr–Zr alloy exhibited conductivity exceeding the International Thermonuclear Experimental Reactor (ITER) specifications (>350 W/mK), a feat that is rarely achievable with L-PBF, even after post-treatment [61]. Additionally, the E-PBF-fabricated NAB alloy exhibited superior corrosion resistance in the AB state as compared to its casting counterparts. This highlights the potential of E-PBF to circumvent the need for post-printing heat treatment, thereby expediting the Cu alloy/composite product development process. Finally, E-PBF is limited by part size compared to the L-PBF process.

In summary, the primary challenges associated with E-PBF Cu alloy/composites include the optimisation of process parameters, the selection of feedstock, and the elimination of defects to achieve nearly fully dense Cu alloy/composite components. Currently, E-PBF has been explored primarily for Cu–Cr, Cu–Ag, Cu–Al, Cu–Cr–Zr, and NAB alloys, despite its advantages such as the absence of reflectivity concerns, capability for microstructural manipulation, elimination of post-printing heat treatment, etc. [123]. Future advancements are poised to concentrate on the development of novel E-PBF-compatible feedstocks that not only elevate material properties but also overcome the inherent trade-offs between strength and conductivity, as well as strength and ductility. Furthermore, a deeper understanding of the interrelationship between the processing parameters-microstructure-properties nexus is needed, given that the larger melt pool in E-PBF, compared to L-PBF, leads to distinct solidification dynamics and microstructural evolution. Additionally, future studies should explore comparative assessments between electron beam and laser-based processing—particularly green lasers—using identical feedstocks to evaluate their respective potentials. Moreover, the impact of microstructural variations on material performance, such

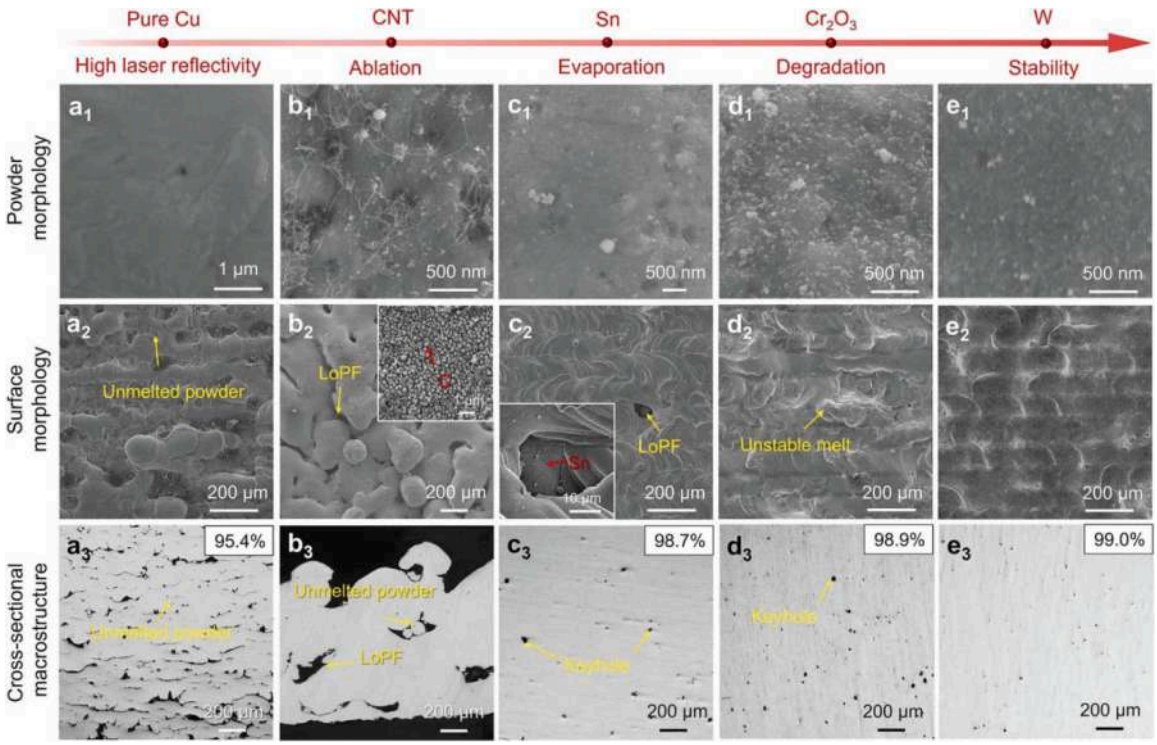


Fig. 12. Correlation between the defect propensity, feedstock composition, and surface morphology in L-PBF Cu alloys (a_1-a_3) Pure Cu; (b_1-b_3) Cu with CNT; (c_1-c_3) Cu–Sn; (d_1-d_3) Cu–Cr_2O_3; (e_1-e_3) Cu–W [52].

as fatigue, in E-PBF Cu alloy/composite components should be examined to assess the long-term structural reliability of parts. Finally, the sustainability of powder reuse in E-PBF warrants investigation, considering the elevated preheat temperatures and the susceptibility of copper alloys to oxidation.

6. Preparation of powder feedstock for L/E-PBF

The entire voyage from powder to build for L/E-PBF begins with feedstocks, which play a crucial role in the material-structure-property relationships. This underscores the paramount importance of feedstocks in controlling the processing, microstructure, and performance of L/E-PBF Cu alloys/composite parts. The overarching objective is to design Cu alloy/composite feedstocks for L/E-PBF that possess the desired microstructure and a broader processing window while also preserving the material properties of nearly fully dense printed parts—potentially by reducing or eliminating process defects—for emerging engineering applications. The need for meticulous oversight of feedstock characteristics is emphasised by the complexity of laser/electron beam-powder interactions, which begin as the Cu alloy/composite feedstock powder is spread for printing. These interactions are primarily governed by feedstock characteristics such as chemical composition, PSD, packing density, morphology, flowability, cohesion between powder particles, powder rheological properties, etc. Beyond the laser/electron beam-powder interaction, the complex multi-physics of melt pool dynamics prevalent in powder bed fusion AM dictate the microstructure and defect propensity. These are influenced by factors such as chemical composition, thermophysical properties of feedstocks, vapourisation and wetting of alloying elements, etc. The processes of evaporation, ablation, and reflectivity to the NIR laser during melting are sensitive to Cu alloy/composite feedstock composition, influencing the propensity for defects and, ultimately, the performance of L-PBF Cu alloys/composites, as illustrated in Fig. 12. Furthermore, feedstock chemical compositions also influence the post-printing heat treatment parameters (time and temperature). Finally, feedstock composition determines the fundamental characteristics of the printed parts, ranging from mechanical to functional properties.

The characteristics of Cu alloy/composite powder feedstock primarily entail two components (particulate properties and bulk properties): particulate properties include morphology (shape, size, and surface texture/roughness), chemical composition (bulk chemistry and surface chemistry), reactivity, thermophysical properties, etc.; and bulk properties encompass apparent density, PSD, flowability, spreadability, and rheological properties. Initially, Cu powder feedstock spreads over the powder bed, where bulk properties play a critical role in achieving uniform and optimised properties of the powder bed (homogeneity and thermal conductivity, etc.). These properties are primarily influenced by the chemical composition of the feedstocks, which is central to the design of Cu alloy/composite feedstocks through "material modification" to address the high reflectivity of NIR fibre lasers. Salvan et al. [124] examined the effects of hydrogen, argon, and oxidation treatments on virgin Cu–Cr–Zr feedstocks and found that oxidation treatment improved both flowability (lowest avalanche angle: virgin powder (59°) > argon heat treatment (59°) > hydrogen heat treatment (44°) > oxidation treatment (32°)) and absorptivity (highest absorptivity: hydrogen heat treatment (41%) < virgin powder (53%) < argon heat treatment (56%) < oxidation treatment (69%)) for NIR laser. The flowability of feedstocks with identical chemistry can be significantly influenced by the amount of alloying elements. In Cu–xSn alloys (x: 5, 10, 15 wt.%), Cu–10Sn alloy exhibited the highest flowability [91]. Likewise, adding 0.05 wt.% carbon to Cu–0.3Cr feedstock increased absorptivity (56%) but reduced flowability (as the Hall flow rate increased from 16.1 to 13.6 s/50 g) compared to Cu–0.3Cr alloy. Despite the increased Hall flow rate, carbon-mixed Cu feedstocks demonstrated acceptable flowability, as the dynamic angle of repose (AoR) remained below 40° (as for pure Cu AoR 43° and unable to flow from the Hall flow meter) [125]. Furthermore, particulate properties modified by feedstock preparation techniques influenced the morphology of the powder, which in turn affected the flowability of the feedstocks. To mitigate morphological discrepancies, a coating technique was investigated as an

Table 2
L/E-PBF Cu powder feedstocks design: a comparison of mechanical mixing and pre-alloyed approaches.

S. N.	Chemistry	Powder route	Morphology (size μm)	Defects	Composition for printing	%RD (>99.0)	Ref.
Mechanical mixing approach							
1	Cu–10Sn	AGA	Spherical (15.3)	Agglomeration	Cu–15Ni–8Sn	Yes	[134]
	Ni	-	Irregular (2.0)				
2	Cu	-	Spherical (15.0-53.0)	Homogeneous distribution and adhesion of Co	Cu–xCo (x: 2.0, 4.0, 6.0 and 8.0 wt.%)	Yes	[29]
	Co		Nearly spherical (0.7–1.0)				
3	Cu	GA	Spherical (52.1)	Non-homogeneous distribution with higher Ag	Cu–xAg (x:10, 20, 30)	No	[144]
	Ag	GA	Spherical (30.2)				
4	Cu	-	Dendrites	-	Cu–25Cr	-	[123]
	Cr	-	Blocky				
5	Cu	GA	Spherical (15.0-45.0)	Cr-rich phase owing to inhomogeneous mixing of powder	Cu–xCr (x: 20, 25)	Yes	[145]
	Cr	-	Irregular (10.0)				
6	Cu	-	45.0	-	Cu–10Fe	-	[146]
	Fe–12Cr–1Mo–1V		45.0				
7	Cu–P	-	45.0	-	Cu–Fe–P	-	[28]
	Fe		20.0				
8	Cu	GA	Spherical (15.0-53.0)	Fe segregation was eliminated after L-PBF	Cu–8Fe	Yes	[26]
	Fe	-	Non-spherical (1.0-9.0)				
Pre-alloyed powder approach							
9	Cu–10Sn	N_2 GA	Spherical (85.0)	-	Cu–10Sn	Yes	[21]
10	Cu–xCr (x: 1.3, 2.5)	-	Near spherical (24.0)	-	-	Yes	[125]
11	Cu–36.8Fe	GA	Near spherical (18.6)	-	Cu–36.8Fe	No	[27]
12	Cu–11.8Al–3.2Mn–0.1Ti	GA	Nearly spherical (38.3)	Some oval or non-circular powders	Cu–11.5Al–2.4Mn–0.1Ti	-	[147]
13	Cu–15Ni–8Sn	AGA	Spherical (15.4)		Cu–15Ni–8Sn	Yes	[134]
14	Cu–15Ni–8Sn–0.3Nb	GA	Spherical (35.0)	-	Cu–14.5Ni–7.8Sn–0.3Nb	-	[148]
15	Cu–0.1P	AGA	Spherical (18.0)	-	-	No	[100]
16	Cu–0.1Zn	AGA	Spherical (14.0)	-	-	No	[100]
17	Cu–3.4Cr–0.6Nb	AGA	Spherical (61.0 ± 12.0)	-	-	Yes	[149]
18	Cu–3Ni–1Si	AGA	20.0–63.0 μm	No intermetallic phases	-	No	[103]
19	Cu–15Ni–8Sn	N_2 GA	Spherical (10.2)		Cu–15.2Ni–7.9Sn	-	[150]
20	Cu–13.2Al–3.5Ni	GA	Nearly spherical (31.5)	Fewer satellite particles, no segregation	Cu–13.2Al–3.5Ni	Yes	[111]
21	Cu–0.3Zr–0.1Ag	-	Nearly spherical (61.0)	-	Cu–0.2Zr–0.1Ag	Yes	[59]
22	Cu–15Sn	GA	Spherical (33.0)	Fewer satellites	Cu–15Sn	Yes	[21]
23	Cu–xSn	GA	Spherical (36.0-38.0)	-	Cu–xSn (x: 5, 10 and 15 wt.%)	Yes	[91]
24	Cu–10Zn	AGA	Spherical (29.4)	-	Cu–11.7Zn–0.9O	Yes	[47]
25	Cu–7.2Ni–1.8Si–1Cr	N_2 GA	Spherical (24.1)	Small particles with clusters and large particles with satellite.	Cu–7.5Ni–1.8Si–0.9Cr	Yes	[151]
26	Cu–1Cr–Zr	AGA	Spherical (42.1)	Occasional satellite formation	Cu–0.7Cr–0.1Zr	Yes	[152]
27	Cu–12.9Zn–2.5Si	AGA	Spherical (26.1)	-	-	Yes	[153]

AGA: Argon gas atomisation.

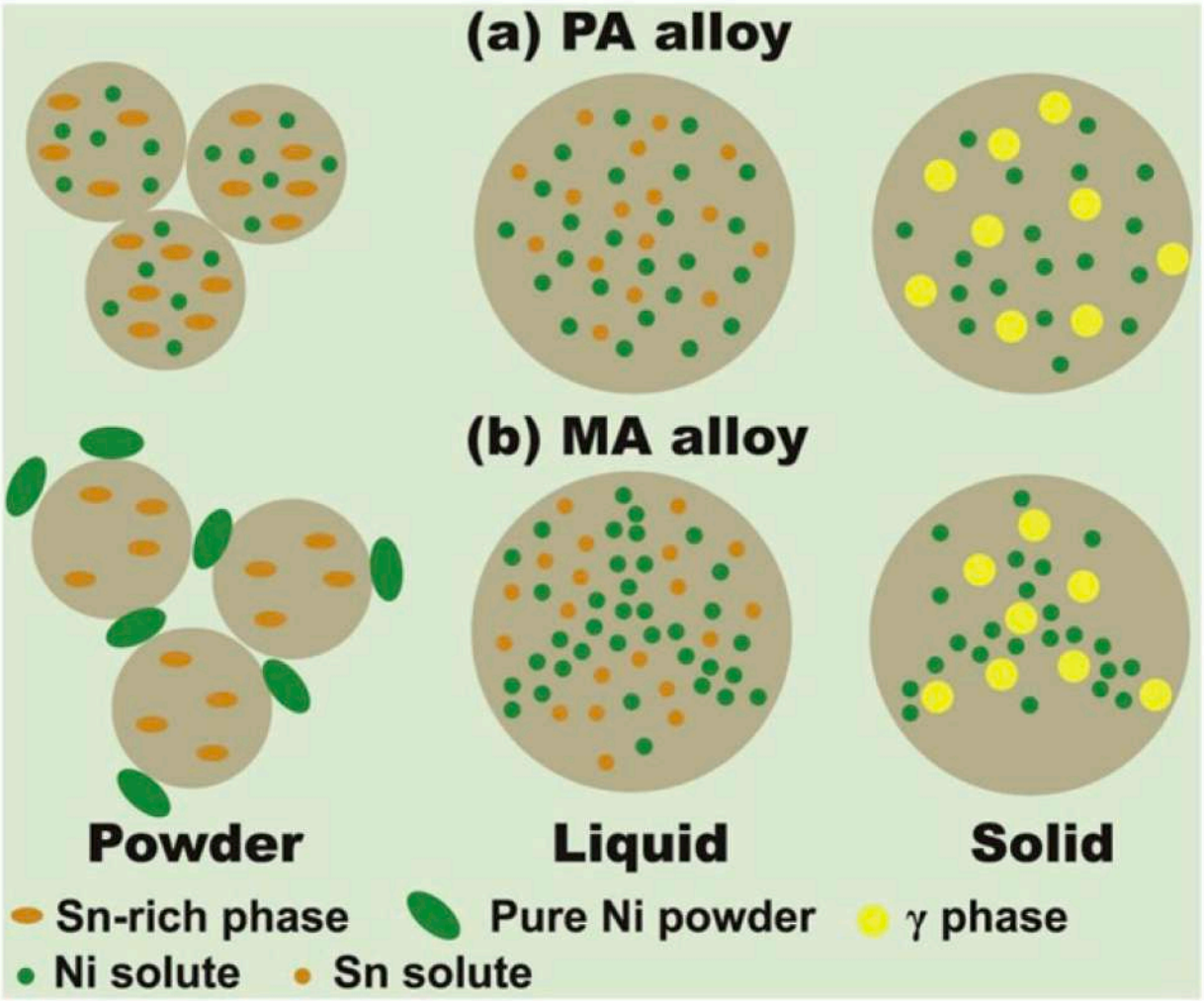


Fig. 13. Schematic illustration of phase distribution in L-PBF Cu alloys following solidification (a) pre-alloyed; (b) mechanically mixed powders [134].

alternative to mechanical mixing for feedstock design to address NIR laser reflectivity. Y_2O_3-coated Cu–Cr–Zr feedstock demonstrated increased absorptivity (from 32.8% to 61.2%) while maintaining flowability (Hall flow rate: 21.4 s/50 g than 21.2 s/50 g virgin) [110]. Thus, both the bulk and particulate properties of Cu feedstock are crucial for optimising the powder bed while designing feedstocks to overcome NIR laser reflectivity challenges and enable the printing of high-performance parts.

The chemical composition of feedstock is primarily described by three types of alloying: metallic elements (micro/nano), carbon (micro/nano), and ceramics (micro/nano). Alloying serves as a solution to processing challenges by enhancing NIR laser absorption and improving material properties through the intentional incorporation of additional elements into the Cu matrix. These alloying elements, such as Ni, Co, Cr, Si, Zr, Ti, Al, Zn, Nb, Fe, Ag, Mn, P, TiB_2, graphene, CNP, etc., can considerably augment NIR laser absorption, making NIR L-PBF processing more efficient [82]. The presence of alloying components in the Cu matrix influences solute trapping, lattice distortion, dislocation cell formation, hetero-deformation-induced strengthening, grain size, dislocation density, stacking fault energy, precipitation, phases, segregation, melt pool stability, etc. These factors collectively determine microstructural evolution, defect susceptibility, post-heat treatment efficacy, and, ultimately, material properties. The rapid cooling inherent in AM alters solute transport, leading to solute entrapment and the formation of a supersaturated solid solution in α-Cu. This, in turn, dictates lattice distortion, which depends on solute size and influences lattice friction stress. For instance, in L-PBF Cu–13Sn–0.9Zn alloys, the 6.2 wt.% Sn in the supersaturated solid solution in α-Cu exceeded the solubility limit (1.3 wt.% in Cu at 200 ℃) with the substantial size disparity between Sn (~225 pm) and Cu (~128 pm), distorting the lattice. This distortion contributed 41% to the yield strength via lattice friction stresses, which remained unchanged even after heat treatment due to Sn retention in the α-Cu matrix [126]. This highlights the critical role of solute atom size and concentration in optimising the performance of AMed Cu alloy components. Additionally, the formation of dislocation cells is influenced by the presence of solute elements, which further enhance the material properties. L-PBF Cu–Sn exhibited a 45% contribution to YS from a cellular dislocation structure (~600 nm), which diminished after heat treatment [126]. Similarly, the L-PBF Cu–Cr–Zr alloy displayed dislocation cells that disappeared following aging treatment [127]. However, Cu–Zn alloys did not exhibit dislocation cells, suggesting that the choice of alloying element is critical in determining dislocation cell formation. The mechanism of dislocation cell generation remains a topic of debate and warrants further investigation. To disrupt the strength-ductility trade-off, hetero-deformation induced (HDI) strengthening was observed in L-PBF Cu–Sn and Cu–Cr–Zr alloys but not in L-PBF Cu–Zn alloys [126,128], suggesting that solute elements play a pivotal role in resolving this trade-off. Additionally, alloying elements influence heterogeneous nucleation during L/E-PBF, modulating the G/R ratio and thereby increasing nucleation density,

which promotes grain refinement through the columnar-to-equiaxed transition (CET) [129]. This effect can be enhanced by ex-situ particle addition (inoculation), in-situ precipitation, or the presence of the pro-peritectic phase. The columnar-to-equiaxed transition was demonstrated in L/E-PBF Cu alloy/composite by Y_2O_3 in Cu–Cr–Zr [110], primary precipitates in Cu–Cr–Zr [112], and the pro-peritectic phase in Cu–Co [29]. The amount of alloying element not only affects grain size but also influences dislocation density, as reported in Cu–50Ni (1.63×10^{14} m^{-2}) and Cu–30Ni alloys (2.92×10^{14} m^{-2}) [130]. Additionally, stacking fault energy is regulated by solute atoms, determining the nucleation and growth of deformation twins (DT), thereby impacting the deformation mechanism. This was corroborated by L-PBF Cu–Sn alloys [126], which exhibited predominant deformation following heat treatment, whereas no DT was observed in Cu–Cr–Zr and Cu–Ni–Sn alloys [112,131]. Further research is needed to examine the microstructure-deformation nexus in various Cu alloys to achieve a more comprehensive understanding. Melt pool stability is also influenced by low-boiling-point alloying elements. In Cu–Zn alloys, Zn evaporation caused melt pool instability, leading to defect formation [47]. Additionally, insoluble particles in the α-Cu matrix may result in elemental segregation, increasing defect susceptibility and complicating the fabrication of highly dense printed parts and reproducible material properties. Alloying elements also influence melt surface tension, which governs the Marangoni effect (temperature-induced surface tension gradients), a critical factor in melt pool stability. Furthermore, alloying components dictate the feasibility of precipitation hardening, offering a means to tailor the properties of printed components. Cu–Cr–Zr alloys, a precipitation-hardening alloy, successfully addressed the strength–conductivity trade-off following post-processing heat treatment—an outcome not achievable with Cu–LaB_6 [71,112]. Lastly, alloying elements impart specific functionalities to Cu alloys/composites, including the shape memory effect, nearly full amorphous state in BMG, corrosion resistance, etc. Therefore, the strategic selection of Cu feedstock is essential to achieve homogeneous and reproducible high-performance properties in L/E-PBF Cu alloy/composite components.

Broadly, Cu alloys are classified into two categories: strength-conductivity alloys and strength-property alloys. Strength-conductivity alloys prioritise electrical conductivity over tensile strength (Cu–Cr–Zr, Cu low alloyed/lean alloys (< 5 wt.%), etc.) [132]. Conversely, strength-property alloys emphasise wear, corrosion resistance, functional properties, etc. (Cu–Ti alloy, Cu–Ni alloy, NAB alloys, SMAs, etc.) [132]. Cu alloys with UTS $\geq$ 600 MPa and electrical conductivity $\geq$ 80% IACS are recommended for applications requiring both high strength and electrical conductivity [133].

The design of Cu feedstock for L/E-PBF primarily aims to enhance processability by mitigating the reflectivity challenge inherent to the copper system while simultaneously augmenting the functionality of the printed components. This is achieved through the following approaches.

6.1. Mechanical mixing

The mechanical mixing technique utilises a mechanical mixer (duration varied between 0.5 and 24 h) to integrate the alloying element or pre-alloyed powder to formulate Cu feedstock. This method offers greater compositional flexibility, expedites the development of new feedstock, reduces costs for feedstock development, requires fewer alloying elements, and is well-suited for preliminary experimental investigation. However, the primary challenge in mechanical mixing is the prevalence of inhomogeneity and segregation (Table 2). Zhao et al. [134] reported the presence of Ni-rich and Ni-poor zones in L-PBF parts fabricated from mechanically mixed elemental powders (Cu–15Ni–8Sn alloys). These zones exhibited a corresponding decrease in average hardness compared to parts made from pre-alloyed powders due to the formation of chemically distinct phases. These phases arise when Ni is unevenly distributed, resulting in Ni-rich and Ni-poor zones. Finally, inherent differences in the feedstock characteristics led to a critical phenomenon during printing: chemical segregation (Fig. 13). This segregation manifested as localised differences in elemental distribution within the printed part, leading to an anisotropic microstructure and, ultimately, anisotropic material properties or, in some cases, part failure. However, existing limitations can be addressed through in-situ alloying in conjunction with re-scanning/re-melting approaches. This approach enables greater customisation, including compositional gradations, improved microstructure control, and reduced reliance on pre-alloyed powders for rapid alloy design and verification, as well as the potential to address atomisation limitations that may arise due to differences in the melting points and densities of the elements.

6.2. Atomization

Previous studies on L/E-PBF Cu alloys indicate that pre-alloyed Cu feedstock is the predominant selection among researchers for L/E-PBF, as shown in Table 2. This pre-alloyed powder, fabricated by atomisation techniques, yields nearly spherical morphology (often compromised during mechanical mixing), which is beneficial for bed density, homogeneous chemical composition, and, ultimately, the material properties of AM parts [135]. Typically, gas atomisation (GA) techniques utilising nitrogen or argon are favoured due to their ability to produce nearly spherical particles with sizes in the range of 20-80 μm with a high yield and at a lower cost, particularly for large-scale production. In addition to GA, the plasma rotating electrode process (PREP), a non-crucible atomisation, produces Cu alloy powders, especially NAB alloys [23,136,137]. PREP provided advantages over GA in terms of reduced defects such as satellites and hollow particles, improved spherical morphology, and high purity, though at a higher cost [138]. Pre-alloying offers a significant advantage by overcoming a major challenge in conventional casting: grain boundary segregation (where elements preferentially concentrate at grain boundaries, which can lead to cracking and reduced mechanical properties) and low solubility in the solid solution phases. Shi et al. [139] demonstrated that the segregation of Sn was restricted in Cu–16Sn–0.3Ti alloy powders produced by GA. The limited solid solubility of Sn in Cu in the equilibrium process led to brittle Cu–Sn intermetallic phases at Sn content above 10%, reducing plasticity. However, when combined with L-PBF, gas atomisation mitigated these detrimental brittle phases. Researchers have even successfully processed Cu–15Sn alloy, achieving high densification (99%) despite exceeding the traditional solubility limit [91]. Furthermore, an atomisation strategy was employed to tailor a unique Cu alloy composition employing in-situ liquid-phase processes, as reported in the TiB_2/Cu composite powder [140]. However, the limited number of alloys on the market and the presence of defects in pre-alloyed powders, such as satellites, porosity, elongated particles, contamination, etc., remain challenges. Satellites, for example, can significantly reduce flowability and packing density by increasing the apparent sphericity (closer to 0.9). Internal porosity, often caused by gas entrapment, leads to powder-induced porosity in the final part. Furthermore, both small and large particles directly regulate bed density, ultimately affecting the defect susceptibility and performance of printed parts. Researchers observed that a powder packing density of 38–45% reduced balling defects and stabilised the melt pool [141]. However, the constrained composition resulting from atomisation limitations, the high cost of pre-alloyed powders in small batches, and the limited availability of compatible Cu feedstocks for L/E-PBF processes render this approach less appropriate for preliminary investigations (rapid design and verification).

6.3. Selective composite approach

Researchers developed Cu feedstock via a selective composite method using secondary particles (by employing ceramic nanoparticles and carbon-based materials) to tackle reflectivity challenges, lattice distortion, and compositional segregation and to implement grain

Table 3
Selective composite and powder surface engineering approaches for enhancing L/E-PBF Cu powder feedstock performance.

Matrix	Reinforcement	Techniques	%RD (>99%)	Comments	Ref.
Selective composite approach					
Cu	1 wt.% nano-LaB_6 (100 nm)	Direct mixing	Yes	Cost of nanoparticles, not scalable industrially	[71]
Cu	0.1 wt.% CNP (25 nm)	Direct mixing	No	Segregation of carbon nanoparticles, not scalable industrially	[69]
Cu–0.3Cr	0.05 wt.% CNP (25 nm)	Direct mixing	Yes	No significant difference in the L-PBF behaviour of Cu0.3Cr and Cu0.3Cr+CNP, not scalable industrially	[125]
Cu–0.8Cr	0.2 wt.% nano-TiC	Direct mixing	Yes	↑ 96.4% NIR laser absorption, reduced process defects	[55]
Cu–1Cr	0.1 wt.% CNP (25 nm)	Direct mixing	Yes	300 W laser power achieved >98% density	[154]
Cu	0.5 wt.% MWCNT (ϕ 4-6 nm)	Direct mixing	No ~85%	CNT did not efficiently transfer energy to the Cu particles, ↑ process defects, agglomeration	[155]
Cu–15Ni–8Sn	1 wt.% TiB_2 (600 nm)	Direct mixing	Yes	↑ 48.1% NIR laser absorption, defect-free microstructure, ↓ Sn segregation	[70]
Powder surface engineering approach					
Cu–1Cr	Cr_2N and CrN	N_2 heat-treatment	No	Formation of Cr_2N, and CrN phases, higher absorbing phases	[54]
Cu	0.8-8.5 wt.% Sn	Immersion deposition method	No $\geq$ 98.0	Although absorption improved in both, the defect tendency varied with the element	[156]
Cu	1.5-2.4 wt.% Ni	Immersion deposition method	No $\geq$ 98.0		[156]
Cu	0.4-1.5 wt.% Ni	Co-precipitation plating method	Yes	30% reduction in NIR laser reflectivity, eliminating process defects.	[157]
Cu	0.25, 0.5 and 1.0 vol. % W	Liquid-mixing route followed by thermal gaseous reduction	Yes	0.5 vol% W particles reduced laser reflectivity by 56.7%, W agglomerates at the melt pool boundary, W distribution influenced the electrical conductivity	[52]
Cu	0.1, 0.3 and 0.5 wt. % Cr_2O_3	Sol-gel method	Yes	No lattice distortion, high electrical conductivity (91.8 % IACS) and thermal conductivity (371 W/mK) without requiring post-heat treatment	[158]
Cu–Cr–Zr	0.5 wt.% Y_2O_3	In-situ chemical method	Yes	↓ NIR laser reflectivity by 42.3%	[110]
Cu	0.3 wt.% Sn	Immersion plating technique	Yes	Absorption improved by ~170 %	[68]

boundary engineering in Cu alloy/composite for tailoring parts during L/E-PBF (Table 3). The selection of secondary particles is based on the following characteristics.

- High NIR laser absorption elements: These improve processing efficiency by selecting elements or particles that absorb laser energy better than Cu [68].
- Low solid solubility in Cu matrix: Barely dissolved elements are added to minimise lattice distortion and mitigate negative impacts on conductivity [71].
- Low wetting angle: This prevents clustering and ensures uniformity, etc. [71].

Using this selective composite approach, L-PBF-fabricated Cu-LaB_6 demonstrated an excellent combination of electrical conductivity and strength, while L-PBF of Cu-Ni-Sn alloys with TiB_2 as a selective reinforcement effectively suppressed segregations. Although promising, this approach faces challenges related to nanoparticle cost and scalability. Future research could explore hybrid reinforcement for Cu feedstock design to overcome current limitations and enhance overall performance.

6.4. Powder surface engineering

The powder surface engineering approach, utilising both physical and chemical methods to modify the characteristics of Cu powder feedstock, enhances the processing efficiency by increasing the Cu absorptivity for NIR lasers, improving flowability, and introducing strengthening phases, thereby improving the performance of L/E-PBF Cu alloys/composites (Table 3). Cu feedstocks modified with W, Cr_2O_3, and Y_2O_3 demonstrated enhanced densification (Table 3), overcoming the trade-off between strength and conductivity while also extending the storage life of Cu feedstocks. However, the selection of coating material is crucial, as Cr_2O_3 degradation and evaporation in Cu-Sn feedstocks induced process defects [52]. Additionally, the wettability factor and content of coating materials are key to achieving maximum performance benefits. In lieu of upgrading to blue/green laser machines, future developments in powder surface engineering may explore more affordable materials to mitigate the high cost of nanoparticles and enhance the scalability of coating processes, thereby facilitating wider deployment.

6.5. Multi-material approach

The enhancement of functionality and the need for site-specific properties of printed components have driven the emergence of multi-material methods. This approach investigates the use of Cu alloy in conjunction with Fe alloy, Ti alloy, Ni alloy, etc. [6,7,142] for L/E-PBF processing.

In a nutshell, mechanical mixing, atomisation, selective composite approach, and powder surface engineering have been investigated to improve the processability of Cu feedstock for achieving desirable material properties of printed parts. Meanwhile, the multi-material approach is utilised to overcome the performance ceiling of copper alloys for a unique combination of attributes and functionalities. Current research on copper feedstocks is primarily focused on heritage alloys; therefore, the integration of computational and machine-learning methodologies is essential for developing the alloys of tomorrow. Although machine learning has been applied to Cu alloy design [143], its application to copper feedstock design for powder bed fusion remains unexplored. Consequently, future studies are expected to focus on applying machine learning/computation for feedstock design to enhance the performance of Cu alloys, address the strength-conductivity and strength-ductility trade-offs, and impart more functionality.

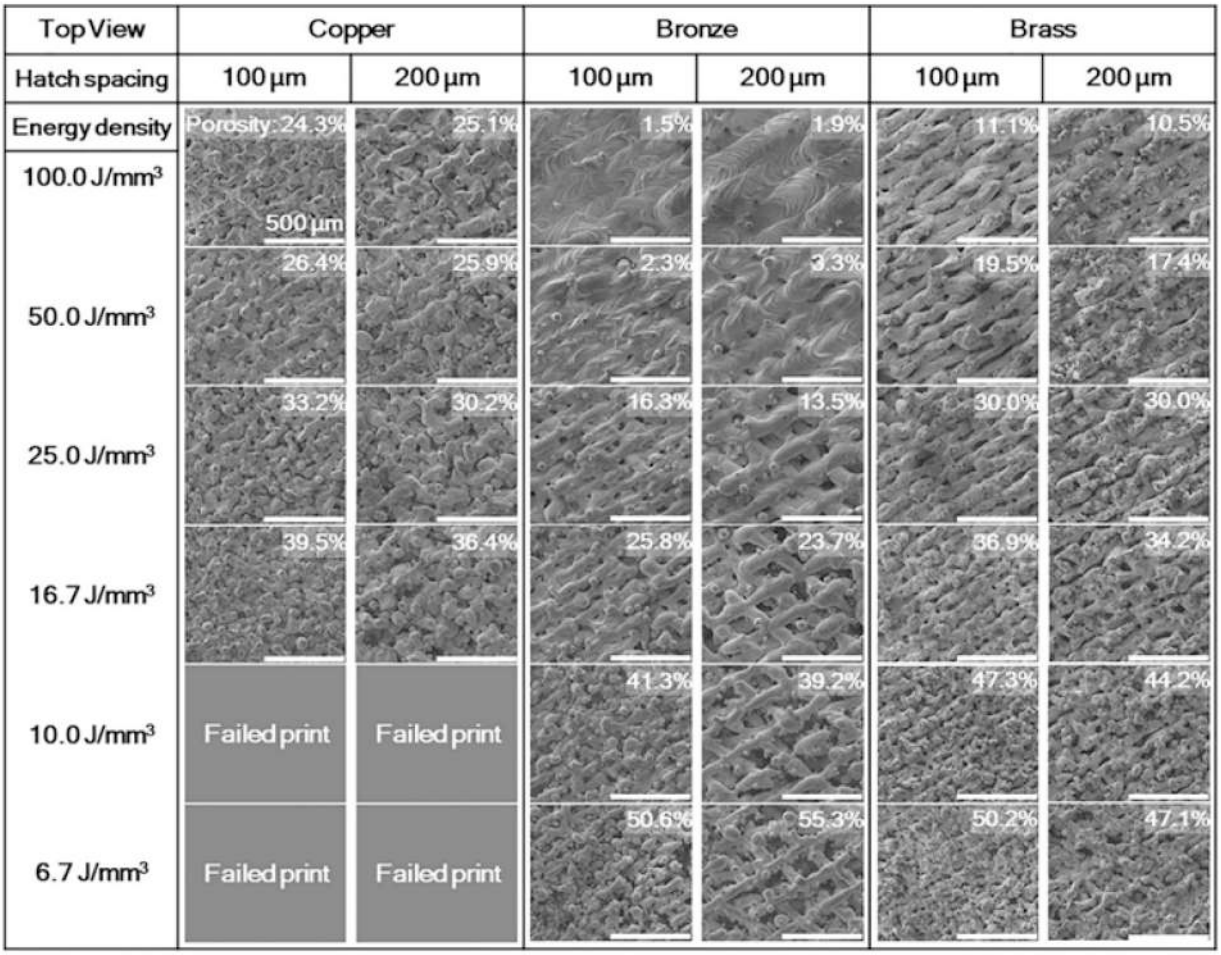


Fig. 14. Percentage porosity variation and lack of fusion in relation to energy density for L-PBF Cu, bronze, and brass [166].

7. Formation of metallurgical defects and remedies

The occurrence of predictable defects and unanticipated defects often plague metallic printed parts. Predictable defects are linked to powder feedstock characteristics, process parameters, and post-printing heat treatments [159]. These process-induced defects adversely impact performance, encompassing corrosion behaviour, mechanical, electrical properties, etc., as well as the quality and consistency of printed parts [160]. If predictable defects are not effectively addressed, the performance of AMed components may be inferior to that of their cast counterparts. Therefore, understanding the root cause of these defects is critical for palliating their adverse effects and optimising the performance and consistency of L/E-PBF Cu alloy/composite parts.

According to the available research, defects in digitally designed parts employing L/E-PBF for Cu alloys/composites can be categorised into three primary categories: geometry and dimensional, surface, and microstructural defects [161]. Geometry and dimensional defects impact part shape and size, while surface defects influence surface quality and performance, particularly fatigue [162]. However, microstructural defects severely compromise the overall performance of printed parts [163].

7.1. Microstructural defects

7.1.1. Internal pores

In L-PBF or E-PBF, the inevitable and stochastic internal pores result from fine-tuning process parameters that are inadequate to guarantee melt pool stability as localised variations in particle size (powder bed non-uniformity) and scan strategies impact the energy density and, consequently, the geometry of the vapour depression [164]. Finally, vapour depression instability can alter material-energy interactions, leading to unexpected and stochastic defects such as the emergence of pores, with printed parts barely attaining complete densification. The reduced density of L/E-PBF Cu alloy components results in subpar performance compared to traditional counterparts [165,166]. Typical internal pore defects can be categorised as lack of fusion (LoF), metallurgical, and keyhole pores.

Metallurgical pores are formed when diffused gas, primarily originating from the powder feedstock and shielding gas (used to prevent oxidation in the L-PBF process), is unable to escape from the melt pool due to rapid solidification. Additionally, the increased gas solubility in liquid metal at high melt pool temperatures fosters the formation of pores upon solidification in Cu alloys/composites. Metallurgical pores are typically spherical, with sizes below 50 µm, and are ubiquitously distributed inside printed parts.

LoF is caused by insufficient energy density, often due to untuned process parameters, resulting in partial melting of the powder and inappropriate bonding with the previously solidified layer. The LoF signature is characterised by large irregularly shaped defects (sphericity factors < 0.6) with sizes ranging from 50 µm to several hundred microns, scattered in discrete vertical and horizontal morphologies along the melt track interface, often accompanied by unmelted particles. In L-PBF Cu alloys/composites, untuned process parameters—such as high scan speed and low energy density—contribute to LoF defects. Even when

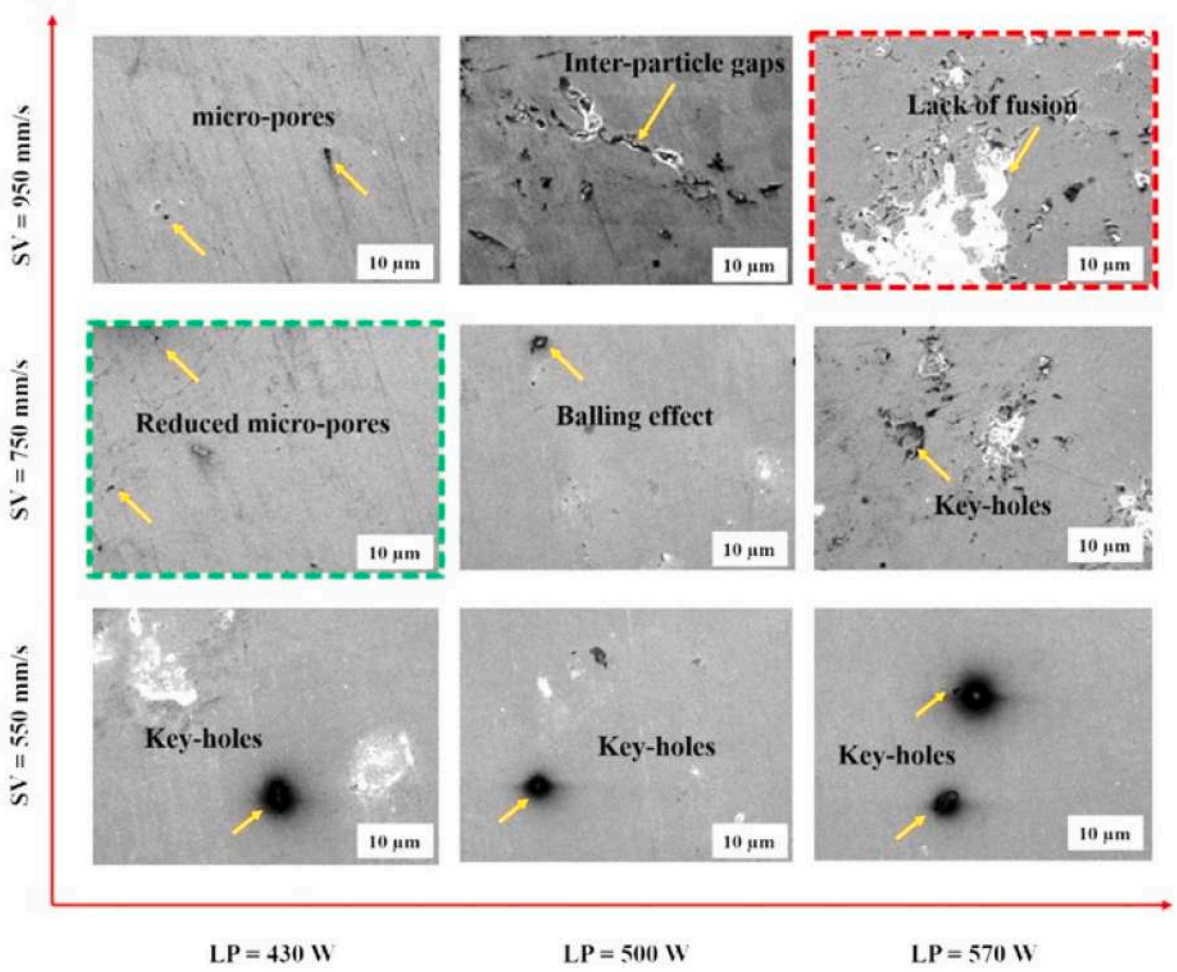


Fig. 15. L-PBF Cu alloy defects: Unveiling the impact of scanning speed and laser power [168].

parameters are optimised, LoF defects cannot always be eliminated in other Cu-based alloys (brass and bronze), as shown in Fig. 14. This anomaly typically arises from the limitations of the standard equation Eq. (7.1) for calculating volumetric energy density (VED), which only considers factors such as laser power (P), scanning speed (V), hatch spacing (HS), and layer thickness (LT). Nevertheless, optimised VEDs do not always guarantee the desired level of densification, as other critical factors—including laser spot size, Cu alloy absorption for NIR lasers, scan strategy, and platform temperature—are not accounted for. These supplementary factors significantly influence melt pool width and depth, the cooling rate (melt pool dynamic), ultimately contributing to the manifestation of LoF. Future research should leverage machine learning and artificial intelligence to account for the stochastic nature, in conjunction with advanced characterisation synchrotron X-ray imaging, to identify defect formation mechanisms and readily produce high-density L/E-PBF Cu alloy/composite parts.

$$\text{VED} = \frac{P}{V \times HS \times LT} \tag{7-1}$$

The formation of keyholes may occur due to untuned process parameters, powder feedstock variability, and protective atmosphere variables (type and pressure of gas) during the printing process [167]. The higher power density ($\sim 10^5$-10^7 W/cm^2) in L-PBF, after surpassing the boiling point, causes vaporisation. Rapid vapour expansion exerts recoil pressure on the melt pool, increasing penetration. Gas bubbles are drawn to the bottom edge of the melt pool by convective currents and become trapped due to rapid solidification, resulting in nearly spherical pores. The distinctive features of keyholes include an elongated circle shape in the build direction, a circle in the horizontal direction (sphericity > 0.80), or a pore at the end of the track with a laser spot dimension. Prolonged exposure (lower scanning speed 550 mm/s), regardless of particle, resulted in keyhole formation in the Cu–Cr–Zr alloy and increased with laser power (from 430 to 570 W), as illustrated in Fig. 15 [168]. L-PBF of Cu–10Sn alloys revealed keyhole diameters ranging from 10 to 100 µm. As scanning speed increased (from 100 to 1000 m/s), pore dispersion reduced, while further increasing speed led to LoF [109]. Robinson et al. [144] revealed that the number of pores (87%) and average pore size (40%) decreased as Ag content increased from 10 to 30 wt.% for Cu–xAg alloys (x: 10, 20, 30) during the L-PBF process (Fig. 16). Researchers used computed tomography (CT) analysis for the internal pore of L-PBF Cu–Al–Ni–Mn components and emphasised the importance of optimising laser power to minimise porosity as pore size ranged from 12-532 µm at 300 W and expanded to 112-845 µm at 450 W [169]. Moreover, studies revealed that internal pores acted as stress concentrators in Cu–Sn alloys, leading to crack initiation, necking, and material failure under tension. As shown in Fig. 17, pore growth initially transpired due to plastic strain, with large pores eventually reaching the surface and forming a significant surface depression, ultimately causing component failure. Li et al. [170] noted that the corrosion behaviour of L-PBF Cu–Cr–Zr was adversely affected by defects such as pores and microcracks formed during the printing process. Similarly, porosity negatively impacted the density, mechanical properties, electrical properties, and thermal properties of the L-PBF copper alloy parts

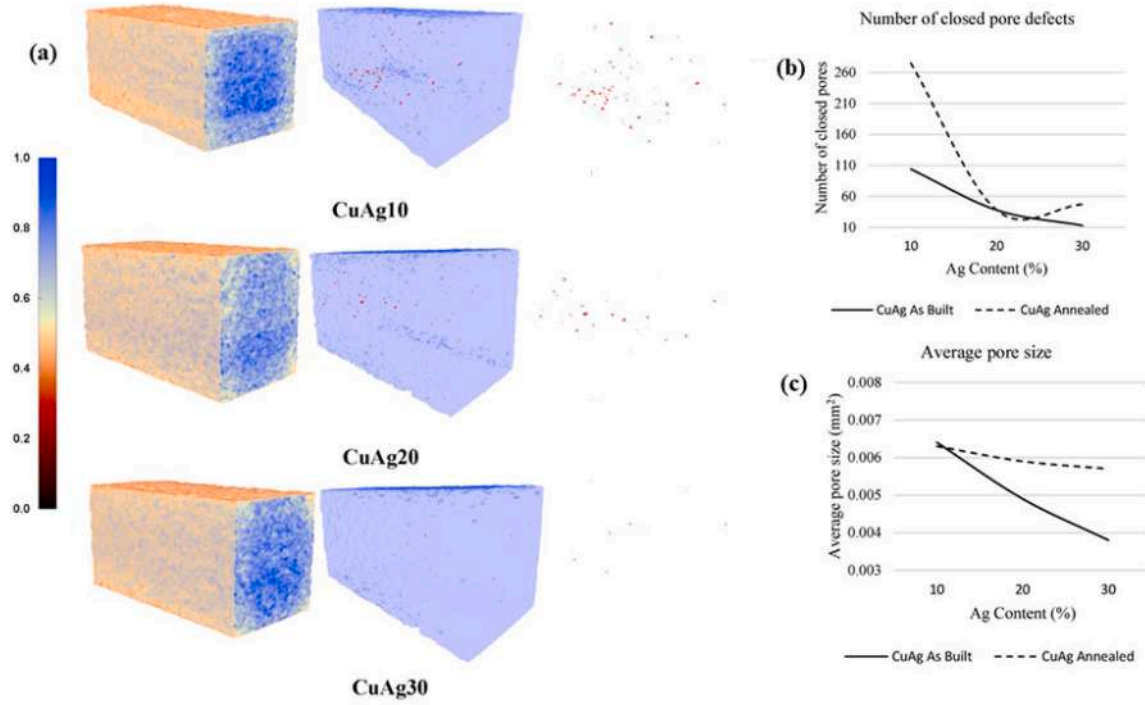


Fig. 16. (a) 3D visualisation of pore size and distribution; (b) Total number of closed pores; (c) Average pore size in Cu alloys with Ag addition during the L-PBF process [144].

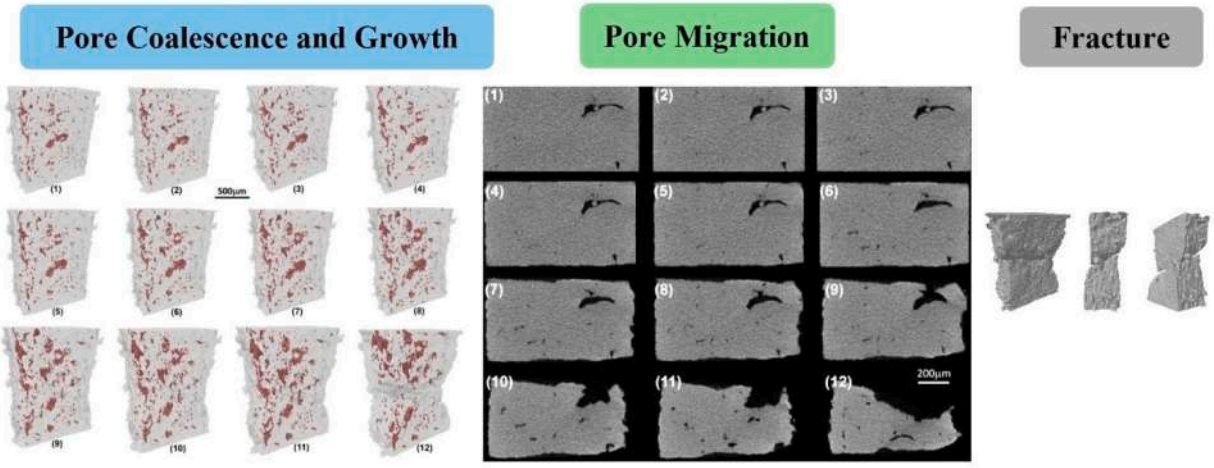


Fig. 17. Component failure during in-situ uniaxial tensile testing due to pore coalescence and growth in L-PBF Cu–Sn alloys [172].

[144,157,171]. Therefore, eliminating porosity is crucial for tailoring high-performance L/E-PBF Cu alloy components through process parameters optimisation, feedstock selection, and modification strategy.

7.1.2. Elemental evaporation

The coupling between printing parameters (e.g., laser power, layer thickness), powder feedstock composition, and the processing environment largely dictates elemental evaporation [173]. During powder-based AM processes, high laser or electron beam power density ($\sim 10^5$-10^7 W/cm^2) causes elements to evaporate swiftly, leading to gas expansion and recoil pressure on the melt pool. However, a greater number of alloying components make this evaporation more selective and complex. Yin et al. [47] demonstrated that severe Zn vaporisation caused explosions during the Cu–10Zn L-PBF process, with explosion-induced crater characteristics strongly correlated with laser power and scanning speed. When heat input was limited at laser power (1000 W), the melt pool vapour pressure remained below ambient pressure, minimising explosive vaporisation and resulting in a continuous melt track with fewer craters. However, as the laser power increased (from 1000 to 2000 W), the temperature within the melt pool escalated, leading to violent vaporisation explosions. These explosions disrupted the molten material, causing discontinuous track formation and defects (Fig. 18a). Yang et al. [174] found that Zn evaporation during the L-PBF process led to ZnO formation and a 20% loss of Zn in the Cu–Zn–Si alloy (Fig. 19). Zhuo et al. [175] established that high energy density (300-324 J/mm^3) during L-PBF of Cu–Zn–Al SMA caused 60% Zn evaporation from the melt pool, resulting in spherical pores, reduced RD (~97%), and droplet splashing, which altered surface roughness, increased roller-powder bed

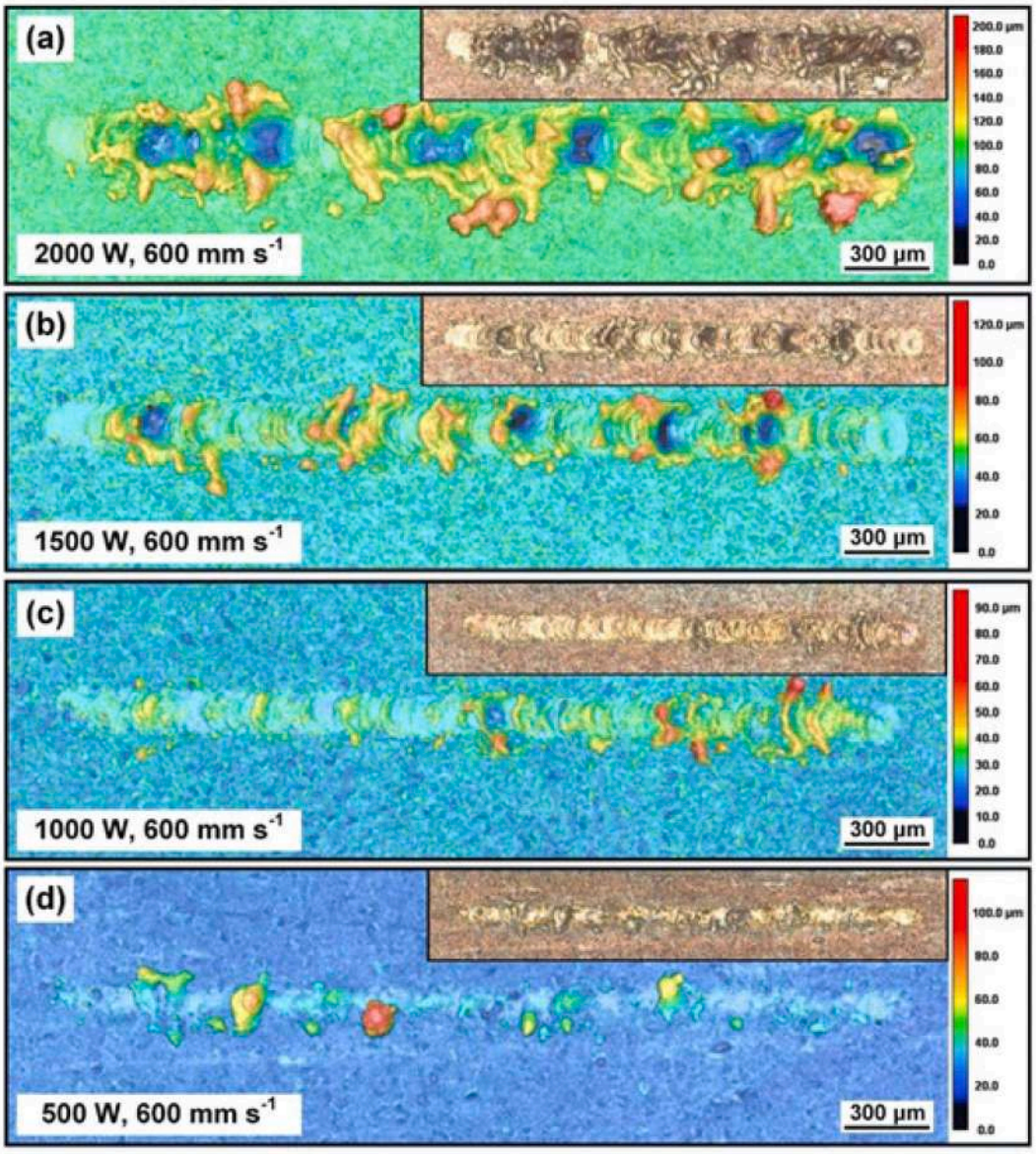


Fig. 18. L-PBF Cu–10Zn melt track variations with laser power at a constant scanning speed of 600 mm/s (a) 2000 W; (b) 1500 W; (c) 1000 W; (d) 500 W [47].

friction, and diminished powder flowability. Additionally, Zn loss modified the phase composition, reducing the brittle and hard β' phases and decreasing overall hardness. If preferential Zn evaporation becomes substantial and falls below the critical limit (16–30 wt.% Zn), shape memory behaviour is compromised. For L-PBF Cu–Al–Mn–Nb SMA samples, as laser energy density increased (from 120 to 190 J/mm^3), Mn evaporation reached 18 %, leading to an increase in the martensite transition temperature [176]. Furthermore, Yin et al. [47] demonstrated that vaporisation explosion contributed to droplet spattering during L-PBF of Cu–10Zn alloys, even under optimal process parameters (see Fig. 20). This emphasised the crucial role of the Cu alloy feedstock composition in conjunction with the meticulous selection of optimal process parameters to achieve fully dense components. Additionally, spattering is a crucial factor in determining powder reusability. In conclusion, regulating elemental evaporation is essential for achieving the desired microstructure, which subsequently influences transformation behaviour and material properties, minimises internal defects, and enhances powder reuse. This can be achieved through compositional adjustments, process parameter optimisation, and atmospheric control.

7.1.3. Oxidation

Residual oxide film on particles, moisture, and oxygen from the chamber atmosphere (for L-PBF) are often inevitable sources of oxygen. To minimise oxygen pickup during AM, it is crucial to consider both the Cu powder feedstock (oxygen affinity) and the specified process parameters. Oxidation alters melt pool dynamics, promoting defect formation and compromising printed part performance. However, the controlled oxidation of Cu alloy feedstock can be beneficial, as it enhances laser absorption and reduces the laser power required for L-PBF [125,177]. The oxygen levels below 6000 ppm have demonstrated a positive impact on NIR laser absorption, as well as the mechanical properties and electrical properties of L-PBF Cu alloys. While the detrimental effects of elevated oxygen levels in L/E-PBF Cu alloy on material properties and printability are not yet fully established in the literature, further research is necessary to determine the threshold oxygen levels and identify the specific oxide types that influence printability and material properties of L/E-PBF Cu alloys and composites.

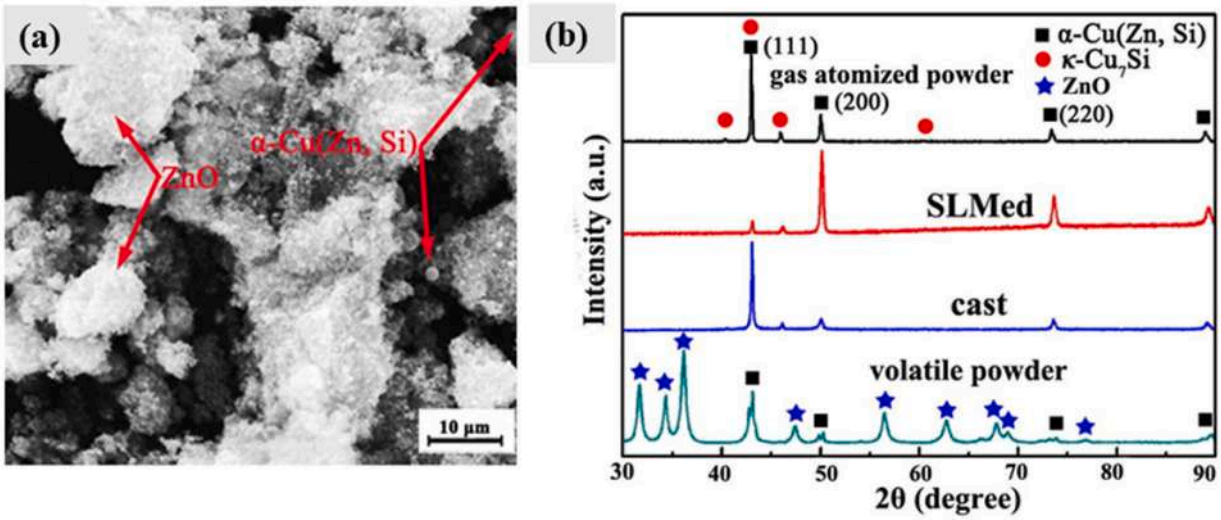


Fig. 19. (a) SEM morphology; (b) XRD characterisation of the volatile byproduct ZnO from L-PBF Cu–15.5Zn–2.8Si alloys on the inner walls of the chamber [174].

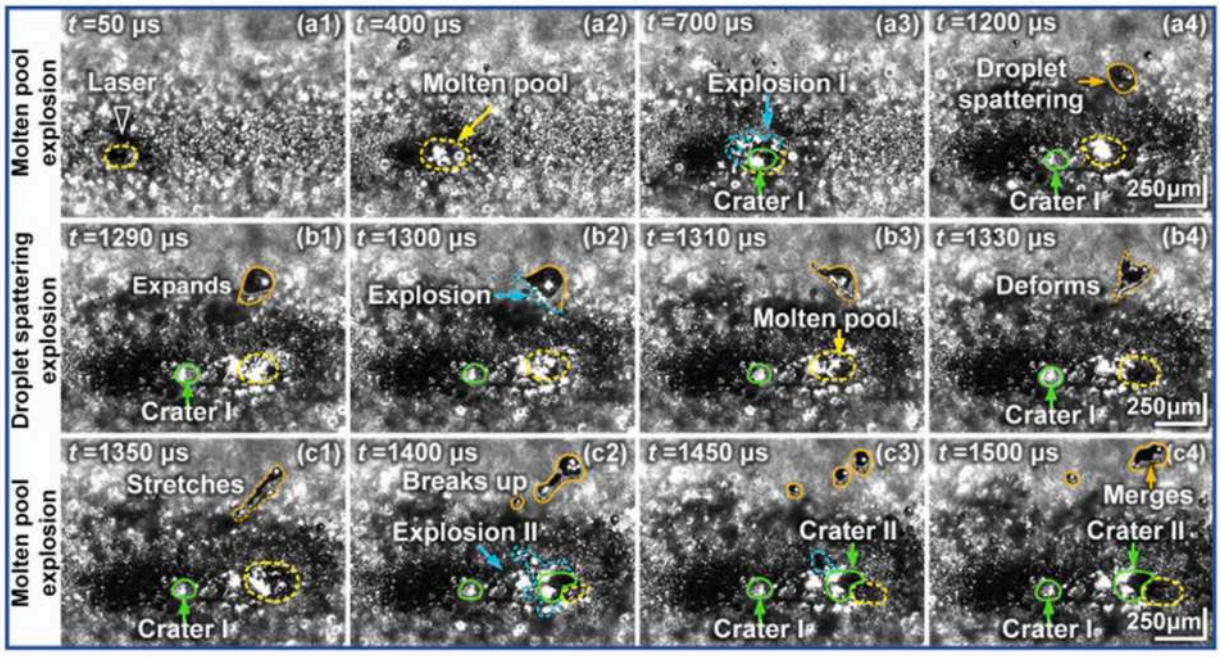


Fig. 20. Spatter formation over time (after t=1200 μs, orange outline) in L-PBF Cu–Zn alloys under high power (2000 W, 600 mm/s) [47].

Prior studies have highlighted the adverse impact of oxygen on powder flowability, mechanical properties, etc. For instance, carbon has been used as a deoxidiser in Cu–Cr alloy (149 ppm oxygen) and preventing Cr from forming oxides during post-printing heat treatments. This deoxidation process resulted in enhanced mechanical properties of the L-PBF part compared to virgin Cu–Cr alloy with higher oxygen levels (1100 ppm oxygen) [125]. Moreover, oxidation affects powder flowability by influencing the avalanche angle, where a lower angle indicates better flowability. Oxidised Cu–Cr alloy powder (> 2000 ppm oxygen), with lower oxidation tendencies, exhibited improved flowability due to a lower avalanche angle [54,178]. Additionally, oxygen uptake by particles narrows the processing window by inducing defects such as keyholes, leading to reduced RD [54]. High oxygen levels can also hinder the glass-forming ability of BMG. For instance, in L-PBF, Cu–Ti BMG powders, oxygen content exhibited rising levels from feedstock to L-PBF processing. While this increase remained below a critical threshold, preserving the amorphous state, exceeding the critical oxygen level prevented L-PBF from successfully producing BMGs [179]. Finally, it is essential to recognise that powder feedstock, due to its high surface area, is highly susceptible to oxidation. This makes controlling oxygen levels challenging, and its inevitable presence may impair wettability, performance, and powder reusability.

7.1.4. Cracks

Cracking susceptibility in copper alloys/composites during L/E-PBF is mainly driven by solidification, liquation, and solid-state cracking (transpiring at temperatures below the solidus). Solidification cracking is commonly observed in Cu alloy/composite parts during AM due to the development of tensile strain from shrinkage and external restrictions during the final stage of solidification, resulting in the rupture of the liquid layer in the mushy zone (growth zone of dendrites), which has a locally lower melting point than the surrounding matrix. Solidified

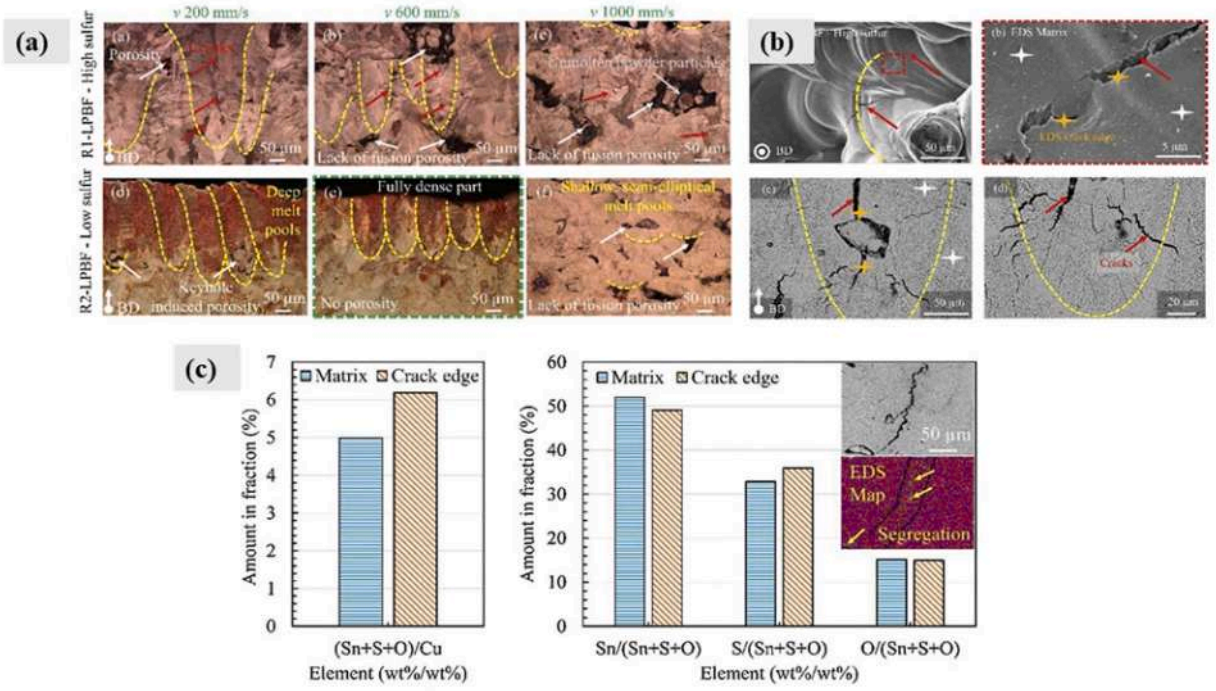


Fig. 21. Solidification crack susceptibility in Cu alloys: (a) Effect of increased scanning speed; (b) Enlarged view at 200 mm/s; (c) Elemental contribution at the matrix and cracking edge, initiated within the melt pool [68].

dendrites further block the remaining liquid, limiting the passage of liquid metal into the dendrite gaps. Solidification cracks exhibit a dendrite-like branching pattern and propagate mainly within the solidifying molten pool (as shown in Fig. 21a, b). Jadhav et al. [68] identified that solidification cracking in L-PBF Cu–Sn alloys was caused by high sulfur contents (910 ppm), with cracks propagating in intergranular regions within the melt pool due to low-melting-point sulfide phases (SnS_2, SnS, or CuS) relative to the surrounding Cu–Sn matrix (as shown in Fig. 21). However, reducing sulfur content to 20 ppm effectively prevented solidification cracking. Additionally, the number of cracking sites is controlled by the scanning speed for high-sulfur compositions (910 ppm). Besides impurities and process parameters, whether a single or combination alloy feedstock (for functionally graded materials and multi-material Cu alloy with 316SS, IN718 printing) is used in L/E-PBF significantly impacts crack susceptibility. For instance, L-PBF Cu–Co alloys with higher Co content exhibited reduced crack susceptibility, according to Liu et al. [29]. In the case of Cu–Sn/316L multi-material L-PBF, Chen et al. [180] identified four distinct crack zones on the multi-track cross-section: within the melt pool, crossing the melt pool boundary, crack extension to the substrate, and copper penetration cracks. This cracking susceptibility of multi-material L-PBF is influenced by process parameters due to variations in their thermophysical properties (CTE, thermal conductivity, heat capacity, melting point, laser absorption, etc.) with particular sensitivity to scanning speed and layer thickness. These variables altered the wetting angle and alloying elements content ratio, which in turn affected the cracking susceptibility [180]. Moreover, intergranular cracking in 316 stainless steel occurred when liquid Cu penetrated the grain boundaries, an occurrence known as liquid metal embrittlement (LME) [142,181]. This presented a significant challenge to developing a crack-free interface in FGMs using L-PBF for stainless steel/Cu alloy. Microcracks formed during Cu alloy L-PBF compromised the corrosion resistance of the printed component due to intergranular corrosion, which affected part performance and may have led to failure [170]. To mitigate cracking and ensure a crack-free interface for multi-material, optimising process parameters was crucial, which included increasing laser power, hatch spacing, and decreasing scan speed (no cracks: laser power 400 W, scanning speed 800 mm/s, hatch spacing 140 μm). Additionally, the use of post-treatment strategies (HIP, aging treatment in line with L-PBF) and ring-mode laser has shown the potential for reducing cracks [6,182–185]. Since cracks were identified in multi-material L-PBF of tool steel/Cu–Cr–Zr [186] and Cu–Sn/steel [181], etc., future research may leverage machine learning and modelling to gain deeper insight into interface dynamics (Marangoni convection, elemental segregation, etc.), coupled with in-situ monitoring to develop crack-free interfaces in Cu alloy FGMs for multifunctional parts.

7.1.5. Microstructural anisotropy

Preferred grain growth due to rapid solidification is a key factor contributing to anisotropy in L-PBF and E-PBF digitally designed parts. Localised, intense melting and rapid solidification generate steep temperature gradients, causing crystals/grains to grow in their preferred orientation [187]. This preferred orientation distribution of crystal is referred to as crystallographic texture and is an integral part of the as-printed microstructure, which ultimately controls performance through the microstructure-property correlation. The ability to regulate the crystallographic texture of an AMed component provides a distinctive prospect for additional customisation of the material (Cu alloys/composites). AM enables the formation of an extensive range of crystallographic textures, from random crystallographic orientation to highly textured microstructures with significant preferential crystallographic orientation [53,128]. The direction of local heat flux and the crystallographic direction (one of the six <100> favourable for crystal growth in Cu alloys during the AM process) both influence the crystallographic texture [188]. As a result, tailored crystallographic texture can be developed by adjusting the local heat flux of the melt pool, which determines the melting mode, the melt flow, and the geometry of the melt pool. These factors influenced the solid-liquid interface migration velocity or solidification rate (R) and the local thermal gradient (G). Ultimately, the interplays between G and R determine the

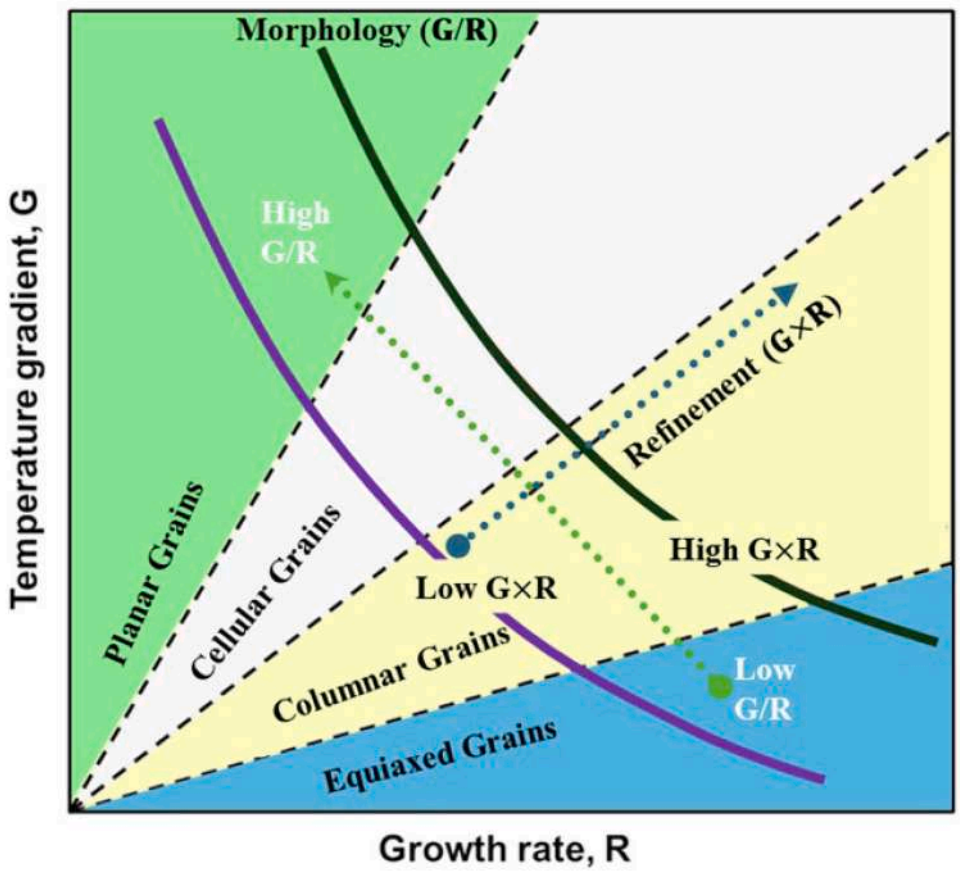


Fig. 22. Grain morphology map: Temperature gradient (G) vs. solidification rate (R), adapted from S Kou [190].

crystallographic texture of AMed parts. Eq. (7.2) defines the local G during AM as the result of prolonged heating and rapid cooling.

$$G = \frac{dT}{dx}\ (\mathrm{K/m}) \tag{7-2}$$

The R variable determines how quickly molten metal solidifies and is closely related to the scanning speed (v) and the angle between the growth vectors (φ) [189], according to Eq. (7.3).

$$R = \frac{dx}{dt} = V\cos\varphi\ (\mathrm{m/s}) \tag{7-3}$$

The solidification morphologies are determined by the ratio of the G/R, whereas the product GxR represents the cooling rate and dictates the size of the solidification morphology [190]. The G parameter typically increases (minimum at the top) from the top to the bottom of the melt pool, whereas the R parameter generally decreases (minimum at the bottom) [191]. Therefore, the relative prevalence of G and R in the melt pool induces a morphological shift from equiaxed dendritic (G/R lower) to planar (G/R higher), as shown in Fig. 22. Moreover, an increase in GxR results in finer solidification morphology (as shown in Fig. 22). In contrast, G/R varies across the melt pool, with the highest value at the bottom and the lowest at the top surface [192]. The importance of material properties in evolving solidification morphology is further emphasised by subsequent equations derived from the one-dimensional Rosenthal Eq. (7.4) [190].

$$G \times R = 2\pi k(T_S - T_O) \times (T_L - T_O) \times \frac{V}{\beta \times P} \tag{7-4}$$

where V is the scanning speed, P is laser power, β is the laser absorption coefficient, T_o is the platform temperature, k is thermal conductivity, T_s is the solidus temperature, and T_L is the liquidus temperature.

Table 4
G and R range for L/E-PBF processes [193].

Parameters	E-PBF	L-PBF
G (K/m)	10^3–10^5	10^4–10^8
R (m/s)	0.001–1.0	0.01–1.0

This demonstrates that the material properties and process parameters, ranging from columnar to equiaxed microstructures, are crucial for controlling crystallographic textures. Further, L/E-PBF processes have different local G and R values, making crystallographic texture tailoring challenging, as shown in Table 4 [193]. Additionally, the intensity of crystallographic texture during AM is determined by the progression of epitaxial crystal growth from an already solidified layer.

Thomas et al. [194] demonstrated cube or gross textures could be achieved by manipulating melt pool geometry in pure Cu. The flat melt pool (aspect ratio: melt pool depth/melt pool width << 0.3, as shown in Fig. 23) in E-PBF favoured the development of a cube texture, which is not possible in L-PBF due to the absence of preheating and slower scanning speeds. This variation in crystallographic texture is significant for Cu alloys due to their inherently low absorption of IR laser, with E-PBF offering an alternative free of such limitations. Moreover, L-PBF Cu–Cr–Zr alloys exhibited a strong texture parallel to the build direction of <110>, with differences in texture between horizontal and vertical directions and grain size variations of 49.7 μm horizontally and 94.6 μm vertically, as shown in Fig. 24 [195]. Additionally, the L-PBF Cu alloy with meander and chessboard scanning strategies showed strong {101} crystallographic texture in the horizontal plane. Interestingly, the

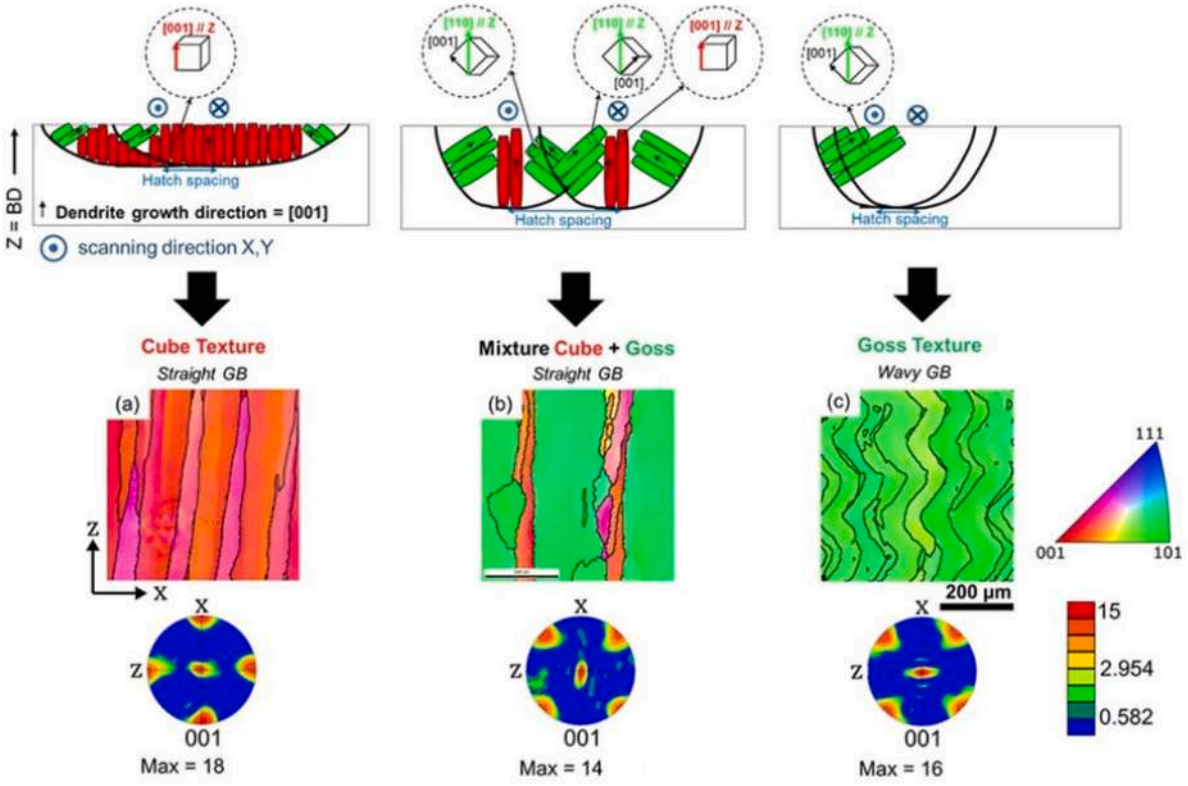


Fig. 23. Control of crystallographic texture through melt pool geometry [194].

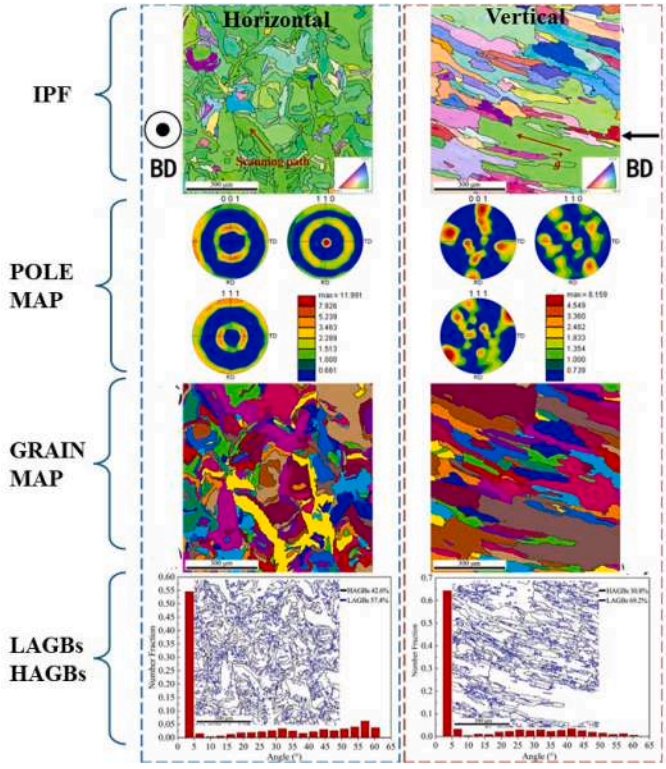


Fig. 24. EBSD map for L-PBF Cu alloy in the horizontal and vertical planes, showing inverse pole figure maps, pole figures, grain maps, and variations in orientation [195].

meander strategy showed a higher intensity of the {101} texture than the chessboard strategy. Conversely, the vertical plane of both specimens displayed ripple patterns with nearly random crystallographic texture, regardless of the scanning approach. This crystallographic texture is one factor that determines the strength anisotropy of AMed Cu alloy parts (Fig. 25) [104]. Babacan et al. [53] investigated the effect of scan vector rotation on the stripe scanning strategy of L-PBF Cu-based SMAs and found that the maximum texture intensity at 79° was almost three times that at 0°, and scan vector rotation resulted in a stronger [001] texture than without rotation, which is beneficial for superior superelastic characteristics (Fig. 26). Zhou et al. [196] examined how crystallographic texture regulates TC anisotropy in the Cu–2.4Ni–0.7Si alloy and found that vertical plane-dominated columnar grains strongly favoured the (100) crystallographic orientation, relative to horizontal plane equiaxed-like grains with mixed orientations (100), (101), and (111). However, variations in texture led to significant conductivity anisotropy, with vertical thermal conductivity (62.9 W/m K) 198% higher than horizontal at ambient temperature. In the case of L-PBF Cu–Co alloys, Liu et al. [29] observed that a strong texture <011> parallel to the BD emerged when Co addition remained below the maximal solid solubility in Cu (about 4.75 wt.%). However, no prominent texture formation was evident for Co additions exceeding the solubility limit (6 and 8 wt.%). Further, the incorporation of nano TiB_2 in the Cu–15Ni–8Sn alloy during L-PBF yielded strong {100}, {110}, and {111} textures, resulting in improved mechanical performance, as {110} and {111} textures are known to provide an optimal combination in the FCC system [70]. Karthik et al. [197] reported that L-PBF Cu–Sn parts exhibited minimal anisotropy (maximum deviation in tensile strength ~32 MPa, YS ~18 MPa, and uniform %EL ~10%) when the texture was substantially random (with some <100> component) with similar intensities in all three directions. Furthermore, crystallographic texture governs the anisotropy of functional properties in L/E-PBF Cu

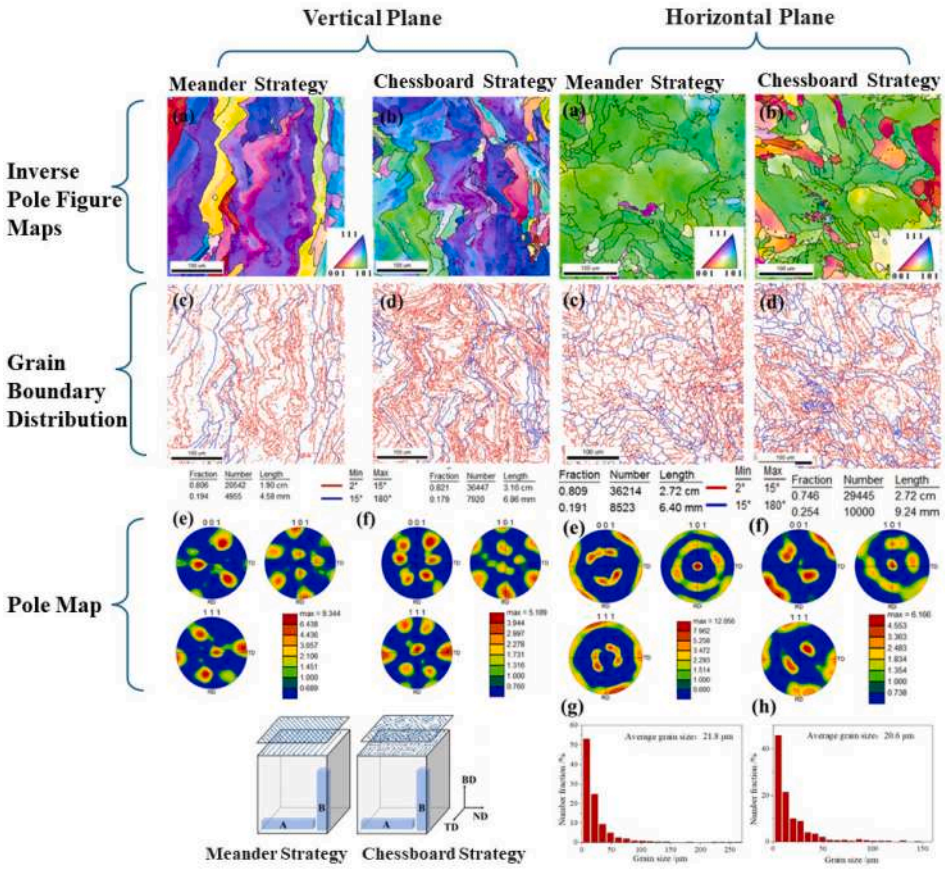


Fig. 25. Influence of scanning strategy on crystallographic texture and grain boundary distribution with varying orientations for L-PBF Cu alloy [104].

alloy/composite, such as electrical and thermal conductivity owing to stronger {110} grain orientation [12], shape memory behaviour [53], etc. Notably, changing the thickness of the Cu alloy L-PBF samples manifested no significant effect on the crystallographic texture [198]. However, the crystallographic texture was altered by post-heat treatment, presenting a potential approach to minimising anisotropy. As reported for L-PBF Cu–Cr–Zr alloys, the texture transitioned from <101> to <111> following post-heat treatment [199]. Overall, feedstock characteristics, process parameters, and post-heat treatment parameters can be adjusted to modify the crystallographic texture and minimise texture variations in L/E-PBF Cu alloy/composite parts. This enables the control of mechanical, electrical, thermal, and functional properties and facilitates the fabrication of printed parts with reduced material properties deviation—attributes that are otherwise unattainable by any other process.

7.1.6. Micro-segregation

Conventional manufacturing methods, such as casting and welding, trigger considerable solute segregation in Cu alloys/composites, which adversely affects alloy performance and processing due to the formation of undesired phases, such as enriched interdendritic regions and macro-segregation of elements [200]. However, AM processes (L-PBF and E-PBF) are susceptible to micro-segregation, referring to the uneven distribution of elements within the microstructure due to rapid solidification, insufficient time for elemental diffusion during solidification, and variations in solubility of solute atoms in the liquid and solid phases. Micro-segregation is further influenced by two key factors: feedstock characteristics and process parameters, both of which directly impact the diffusion coefficient of solutes in the solid, the local liquid solidification time, and the equilibrium partition coefficient [131,201].

Micro-segregation exhibits a complex interplay, serving as a double-edged sword for AMed parts. The positive effect of lattice strain-induced cellular structures increases strength, while the deleterious effect of transformations during heat treatment leads to the formation of detrimental phases, thereby reducing plasticity [131,150]. Wang et al. [202] recognised the benefit of L-PBF in avoiding macro-segregation compared to traditional methods. However, micro-segregation of Sn persisted within the L-PBF Cu–15Ni–8Sn alloy in the spacing between cellular structures. This micro-segregation appeared darker (using atomic number contrast) in transmission electron microscopy (TEM) analysis, as shown in Fig. 27, and may have been missed by X-ray diffraction (XRD) or energy dispersive spectroscopy (EDS) due to limited phase content and size (Fig. 28). This form of micro-segregation contributed positively to mechanical characteristics because dislocations became entangled in the Sn-rich zone. However, heat treatment of the L-PBF Cu–15Ni–Sn alloy transformed the Sn-enriched areas into two distinct precipitate network structures (lamellar discontinuous precipitates or grain boundary networks), resulting in reduced plasticity and a shift in fracture mechanism from plastic to brittle (intergranular fracture or transgranular fracture) [150]. Moreover, post-printing heat treatments on Cu–Sn alloys eliminated cellular segregation of Sn and second-phase δ ($Cu_{41}Sn_{11}$), resulting in enhanced corrosion resistance relative to the AB sample [203]. Zuo et al. [204] investigated the impact of nanoscale Sn segregation formed during L-PBF of Cu–15Ni–8Sn alloy on corrosion behaviour and found that fine dispersion contributed to increased corrosion resistance through passivation kinetics by reducing the outward diffusion of Cu ions. However, no consensus has been reached on the impact of segregation on the overall corrosion behaviour of printed components, leaving a lingering question for future inquiry. Jadhav et al. [125] employed CNP to tackle laser reflection concerns in Cu alloys. However, the low density and poor wettability of CNP in liquid Cu promoted segregation near the melt pool. In order to address

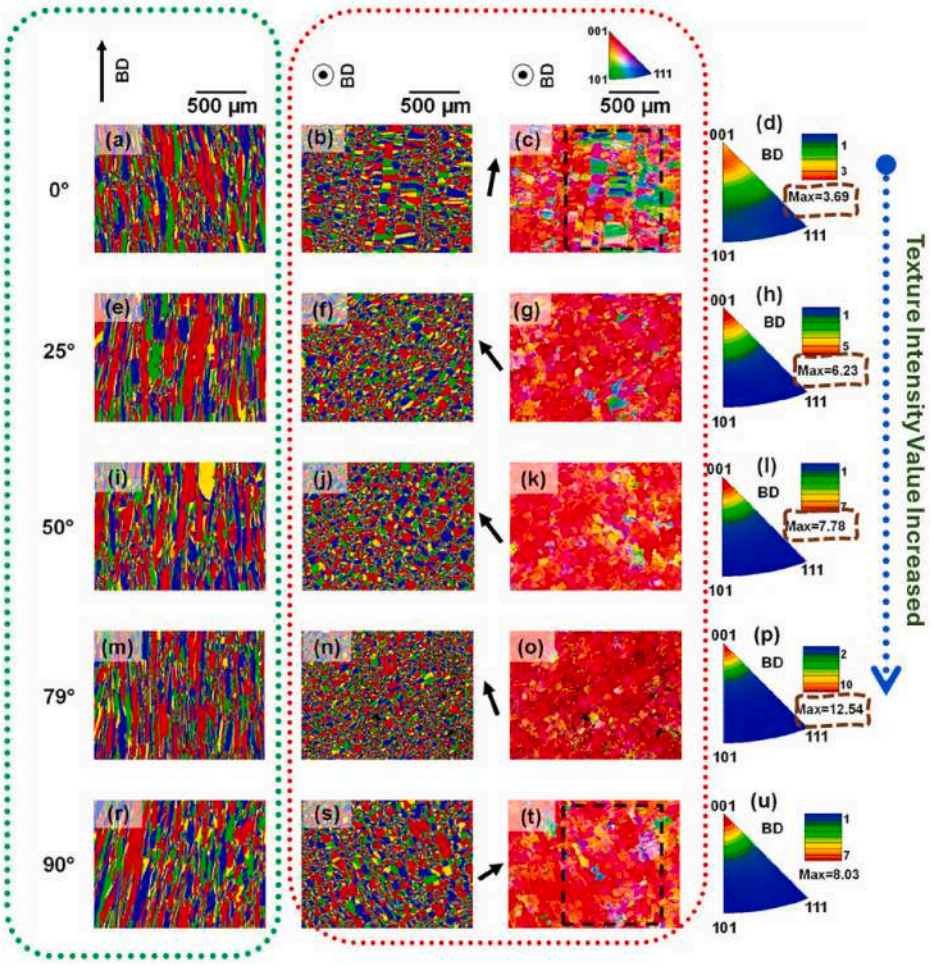


Fig. 26. EBSD maps depict the effect of scan vector rotation on grain structure in the build (green box) and perpendicular directions (red box). The blue arrow indicates the range of highest intensity, from 3.7 to 12.5 in L-PBF Cu-SMA [53].

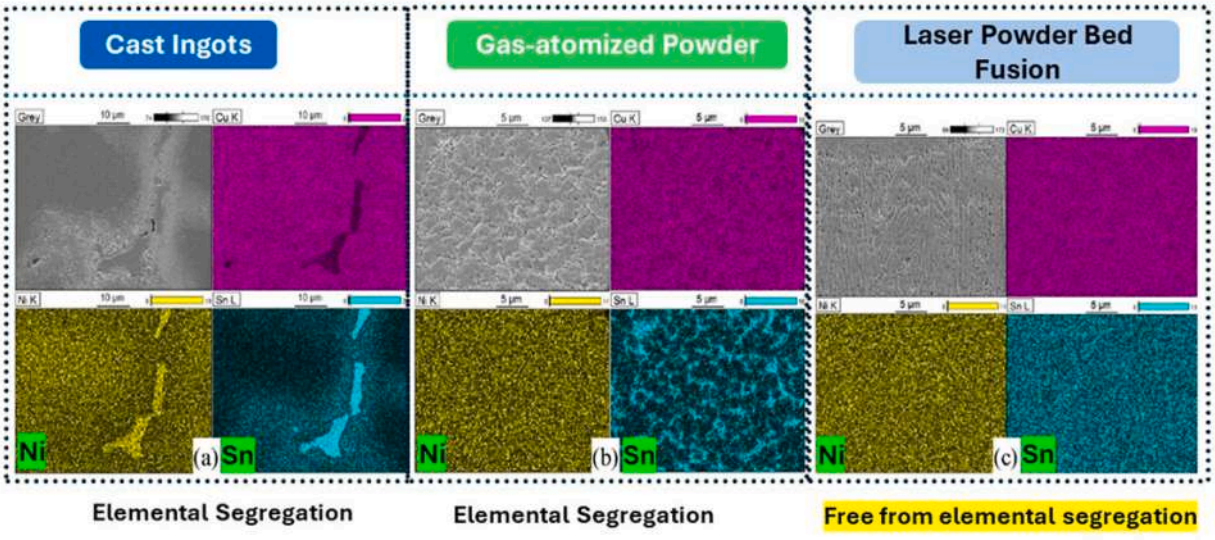


Fig. 27. Process-dependent element segregation for Cu–15Ni–8Sn alloys: (a) Casting; (b) Alloy powders; (c) L-PBF parts [202].

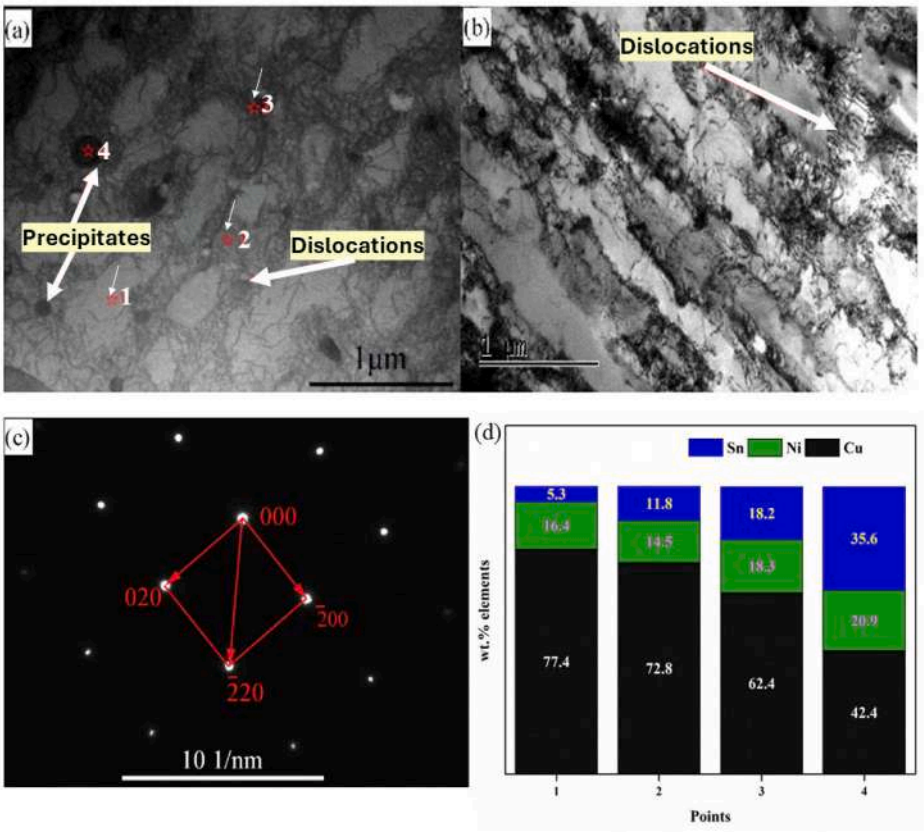


Fig. 28. TEM bright field images of L-PBF Cu–Ni–Sn alloys: (a) Cross-section of the cell structure (1: without dislocation, 2 and 3: with dislocation, 4: fine precipitates (80–200 nm)); (b) Longitudinal section of the cell structure; (c) Selected Area Electron Diffraction pattern; (d) EDS maps of points 1 to 4 (Fig. 28a) [202].

segregation, TiB_2 particles (1 wt.%) were employed to reduce Sn segregation in Cu–Ni–Sn alloys during L-PBF, with process parameters optimised to avoid or regulate the size of the segregated phase [70]. By fine-tuning process parameters, post-treatment strategies, and modifying the feedstock, it is possible to control segregation, minimising its adverse impact on the mechanical, corrosion behaviour, etc., of printed copper components. In addition, micro-segregation drives the formation of dislocation cell structures during L-PBF. Notably, thermal history is a key factor influencing the development of dislocation cells, as L/E-PBF processes exhibit varying thermal histories throughout processing [205,206], with the processing pathway in AM also influencing the Marangoni effect. Consequently, factors such as the diffusivity of elements (Marangoni convection modified the diffusion process), which affect solute-dislocation interactions, are crucial in mitigating the detrimental effects of micro-segregation. By exploring the interplay between process parameters (such as scanning speed, hatch spacing, and remelting strategy) and microstructural features, researchers could gain critical insights into optimising L/E-PBF processes for Cu alloys, thereby achieving an ideal balance in overall performance while enabling control over solidification structure and micro-segregation.

7.1.7. Powder denudation

During laser beam progression on the powder bed, metallic particles near the laser spot drifted away and caused denudation around the laser-melted track. This denudation occurred during the laser-induced vaporisation of Cu–Zn alloy due to the explosive evaporation of Zn, which is attributed to its low boiling point [47]. Additionally, the ambient gas vortex movement dragged particles near the vapour jet, causing denudation according to the Bernoulli effect [207]. Cu alloys exhibit high reflectivity toward NIR lasers; therefore, high laser power is often employed to achieve full densification. However, the use of high laser power (400 W) during L-PBF proved detrimental, as it increased the likelihood of powder denudation and resulted in increased porosity of the L-PBF Cu–Ni–Al–Mn alloy samples [169]. Furthermore, denudation led to the formation of LoF pores in L-PBF Cu–Cr–Nb–Ti alloys at scanning speeds below 800 mm/s [207]. For Cu–Cr–Nb alloys, high scanning speeds (800 mm/s) combined with moderate power (110-130 W) caused excessive powder denudation by the melt pool, which inhibited part build-up [128]. To mitigate particle denudation, it is imperative to meticulously select L-PBF process parameters such as scanning speed, laser power, protective gas flow velocity, etc., in accordance with the composition of Cu alloys under consideration to avoid premature part failure and reduce porosity and surface roughness.

7.2. Surface defects

7.2.1. Balling effect

Balling implies the segmentation of continuous melt pools into discrete islands (Fig. 29). These distinct islands, known as balls, appear along the trailing end of the melt pools (unstable single melt track). The three primary mechanisms responsible for the formation of balling in single-track melt pools of L/E-PBF Cu alloys/composites are Plateau-Rayleigh instability, wetting instability, and Marangoni instability. For Cu alloys, hydrodynamic capillary instabilities have been identified as a potential mechanism for balling under lower energy density or higher scanning speed [208]. As the scanning speed increased, the melt pool lengthened and narrowed. If the length-width ratio of the melt pool is surpassed, Plateau–Rayleigh instability transpires [209]. Gustmann et al. [210] noticed balling in the Cu–11.8Al–3.2Ni–2.9Mn alloy as the scanning speed increased from 200 to 3000 mm/s, as shown in Fig. 29. The balling zone was detected at high scanning speeds with both high (> 300 W) and low (100 W) laser powers, as well as at lower scanning

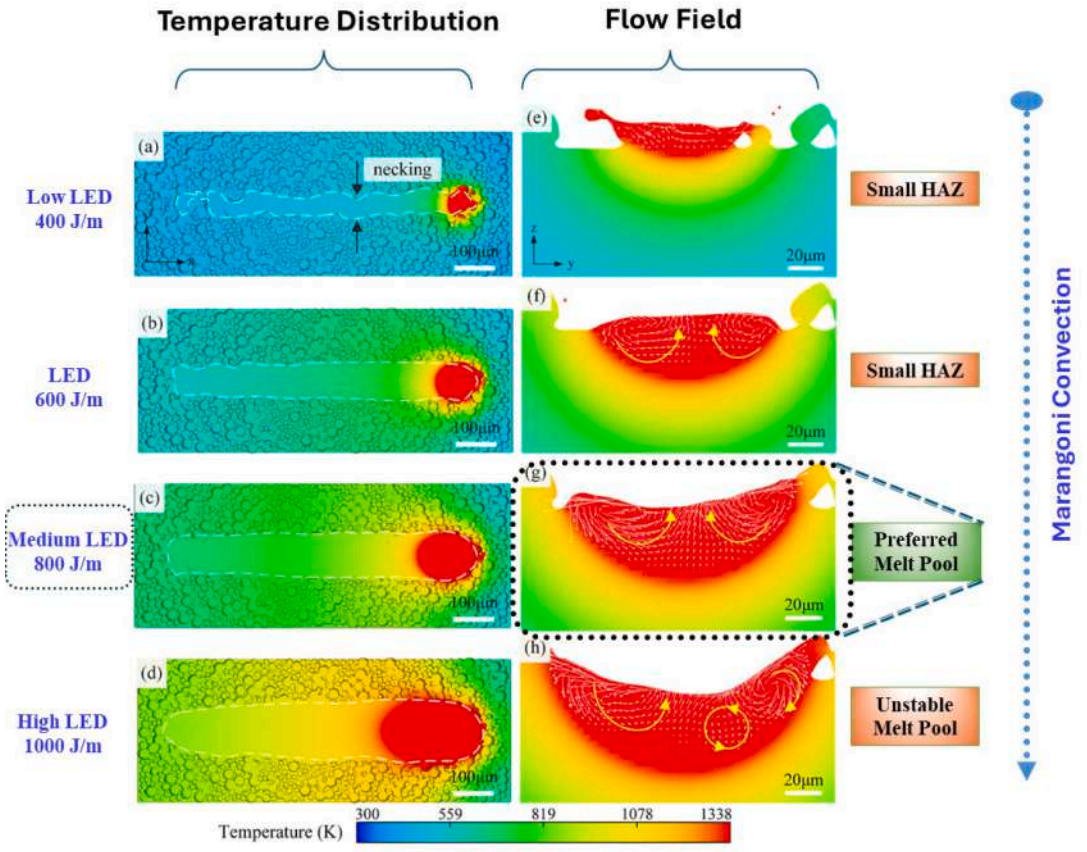


Fig. 29. Single track morphologies of Cu–Al–Ni–Mn alloy during L-PBF at scanning speeds of 200, 700, 1200, and 3000 mm/s are wide: (a) wide; (b) narrow; (c) irregular; (d) balling; and (e) laser power-scanning speed processing maps (with the laser moving from the tail to the head of the arrow)[210].

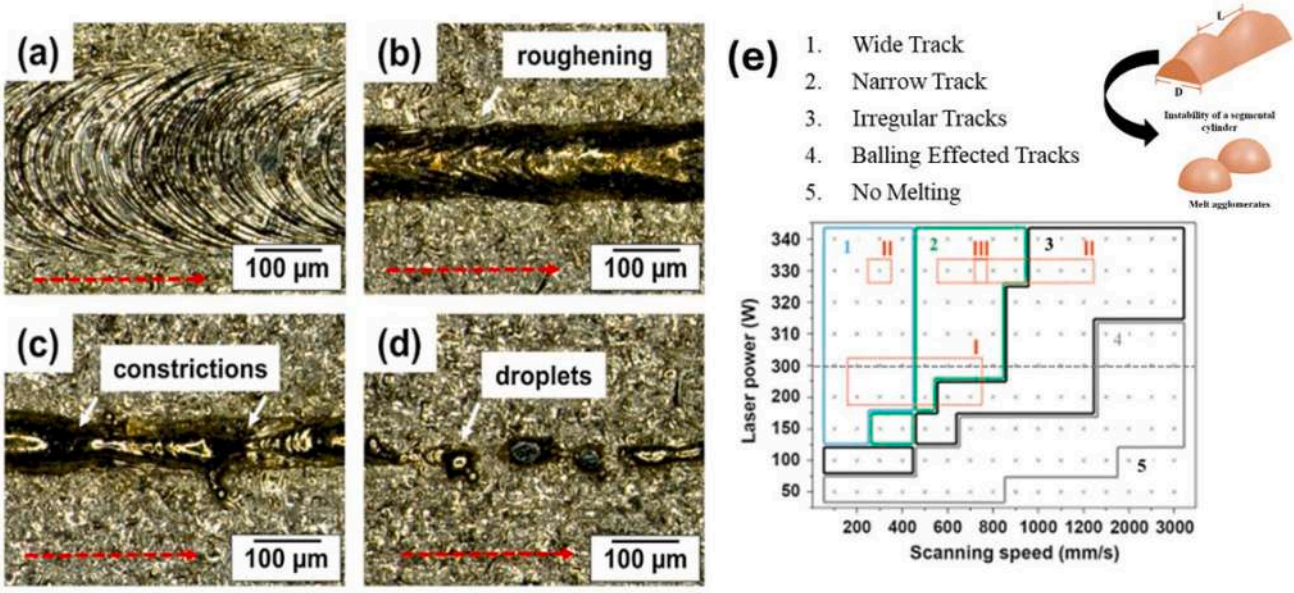


Fig. 30. Temperature distribution and flow field within a Cu alloy melt pool illustrate the influence of energy density on melt pool stability [211].

speeds with low power (< 100 W) (Fig. 29**e**). Similarly, Wang et al. [211] observed balling attributed to the Plateau-Rayleigh instability in their 3D simulations for the Cu–Cr–Zr alloy at low energy density (400 J/m), as shown in Fig. 30. Marangoni convection, induced by high-temperature gradients, has the potential to disrupt tracks and contribute to the formation of balling in L/E-PBF Cu alloy/composite parts by reducing surface energy through capillary forces (shrinking to a smaller surface area). Modelling analysis of L-PBF Cu alloys revealed that Marangoni instability increased as energy density increased. A melt pool with a concave area was formed by high energy density (1000 J/m)

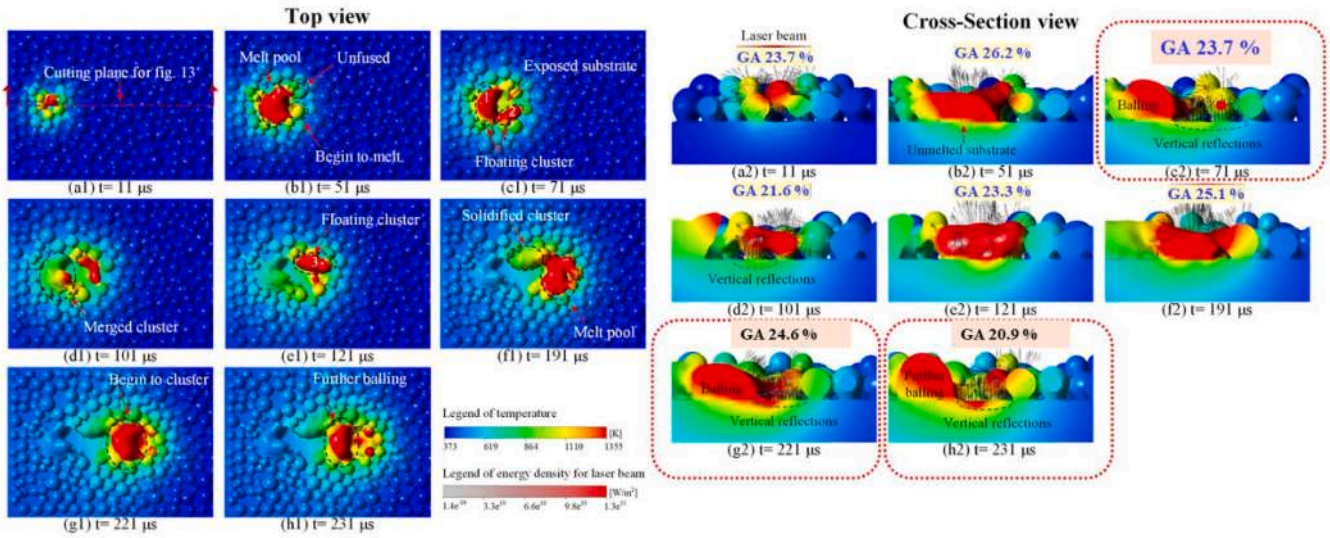


Fig. 31. Effect of global absorptivity and balling tendency (highlighted in the box) on Cu alloy melt pool stability at lower energy density [60].

as a result of recoil pressure and Marangoni convection, which were conducive to balling formation (Fig. 30). Furthermore, poor wetting between the molten metal and substrate may exacerbate balling. While Cu oxides remain stable up to 1300 °C and may dissolve during the L-PBF process, studies suggest that the presence of oxygen likely exerts minimal impact on balling formation in Cu alloys. This could be due to the increased absorption of the oxidised surface when compared to pure Cu feedstocks [201]. Further investigation is warranted to validate this oxidation hypothesis and mitigate balling during L/E-PBF processes for Cu-based feedstocks. Balling is also influenced by process parameters that directly affect the solidification rate. At lower scanning speeds, "self-balling" is observed due to the extended time required for surface tension effects to trigger breakup in a large melt pool (the high energy content within the melt pool (more liquid) drops the rate of solidification) [208]. Ball formation is also found at low energy density, where it is induced by high melt viscosity and poor wettability of the molten metal (insufficient fusion). The low power density caused partially melted particles and unmelted substrate beneath the powder. To minimise the surface energy, the melt pool aggregates into clusters rather than spreading out and wetting the entire surface. Initially, small floating clusters of molten metal form, leaving areas of the substrate exposed to the laser beam, which diminishes overall absorption. As melting progresses, these floating clusters may merge with each other, forming larger "melt island aggregates" (Fig. 31). Furthermore, at lower energy density, the combination of lower temperatures, increased melt viscosity, and elevated surface tension accelerates the process further [60].

The ratio (balling susceptibility index) of solidification timescales ($\tau_{solidification}$) to melt spreading timescales (τ_{spread}) is an indicator of balling formation or nodularization in any alloy and is determined by alloy compositions as well as process parameters. Balling during processing is less likely, with a higher balling susceptibility index. Conversely, a lower balling susceptibility index indicates a higher likelihood of balling. Vela et al. [212] identified that pure metals with high diffusivity, like W and Cu, tend to exhibit lower balling susceptibility indexes (they are more prone to balling). Interestingly, alloys of these high-diffusivity elements (like Cu-based alloys) can exhibit higher resistance to balling than their pure counterparts due to the lowering of thermal conductivity. The balling susceptibility index of Cu alloys is significantly lower, rendering them highly susceptible to balling (Cu–10Ni > steel > Mg alloys > Ti alloys > Ni–Ti alloys) [212]. Consequently, for fully dense L/E-PBF Cu alloys/composite components, it is critical to regulate the balling of Cu alloys, as balling disrupts the formation of a smooth surface, interlayer bonding, and leaves voids or pores that ultimately influence the material properties and appearance of the component [213]. Regulating balling in single-track melting is key

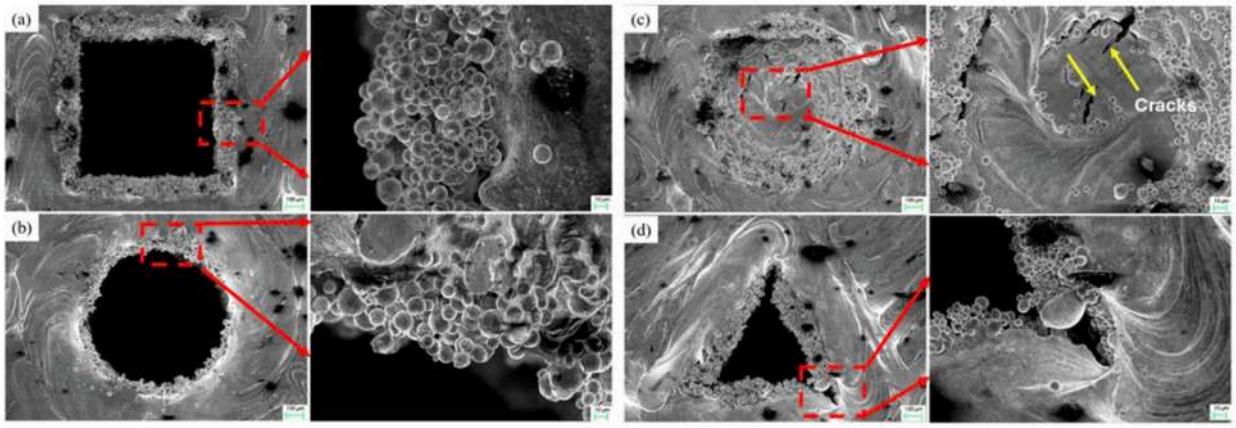


Fig. 32. Presence of partially sintered powder particles varies with surface texture shape for the Cu–10Sn alloy: (a) Square; (b) Circular; (c) Hemispherical; (d) Triangular [216].

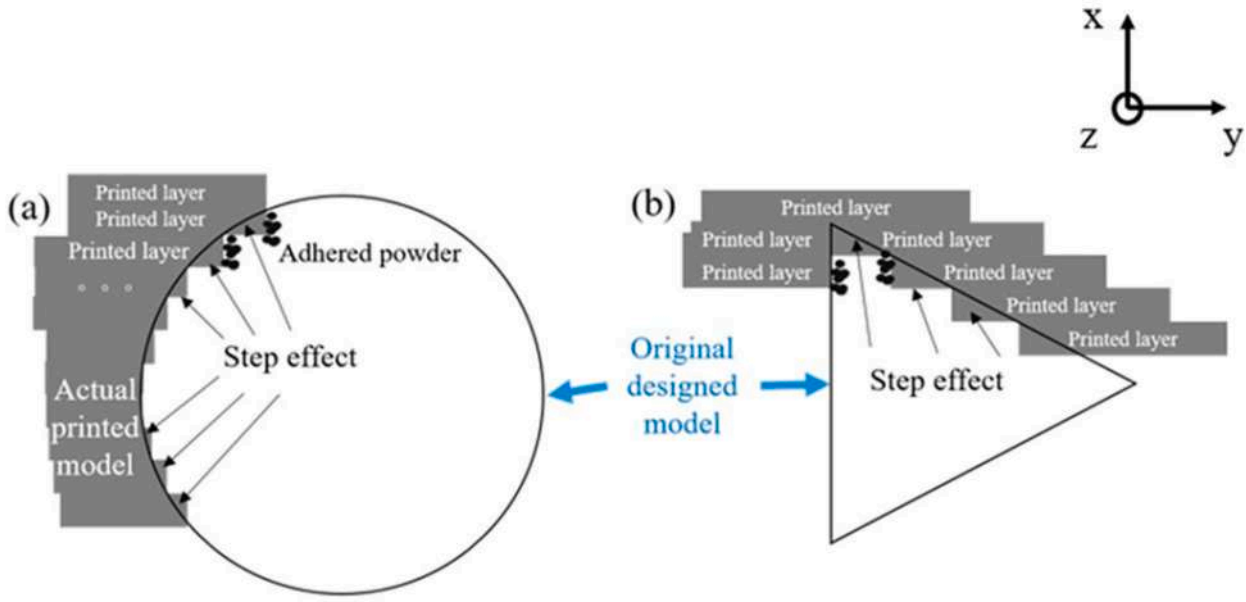


Fig. 33. Part discretisation into layers fosters the staircase effect, highlighting the importance of geometry for dimensional accuracy [216].

to fabricating near-fully dense L-PBF parts since balling originates in single-track solidification. Cu alloy balling can be reduced by altering material parameters (changing composition) and tweaking process parameters such as laser power, scanning speed, hatch spacing, and layer thickness [214]. Ren et al. [60], in simulated research on Cu alloys, revealed that minimising balling through optimal process parameters and possibly adding higher linear energy density (LED) when applicable is critical for attaining steady and efficient laser energy absorption in the L-PBF process. Lindström et al. [215] stated that increased feedstock powder absorptivity, elevated laser power, reduced thermal conductivity, and substrate pre-heating are feasible strategies for enhancing the process window for efficient melting while minimising balling. Moreover, it is essential to exercise caution when increasing the scanning speed for Cu alloy printing, as although it can enhance productivity, it should not exceed a threshold that leads to melt-pool instability or balling. Balling, which is frequently observed at higher laser powers, can be exacerbated by the necessity for increased power stemming from reflectivity discrepancy for Cu alloy/composite feedstock. Future research should focus on optimising energy density (LED/VED) using a single-track method to reduce the likelihood of balling. Overall, tailored process parameters and feedstock characteristics (control the melt pool size, along with its thermal and fluid characteristics) are effective strategies for regulating balling, ensuring better surface finishes, and minimising defects to achieve near-fully dense L/E-PBF Cu alloy/composite parts.

7.2.2. Unconsolidated powder

Partially melted or non-melted particles on the surface of AMed L-PBF Cu alloy parts modify the surface roughness (dimensional tolerance), while the interior of the sample increases porosity, inhibiting the printing of dense components. The sharp corners (squares and triangles) exhibited increased powder adhesion in L-PBF Cu–10Sn alloy parts, resulting in rougher surfaces. Conversely, smooth geometries (hemispheres) showed less adhesion and a smoother finish (Fig. 32). This variation arises from the influence of texture shapes on heat dissipation and melt pool stability [216]. Mehta et al. [109] observed that, for Cu alloys, unconsolidated particles adhered to the lateral surfaces of cubic specimens, altering surface roughness, particularly at slow scanning speeds, regardless of power, due to the high thermal conductivity of Cu alloys, which resulted in substantial heat transfer to adjacent particles. The degree of sintering of the powder diminished with the escalation of scanning speed under a consistent laser power or with the reduction of laser power under constant scanning speed. Moreover, for lattice structure printing of a Cu alloy, partially melted or unmelted particles clung to the cell node and strut of the lattice structures [217]. However, these partially melted or unmelted particles acted as nucleation sites for new grains during solidification, allowing the lattice structure to exhibit the intended mechanical properties [218]. Despite this potential benefit, unmelted or partially melted particles remain a significant concern in L-PBF Cu alloys, as they compromise surface quality, dimensional accuracy, and potentially the mechanical properties of the final part. To mitigate these issues, careful selection of process parameters, particularly scan speed, and potentially considering part geometry design, is crucial for achieving near-fully dense L/E-PBF Cu alloy/composite parts.

Table 5
Surface roughness values of Cu-based parts fabricated by the L/E-PBF processes.

Position	L-PBF	E-PBF	Ref.
Top surface roughness R_a (μm)	7.0–1000.0	41.7–119.1	[120,221,223]
Side surface roughness R_a (μm)	3.3–3.4	–	[74]

7.2.3. Stair-step effect

The stair-step effect is associated with the distinctive stepping pattern observed on the lateral surfaces of AMed parts, leading to discrepancies between the intended and manufactured geometries (as shown in Fig. 33). The stair-step effect is the major contributor to the unevenness of edges on an AM component and is quantified as follows using Eq. (7.5) [219].

$$\mathrm{Ra} = 1000\mathrm{tsin}\left(\frac{90-\theta}{4}\right)\tan(90-\theta) \tag{7-5}$$

where t is the layer thickness (mm), and θ is the build angle ($^{\circ}$), Ra is the arithmetic mean surface roughness (μm).

Factors contributing to the staircase effect include layer thickness, complexity of geometry to print, and machine calibration. Complex overhang geometries enable the staircase effect apparent in the lattice construction of Cu alloys [218]. Min et al. [216] revealed that the texture shape during L-PBF of Cu alloys influenced the staircase phenomenon. The staircase effect resulted in poor surface quality, significantly compromising fatigue characteristics and ultimately necessitating

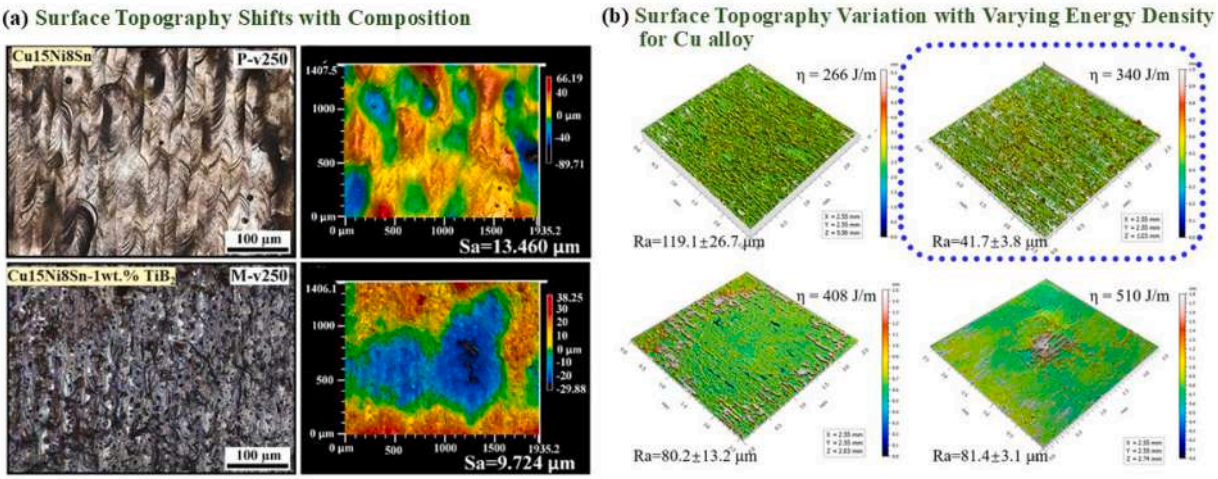


Fig. 34. Variation of surface roughness on Cu alloy top surfaces: (a) Influence of alloy composition; (b) Effect of process parameters [70,120].

post-processing [213,220]. Overall, the stair-step effect is unavoidable for the L-PBF-fabricated Cu alloy/composite parts. While machine calibration, layer thickness reduction, etc., can minimise its impact, they remain incapable of complete eradication.

7.2.4. *Surface roughness*

The surface roughness of AMed Cu alloy parts is often higher than the formative and subtractive methods, with R_a ranging from 7 to 1000 µm (Table 5) [100]. Ladani et al. [81] noticed that Cu–CNT composites exhibited higher surface roughness (Ra as large as 1 mm) compared to L-PBF-fabricated Cu parts (Ra below 20 µm) and with roughness varying according to VED. Gao et al. [70] emphasised the importance of laser absorptivity in Cu alloys, reporting that TiB_2 minimised surface roughness in Cu–15Ni–8Sn L-PBF components by 28 to 40%, due to its higher laser reflectivity, which regulates alloy melting and solidification (as shown in Fig. 34**a**). Moreover, laser power significantly influenced the roughness of the Cu–10Sn alloy during L-PBF, as demonstrated by ANOVA analysis [107]. Seltzman and Wukitch [221] showed that the surface roughness (which can minimise RF losses, improve cleaning efficiency, and reduce the risk of arcing) is crucial to the functionality of GRCop–84, and they suggested a multi-step mechanical and chemical method to improve roughness. Additionally, GRCop–84 in the as-built condition exhibited a rougher top surface (Ra of 11.6 µm) with a hatch pattern, compared to the vertical side wall (Ra of 3.3 µm), which displayed ripples due to feedstock adhesion. Aksa et al. [222] found that post-processing at high temperatures increased the surface roughness of silver-coated Cu alloy, thereby conditioning their tribological performance. Lintel et al. [57] noticed that using a multiple exposure strategy reduced top surface roughness from 40 ± 5 to 9 ± 2 µm, with roughness increasing with laser power. Interestingly, the top surfaces showed lower roughness than the side surfaces, likely due to the multiple exposure strategy. L-PBF Cu alloy surface roughness increased with scanning speed and reduced laser power, as well as when the hatch spacing was either very low or high [128,223,224]. In contrast, lower laser energy densities (< 200 J/mm^2) for L-PBF Cu–Al alloy parts resulted in significantly higher surface roughness exceeding 20 µm, while higher energy densities yielded smoother surfaces (< 10 µm) regardless of Al content (0.75, 1.5, or 3 wt.%) [225]. E-PBF-fabricated Cu–Cr–Zr alloy samples showed rough surfaces (> 80 µm) at both high (510 J/m) and low (216 J/m) linear energy densities (Fig. 34**b**). However, medium energy densities (340-408 J/m) resulted in lower surface roughness (40-80 µm) [120]. Using confocal microscopy, single layers of L-PBF Cu–Sn–Ti alloy specimens showed a significant reduction in surface roughness (from 40 µm to 5 µm) with higher laser energy densities (5-10 J/mm^2), attributed to improved wettability and melting at higher energy densities, leading to a smoother surface with fewer irregularities that could adversely impact subsequent powder spreading and layer formation [226]. Uneven protrusions near the melt track during the printing of Cu–Zn alloys, caused by explosion-induced droplet spatter, may deteriorate surface roughness and increase friction during the deposition of new powder layers [47]. Additionally, the roughness of AMed Cu alloy parts was influenced by the staircase effect, unconsolidated powder, spatter, and balling. While lower surface roughness in AMed components helps improve corrosion and fatigue resistance [227], the surface roughness of Cu feedstock is associated with the morphology, and the presence of satellites plays a crucial role when selecting powder feedstocks to attain dense and smooth components. Overall, ensuring a smooth surface (Ra < 1 µm) for L/E-PBF printed Cu alloy/composite parts is a formidable task, achievable only through meticulous feedstock design and optimised process parameters. Consequently, post-processing procedures and advanced machining technologies are essential. There is currently a scarcity of literature on post-processing and innovative machining procedures for realising smooth surfaces on AMed Cu alloy parts; therefore, this topic is open to further exploration. Despite the current progress in L/E-PBF of Cu alloys/composites, future research needs to better establish the link between surface roughness, build orientation, residual stresses, and fatigue life, with a focus on process optimisation and a deeper understanding of solidification and cooling mechanisms.

7.3. *Geometry and dimensional defects*

Geometrical and dimensional defects in AMed parts, such as warpage, delamination, and deformation, are attributed to macroscopic residual stresses (RS). Non-uniform stress fields, which are the origin of RS, resulting from intricate thermal histories/phase transformations, are influenced by the geometry of the printed part, process parameters, and feedstock characteristics. The effective management of RS is essential for minimising the scattering of properties and maintaining the structural integrity of L/E-PBF Cu alloy parts, which is elaborated upon in the subsequent section.

7.3.1. *Residual stress*

Intense localised heating (for 1 to 4 ms), rapid cooling (~10^4-10^8 K/m), solid-state phase transition, and layer-by-layer deposition with restricted shrinkage all contribute to a substantial temperature gradient (~10^3–10^4 K/mm) within the component during the L/E-PBF processes [228]. These transient thermal gradients ultimately manifest as residual stresses after solidification. Indeed, the temperature dependence of powder feedstock properties (viscosity, thermal conductivity, and

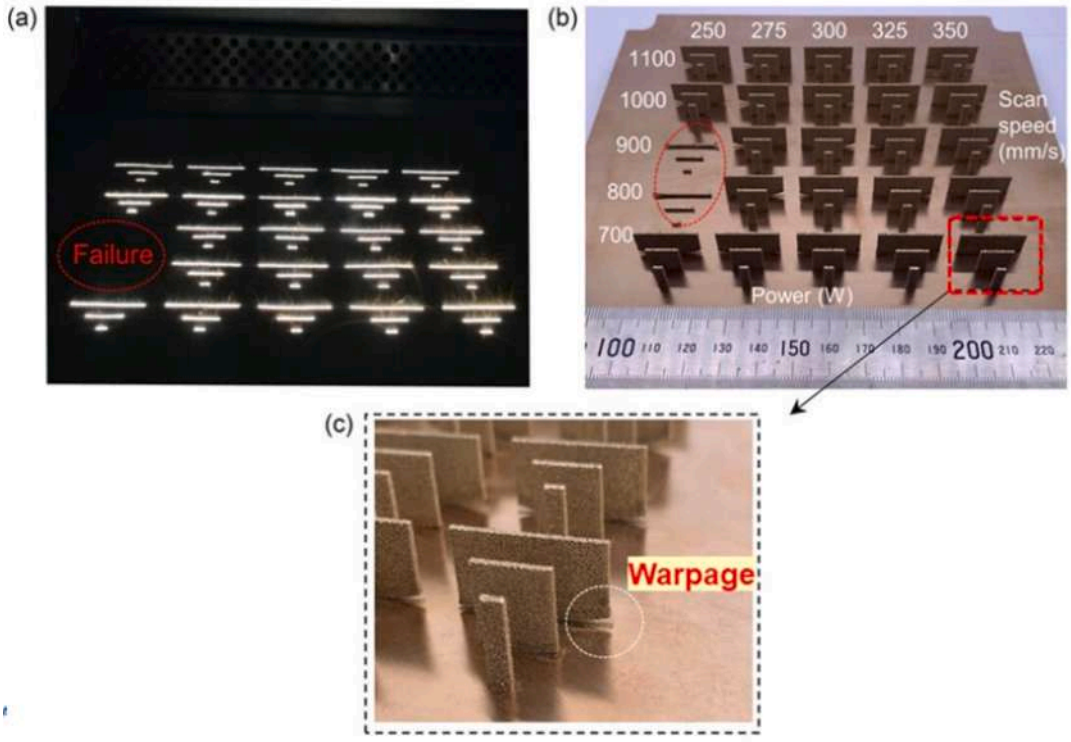
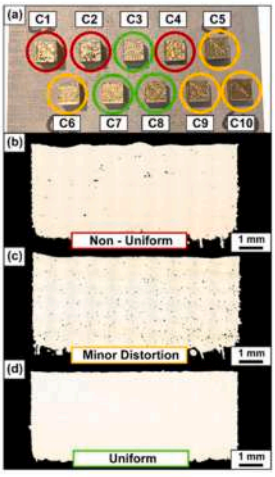


Fig. 35. Illustration of warpage formation in thin parts during L-PBF with suboptimal process parameters for Cu alloy [231].



Sample No.	Laser Power (W)	Scan Speed (mm/s)	Hatch Distance (μm)	
C1	200	500	70	Non-Uniform
C2	200	700	66	Non-Uniform
C3	200	900	66	
C4	225	900	55	Non-Uniform
C5	225	1100	50	Distortion and Raised Edges
C6	200	500	94	
C7	200	700	90	
C8	200	900	90	
C9	225	900	74	Distortion and Raised Edges
C10	225	1100	67	

Fig. 36. Suboptimal process parameters lead to defects: non-uniformity (red), distortion, and elevated edges (orange) [119].

specific heat) complicates AM thermal gradients. RS can be classified into three types based on their length scale: Type I (macro or larger than 1 mm) affects all parts through warpage, delamination, distortion, and curling; Type II (intergranular RS/multiple grains-level or 0.01 mm–1.0 mm); and Type III (intragranular RS/within grain-level or < 0.01 mm) residual stresses are intrinsic to polycrystalline materials, stemming from inherent variations in grain orientation, the stress field of dislocations at the atomic level, and coherency at interfaces [229]. The presence of Type I macroscale RS in AMed Cu alloy parts causes distortion, warpage, and delamination from the support structure and build plate [169,230,231]. Lin et al. [231], for instance, emphasised the relevance of geometry in thin-walled NAB L-PBF parts and noticed that larger samples exhibited higher warpage at the interface between the build platform and the sample due to excessive thermal contraction of the alloy during solidification and solid-state phase change, and the intensity of warpage varied with laser power and scanning speed (as shown in Fig. 35). Similarly, such warpage/edge elevation was identified at the interface between the build plate and the AMed part at different hatch spacings with constant laser power and scanning speed, as shown in Fig. 36 **C5 and C10** samples. Otherwise, distortion of the AMed parts following separation from the support structure, as demonstrated in Fig. 37**,** was caused by non-uniform RS at the edges and could restrict L-PBF part quality. Warpage in another scenario may result in damage to the recoater blade, as illustrated in Fig. 38**a** [232]. Alternatively, these Type I macroscale RS may result in the failure of the printed part of the Cu–Al–Ni–Mn alloy between successive layers

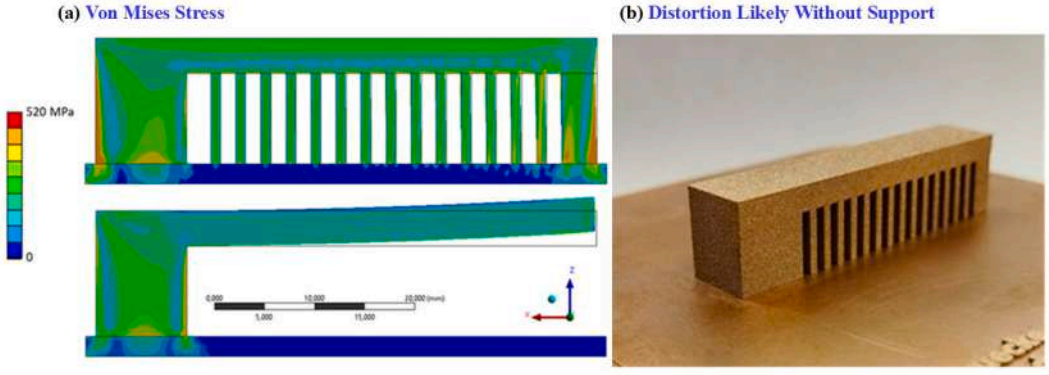


Fig. 37. (a) Von Mises stress simulation comparing supported and unsupported parts; (b) Residual stress imbalance in Cu–Sn alloy printed part leading to component distortion failure [230].

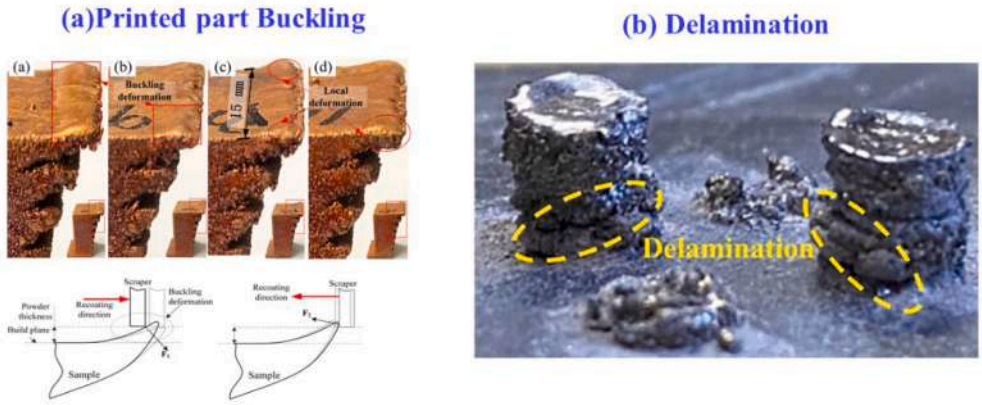


Fig. 38. (a) Buckling; (b) Delamination of Cu alloy parts during L-PBF [169,232].

(delamination) or through multiple layers (cracking) at higher scanning speeds (> 300 mm/s), as illustrated in Fig. 38**b** [169]. Overall, residual stresses cause detrimental effects on Cu alloy components, including geometry loss, detachment from build platform/support structures, and component failure.

The RS in the AMed components were predominantly composed of three distinct categories of stresses: mechanical, structural, and thermal. During AM, the laser/electron beam melts powder, forming a melt pool; intense localised shrinkage of liquid metal occurs in the vicinity of the melt pool; mechanical stress ensues (liquid stage). A phase transition occurs from liquid to solid as the molten metal cools and solidifies. This phase transition may be accompanied by a volumetric change, leading to structural stress. When the metal cools to ambient temperature in the final stage or solid phase, localised transient rapid heating and cooling during AM elicit a severe thermal gradient, which culminates in thermal stress. Therefore, reducing residual stresses of AMed components is accomplished by minimising any of these stresses while understanding the formation mechanism. Type I RS in L-PBF parts can be explained by two models: the temperature gradient mechanism (TGM) and the cool-down phase model (CDPM) [233]. As per the TGM, residual stresses in a single melt track are generated due to the restriction of the molten material expansion by the surrounding cooler material under high-temperature gradients. When the laser beam irradiates a newly deposited track, the high temperature induces expansion in the heated area. However, the surrounding colder material restricts this expansion, resulting in compressive stresses in the heat-affected zone. Once these stresses reach the yield strength (YS), concave deflection occurs in the opposite build direction of the additive manufacturing (AM) component due to the absence of mechanical restrictions. Furthermore, as the laser

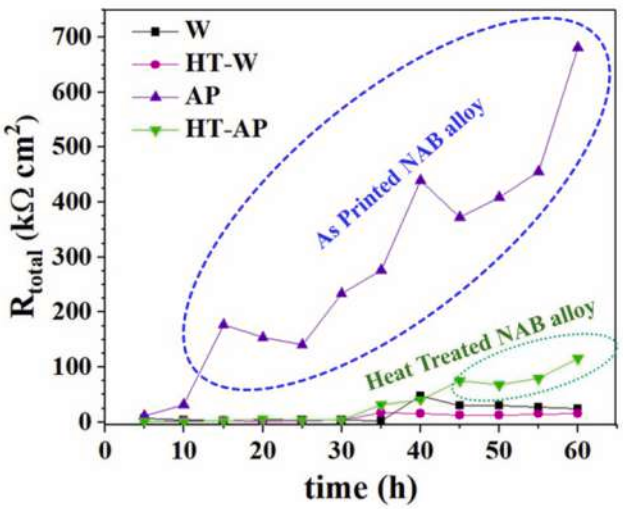


Fig. 39. Distinct microstructure of AB NAB alloy samples correlates with superior corrosion resistance in a 3.5 wt.% NaCl solution (5-hour R_{total} measurements, W: wrought alloy, HT: heat treated) [234].

moves and the heat source is removed, the previously heated region cools and undergoes shrinkage. However, this shrinkage is constrained by the compressive stresses formed during the heating phase, leading to the development of tensile residual stresses (RS), which cause deformation in L-PBF-fabricated parts. Contrary to the TGM, the CDPM

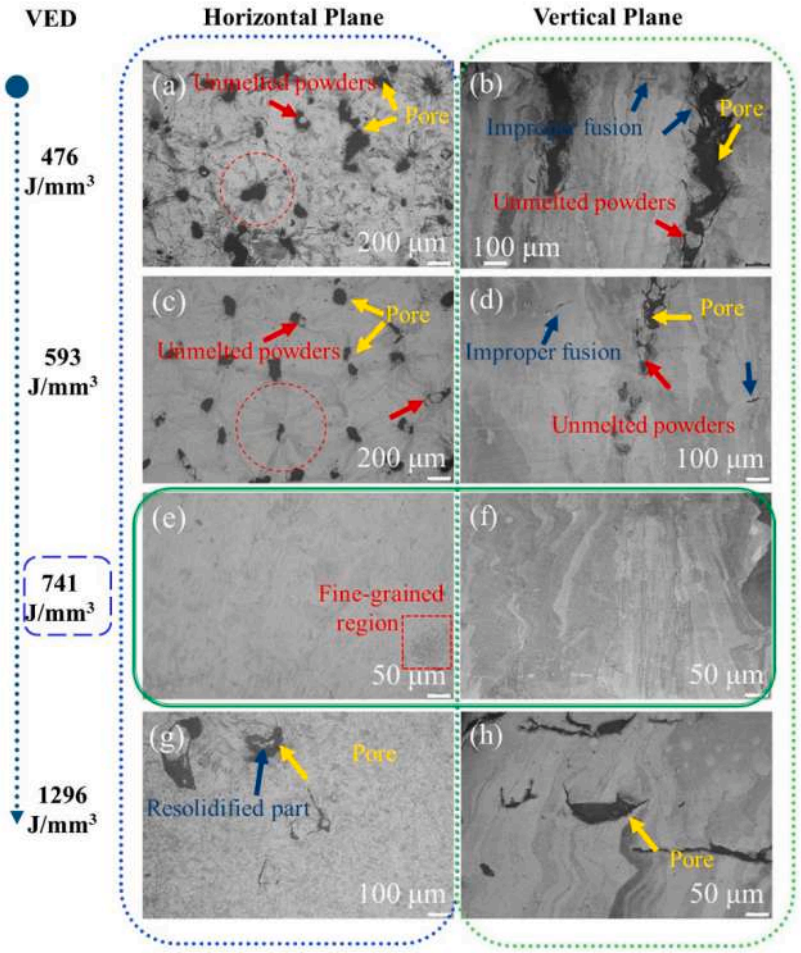


Fig. 40. Comparison of VED optimisation (741 J/mm^3) and process-induced defects in Cu alloy printed parts [51].

describes the behaviour of a fully melted powder region, where the newly deposited layer has a higher temperature than the previously deposited layer. Upon solidification and cooling, the newly deposited layer contracts; however, the underlying solidified layer partially resists this contraction, generating tensile stress in the top layer and compressive stress in the layer beneath. Notably, compressive stress tends to accumulate in the previously deposited layer as the number of layers increases, while tensile stress becomes more pronounced in the topmost layer. This results in the accumulation of stress nuances in AMed parts, where the interior stress field is predominantly compressive, and the surface stress field is more pronounced in tension [228]. Suppose the RS surpasses the YS of the L/E-PBF Cu alloy/composite parts. In that case, the material will release additional stress via plastic deformation, resulting in warpage, distortion, delamination, and curling in AMed parts, ultimately leading to component failure. However, the inherently high RS of as-built L-PBF NAB alloy parts enhances corrosion resistance, attributed to the presence of a martensitic supersaturated solid solution with a uniform microstructure (Fig. 39). Additionally, the rapid formation of a corrosion-resistant film is facilitated by the ability of martensite nano-twins [234]. Conversely, in L-PBF Cu-Sn alloy samples, residual stress exerted a negligible influence on corrosion performance, which was predominantly governed by dislocation density [203]. In the future, further exploration is necessary to address the lack of a clear consensus and consistency regarding the kinetics of corrosion initiation and propagation behaviour of AB Cu alloy printed parts. Primarily, two main approaches are employed to mitigate RS: in-process control (process parameters, preheating) and post-processing techniques (heat treatment, surface modification). However, despite residual stress being the most detrimental defect, there is a paucity of research on L/E-PBF printed Cu alloys/composites regarding an in-depth investigation of the interplay between process factors and their collective influence on residual stresses (Type I, Type II), as well as the impact of RS on mechanical properties, fatigue, creep, and corrosion behaviour, which can be investigated in the future.

Alongside the three aforementioned categories of defects, other defects that occur during L-PBF or E-PBF fabrication of Cu alloy components include interparticle gaps, spatters, and interfacial defects such as branch microcracks and intermittent cracks [170,235]. These anomalies can be elucidated as the energy transmitted during L/E-PBF for Cu alloys/composites affects melt viscosity and surface tension, as delineated by the following Eq. (7.6), which subsequently influences the tendency for porosity formation in Cu alloy/composite parts.

$$\sigma_{\text{Cu liquid}} = 1330 - 0.23\,(T - Tm) \tag{7-6}$$

Where $\sigma_{\text{Cu liquid}}$ (m/Nm) is the surface tension of the Cu melt, and the Cu melting temperature (T_m) is 1085 °C. As VED increases, the temperatures (T) during laser-particle interaction also increase, resulting in a decrease in the viscosity of the Cu in the melt pool. Moreover, the dynamic viscosity (mPa•s) of Cu melt is linked to surface tension and temperature according to the Fowler-Born-Green Eq. (7.7), as follows [236]:

$$\mu_{\text{Cu liquid}} = \frac{16\sigma_{\text{Cu liquid}}}{15}\sqrt{\frac{m}{kT}} \tag{7-7}$$

where $\sigma_{\text{Cu liquid}}$ (m/Nm) is the surface tension of the Cu melt, m is the atomic mass, k represents the Boltzmann constant, and T is the

Table 6
Breakdown of defects observed for Cu alloys/composites during L/E-PBF.

Defects	Causes	Consequences	Mitigation strategies	Need more research?
Warping, Curling, Edge elevation, Distortion, Delamination	RS > YS, inadequate layer bonding	Part failure, oversize, dimensional inaccuracies	Preheating, optimising process parameters	Yes, optimising substrate structural design for Cu-SMA, modelling and prediction
RS	High cooling rate, temperature gradients	Crack, curling, delamination, distortion, edge elevation, ↓ fatigue performance, corrosion properties	Preheating, tuned process parameters, post-AM treatments	Yes, a comprehensive study of RS, properties, and simulation
Stair-step effect	Higher layer thickness, geometric intricacy of design, improper machine calibration	↓ geometric precision, roughness, fatigue properties	Optimised layer thickness and orientation, post-processing techniques	Yes, adaptive layer thickness for lattice structures
Unconsolidated powder	Improper VED, spatter, high TC, feedstock characteristics, oxidation	↓ geometric precision, mechanical properties, porosity	Optimised VED, preheating, and feedstock selection	Yes, adaptive process control, in-situ monitoring
Balling	Melt pool instability, poor wettability, oxidation, feedstock characteristics	Roughness, porosity, impeded flowability, impaired performance, geometrical precision	Adjusting alloy composition, process parameters	Yes, modelling and adaptive strategies
Surface roughness	Feedstock composition, untuned process parameters, balling, staircase, spatter, unmelted or partially melted powder	Rough surface, poor fatigue performance, aesthetic quality	Minimised defects (balling, staircase, spatter), tuned process parameters, remelting, post-processing techniques	Yes, the relation between roughness, fatigue, and corrosion performance
Internal pores (LoF, keyholes, metallurgical pores)	Atmospheric variables, entrapped gas, improper VED, selective evaporation	↓ mechanical, electrical, fatigue properties, corrosion resistance	Tuned VED, protective atmosphere variables, altered feedstock characteristics, remelting	Yes, pore size, distribution, fraction, shape correlation to fatigue, corrosion, creep properties
Loss of alloying elements	Low low-boiling-point elements, high VED, vacuum environment	↓ mechanical performance may change shape memory behaviour, induce defects, ↓ reusability of powder	Tuned process parameters, altered compositions, in-situ monitoring	Yes, evaluate selective evaporation sensitivity in SMA alloys
Oxidation	Powder/processing chamber residual oxygen	↓ flowability, mechanical properties, BMG behaviour, reusability of powder	Proper storage of powder, controlled ambience of protective gas	Yes, oxygen impacts glass-forming in L-PBF Cu alloy, powder reuse
Cracking	Chemical composition, solidification microstructure, process parameters, tensile strain, low melting phases	Loss of performance, ↓ corrosion resistance, premature failure	Alter alloy composition, tune process parameters, pre-heating, materials compatibility for multi-materials	Yes, cracking control for multi-materials, cracking-resistant new alloys
Anisotropy	Variation in G, R, local heat flux	Material properties deviation	Scanning strategy optimisation, post-AM heat treatments, modifying alloy composition	Yes, trade-offs in texture reduction and material properties
Micro-segregation	Process parameters, alloying elements	Improved strength, unfavourable post-printing heat treatment effects on mechanical properties	Tuned parameters, optimised heat treatment, alloy composition	Yes, Cu alloy composition and process parameters affect dislocation cells
Denudation	Zn evaporation, process parameters	LoF, porosity	Control melt pool flow, tune parameters, alter compositions.	-

temperature within the molten pool. Lower VED results in higher surface tension and lower melt temperature overall, leading to higher viscosity inside the melt pool, impeding fluidity, and promoting porosity (inter-particle gap, irregular porosity). As shown in Fig. 40, poor adhesion of layers and unmelted particles is due to low VED, which could be caused by high viscosity. The situation becomes even more complex during L-PBF Cu-based multi-material fabrication, where researchers have reported interparticle gaps, unmelted particles, cracks, etc., as potential causes of premature failure and compromised material properties [180]. Specifically, the interparticle gaps resulting from low laser power and wide hatch spacing decreased the indentation resistance of the L-PBF Cu–Cr–Zr alloy samples [237]. Similarly, interfacial defects weaken the mechanical strength at the interface of multi-materials, a challenge that can be alleviated through the optimisation of process parameters, post-processing heat treatments, etc.

In summary, the challenge of obtaining nearly fully dense parts in L/E-PBF Cu alloys/composites persists due to process-induced defects, even with optimised process parameters and post-treatments in certain cases. In order to enhance the comprehension of defect minimisation and establish effective mitigation strategies, future studies should integrate experimental-simulation-ML integration for defect reduction in the printing of customised L/E-PBF Cu alloy/composite parts. Furthermore, it is imperative to explore the use of advanced tools (synchrotron X-ray imaging) to monitor molten pools in conjunction with multi-physics modelling, artificial intelligence (AI), and machine learning (ML) to reach a definitive consensus on defect evolution mechanisms. Table 6 summarises the defects and potential future research directions for Cu-based alloys/composites/multi-materials in the L/E-PBF processes.

8. Material properties

Understanding the mechanical properties of AMed components is essential, as they determine how a component will respond under static and dynamic loading in its intended applications. Hardness, tensile/compressive strength (YS and UTS), fatigue strength, creep strength, and tribology all fall under the umbrella of mechanical properties. As previously indicated, defects in Cu alloys/composites produced by AM are triggered by process parameters and powder feedstock characteristics. These defects, in turn, impact the material performance of L/E-PBF Cu alloy/composite parts, encompassing mechanical, electrical, thermal, and corrosion behaviour. Therefore, understanding the complex relationship among material, structure, and performance is crucial for designing feedstock with optimal process parameters, which will enable L/E-PBF Cu alloy/composite components to exhibit superior, bespoke material properties and minimal defects.

Following rapid solidification, the solidified L/E-PBF parts exhibited peculiar non-equilibrium microstructures (multi-scale microstructure with macro-, meso-, micro-, and nano-scale), eliminated macro-segregation, and offered extensive tailorability. These features

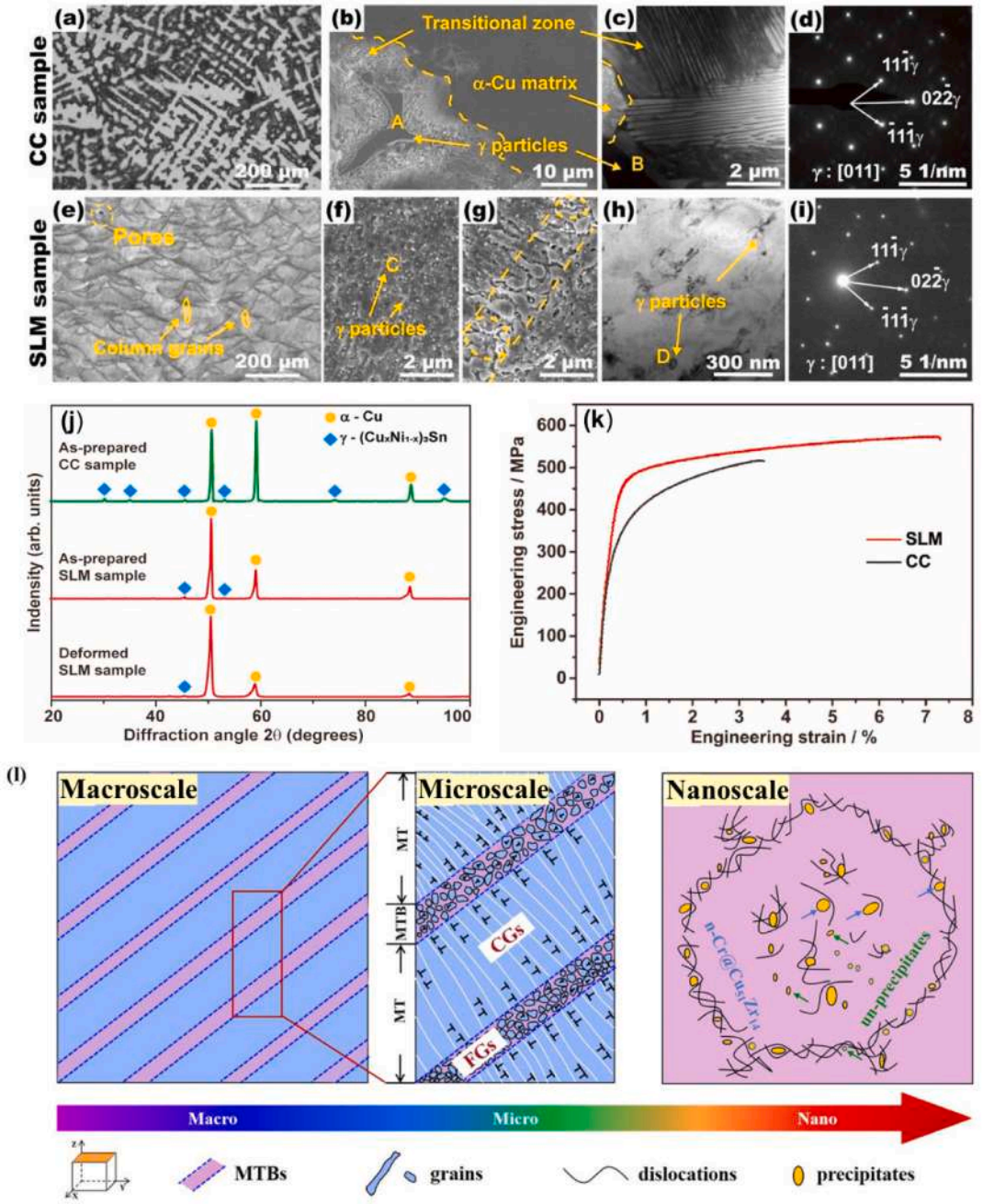


Fig. 41. (a-d) Microstructural alterations of Cu–Ni–Sn alloy during traditional manufacturing; (e-i) AM processes; (j) Comparative phase distribution via XRD; (k) L-PBF Cu alloy performance in stress-strain; (l) Peculiar microstructural hierarchy, featuring a cellular structure with dislocations and precipitates [112,238].

contributed to overcoming the strength-ductility and strength-conductivity trade-offs compared to traditional processing methods. As demonstrated in Fig. 41, L-PBF parts developed a layered microstructure with ripple patterns along the BD, whereas the cast alloy exhibited a dendritic structure in the Cu–Ni–Sn alloy. Although the γ phase was present in both casting and L-PBF samples, its morphology and distribution differed. Rapid solidification during L-PBF confined Sn atoms within the α-Cu lattice, resulting in a supersaturated solid solution and a reduction in γ phase formation. Consequently, differences in solidification rates influenced the microstructure, resulting in enhanced ductility in L-PBF Cu–Sn–Ni alloy components while maintaining strength [238]. Beyond overcoming the strength-ductility trade-off, the formation of nonequilibrium hierarchical microstructures during L/E-PBF significantly impacts key characteristics, including electrical, creep, fatigue, corrosion behaviour, etc. This highlights the potential for achieving a high strength-ductility-conductivity trifecta with superior functional properties [71,128]. The capacity to enhance performance stems from the presence of multi-scale microstructural features, ranging from macro to nano, including a high fraction of low-angle grain boundaries, cellular solidification structures, high-density dislocation, precipitates, etc., as illustrated in Fig. 41. As a result, Cu alloys are strengthened through various mechanisms, including solid solution, dislocation, grain boundary, precipitation strengthening, etc. The formation of non-equilibrium hierarchical microstructures in L/E-PBF Cu alloys is governed by process parameters, feedstock characteristics, and post-printing heat treatments. As previously mentioned, optimising process parameters is crucial for minimising defects, directly influencing the RD of AMed Cu alloy components and, consequently, the superior

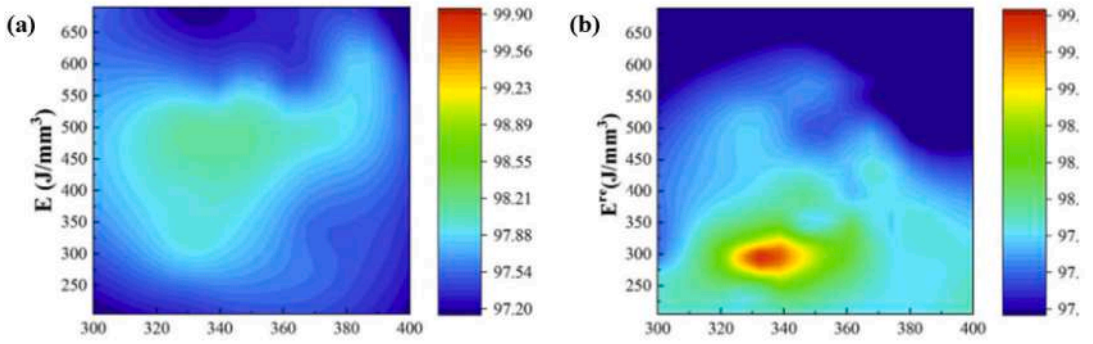


Fig. 42. Relative density variation for Cu–Cr–Zr alloy with process parameters: (a) Non-remelting; (b) Remelting [240].

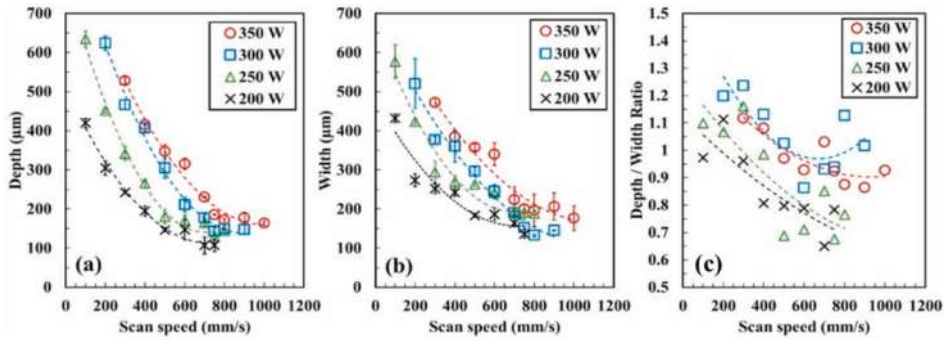


Fig. 43. Variation of melt pool geometry with process parameters for Cu–Sn alloy (a) Depth; (b) Width; (c) Depth/Width [109].

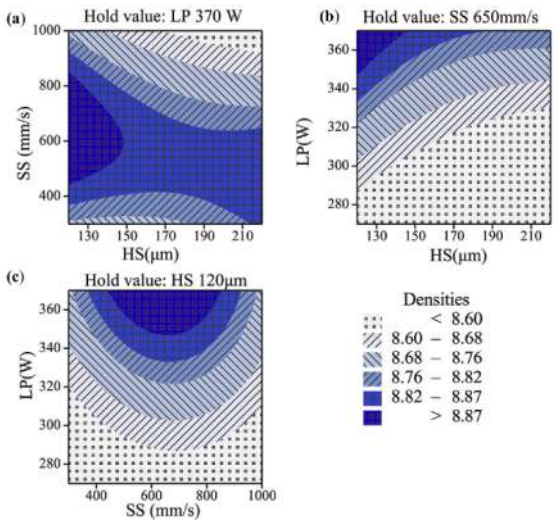


Fig. 44. Density maps of L-PBF Cu alloy: (a) Fixed laser power (370 W); (b) Fixed laser scanning speed (650 mm/s); (c) Fixed hatch spacing (120 μm) [93].

overall performance of printed parts. According to the literature, volumetric energy density (VED) has been widely used as a key design parameter in Cu L/E-PBF studies. As shown in Fig. 42, VED regulated the density of printed components using both non-remelting and remelting techniques. Interestingly, the remelting strategy resulted in near-fully dense components (Fig. 42: distinct red central zone on the map) compared to the non-remelting strategy. This finding underscores the limitations of VED in accurately capturing the intricate physical processes occurring within the melt pool during Cu alloy printing. This limitation primarily arises from complex melt physics and the disregard of parameters such as beam size, focus position, etc. Even when identical VED values were achieved by varying the scanning speed, hatch spacing, and laser power, variations in laser–powder interaction altered melt pool geometry, leading to distinct microstructures and material properties in L-PBF Cu alloys/composites. Mehta et al. [109] corroborated that the melt pool geometry of L-PBF Cu–10Sn alloys was influenced by scanning speed and power (Fig. 43). At low scanning speeds, the process shifted to keyhole mode, producing a wider and deeper melt pool, which facilitated a smoother surface but introduced high porosity. Conversely, higher scanning speeds (>800 mm/s) transitioned the process to conduction mode, resulting in a narrower and shallower melt pool with lower porosity but higher surface undulation (Fig. 43). Furthermore, Ma et al. [93] examined the impact of laser power, hatch spacing, and scanning speed on the densification behaviour of L-PBF Cu alloy using a density model. Their findings revealed distinct density variation zones, highlighting that modifying two parameters while keeping a third constant led to changes in the maximum density (Fig. 44). Thus, tuning process parameters beyond optimised VED is crucial for achieving a tailored microstructure with near-fully dense parts that are free from multi-scale defects. While existing research frequently identifies a single optimal value for process parameters (**see** Appendix A – **Table S1** [23,26,29,45,48,52,54,55,59,68–72,91,100,104,109,110,112,113,119,127,128,131,144,150,151,154,157,197,199,223,244,248,253,255,261–265]**)**, such values may not be universally ideal for all Cu alloys/composites. In addition to optimising VED, factors such as Cu alloy/composite feedstock characteristics, phase transformation temperature, etc., must be considered when defining a broad process parameter window to achieve the requisite performance. For instance, L-PBF Cu–Al–Ni alloys, Cu–Al–graphene composites, and Cu–Al–Ni–graphene composites exhibited different optimal VEDs due to variations in scanning speeds of 400, 200, and 300 mm/s, respectively, which were influenced by compositional differences. Even within the same Cu-based alloy system, differences in element composition (GRCop–42 vs. GRCop–84) affected strengthening mechanisms, such as Orowan

Table 7
Testing standards and conditions for tensile testing of L/E-PBF copper alloy/composite.

Standards	Crosshead speed/strain rate	Elevated temperature	Ref
ISO 6892	0.4–2 mm/min	×	[68,243,244]
ASTM E8/E8M	10^{-5}/s to 1/s	×	[100,119,242,245]
Chinese GB/T 228.1–2021	2 mm/min	×	[113]
GB/T 228	2 mm/min	✓ (300 and 500 °C)	[45]
GB/T228–2002	0.5 mm/min	×	[158]
German DIN 50125	–	×	[89]

strengthening, due to variations in precipitate size after printing, ultimately leading to distinct material properties [239]. Moreover, feedstock composition in L/E-PBF not only governs the printing window and material behaviour but also determines the likelihood of microsegregation, undesirable texture, and the tendency for elements to evaporate, etc., all of which can degrade material properties, as discussed earlier. Another significant challenge in achieving consistent material properties in Cu alloy L/E-PBF parts is microstructure anisotropy. Post-AM heat treatments have emerged as an effective and widely used approach to optimising material properties by manipulating microstructure. However, careful selection of post-printing heat treatment parameters is crucial to achieving desirable material performance. Overall, a comprehensive understanding of feedstock characteristics, optimised printing parameters, and tailored post-printing heat treatments is necessary to fabricate high-performance Cu alloy/composite parts using L/E-PBF. Consequently, the mechanical, electrical, tribological, corrosion, creep, and fatigue behaviour of the L/E-PBF Cu alloys/composites—governed by process parameters, feedstock characteristics, and post-heat treatments—alongside the implementation of various test conditions and standards, are discussed in the subsequent sections.

8.1. *Tensile properties*

The engineering/true stress-strain curves from tensile testing provide valuable insights into elastic moduli (EM), YS, UTS, and plastic strain (% EL) of AM parts. These curves highlight the critical design parameter of "strength-ductility optimisation" in printed parts. Table 7 shows that the standards used for tensile tests are ISO, ASTM, Chinese GB/T, and DIN to evaluate the stress-strain relationship, most of which are performed at room temperature. Yang et al. [45] reported a 3% reduction in YS, a 13% reduction in UTS, and a 9% reduction in %EL when the tensile testing temperature was increased from room temperature to 300 °C. However, at 500 °C, YS increased by 25%, UTS increased by 5%, and %EL decreased by 38% in as-built Cu alloy samples. Similarly, the YS of the LPBF Cu-Cr-Zr alloy exhibited a non-linear trend, demonstrating superior YS at elevated temperatures compared to both its room-temperature counterpart and wrought alloys, as shown in Fig. 45, reaching its highest value at 500°C due to the formation of nanoscale Cr-rich precipitates within the Cu matrix before declining at 600°C. This anomalous, temperature-dependent strengthening behaviour emphasises the importance of high-temperature tensile testing for future L/E-PBF Cu alloy/composite parts. Despite its importance, studies on the high-temperature stress-strain behaviour of L-PBF Cu alloys/composites are scarce, which is necessary for developing reliable high-temperature L/E-PBF Cu components (as indicated in Fig. 46, the application temperature for the Cu alloy heat sink is not the same as the room temperature) and establishing a unified consensus on the high-temperature performance of L/E-PBF Cu alloy/composite parts. Similarly, Cu-based SMAs intended for high-temperature actuation (100-200 °C) require dedicated high-temperature testing [241]. Furthermore, the impact of strain rate on the tensile characteristics of L-PBF Cu alloys and composites remains largely unexplored. Jeyaprakash et al. [242] noticed that increased strain rates led to reduced UTS and a transition from ductile to brittle behaviour, resulting in decreased elongation. This transition was evidenced by cleavage facets in fractography, depicted in Fig. 47. In contrast, lower strain rates promoted ductile behaviour due to the synergistic effects of α-Cu and nano Cu_2O precipitates. Thus, accurately reporting the tensile behaviour of L/E-PBF Cu alloys requires testing across relevant strain rates, as strain rates influence strength, ductility, and failure mechanism. To ensure the reliability of L/E-PBF Cu printed parts, future research should explore dynamic conditions by investigating the effects of varying strain rates, as the current literature has exclusively focused on a single strain rate (**see** Appendix A – **Table S1**). Moreover, the lack of clear standards outlining how Cu alloy AM parts should be effectively and repeatably evaluated poses substantial challenges in comparing results (Table 7). This significant deficit requires an immediate response.

The L-PBF AB component exhibited a superior YS compared to the as-cast part; nevertheless, the L-PBF process managed to achieve high strength while preserving ductility, demonstrating a synergistic effect where AM parts exhibited a 400% increase in ductility and a 57% improvement in YS [197]. This improvement is ascribed to the heterogeneous microstructure of L-PBF parts, which comprises a cellular structure, a dislocation network, the absence of macro-segregation, and deleterious phases (for instance, Fig. 48 revealed that L-PBF Cu–Sn alloys have a fine, lower fraction, and discontinuous hard intermetallic (δ-phase)), fine grains, and nano-precipitates over as-cast parts. Moreover, the build direction of the AMed component modulated the microstructure due to variations in cooling rate, leading to anisotropy in microstructure and mechanical properties, as illustrated in Fig. 48**,** showing variation in $\sigma - \varepsilon$ within the three orthogonal orientations. The tensile properties of AMed Cu alloy samples were direction-dependent, with superior performance observed in the direction perpendicular to the build layers compared to the transverse direction [197].

The literature highlights anisotropy in the mechanical properties of L/E-PBF Cu alloys/composites induced by changes in heat input, which influence the melt pool geometry and, in turn, affect the microstructure characteristics and defect propensity of the printed Cu alloy/composite. Fig. 49 highlights the importance of fine-tuning laser power and scanning speed in Cu alloy AM for producing defect-free parts with remarkable strength-ductility synergy and minimised anisotropy in mechanical properties. Vertical orientation typically offers superior mechanical properties, but horizontal orientation results in inferior mechanical properties (lower strength and ductility) under similar process parameters on the map. Beyond scanning speed and laser power, L/E-PBF Cu alloys leverage scan vector rotation, deposition strategy, and re-melting to tailor energy density for superior mechanical properties. This underscores the importance of optimising process parameters to fabricate defect-free L/E-PBF Cu alloys/composites with outstanding mechanical properties and improved strength-ductility synergy.

Powder feedstock characteristics are critical in the L-PBF or E-PBF processes, significantly influencing mechanical performance. Lu et al.

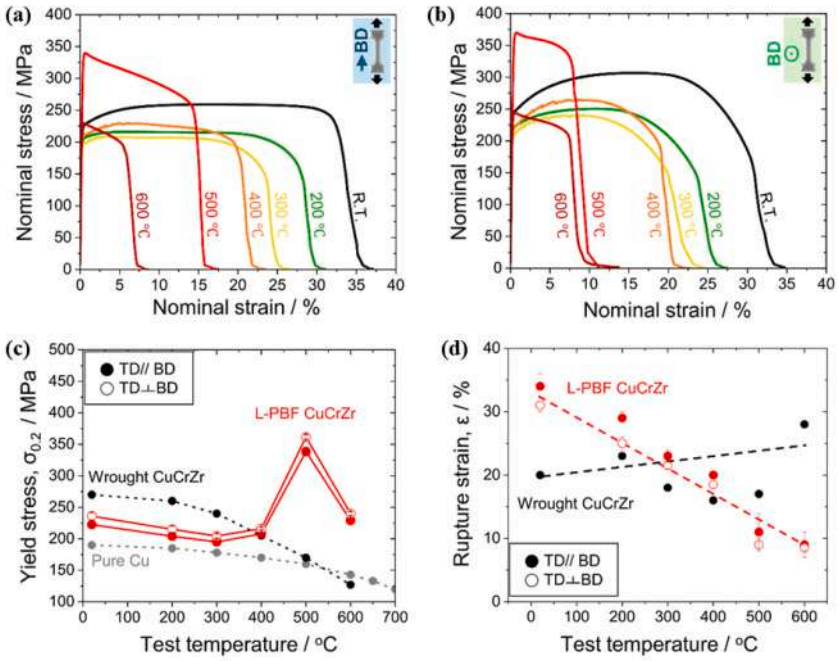


Fig. 45. Trends of stress-strain with temperature changes across different tensile directions (TDs) (a) Parallel; (b) Transverse to build direction (BD). Temperature-dependent changes in (c) YS and (d) % EL for Cu–Cr–Zr alloy [246].

[23] utilised E-PBF to develop a high-strength, high-ductility, and isotropic NAB alloy with four varied PSD ranges: 45-63 (S_S), 63-75 (S_M), 75-105 (S_L), and 45-105 μm (S_{Mix}). Despite variations in powder size, tensile YS varied by only 7%, while %EL showed a 10% variation. Notably, the SS (45–63 μm) PSD exhibited inferior UTS compared to the other PSDs, likely due to its lower RD (95.8%), which was attributed to inadequate flowability and the tendency to form agglomerates of fine powder particles. This highlights the critical role of powder feedstock attributes in optimising the strength-ductility synergy. Another study examined alloy composition to optimise the microstructure and mechanical behaviour of L-PBF Cu–Co alloys. It was observed that L-PBF Cu–Co alloys with Co additions exceeding their maximum solid solubility (6–8 wt.%) in Cu (4.75 wt.%) resulted in grain refinement and improved tensile YS, UTS, and %EL. The L-PBF Cu–Co alloy containing 6 wt.% Co demonstrated the optimal synergy between strength and ductility, achieving a 200% increase in YS, a 170% increase in UTS, and a 210% enhancement in total elongation to fracture [29]. However, increasing Sn content to 15 wt.% (from 5 to 15 wt.%) in L-PBF Cu alloys inhibited the strength-ductility synergy, as it enhanced UTS to 738 MPa but reduced total elongation to 9% [91]. Gao et al. [70] incorporated submicron TiB_2 (1 wt.%) particles to modulate the mechanical properties of the L-PBF Cu–15Ni–8Sn alloy, achieving an 11% increase in tensile YS and a 14% increase in UTS, albeit with a minor ductility loss of 17.8% compared to the Cu–15Ni–8Sn alloy (21.5%). While the choice of feedstock reduces reflectivity and enhances mechanical performance while addressing the strength-ductility trade-off in L/E-PBF Cu alloys/composites, meticulous control and optimisation of feedstock parameters remain essential. Unoptimised feedstock characteristics, in conjunction with process parameters, can induce defects such as unmelted powder, evaporation of alloying elements, keyhole formation, and lack of fusion (LoF), all of which degrade the mechanical behaviour of L/E-PBF Cu parts [52]. For instance, Liu et al. [71] observed that nanoparticle agglomeration led to reduced ductility and strength (YS: 270 MPa, 20%) of the L-PBF Cu–2LaB_6 alloy, which earlier exhibited superior mechanical properties (YS: 347 MPa, 22.8%) for the Cu–1LaB_6 alloy (1 wt.%). Zheng et al. [157] explored surface alloying techniques by utilising Ni–coated Cu alloy, partially Ni–diffused Cu alloy (partial surface alloying), and surface Ni–alloyed Cu powder (complete surface alloying) for L-PBF and found that surface alloying Ni onto the Cu powder surface resulted in improved YS (~53.3 MPa), UTS (~253 MPa), and %EL (29%) compared to other methods where YS ranged from 46 to 51 MPa, UTS 120 to 196 MPa, and %EL 4 to 11%. These improvements were attributed to reduced unmelted powder and LoF defects, which were more pronounced in the partially surface-alloyed and coated Cu powders. However, increasing the coating content does not always guarantee improved mechanical properties. Jadhav et al. [68] reported a decline in RD (<96%) as coating content increased. Similarly, carbon addition to the L-PBF Cu-1Cr alloy led to LoF defects, reduced RD (96%), and hindered optimal performance [154]. This suggests that strategies aimed at enhancing NIR laser printability do not necessarily translate to superior mechanical properties in L-PBF Cu alloys. Thus, achieving outstanding mechanical performance and strength-ductility synergy in L/E-PBF Cu alloy/composite parts requires careful control of alloy composition alongside optimised process parameters.

A further noteworthy characteristic is that the significant local heat gradients induced by L-PBF result in anisotropic microstructural features and, consequently, anisotropic tensile properties. Wang et al. [199] reported anisotropic tensile behaviour in L-PBF Cu–Cr–Zr alloys when comparing samples printed horizontally (SLM-0°) and vertically (SLM-90°). The YS values (0°: 175.2 MPa, 90°: 186.2 MPa) and UTS values (0°: 265.5 MPa, 90°: 268.6 MPa) did not differ significantly between the two orientations; however, plasticity was enhanced by 45% in the SLM-90° direction (90°: 71.7%, 0°: 49.4%). Further tensile fracture analysis revealed ductile failure in the vertical sample, characterised by mixed dimples, whereas the horizontal sample exhibited unmelted particles and pores. These defects acted as stress concentrators, leading to premature failure under tensile loading. The lower RD of the SLM-0° sample (98.6%) compared to the SLM-90° sample (99.1%) further corroborates these findings. Similarly, L-PBF Cu-Cr alloys exhibited anisotropic tensile behaviour, with disc-shaped imperfections parallel to the build layers acting as stress concentrators and facilitating crack propagation, resulting in lower tensile strength in 0° direction (parallel to the stacking direction) AM specimens than in 90° direction specimens (7-19% higher) [248]. Xie et al. [12] demonstrated that changes in the Schmid

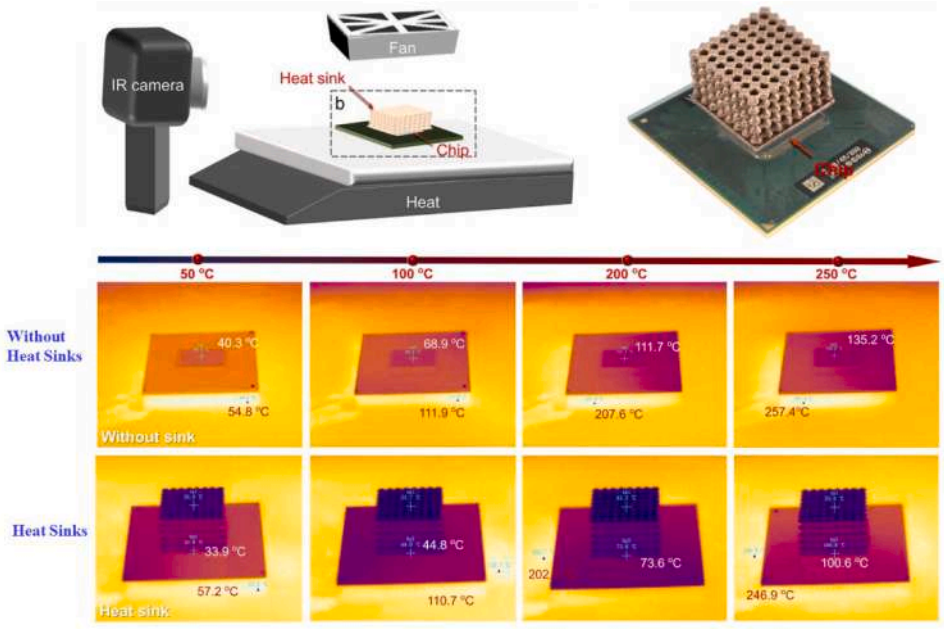


Fig. 46. Temperature variation with and without AMed Cu alloy heat sinks [158].

factor (SF) due to grain orientation distribution contributed to tensile strength anisotropy in L-PBF Cu–Cr–Zr alloy samples. A higher SF allowed for easier slip activation and reduced YS, with the build direction (BD) exhibiting a higher SF than the transverse direction (TD). The TD demonstrated a 66% increase in YS and a 52% increase in UTS, whereas tensile ductility in the BD increased by 290%, as evidenced by necking on the fracture surface. In another research on L-PBF C–18150 parts in their AB state, YS remained unchanged regardless of fabrication direction (horizontal, angled, or vertical) irrespective of grain size. However, angled samples exhibited significantly higher UTS and ductility than their vertical and horizontal counterparts [249]. Unlike other L-PBF Cu alloys, vertical samples demonstrated reduced ductility due to LoF defects, primarily attributed to unmelted powder clusters. Beyond build orientation effects, the geometry of printed parts plays a crucial role in determining tensile behaviour anisotropy in L/E-PBF Cu alloys. Variations in microstructure and process-induced defect distribution are influenced by the printed geometry. In AB GRCop–42, reducing tensile specimen thickness from 2.1 to 1.5 mm led to a decrease in YS, UTS, and %EL due to internal defects, indicating that size effects, in addition to orientation, may influence tensile behaviour [250]. Therefore, design optimisation and build orientation must be carefully considered when printing L-E/PBF Cu components to minimise anisotropy in tensile behaviour.

Attaining balanced mechanical properties for specific copper feedstock is achievable through microstructural modulation and process-induced defect management during L/E-PBF, which is directly linked to optimised process parameters. Scanning strategies, primarily governed by scan vector length and rotation, significantly influence temperature gradients and cooling rates across the melt pool, thereby conditioning the mechanical properties of the final component [62,251]. Various scanning strategies—including rotational, chessboard, island, meandering, unidirectional, and bi-directional—are commonly employed for L/E-PBF Cu alloy/composite fabrication. Using a 2000 W high-power laser, Zhang et al. [251] examined the effects of a rotational scanning strategy on the microstructure and mechanical properties of L-PBF Cu–Cr alloy parts by varying the scan vector rotation across four angles (0°, 67°, 90°, and 105°). As the scan vector rotated from 0° to 105°, cooling rates within the melt pool fluctuated, leading to variations in grain size, Cr solubility, and texture strength, which in turn influenced the mechanical properties of the fabricated parts. The AB sample with a 105° scanning rotation angle exhibited the highest UTS (251 MPa), 90° exhibited the highest YS (174 MPa), and 0° showed the highest ductility (38.4%). Similarly, Sabelle et al. [105] found that the mechanical behaviour of L-PBF Cu–Sn–Ni alloys was influenced by the rotation scanning strategy, which involved rotating the laser scan vector by 0, 30, 45, 60, and 90°. Lower rotation angles (0°–30°) led to excessive heat overlap, resulting in thicker melt pools that trapped more gas, contributing to pore formation, reduced RD, and diminished mechanical performance. Conversely, intermediate angles (45°–60°) achieved an optimal balance between sufficient melting and controlled heat accumulation, producing denser parts with a UTS of 100 MPa. Angles approaching 90° resulted in excessive heat accumulation, resulting in challenges akin to those linked with low angles. Further, the L-PBF Cu–Cr–Zr alloy showed negligible differences in UTS (269-279 MPa), YS (199-206 MPa), and %EL (22.6% to 23.1%) between meander (M) and chessboard (C) scanning strategies for transverse specimens. However, longitudinal specimens exhibited lower YS (148-162 MPa) and UTS (214-219 MPa) alongside increased %EL (26.3% to 31.0%) for both M and C scanning strategies [104]. Kuai et al. [62] reported relative density exceeding 99.5% in L-PBF Cu alloys by employing a chequerboard laser scanning strategy among four scanning strategies (short linear, long linear, checkerboard, and contour offset), which usually translates to better mechanical properties and reduced process defects. In L-PBF Cu alloys, increased laser power promoted grain refinement and reduced grain orientation anisotropy within a given plane, thereby weakening texture strength and altering mechanical properties. Li et al. [252] found that when the scanning speed is varied from 500 to 800 mm/s and the laser power is varied from 300 to 400 W for a Cu–Cr–Nb–Ti alloy, the optimum tensile properties for laser power 325 W and scanning speed 800 mm/s are 416 MPa and 27.8%, respectively. Likewise, L-PBF Cu–Al–Ni–Ti SMAs with moderate energy density (107 J/mm^3) showed the highest UTS (541 MPa) and %EL (7.6%) compared to lower (77 J/mm^3) and higher energy densities (147 J/mm^3). However, lower energy density caused partial melting and voids, while higher energy density caused melt pool splatter and pores, decreasing mechanical performance [253]. Li et al. [254] reported that laser power had a substantial effect on enhancing the mechanical properties of L-PBF Cu–Cr–Zr alloys, whereas scanning speed exhibited a moderate negative influence on strength, and hatch spacing had negligible impact, as shown in Fig. 50. In conclusion, optimising process parameters is essential for controlling

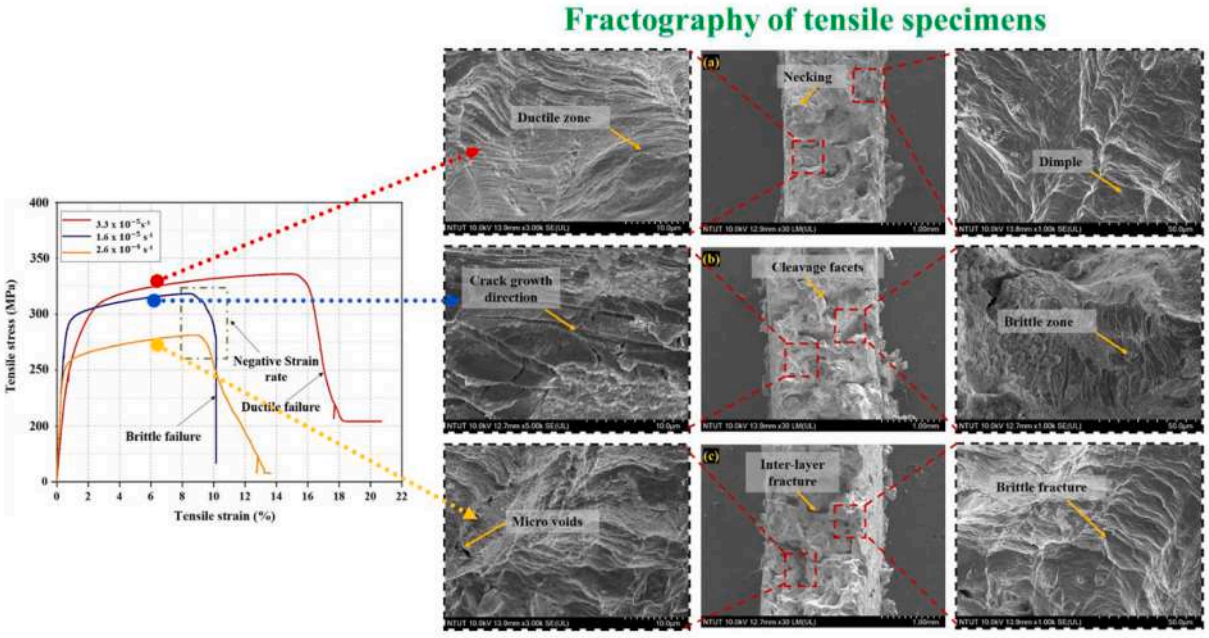


Fig. 47. Failure characteristics of tensile sample at varied strain rates for AMed Cu alloy [242].

the microstructure, minimising defects, and ensuring desirable phase transitions, density, and dimensional precision. These factors collectively contribute to the superior mechanical performance of L-PBF Cu alloy/composite parts.

As previously elucidated, the non-equilibrium microstructures inherent to L/E-PBF Cu alloys manifest as disproportionate grain morphologies, metastable phases, pronounced textural variations, and an elevated defect density, culminating in anisotropic mechanical behaviour. Beyond the intrinsic feedstock attributes and processing parameters, judiciously tailored ex-situ heat treatments have emerged as a formidable strategy to rectify microstructural heterogeneity, thereby attaining superior mechanical performance while mitigating anisotropy in L/E-PBF Cu alloys. Crucially, such treatments offer an avenue to circumvent the conventional strength-ductility trade-off. Yang et al. [255] successfully engineered a synergistic enhancement of strength and ductility in L-PBF Cu–10Sn alloy via post-AM heat treatment, effectuating a substantial increase in both UTS (from 749 to 840 MPa) and %EL (from 29% to 56%) relative to the as-built state. This improvement was attributed to the interplay of annealing twins and the formation of equiaxed grains. Analogously, post-AM heat treatment of L-PBF Cu–Fe alloy augmented UTS (from 402 to 463 MPa) while preserving an exceptional level of ductility (30.4%) in contrast to its AB counterpart [26]. Furthermore, heat treatment serves as an indispensable technique for optimising the tensile properties of precipitation-hardening L-PBF Cu alloys, such as Cu–Cr–Zr, Cu–Ni–Si, Cu–Ni–Sn, etc. For instance, L-PBF Cu–Cr–Zr alloys exhibited a substantial gain in tensile strength (290 to 515.5 MPa) after direct aging (DA) treatment due to precipitation strengthening [256]. However, microstructural evolution—which ultimately dictates property enhancements in printed parts—depends on the optimal combination of holding time and treatment temperature during post-AM heat treatment. In an illustrative case, post-AM heat treatment (recrystallised annealing at 600 °C for 1, 2, and 4 h) for the L-PBF Cu–12.9Zn–2.5Si alloy exhibited microstructure refinement, with cellular structure replaced by annealing twins, Si dissolved from boundaries, and high-angle grain boundaries formed (misorientation angle of 60°). This initially improved ductility (8.1% vs. 7.5%), yet prolonged annealing durations (> 2 hours) led to the concomitant deterioration of both strength and ductility [153]. Zhang et al. [148] developed a high-strength L-PBF Cu–15Ni–8Sn alloy after heat treatment using DA and solution+aging (SAT), wherein precipitation-modulated strengthening was pivotal. In the AB state, mechanical strength primarily stemmed from solid solution strengthening (54.9%), dislocation strengthening (31.5%), and grain boundary strengthening (12.2%). However, the post-printing heat treatment induced precipitation, wherein precipitation strengthening became dominant (72.3% DA, 82.9% SAT), while the roles of dislocation (19.9% DA, 5.5% SAT) and grain boundary strengthening (7.8% DA, 11.6% SAT) diminished correspondingly. Both DA and SAT processes prioritised strength augmentation, wherein UTS and YS surged significantly during the initial hour of ageing before reaching a plateau, whereas %EL exhibited a declining trajectory before stabilising. To ameliorate the associated ductility deficit, lower-temperature solution annealing was implemented, instigating spinodal decomposition and engendering a modulated microstructure, which substantially enhanced ductility (> 50%) with only a marginal trade-off in strength for L-PBF Cu–15Ni–8Sn alloy parts. Overall, post-AM heat treatment constitutes a compelling approach to resolving the inherent strength-ductility dichotomy while refining the mechanical properties of L/E-PBF Cu alloys via microstructural modulation. Nonetheless, the optimal thermal processing parameters remain composition-dependent, necessitating meticulous calibration of temperature and duration. While extant literature predominantly explores ex-situ heat treatments, future investigations should pivot towards in-situ methodologies as a viable alternative, potentially mitigating the cost and time constraints associated with conventional post-processing while enabling the bespoke tuning of mechanical properties.

The process parameters and resultant tensile properties (UTS, YS, and %EL) of previously investigated L/E-PBF copper alloys and composites are comprehensively delineated in Appendix A – Table S1. The investigated ranges for laser power (70-2000 W), scanning speed (100-1600 mm/s), and hatch distance (36-200 μm) encompassed a broader spectrum than the identified optimal intervals of 120-2000 W, 200-1100 mm/s, and 50-200 μm, respectively. In addition to optimal scanning speed, power, and hatch distance, layer thickness in the 25-200 μm range was investigated to determine the best combination for acceptable VED in printed Cu alloys. Despite identical processing conditions, L/E-PBF Cu alloy/composite exhibited a disparate and often unpredictable response to the strength-ductility trade-off upon undergoing post-heat

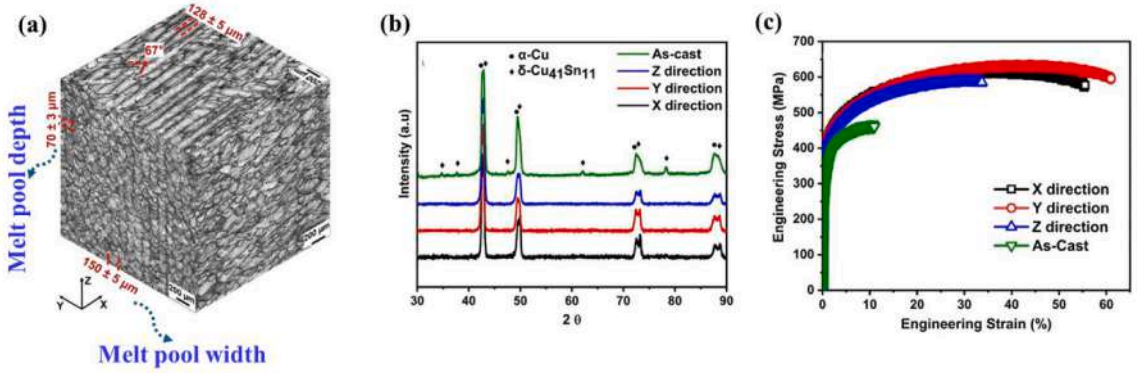


Fig. 48. (a) 3D optical micrographs revealing melt pool geometry; (b) Phase variation for cast/L-PBF Cu alloy; (c) Stress and strain variation for cast and L-PBF Cu alloy [197].

treatment in comparison to their AB state. Notably, certain compositions (Cu–Sn alloys) demonstrated a concurrent augmentation in both tensile strength and ductility following heat treatment, whereas alternative compositions experienced a pronounced decline in ductility, albeit with an attendant increase in strength. In their AB state, most L/E-PBF alloy parts fall within the medium strength (< 600 MPa) and medium ductility (< 40%) regime (the white zone of Fig. 51). The scarcity of L/E-PBF Cu alloys reaching the high-strength, high-ductility zone (the yellow zone of Fig. 51), even with heat treatment, suggests a framework for future research to identify new exotic Cu alloys/composite feedstocks. Although Cu alloys are workhorse materials for electrical applications, optimising both strength and ductility is essential for developing high-performance components. The trade-offs between strength and conductivity, as well as strength and ductility, continue to present formidable challenges in Cu alloy processing via conventional manufacturing methodologies. However, L/E-PBF has shown promise in overcoming these limitations for specific Cu alloys, as shown in Fig. 51 (Figs. 51 and 52 summarise Appendix A – Tables S1 and S2 ([48,93,151,197,202,238,266,267])). For instance, L-PBF Cu–Sn alloys exhibited a strength-ductility synergy superior to that of conventionally manufactured parts, which was further enhanced by post-AM heat treatments. The influence of energy sources (laser vs. electron beam) on the strength–ductility relationship is evident, even for the same alloy (NAB alloys refer to Fig. 51), underscoring the significance of process optimisation tailoring mechanical properties. Additionally, the strength-ductility trade-off is governed by sample orientation relative to the printing direction; vertical samples (depending on composition) showed either higher or lower strength than horizontal samples, while %EL often showed an inverse correlation with YS/UTS. These variations are attributed to microstructural differences, such as grain size and crystallographic texture, which are controlled by printing process parameters, powder feedstock characteristics, and post-printing heat treatments. Therefore, future research should focus on the minimisation of anisotropy in the mechanical properties of L/E-PBF Cu parts, as evidenced by significant ductility differences between horizontal and vertical samples (Fig. 51 circled in images). Prior studies on L/E-PBF Cu alloys (Fig. 52) have identified an optimal VED below 500 J/mm^3, as higher VED values (> 500 J/mm^3) compromise both ductility and strength (YS and UTS). Moreover, compositions prone to vaporisation, such as Cu–Zn alloy, exhibited process-induced defects at elevated VED levels, limiting their performance. While green lasers can overcome reflectivity challenges for Cu alloys, enabling the use of higher VEDs, a strength–ductility trade-off persists. Future research should address the use of lower VED green laser techniques to develop high-performance Cu alloy parts. Beyond the four primary VED variables, additional process variables—including preheat temperature, gas flow, and beam shaping—warrant further investigation to establish a comprehensive understanding of the nexus between microstructure and properties. Given real-world application constraints, another critical research direction is the development of L/E-PBF Cu alloys with superior comprehensive performance in the AB state (no heat treatment required). Additionally, fracture toughness (K_{Ic}), which is the ability to resist cracks, is a critical aspect of design consideration for structural applications to ensure safety and reliability, in addition to the strength (YS/UTS) and ductility of components [257,258]. While higher ductility typically enhances crack tolerance, the current review suggests that predicting fracture toughness from ductility in AM components remains unreliable [259]. Given the scarcity of research on the strength-fracture toughness trade-off (mutually exclusive) in L/E-PBF Cu alloys/composites, which have the potential to be exploited in structural applications, lattice structures, etc. [22,31,260], it is imperative to comprehend the impact of multi-scale microstructure (macro-, meso-, micro-, and nano-scale) on the strength-fracture toughness nexus. This comprehension will broaden the microstructure-property relationship and improve the mechanical performance of future L/E-PBF (NIR, blue, green, electron beam, hybrid laser) Cu alloy components. Furthermore, the green laser and electron beam printed Cu alloys exhibited reduced complexity in terms of absorptivity; however, their UTS remained below 350 MPa, indicating potential for further investigation (Fig. 52). Finally, future research should address the paucity of high-temperature tensile behaviour in L/E-PBF (NIR, blue, green, electron beam, hybrid) Cu components to provide reliable performance under extreme conditions for new engineering applications.

8.2. *Compressive properties*

Tensile behaviour is often prioritised due to its prominence in structural design, but compressive behaviour is equally vital in specific applications, particularly in shape memory alloys (SMAs) and lattice structures, which rely heavily on compressive behaviour for their overall performance. More importantly, L/E-PBF processes have been successfully employed in various Cu alloys (Cu–Al–Ni–Fe, Cu–Zn, Cu–Sn, Cu–Ni–Sn, and Cu–Zn–Si, etc.), showcasing their capability to achieve outstanding compressive behaviour. For instance, the L-PBF Cu–11.8Al–3.2Mn–0.1Ti alloy exhibited a higher compressive fracture strain (27.6%) and compressive strength (14.7%) compared to its cast counterpart (Cu–12.9Al–8.3Mn–0.5Ti alloy) [147]. Similarly, L-PBF parts demonstrated promise for compressive behaviour, as confirmed by L-PBF Cu–Cr–Zr lattices (highly ductile), which exhibited excellent compression behaviour with stable stress plateaus (unlike brittle materials) [217]. Thus, the enhanced compressive behaviour enabled by L-PBF in Cu alloys presents opportunities for the development of novel Cu alloys/copper-based multi-material/BMGs in novel lattice structures for next-generation applications in the future. These advancements could

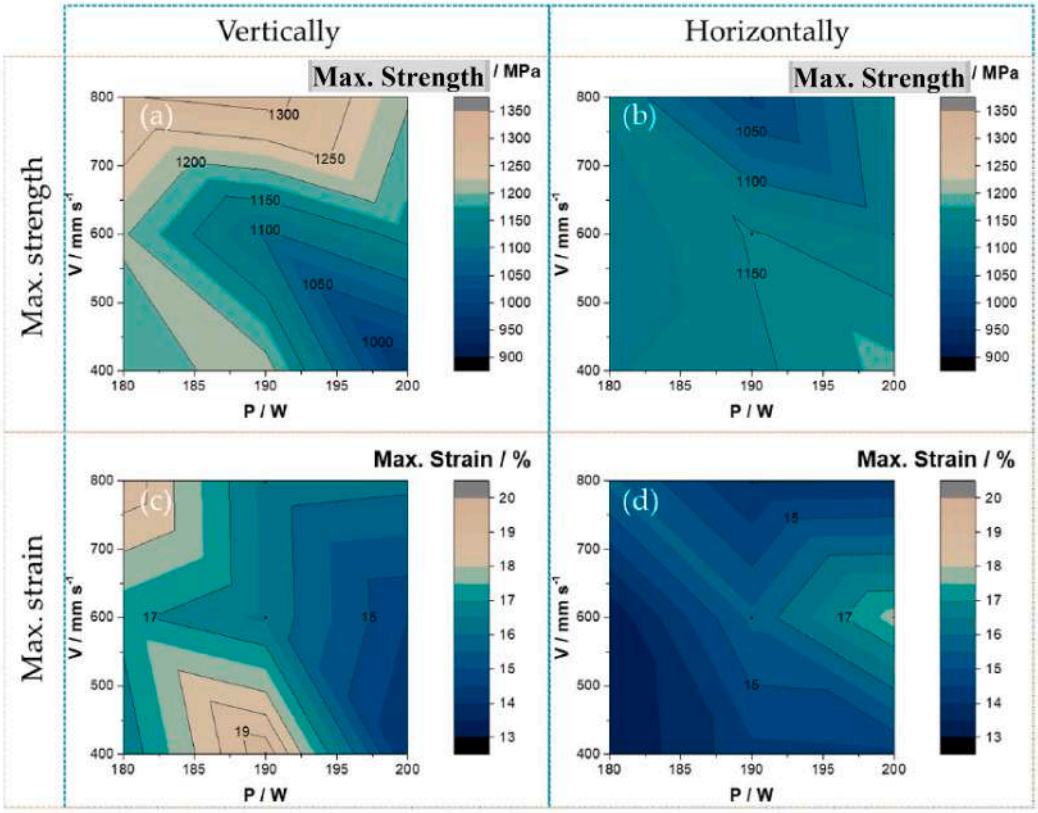


Fig. 49. Interplay between laser process parameters and mechanical properties anisotropy in L-PBF Cu–Al–Ni–Fe alloy for vertical orientation: (a,c) and horizontal orientation: (b,d) [247].

pave the way for new applications in structural and functional materials, further expanding the capabilities of AMed Cu alloy parts.

One of the significant challenges in L-E/PBF Cu alloy printed parts is the anisotropic nature of their compressive properties, which can arise from variations in defect density and the complex thermal history associated with build orientation, topology, and geometry. The L-PBF Cu alloy samples exhibited anisotropy, with the horizontal direction (loading direction aligned with build direction and slip direction) showing lower strength (507 MPa for sample A (0° build orientation), 470 MPa for sample B (90° construction orientation)) compared to the vertical direction (540 MPa for sample A, 512 MPa for sample B). This anisotropy is due to texture: favourable grain slip in the horizontal direction (aligned with loading and slip directions), leading to lower strength compared to the vertical direction [268]. Moreover, studies on Cu–11Al–5Ni–4Fe alloys exhibited superior compressive behaviour (1300 MPa, 20% strain) when fabricated vertically [247]. This enhancement is due to faster solidification from shorter scan areas, although the martensitic phase limits overall plastic deformation. Furthermore, Gyroid microlattices of L-PBF Cu–Cr–Nb alloys outperformed Octet and BCC microlattices, demonstrating over three times the compression strength and four times the energy absorption [269]. However, the size-dependent compressive behaviour of L/E-PBF Cu alloys/composites is barely understood, particularly in terms of process-induced defects, which can be investigated systematically in the future. Temperature-dependent compressive behaviour and defect density further exacerbate the anisotropic nature. For instance, L-PBF Cu–Ni–Sn alloys showed superior compressive strength at room temperature (230 MPa AB, 346 MPa heat-treated) but deteriorated with higher temperatures (room temperature to 400 °C). Interestingly, at 400 °C, the AB sample (210 MPa) was superior to the heat-treated one (101 MPa) because of a shift in the strengthening mechanisms [270]. This highlights the interplay between the feedstock composition, microstructure, and phase transformations, which govern compressive strength behaviour across temperature ranges. Further investigations into L-PBF Cu–10Sn and Cu–40Zn alloys revealed a critical link between porosity and compressive strength [166]. In Cu–10Sn alloys, compressive strength declined from 390.2 to 25.8 MPa as porosity increased from 1.9% to 42.6%. Similarly, in Cu–Zn alloys, compressive strength

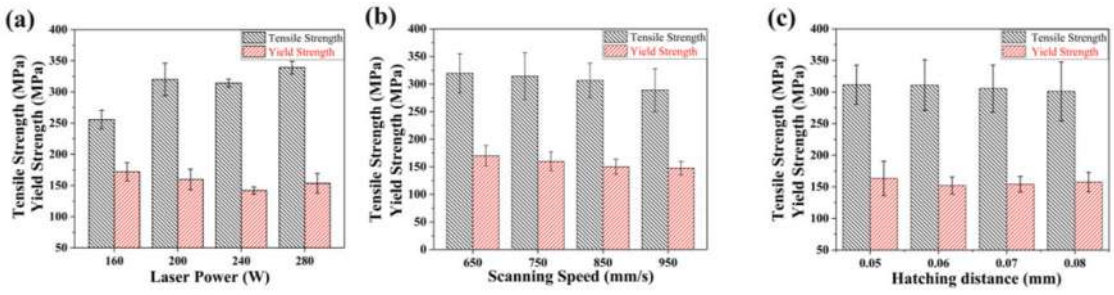


Fig. 50. Strength (YS/UTS) as a function of: (a) Laser power; (b) Scanning speed; and (c) Hatch spacing for L-PBF Cu alloys [254].

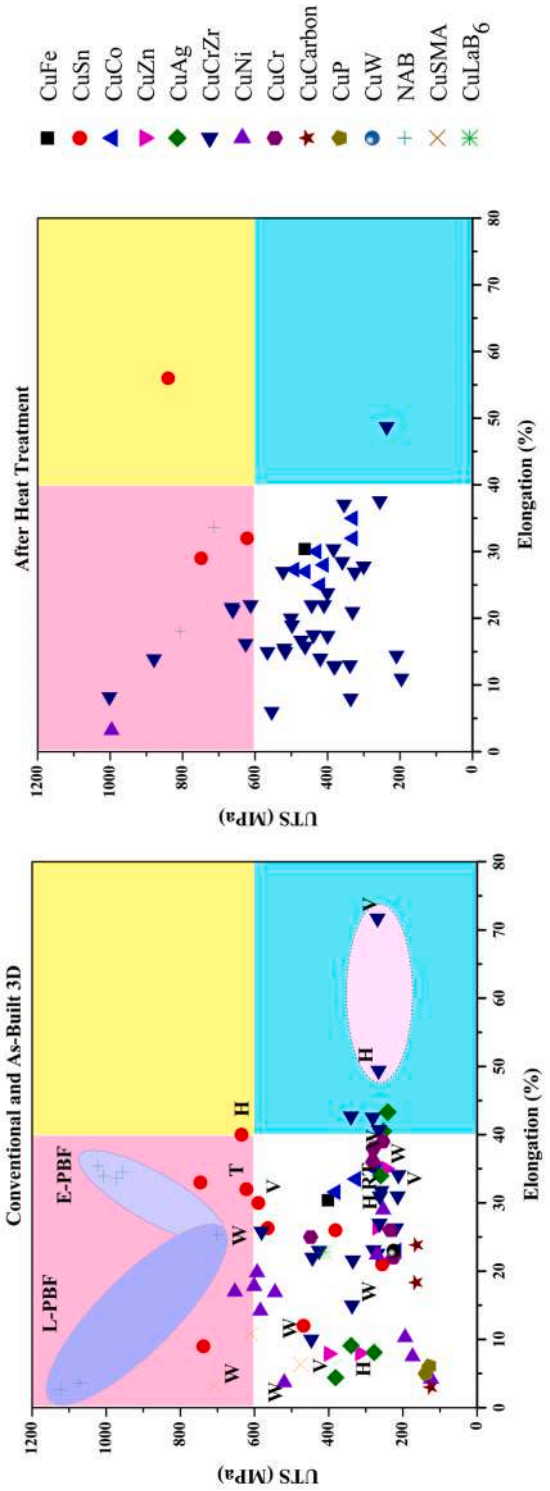


Fig. 51. Tensile behaviour and strength-ductility trade-off for L/E-PBF Cu alloys (W: conventionally manufactured parts; H: horizontal AM specimens; V: vertical AM specimens; T: transverse AM specimens; RT: room temperature properties of the L-PBF Cu–Cr–Zr alloy, with ~262 MPa UTS and 31% plasticity).

declined from 267.4 to 18.0 MPa as porosity increased from 8.7% to 46.8%. Achieving a balance between tensile and compressive properties remains a challenge in L/E-PBF processes, as highlighted by the development of Cu–13.2Al–3.5Ni SMAs, which were explored as an alternative to Ni-Ti alloys. Although these alloys showed remarkable compressive strength (1590 MPa) and strain (23%), their tensile performance was lower (1% elongation, 312 MPa), owing to the narrow, columnar grain structure present in the as-built state after the L-PBF process [111]. Additional future research is required to substantiate these findings. Thus, attaining the desired microstructure while minimising process-induced defects is crucial for superior compressive behaviour by optimising process parameters and feedstock characteristics, ultimately enhancing the mechanical performance of L/E-PBF Cu alloys.

Prior research has highlighted the critical role of initial feedstock composition in L/E-PBF for achieving a balance between printing parameters and compressive behaviour, including functional properties such as shape memory characteristics. For instance, a 300 W laser effectively fabricated Cu-based SMAs with varying optimum scanning speeds for each composition (Cu–Al–Ni: 400 mm/s, Cu–Al–GN: 200 mm/s, Cu–Al–Ni–GN: 300 mm/s, where GN: graphene). Interestingly, GN reinforcement improved the shape memory behaviour of the L-PBF Cu–Al–GN alloy, although the Cu–Al–Ni–GN composite demonstrated superior performance during the initial shape recovery cycles [147,271]. Moreover, the content of alloying elements plays a critical role in optimising the performance of Cu-based SMAs fabricated via L-PBF. For instance, incorporating 1 at.% Nb content resulted in superior shape memory response and compressive strength due to fine precipitates, which effectively prevent plastic deformation (Cu–Al–Mn–Nb alloy). However, excessive Nb addition led to the formation of larger precipitates, which hindered variant mobility and consequently reduced the recoverable strain [272].

Adjusting key L-PBF process parameters can surmount the anisotropy challenge and fabricate defect-free parts to achieve superior compressive and tensile behaviour for printed components. In L-PBF processing of Cu-based SMA, 380 W laser power has been established as the optimal power for energy density. This specific power (380 W) promoted superior tensile (492.9 MPa stress and 1.5%EL) and compressive behaviour (1191.4 MPa stress and 11.14% compressive strain) by facilitating the formation of a peculiar microstructure rich in thin needle-type β' martensite, surpassing the lamellar-type structures observed at 360 W and 400 W [273]. Xi et al. [176] observed a critical correlation between the optimal shape memory behaviour and superior compression performance (strength and strain), resulting from precisely controlled laser energy input (123-185 J/mm^3) in L-PBF Cu-based SMAs. Although the 154 J/mm^3 VED achieved the most favourable outcomes (1652 MPa, 15.1%, high recovery rate, and recoverable strain), higher energy inputs exacerbated manganese evaporation, altering phase composition and raising the martensite transformation temperature. Moreover, martensite morphology varied in L-PBF Cu–Al–Mn alloys with increased laser power (275 W vs. 325 W), leading to a trade-off between strength and shape memory behaviour. The 175 W processed sample (austenitic) exhibited the highest YS (250 MPa) and superelasticity (2.8% recovery). Conversely, samples processed at 275 W and 325 W, with acicular and stepped martensites, respectively, displayed lower YS (100 MPa) and lacked superelasticity [4]. Similarly, the L-PBF of the Cu–Fe–P alloy highlighted the importance of LED as a key parameter in compressive behaviour. The optimal LED (133 J/m) demonstrated the highest compressive strength (~1 GPa) and significantly enhanced plastic strain (27%). However, low LED led to insufficient melting, resulting in porosity and decreased strength/ductility, while excessive LED promoted Fe_2P formation, increasing brittleness and impairing ductility [28]. Another study found that changing scan vector rotations significantly enhanced shape memory behaviour (compressive loading and unloading experiment) in L-PBF Cu–Al–Mn alloys without post-printing heat treatments, surpassing traditional methods and even exceeding

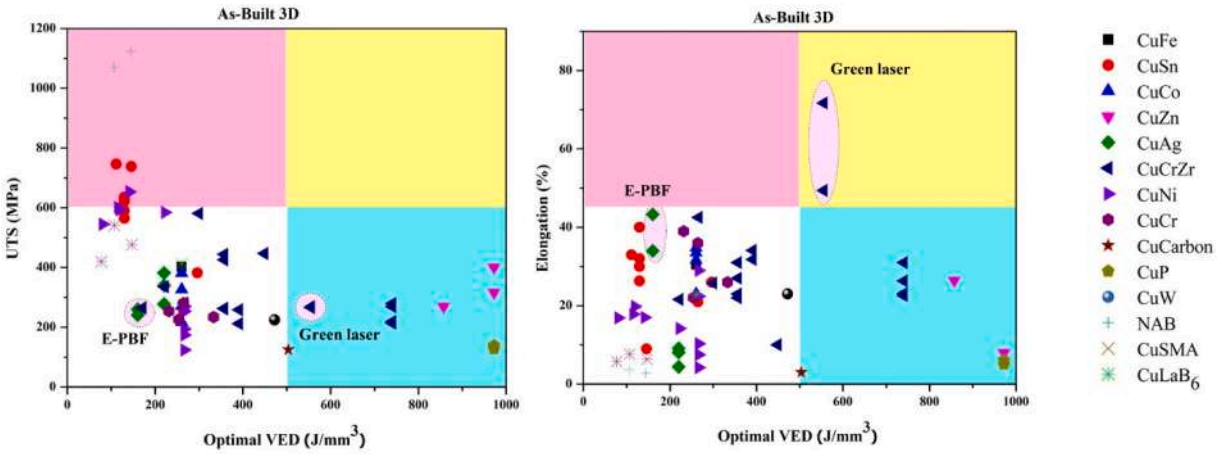


Fig. 52. Variations in UTS and ductility with optimal VED during L/E-PBF Cu alloys.

values reported for established SMAs (Ni–Ti, Fe–Mn–Al–Ni, Co–Ni–Ga, conventional Cu–Al–Mn SMAs). The 90° scan rotation yielded the best shape recovery (6.1%) due to strong texture formation, significantly higher than other rotations (1.4-4.1%) [53]. Additionally, selective laser remelting (SLR) effectively densified Cu–11.8Al–3.2Ni–3Mn SMA (> 99.5%), achieving near-fully dense parts with minimal impact on compressive performance compared to L-PBF (SLR: 1512 MPa strength, 13% strain vs. L-PBF: 1511 MPa, 14% strain) [274]. However, a trade-off emerged in tensile behaviour—while SLR improved ductility (9.3%) by reducing porosity and potentially smaller grains, it yielded slightly lower tensile strength (492 MPa) compared to L-PBF (617 MPa). Notably, excessively high SLR (> 100 J/mm^3) reduced parts density (< 98.5%) and compromised compressive properties (strength reductions of 5 to 29%), underscoring the importance of precise process parameter optimisation for achieving optimal compressive performance in L-PBF-fabricated Cu-based SMAs. Another study demonstrated that carefully selecting remelting approaches in L-PBF Cu–Al–Mn SMAs significantly enhanced superelasticity, particularly using a lower energy density (72.2 to 173.3 J/mm^3), resulting in a more considerable recoverable strain (4.8%) than with a higher energy density [66]. In addition, energy density altered phase composition, grain size, and chemical composition, all of which stimulated shifts in the superelastic behaviour of Cu SMAs. For instance, in Cu–Zn–Al SMAs, Zhuo et al. [175] observed that energy density variations (79.8, 99.2, 119.0, 208.3, and 324.1 J/mm^3) directly influenced superelasticity due to Zn evaporation. Lower energy density resulted in brittle and hard β' phases, while higher energy inputs (>60% Zn loss) led to α phase dominance, influencing mechanical properties. Thus, energy density acts as a double-edged sword, favourable for higher-density components but detrimental due to the evaporation of high Zn contents, which regulates superelastic performance. The best superelasticity was observed at an energy density of 99.2 J/mm^3, as irrecoverable strain increases with higher energy density.

The effects of post-printing heat treatment on the non-equilibrium microstructure and properties of L/E-PBF Cu alloy/composite parts can vary significantly, sometimes in a conflicting manner. For example, the L-PBF Cu–12.9Zn–2.5Si alloy showcased a trade-off between compressive and tensile properties following heat treatment [153]. While the AB state exhibited superior compressive YS (382 MPa) and plasticity (50.1%), heat treatment reduced both compressive strength and ultimate strength. This variation arises due to microstructural changes that regulate cellular structure, texture, dislocation density, phase distribution, and grain size. Interestingly, while heat treatment enhanced compressive ductility, it significantly reduced tensile ductility due to thermal dezincification and the resulting porosity. These pores are more susceptible to cracks under tensile loading but have minimal impact under compression due to a confined stress state. Furthermore, different cooling rates (furnace, air, water quenching) formed distinct microstructures, impacting compression behaviour (furnace: 1250 MPa, 13.8%; air: 994 MPa, 11.5%; water: 1247 MPa, 15.6%) [275]. L-PBF Cu–Cr–Zr alloys achieved substantial compressive strength gains through optimised DA treatment, with YS surpassing 500 MPa (> 150% increase) from the AB state (200 MPa). Yang et al. [276] achieved a remarkable increase in compressive YS (3x to 454.5 MPa) after 2 h of aging treatment, attributed to the optimal size and fraction of

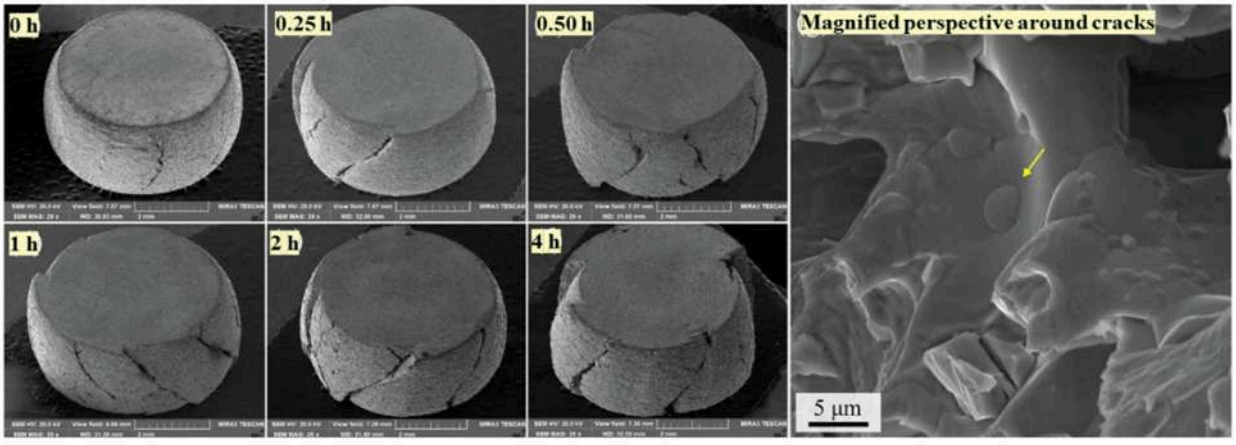


Fig. 53. Surface deformation before and after aging treatments for L-PBF Cu–Ni–Sn–P alloy [276].

precipitates in the L-PBF Cu–Ni–Sn–P alloy. However, the prolonged aging treatment led to more frequent and pronounced shear cracks along the (Cu, Ni)$_3$P phase borders, as evidenced by fractography analysis (Fig. 53), suggesting these precipitates act as crack initiation sites. Therefore, optimising heat treatment parameters (time, temperature, and cooling rate) is critical for superior compressive performance of L/E-PBF Cu alloy components. At present, heat treatment methods are limited to solution heat treatment, solution-aging heat treatment, and aging heat treatment. Future research should explore more efficient and rapid post-printing heat treatment methods, such as electropulsing, to further improve the compressive behaviour of L-PBF Cu alloys/composites.

Further research should investigate the potential of L-PBF Cu alloy/composite lattices beyond mechanical properties, considering broader physical, chemical, and biological attributes. Evaluating compressive-toughness behaviour across different temperatures, strain rates (low to high), and post-printing heat treatment would provide a better understanding of the process defects-microstructure-properties nexus. Research should also focus on multi-scale microstructures and process parameters, as well as the interrelationship between functional and mechanical properties of the L/E (NIR laser, green, electron beam, blue)-PBF Cu alloy/composite parts, which remains poorly understood. Advancing this knowledge is crucial for the development of high-performance L/E-PBF Cu alloy/composite lattices and SMAs.

8.3. Hardness (micro and nanoindentation)

Hardness measures the endurance of materials to resist plastic deformation (with or without elastic deformation and fracture) caused by localised contact with indenters during abrasion or indentation, and it is a crucial fingerprint property for optimising heat treatment cycles for AM components and designing parts for tribological applications (wear and friction). L-PBF holds promises for tribological wear-resistant components, as Jahns et al. [152] demonstrated its potential for fabricating high-hardness Cu components compared to traditional processes was achieved by tuning process parameters, resulting in a L-PBF Cu–Cr–Zr alloy Vickers hardness of 92.0 HV0.1 (41% higher) than its cast equivalent (65.0 HV0.1) in the printed condition. Additionally, hardness offers a rapid, near-non-destructive method for estimating YS in AM alloys (Tabor's equation, $\sigma_y = Hv/3$) [277,278]. However, data on L-PBF Cu alloys revealed a strong correlation ($R^2 = 0.83$) between Vickers hardness and tensile YS for both AB and post-printing heat treated conditions, as shown in Fig. 54 employing the following Eq. (8.1) instead of Tabor's equation.

$$HV = \alpha \sigma_y + \beta \tag{8-1}$$

where HV is Vickers hardness, σ_y is tensile YS, and α, β constant.

Eq. (8.1) proposes that Vickers' hardness can serve as a dependable predictor of YS in AMed Cu alloy/composite parts. However, further research is required to gain a comprehensive understanding and to improve this correlation for broader applicability in L/E-PBF Cu alloys/composites. The Vickers hardness values of L/E-PBF Cu alloys, both as-built (AB) and after heat treatment, are summarised in **Table S3**, spanning from 55 to 637 HV (see Appendix A – Table S3 [23,48,55,59,61,68–70,127,150,151,154,199,244,248,253,261–263]). Low-load Vickers hardness testing, using loads (200-500 gf) and short dwell times (10-20 seconds), is the primary method for determining the Vickers hardness of L/E-PBF Cu alloys/composites.

In L/E-PBF Cu alloys/composites, Vickers hardness hinges on several factors: feedstock characteristics (composition, morphology, pre-processing like pre-alloying or mixing), process parameters, energy source type (green, NIR laser, or electron beam), microstructural features, and post-printing heat treatment conditions applied to the AM components. The data presented in Tables S1 and S3, summarised in Fig. 54, provide insights into the nexus between VED and Vickers hardness in L-PBF Cu alloys and reveal significant variation in Vickers hardness (55-340 HV) during the L-PBF process (except Cu–10Zn alloy and Cu–0.1CNP composite). Most L-PBF Cu alloys (except Cu–10Zn and Cu–0.1CNP) achieved optimal hardness within a VED range of 100-400 J/mm^3 using a NIR laser. Nevertheless, green lasers that operated within a significantly higher VED range (400-600 J/mm^3) exhibited reduced hardness values. This presents an appealing opportunity for future research to optimise the process parameters of the green L-PBF process to improve the mechanical properties of Cu alloys, including Vickers hardness. Furthermore, the primary challenge is to alleviate the anisotropy of texture and phases of Cu alloy during L/E-PBF due to layer-by-layer deposition, composition-driven laser inconsistencies, and variable heat cycling. This resulted in a heterogeneous and anisotropic microstructure and preferential precipitation across the printed Cu alloys. Consequently, L/E-PBF Cu alloys exhibited hardness anisotropy, with higher hardness (8%) observed on the X-Z plane (more melt pool boundaries) compared to the X-Y plane (Fig. 55). Additionally, the L-PBF components outperformed the cast parts due to the grain refinement effect of the Ti element (Cu–Al–Ni–Ti SMA) and the high cooling rate inherent in AM processes [253]. Similarly, Li et al. [279] identified a

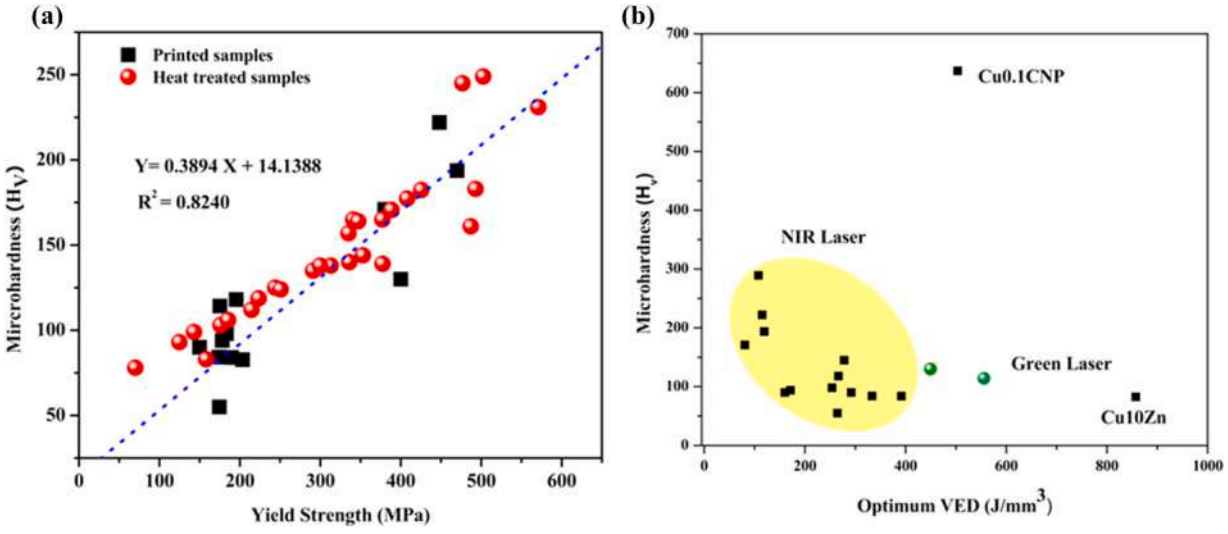


Fig. 54. (a) Vickers hardness and YS correlation of L-PBF Cu alloy; (b) Variation of Vickers hardness and VED.

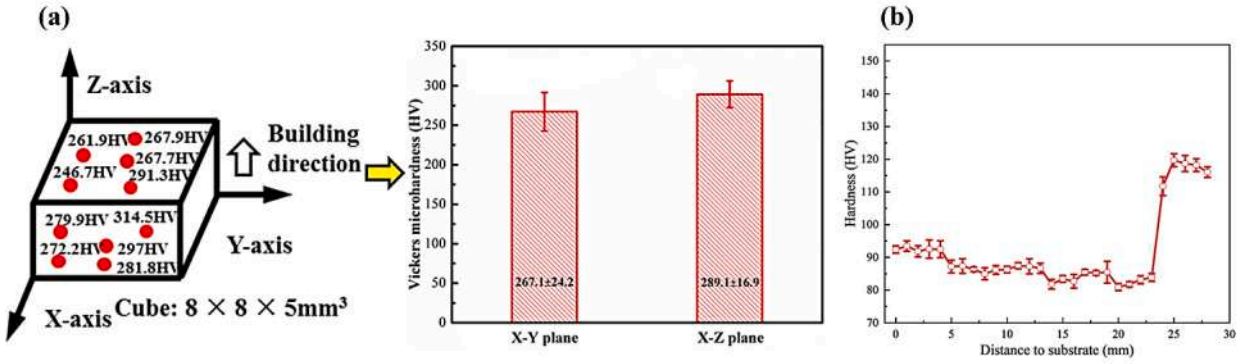


Fig. 55. (a) Variation of Vickers hardness on different planes [253]; (b) Variation of Vickers hardness with deposition height [279].

deposition height-dependent hardness variation (85-115 HV) in the E-PBF Cu–Cr–Zr alloy (Fig. 55). This stemmed from grain morphology transitions from equiaxed near the base (92 HV) to columnar (85 HV) with deposition height, then back to equiaxed with a secondary phase (115 HV) above 25 mm. Unlike E-PBF, L-PBF Cu–Al–Ni–Mn showed lower hardness at the top and higher at the bottom for dense samples (99% at 350 W, Fig. 56**a**) [169]. However, lower density (e.g., 82% at 300 W) resulted in both increased hardness anisotropy/non-uniformity and the overall lowest hardness compared to denser samples (Fig. 56**a**). This indicates that printing defects, in addition to microstructure features, have a substantial impact on the hardness anisotropy of L/E-PBF Cu alloys. Li et al. [252] observed that in L-PBF Cu–Cr–Nb–Ti alloys, Vickers hardness progressively increased as scan speed varied from 500 to 800 mm/s, then plateaued beyond 800 mm/s (Fig. 56**b**). Interestingly, this trend correlated with an increase in fine grain fraction from 12.1% at 500 mm/s to 26.7% at 800 mm/s and then 36.4% at 1100 mm/s. In Cu alloys with evaporative elements like Zn, selecting the optimal VED is crucial [175]. Higher VED levels intensified Zn loss (Fig. 57) and reduced hardness (from 236.8 to 167.6 HV, a 30% drop). This is compounded by the shift towards a softer α phase due to β' phase reduction and potential grain size variations, all regulating overall hardness in the Cu–Al–Zn alloy. Thus, achieving desirable Vickers hardness necessitates fine-tuning VED to reduce Zn loss while modifying phase composition and grain size. However, energy interaction is influenced not only by laser power and scanning speed but also by scan strategies and layer thickness. These parameters influence heat flow and thermal history within the melt pool, ultimately governing microstructure, defect formation, and, consequently, the hardness of AMed Cu parts, which can be investigated for future research on L/E-PBF of Cu alloys.

E-PBF fabrication of NAB alloy reveals a dependence of hardness on both PSD and build orientation [23]. All PSDs (S_S: 45–63 μm, S_M: 63–75 μm, S_L: 75–105 μm, S_{Mix}: 45–105 μm) exhibited higher hardness in horizontal orientations compared to the vertical. Interestingly, the mid-range particle size fraction (S_M: 63–75 μm) achieved the best overall hardness in both orientations. While surface oxides can boost laser absorption and powder bed uniformity, resulting in complete fusion and higher density of Cu alloys, their effect on hardness appears to be limited at lower weight percentages. A study on E-PBF Cu–Ag–Zr alloys showed a negligible hardness difference between the as-received powder (0.011 wt.% oxygen) and the oxidised powder (0.047 wt.% oxygen) at various beam currents (6, 9, 12 mA) [59]. However, further research is needed to determine how increasing oxygen levels may affect the mechanical properties and reusability of Cu alloy powders, particularly in L-PBF. On the other hand, the choice of energy source (electron beam/laser) has a considerable impact on the microstructure and, as a result, the mechanical properties of the printed parts. In the Cu–Cr–Zr alloy, E-PBF facilitated the formation of ultrafine chromium nanoparticles within the Cu matrix, increasing Vickers hardness by 87% (144 HV) over L-PBF (77 HV) [61]. This demonstrates that E-PBF has the potential for manufacturing high-performance Cu components without post-printing heat treatments, albeit more research is required to acquire a deeper

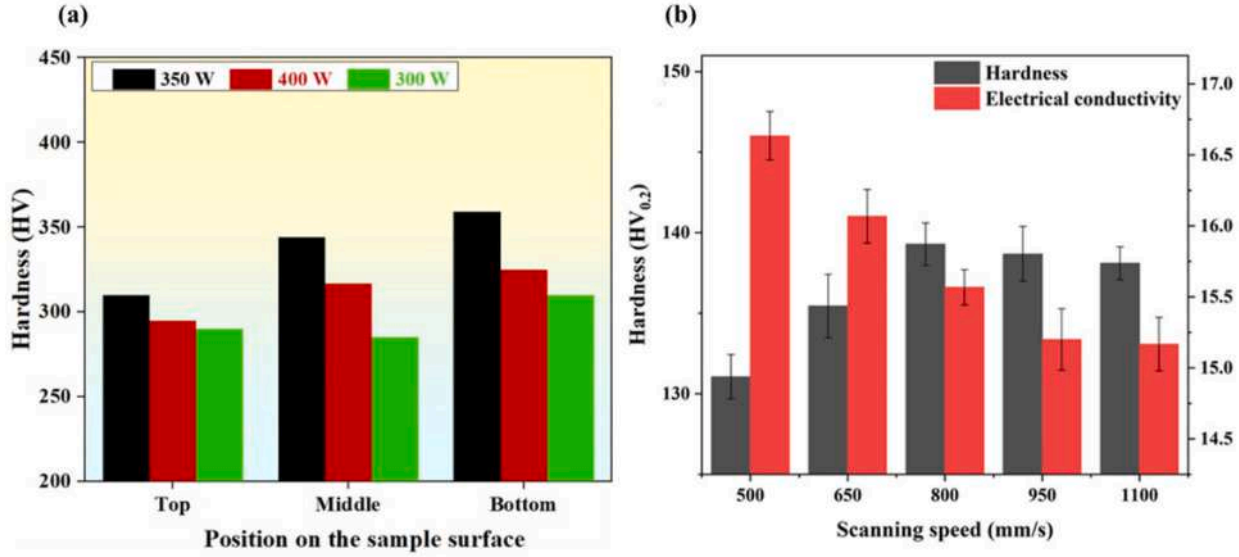


Fig. 56. Vickers hardness variation with process parameters: (a) Laser power; (b) Scanning speed [169,252].

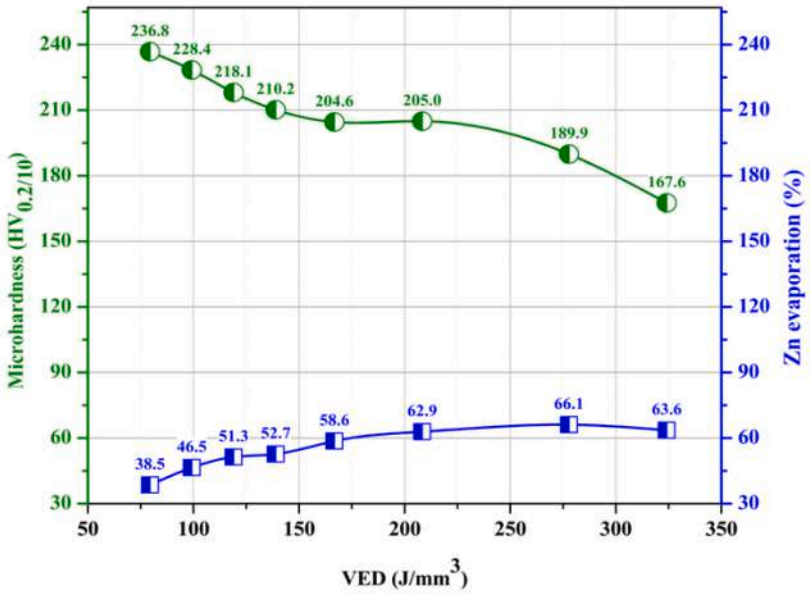


Fig. 57. Vickers microindentation hardness and VED variation with Zn evaporation in L-PBF Cu–Zn–Al SMA [175].

understanding. Researchers examined the possibility of alloying in L-PBF Cu alloys for superior comprehensive performance and NIR laser printability by decreasing the necessary laser energy density. Uchida et al. [248] found that increasing the chromium level in L-PBF Cu alloys from 1.2 to 2.3 wt.% significantly enhanced hardness (> 60%) but reduced electrical conductivity. This underscores the importance of optimising alloying element content to achieve a desirable balance between hardness and electrical conductivity. In L-PBF Cu–Sn–Ni alloys, uneven Ni distribution from mechanical milling (compared to pre-alloyed powders) resulted in lower hardness and higher hardness anisotropy (Fig. 58) [134]. This highlights the critical role of Cu alloy powder feedstock preparation in achieving optimal mechanical properties through L/E-PBF processes. Beyond the influence of Cu alloy composition, powder feedstock characteristics (morphology, preparation method - atomisation vs. mechanical mixing, PSD), and AM process parameters (energy source, VED, scan speed, power), the unique microstructures developed during AM can be further tailored by post-printing heat treatments, ultimately affecting the hardness of Cu alloys. L-PBF Cu–Cr–Zr alloy benefits significantly from post-AM heat treatments in terms of hardness. DA treatment at 500 °C for 2 h significantly increased hardness (41%) compared to the AB state. This enhancement is attributed to the precipitation mechanism, specifically the presence of nano-sized chromium precipitates and the core-shell structure of Zr nanoparticles surrounding the Cr core within the microstructure. Conversely, solution annealing led to a 40% reduction in hardness [261]. While direct aging treatment improves hardness, optimal mechanical properties depend on both the aging temperature and duration. Vickers' hardness increased with aging heat treatment temperature from 400 to 475 °C (AB: 94.4 to 182.4 HV) but then decreased to 106 HV at 620 °C with a constant time of 2 h [127]. The observed hardness peak at 475 °C suggests optimal precipitation for maximising hardness in L-PBF Cu–Cr–Zr alloy. This emphasises the critical role of precisely controlled heat treatment temperature and time, along with exploring different heat treatment approaches, to achieve superior mechanical properties in L/E-PBF Cu alloys.

For L/E-PBF Cu alloys/composites, indentation into pores can misrepresent Vickers microindentation hardness in hierarchical and heterogeneous Cu alloys microstructure. Nanoindentation offers a local solution by measuring hardness and modulus, capturing the cumulative impacts of grain boundaries, dislocations, precipitates, and phase transformation effects, which are anticipated to be less relevant under microindentation hardness. This approach indirectly reveals the homogeneity of precipitates and phases within the microstructure. L-PBF Cu–CNT composites showed an indentation size effect (hardness decreased with depth) but lower overall hardness (0.6-1.1 GPa) and modulus (40-80 GPa) than pure Cu, despite positive strain rate

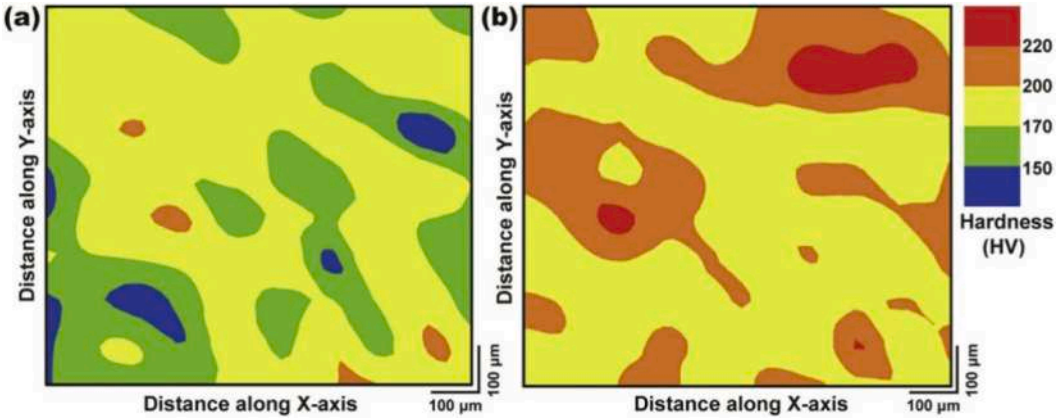


Fig. 58. Vickers hardness map (a) Mechanically milled; (b) Pre-alloyed L-PBF Cu–15Ni–8Sn alloy [134].

sensitivity (hardness increased with strain rate) due to porosity, a weak Cu–CNT interface, and CNT agglomeration. This highlights that alloying alone may not enhance mechanical properties in AM systems; defect-free processing is also essential [155]. Jeyaprakash et al. [242] investigated the hierarchical and heterogeneous microstructure of L-PBF Cu–Cr–Zr alloy using nanoindentation. Cu_2O precipitates (red in mapping) enhanced localised hardness (1.6 GPa) and reduced modulus (137.6 GPa) due to their resistance to indentation, as shown in Fig. 59, indicating their uniform distribution from consistent red dot patterns. This approach allows for identifying a homogeneous distribution of nanophases in complex Cu alloy microstructures formed following AM. In another investigation, the L-PBF Cu–Cr–Zr alloy exhibited increased indentation depth with a higher load (2000 vs. 1000 μN, 1.3x deeper). Additionally, grain structure and defects played a critical role in the variation of nanoindentation hardness, ultimately influencing wear resistance. Equiaxed structures exhibited the highest resistance, while columnar structures showed the lowest [280]. Contrary to the traditional belief that higher H/Er (H: nanoindentation hardness, Er: reduced modulus) and H^3/Er^2 imply better wear resistance, Prabu et al. [281] observed the opposite for L-PBF Cu–Cr–Zr alloys. Using low (3 μm) and high (20 μm) pitch nanoindentation, they found that low-pitch nanoindentation employing nanoindentation hardness and reduced modulus was not appropriate for tribological identification. However, this finding requires further validation in new L/E-PBF Cu alloys. Additionally, identifying L/E-PBF Cu alloy with nanoindentation requires careful consideration of pile-up effects. These effects lead to increased non-uniform material behaviour and unreliable nanoindentation hardness data at higher loads (9000 μN). Furthermore, higher loads generated frictional heat, promoting oxide formation on the indented surface due to interaction with atmospheric oxygen [282]. Overall, nanoindentation is a valuable tool for investigating L/E-PBF Cu alloys, but careful consideration of factors such as microstructure, load, and pile-up effects is crucial for accurate data interpretation. While nanoindentation has successfully been used to investigate NIR L-PBF Cu alloy, research on green/blue, hybrid laser, and E-PBF Cu alloy is sparse. Lastly, nanoindentation using EBSD for microstructure investigation and high-temperature nanoindentation under varied loading rates are understudied, offering promising research perspectives.

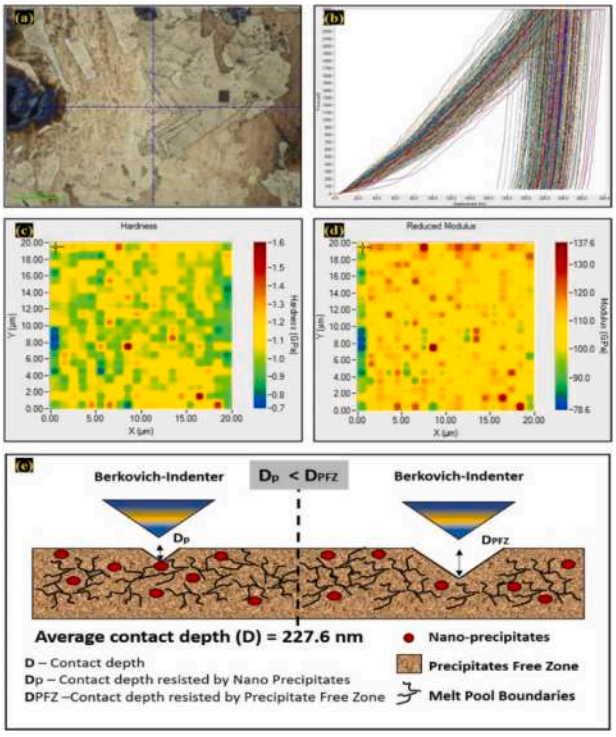


Fig. 59. Nanoindentation with Berkovich indenter at 2500 μN, over a 20×20 μm area: (a) OM image; (b) Indentation load-depth curves on AB Cu alloy; (c) Nanoindentation hardness mapping; (d) Indentation modulus mapping; (e) Mechanism [242].

8.4. Electrical properties

At present, achieving high strength (UTS ≥ 600 MPa) and high conductivity (electrical conductivity ≥ 70% IACS) simultaneously in Cu alloy AMed components presents a significant challenge. This is due to the complex interplay between the factors that influence electrical conductivity, such as alloy composition, precipitating phases, dislocation, and grain boundaries. These factors are governed by Mattiessen's rule, which is correlated using Eq. (8.2) below [283–285].

$$\rho_{alloy} = \rho^{pureCu} + \rho^{D} + \rho^{GB} + \rho^{P} + \rho^{S} \quad 8.2$$

Where ρ_{Total} is the total electrical resistivity; ρ^{pureCu} is the electrical resistivity of pure Cu and ρ^{D}, ρ^{GB}, ρ^{P}, ρ^{S} are the resistivity values to electron scattering by the dislocations, grain boundaries, precipitates, and solid solutions, respectively. Defects such as dislocations, grain boundaries, phases, and vacancies within the microstructure of L/E-PBF Cu alloys/composites act as roadblocks to the movement of free electrons. These defects increase electrical resistance by obstructing the path of free electrons (travel distance). The Cu alloy/composite composition, printing parameters, part geometry, and heat treatment collectively influence the formation of these defects. Additionally, AM process-induced defects such as pores and partially melted particles introduce additional scattering centres, further complicating the conductivity behaviour in L/E-PBF Cu alloys/composites.

Table S4 (see Appendix A **– Table S4** [26,29,45,48,52,54,55,59,68,69,71,72,100,104,110,112,127,128,150,154,157,199,244,248,261–263]**)** summarises the electrical conductivity of L/E-PBF Cu alloy/composite samples. Figs. 60-63 depict the electrical conductivity and UTS of the alloys, dividing them into four important regions: high strength and high conductivity (HSHC), high strength and medium conductivity (HSMC), medium strength and high conductivity (MSHC), and medium strength and medium conductivity (MSMC). In the micro-alloyed Cu-based system (less than 5 wt.%), the strength-electrical conductivity trade-off was observed during L/E-PBF processes (Fig. 60). Most L/E-PBF-fabricated binary Cu alloys fall into two zones: MSMC (UTS < 600 MPa, < 60% IACS) and MSHC (UTS < 600 MPa, > 60% IACS). Achieving the requisite electrical performance for L/E-PBF processes necessitates the careful evaluation of material composition, process parameters, etc. For instance, the type and amount of alloying elements significantly impact laser reflectivity during the NIR L-PBF process. This, in turn, determines the RD (which indirectly implies % porosity) and electrical conductivity of the final components. Furthermore, microstructural defects enhance free electron scattering according to Mattiessen's rule, with solid solution (dissolved elements) causing the most substantial scattering of free electrons [45]. In the AB state for Cu–Cr–Zr alloys, dissolved chromium (BCC) heavily scattered electrons (solid solution), leading to low electrical conductivity (19.1% IACS) [262]. Notably, heat treatment significantly improved electrical conductivity in L/E-PBF Cu alloys by transforming scattering solid solution atoms into precipitates, allowing a few alloys to reach the HSHC zone; for instance, the Cu–Cr alloy (Fig. 60**,** arrowheads denote properties of the heat-treated samples). As illustrated in Fig. 61, solution treatment (ST) of printed Cu–Cr–Zr alloy samples introduced a mixture of BCC Cr particles and FCC precipitates, which reduced electron scattering and enhanced electrical conductivity by 111% compared to the as-built state. Further enhancement was achieved through DA heat treatment, which promoted a higher volume of FCC precipitates, resulting in weaker free electron scattering and a 240% increase in conductivity over the AB state [262]. Moreover, high solubility elements in the Cu matrix during L/E-PBF processing required heat treatment to ensure optimum

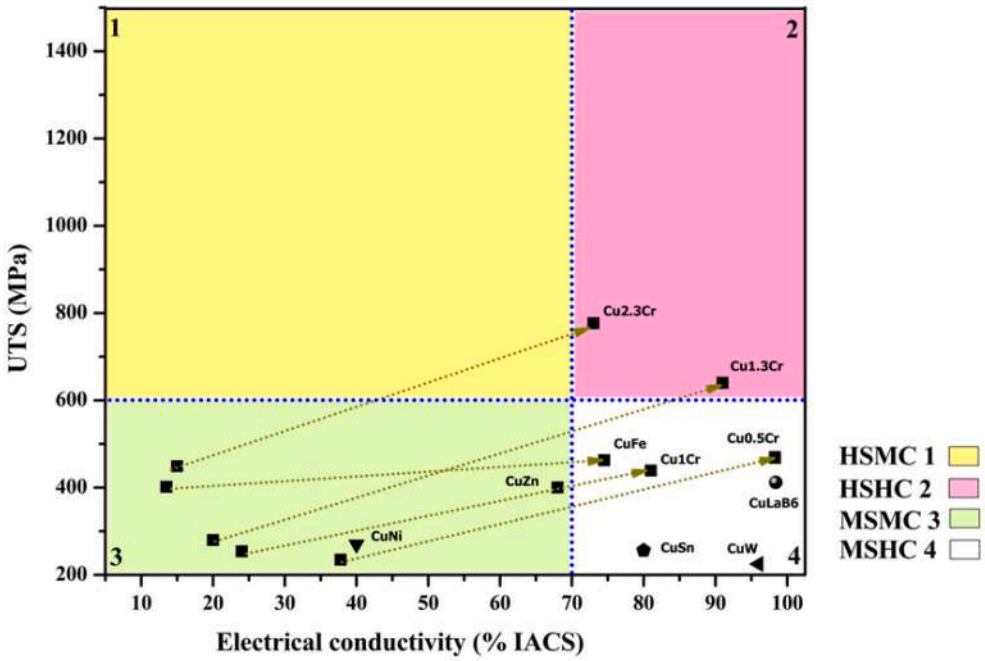


Fig. 60. Variation of UTS and electrical conductivity for L/E-PBF-fabricated Cu binary low alloy (< 5 wt.%) (arrowheads indicate properties of the heat-treated sample).

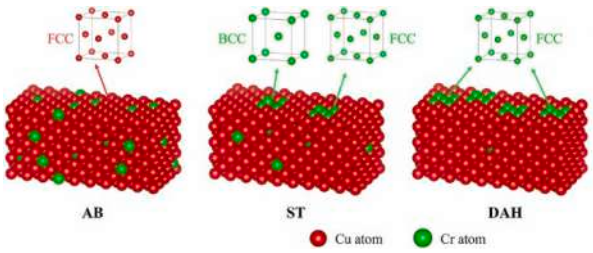


Fig. 61. Schematic diagram of the atomic state after heat treatment for L-PBF Cu alloy [262].

conductivity and strength, which extended production time and complexity. To solve this, researchers have explored low-solubility elements such as LaB_6 in the copper matrix to achieve a balanced combination of properties without sacrificing conductivity [71]. Additionally, LaB_6 reprecipitates during solidification, preventing segregation along the melt pool boundaries, which allows L-PBF Cu–1LaB_6 to achieve high conductivity (98.4% IACS) in the AB state (without heat treatment), thus reducing production time and placing it within the HCMS zone. Similarly, carbon-based nanofillers such as graphene oxide (GO) and CNP were explored to augment laser absorption in pure Cu during L-PBF due to their negligible solubility in copper, thereby lowering distortion to the Cu lattice (**see** Appendix A – **Table S4**). However, both filler types suffered from agglomeration and poor compatibility with the copper matrix (poor wettability and bonding), resulting in parts with moderate electrical conductivity (below 70% IACS) and subpar mechanical properties (strength below 200 MPa). Furthermore, researchers have explored surface coating strategies as an alternative to traditional pre-alloying methods (adding carbon-based particles, ceramic particles, or alloying elements). Zheng et al. [157] found that 0.4 wt.% surface-alloyed Ni on Cu powder achieved a balance between UTS (253 MPa) and electrical conductivity (53.3% IACS) in the L-PBF process. However, higher Ni contents (over 0.4 wt.%) are responsible for the strength-electrical conductivity trade-off, indicating that the coating amount is critical. Additionally, surface alloying outperformed partial surface alloying in achieving the strength-electrical conductivity synergy of L-PBF Cu alloy parts. Similarly, a thin Sn coating (62 ± 14 nm) on Cu powder was found to improve NIR laser absorption from 19 to 51%, yielding printed parts with superior electrical conductivity (80 ± 1% IACS) and UTS (256 MPa). Similarly, W-coating offered even higher laser absorption than Sn, CNT, and chromium oxide (Cr_2O_3) coatings, achieving 99.9% density and 96% IACS conductivity at 0.5 vol% W [52]. Although the adverse effects on the electrical conductivity of L-PBF Cu-based binary micro-alloys were mitigated through strategies such as powder surface engineering, a selective composite approach, control of solid solubility, and heat treatment to precipitate solute atoms, the HSHC zone was not reached, with the exception of the Cu–2.3Cr alloy. Further, researchers have investigated multi-element micro-alloyed L-PBF Cu alloys to achieve HSHC, as shown in Fig. 62 (Cu–Cr–Zr, Cu–Ag–Zr, and Cu–Cr–TiC alloys/composites). No chronicled composition has reached the HSHC zone. In current approaches for L-PBF Cu micro-alloys (< 5 wt.%), the selective composite technique has demonstrated potential for achieving synergy between strength and electrical conductivity through L-PBF, although it faces challenges related to high costs (e.g., costly nanoparticles) and scalability for industrial applications. Additionally, these methods have not achieved compositions within the desired HSHC zone (Figs. 60, 62). This limitation presents an exciting opportunity and challenge: to develop new, cost-effective, and scalable strategies for developing L-PBF Cu micro-alloy parts that fall within the HSHC zone. In contrast to micro-alloys designed to prioritise electrical conductivity, macro-alloys fabricated using L/E-PBF techniques target a broader range of properties (strength, ductility, conductivity, etc.). These macro-alloys, including Cu–10Zn, Cu–6Co, Cu–Cr–Nb, and Cu–Ni–Sn, often contain one or more alloying elements and typically fall within the MSMC zone in their AB state due to free electron scattering by solute atoms (as shown in Fig. 63). Notably, after heat treatment, precipitation enhances electrical conductivity. Wang et al. [128] showed that by employing L-PBF and heat treatment on Cu–Cr–Nb alloys, which featured a heterogeneous nanoprecipitate-dislocation (HND) architecture, the strength-conductivity trade-off was successfully surpassed. This HND architecture improved the tailorability of Cu alloy, as illustrated in Fig. 63. It can be classified as HSHC, which prioritises conductivity (~75% IACS) with moderate

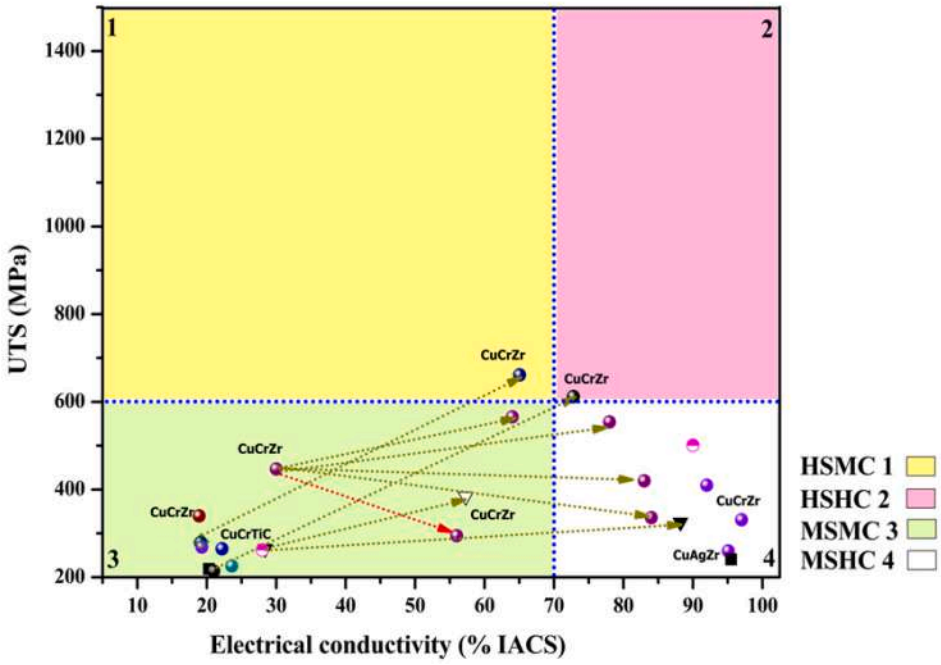


Fig. 62. Variation of UTS and electrical conductivity for L/E-PBF Cu ternary micro-alloys (arrowheads indicate properties of the heat-treated sample, and the red arrow highlights the strength-electrical trade-off).

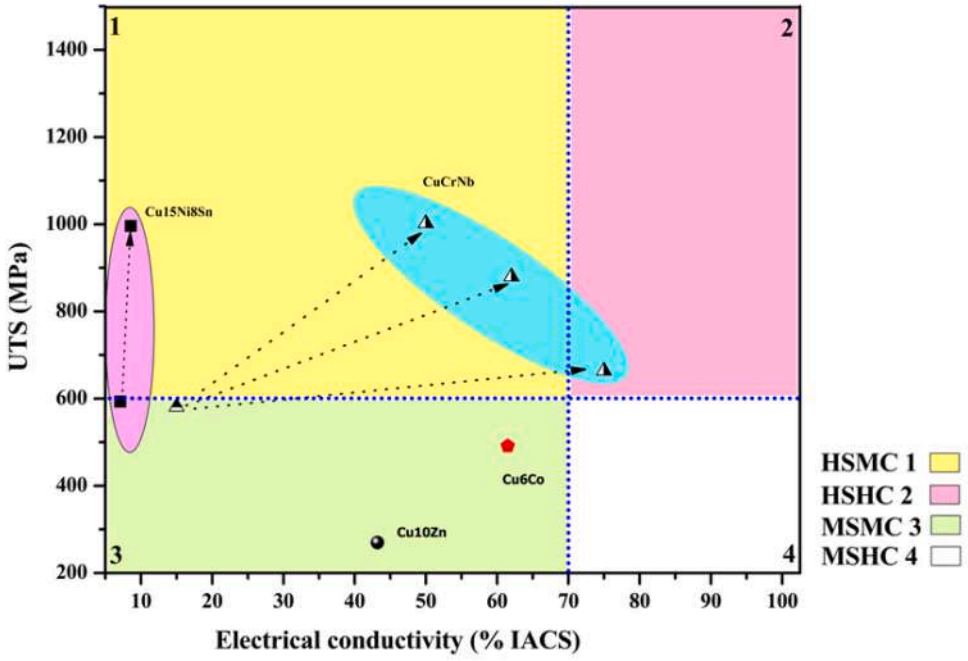


Fig. 63. Variation of UTS and electrical conductivity for L/E-PBF Cu macro-alloys (arrowheads indicate properties of the heat-treated sample).

strength (~664 MPa), and HSMC, which achieves an optimal balance of strength (~1 GPa) and conductivity (~50% IACS) [128]. While L/E-PBF offers unique capabilities, including the development of HND architecture and the management of segregation in high-alloyed copper, achieving the HSMC zone in the AB state remains elusive. Future research should explore innovative Cu alloy/composite compositions through computational and machine learning methodologies to harness the potential of the HSMC zone utilising L/E-PBF for Cu macro-alloys.

Alongside the strength-conductivity trade-off, electrical conductivity anisotropy in L/E-PBF Cu alloy/composite presents a significant challenge, dictated by defect distribution and density, prevailing crystallographic textures, microstructural anisotropy, degrees of lattice distortion, and size-dependent thermal history resulting in anisotropy, as shown in Fig. 64. Electrical conductivity increases with deposition height (78.6% at the top vs. 59.5% IACS at the bottom) due to changes in the size and amount of second phases at different deposition heights [279]. For L-PBF Cu–Cr–Zr alloys, the transverse specimens exhibited lower electrical conductivity than the longitudinal specimens [104]. Moreover, the electrical conductivity of E-PBF Cu–Cr–Zr alloys was found to be size-dependent, decreasing with increasing wall thickness

[286]. Furthermore, processing parameters also play a critical role in the electrical conductivity of L/E-PBF Cu alloys/composites by influencing defect formation and microstructural characteristics. In L-PBF Cu-TiC composites, the relative density (RD) increased from 91.2% to 98.8%, accompanied by a significant improvement in electrical conductivity, rising from 45.7% to 67.9% IACS [287]. Thus, optimising the interplay between strength and electrical conductivity while minimising anisotropy requires careful tailoring of printing parameters, feedstock formulation, and post-processing heat treatment for L/E-PBF Cu alloy/composite parts.

As previously mentioned, the high NIR laser reflectivity of Cu alloys can be addressed by switching to alternative energy sources, such as a green laser or an electron beam. Tang et al. [261] demonstrated a promising balance of strength and electrical conductivity (554 MPa strength, 78% IACS conductivity after post-AM heat treatment) in Cu–Cr–Zr parts using a green laser. Although the RD is lower (98.1%), this suggests further potential for performance improvement using low-power lasers (green/blue), which is anticipated in future research to understand how these low-power lasers influence the microstructure-properties nexus of L-PBF Cu alloys, particularly in terms of their synergistic or antagonistic effects on strength-electrical conductivity. Notably, E-PBF exhibited significantly higher electrical conductivity (> 60% IACS) than L-PBF for Cu–Cr–Zr alloys (usually below 30% IACS) due to precipitation in the as-built state (**see** Appendix A – **Table S4**) [279]. Similarly, Ovalle et al. [59] investigated Cu–Ag–Zr alloy using E-PBF printing and observed near fully dense (> 99%) and excellent electrical conductivity (> 95% IACS) for both pre-oxidised and as-received powders. Therefore, the vacuum environment of E-PBF and minimal reflectivity for Cu alloy/composite offers a unique path to explore fabricating components with superior electrical conductivity in the AB state due to the potential for in-situ precipitation and reduced oxidation. Along with selecting the appropriate beam energy source, optimising the energy density is essential for achieving superior electrical performance in L/E-PBF Cu alloys/composites. Zheng et al. [52] identified a laser scanning speed dependence for electrical conductivity in W-coated Cu alloy L-PBF parts. The optimal speed (500 mm/s) minimised both large W agglomerates (which cause scattering at 300 mm/s) and excessive nanoparticle formation (which increases scattering at 800 mm/s), leading to the highest electrical conductivity (96% IACS) (Fig. 64 **b**). Importantly, L/E-PBF deposition strategies alter the temperature gradient (G, R, and Δ T) within printed materials, resulting in distinct microstructural features (phases, texture, and grain size) depending on the scan pattern used. However, both meander and chessboard strategies yielded similar electrical conductivity but showed anisotropy (higher longitudinal, 21.6, vs. transverse, 19.1% IACS) [104]. This anisotropy arises due to rapid cooling during L-PBF, trapping strain in the lattice (supersaturated solid solutions of alloying elements), and the presence of more grain boundaries that scatter electrons in the transverse direction. Moreover, energy density plays a crucial role in managing porosity in L-PBF Cu alloys, which substantially impacts electrical conductivity. Notably, increased porosity scatters free electrons, reducing electrical conductivity. During L-PBF, Oropeza et al. [166] found that higher energy density (6.7 to 100 J/mm^3) decreases porosity in bronze and brass. Interestingly, hatch spacing can influence the porosity at the same energy density. For instance, at 100 J/mm^3, L-PBF bronze porosity varied from 1.5 (100 μm hatch) to 1.9% (200 μm hatch), and L-PBF brass varied from 11.1 (100 μm hatch) to 10.5% (200 μm hatch). Overall, L-PBF Cu alloys show reduced electrical conductivity with increasing porosity. Besides porosity, the printed geometry in L-PBF also plays a crucial role in electrical conductivity, with cubes demonstrating higher values than cylinders at similar porosities due to thermal history and RS anomalies caused by heat flow during the LPBF process.

Beyond modifying process parameters, post-printing heat treatments are critical in improving the electrical conductivity of AB samples because they contain a significant proportion of supersaturated solid solutions in Cu alloys. This leads to low electrical conductivity due to free electron scattering by solute atoms. Optimising post-printing heat treatment parameters enables control over the size, shape, distribution, microstructure, and sequence of precipitates within the AB microstructure, as well as enhancing the synergy between strength and electrical conductivity. In L-PBF Cu–15Ni–Sn alloys, the aging treatment surpassed the SAT process in electrical conductivity after the initial aging treatment [150]. In contrast, the electrical conductivity of L-PBF Cu–Cr–Zr was significantly higher for SAT (82.3% IACS) than for DA (65.1% IACS) specimens [262]. Aging treatments facilitate the precipitation of nanoscale phases, reducing lattice distortion and electron scattering [128,261,262]. This enhances both electrical conductivity and strengths (YS and UTS), potentially placing Cu alloys in the HSMC/HSHC zone (as shown in Figs. 62, 63). However, achieving the HSMC/HSHC zone in the AB state remains a challenge, offering an exciting avenue for future research in L/E-PBF Cu alloys. The AM of Cu alloys/composites using L/E-PBF suffers from a strength-electrical conductivity trade-off. In the future, researchers should explore new avenues, such as multi-component Cu alloys (beyond binary and ternary) with low-solubility elements that tend to precipitate and use machine learning and computational approaches to identify the best compositions and process parameters for L/E-PBF. Beyond the precipitation hardening alloy, AM can form in-situ precipitates during the process, which can address the bottleneck of the strength-electrical conductivity trade-off by exploring new exotic compositions for L/E-PBF in the future. Moreover, it is essential to investigate the impact of complex part geometries (as existing research primarily compares cubic and cylindrical geometries) on electrical conductivity, as well as the potential of heterogeneous nano-precipitate dislocation (HND) architectures to address the strength-electrical conductivity trade-off. This is critical for the future

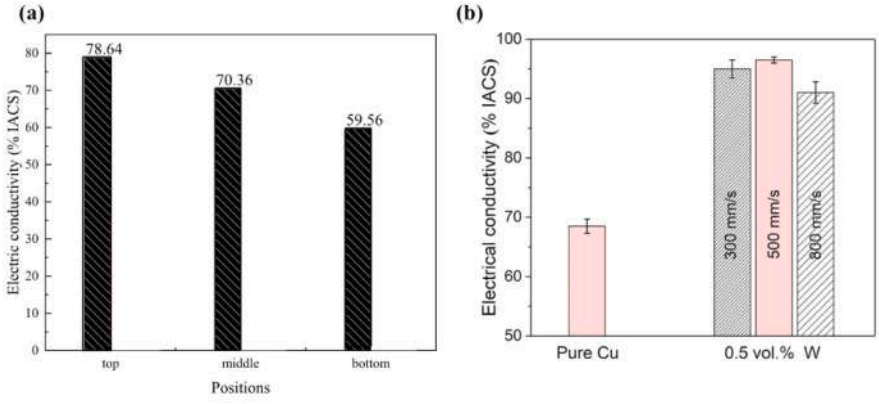


Fig. 64. (a) Variation of electrical conductivity from top to bottom for E-PBF Cu alloy [279]; (b) Variation of electrical conductivity with scanning speed [52].

development of HSMC/HSHC Cu alloys by L/E-PBF processes. Finally, the development of defect-free L/E-PBF Cu alloys/composite components with strength-ductility-conductivity synergy continues to pose a challenge, which may be overcome in the future through novel feedstock compositions, in-situ alloying, lean alloy design, etc.

8.5. Thermal conductivity

In response to miniaturisation and the demand for efficient heat dissipation for advanced applications (nuclear, aerospace), traditional fabricated Cu alloys pose a challenge due to the strength-ductility or strength-conductivity trade-off [31,128,288,289]. Consequently, achieving the optimal combination of strength, ductility, and conductivity is a formidable task. However, L-PBF Cu alloys with a novel HDN architecture have shown promise in attaining a synergy of high strength, ductility, and conductivity [128]. Thermal conductivity (TC) in L/E-PBF Cu alloy/composite is a complex interplay between electron and phonon transport; heat is conducted via electrons (carrying energy) and lattice vibrations (phonons), both of which are significantly influenced by material composition and microstructural features (grain texture, morphology and phases, grain boundaries, precipitates, dislocation density, lattice defects), built-in defects, and part geometry. As previously noted, defects and the microstructure of the printed parts are influenced by Cu alloy/composite powder feedstock characteristics, printing parameters, part geometry, and post-printing heat treatments. Therefore, strategic control of Cu alloys/composite powder feedstock characteristics, printing parameters, and post-printing heat treatment is crucial to optimising microstructure and minimising defects, thereby achieving superior TC. Prior studies have investigated the TC of L/E-PBF Cu alloy samples using both direct and indirect methods. The direct method employed a heat flow technique following ASTM E1225-20 [244]. Indirect methods included the Wiedemann-Franz law [290] (relating thermal conductivity (k) to electrical conductivity (σ) via temperature (T) and Lorentz number (L), as in Eq. (8.3), and the second indirect method uses Eq. (8.4), relating thermal diffusivity (α) (measured using the standard ASTM E2585-09), density (ρ), and specific heat capacity (C), to calculate thermal conductivity [290].

$$k = L \times T \times \sigma \tag{8-3}$$

$$k\,(T) = \rho(T) \times \alpha(T) \times C\,(T) \tag{8-4}$$

Current research has explored three methods (direct heat flow, Wiedemann-Franz law, and ASTM E2585-09) to measure thermal conductivity in L/E-PBF Cu alloy/composite samples. However, a critical gap exists—no studies have compared the accuracy of these methods. Therefore, future research should standardise testing protocols to ensure data comparability between studies.

Most studies have concluded that L/E-PBF Cu alloy/composite parts in the as-built state exhibit lower TC (around 100 W/mK for L-PBF Cu–Cr–Zr alloys) compared to conventionally manufactured counterparts (as shown in Fig. 65) [12,61,249]. This was attributed to factors such as high residual stresses, microstructure, and L/E-PBF process defects (increased electron-phonon scattering). Interestingly, post-processing heat treatment (aging) in L/E-PBF Cu alloys exhibited higher conductivity than wrought Cu alloys due to precipitation-induced microstructure alteration and reduced temperature sensitivity [12,61]. Notably, L-PBF Cu alloys face an additional challenge: thermal conductivity anisotropy. Zhou et al. [196] observed significantly higher TC in transverse samples (187.8 W/mK for Cu–Ni–Si alloys) compared to vertical samples (62.9 W/mK), due to variations in the fraction of HAGB, grain morphology (columnar versus equiaxed, as shown in Fig. 66), and texture. Consistent with Cu–Ni–Si alloys, L-PBF-fabricated Cu–Cr–Zr alloys showed higher TC (307 W/mK) in the transverse samples compared to the vertical samples (255 W/mK) due to a stronger {110} grain texture [12]. Furthermore, the presence of thermally conductive phases within the microstructure—whether in the as-built state or after post-printing heat treatment—is crucial in L/E-PBF components for achieving excellent TC. For instance, L-PBF Cu–10Sn alloys exhibited 10-20% higher TC in the AB state compared to vacuum annealed at high temperatures (800 and 600 °C). This increase stems from the coexistence of α and δ phases. In contrast, annealing promotes the δ phase to dissolve into the α phase, resulting in a single-phase microstructure with lower conductivity [171]. Notably, solute atoms within the metal matrix hinder TC by scattering electrons. In L-PBF Cu–Ni–Sn–P alloys, thermal

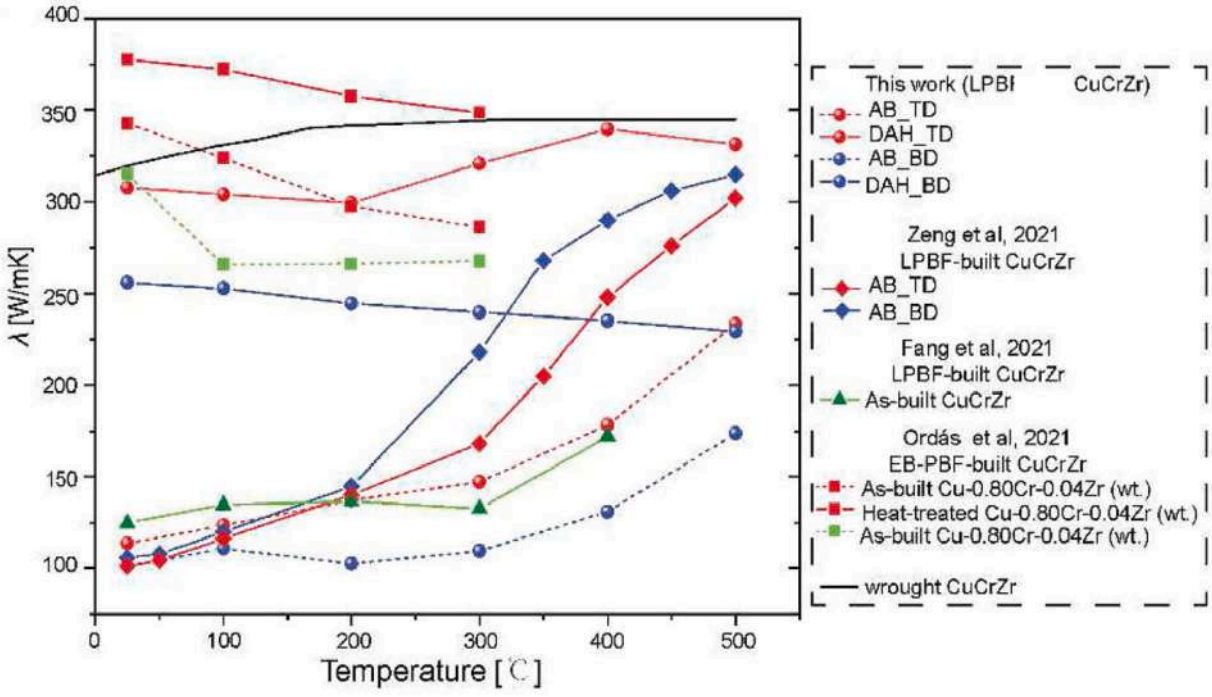


Fig. 65. Comparison of thermal conductivity between L-PBF Cu alloys and wrought alloy [12].

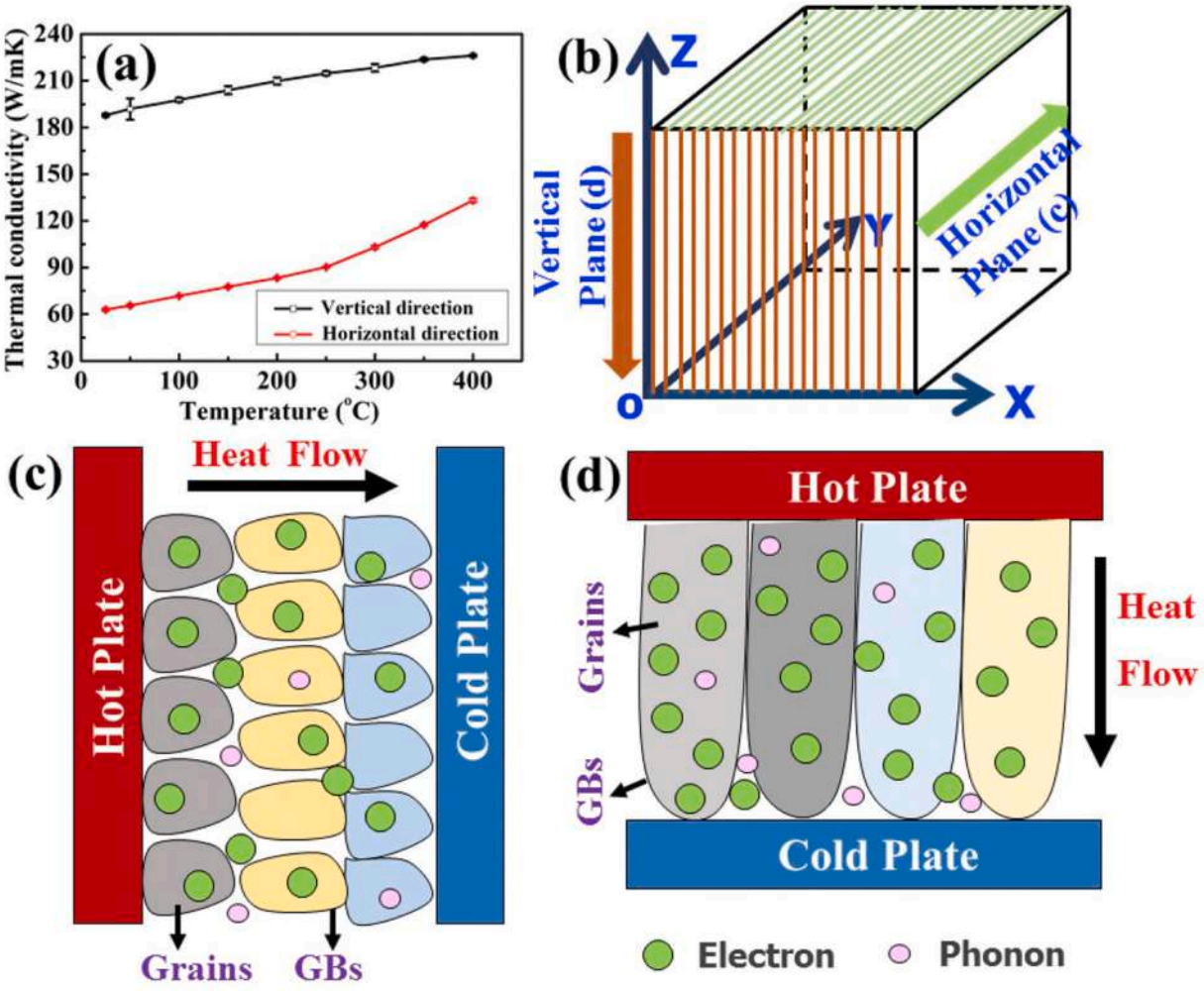


Fig. 66. (a,b) Thermal conductivity anisotropy of L-PBF Cu alloy in horizontal and vertical orientations; (c,d) Mechanism of electron and phonon transport with varied orientations [196].

conductivity was significantly enhanced by 30% after aging heat treatments (2 h) due to the depletion of Ni solute from the matrix caused by the formation of $(Cu, Ni)_3P$ precipitates (precipitates scatter free electrons less) [276]. Thus, optimising post-printing heat treatment parameters (time and temperature) offers a promising strategy for maximising TC in L/E-PBF components while maintaining mechanical properties. For example, Wallis and Buchmayr [291] demonstrated that in L-PBF Cu–Cr–Zr alloys, the SAT process prioritised conductivity (297 W/mK) at the expense of hardness (126 HV), whereas the DA treatment resulted in higher hardness (185 HV) but lower TC (239 W/mK). Although aging treatments enhance thermal conductivity, the chosen temperature and time are crucial for achieving synergy between strength, TC, and ductility. In L-PBF (green laser) Cu–Cr–Zr alloys, DA treatment at 500 °C for 1 h simultaneously improved strength, thermal conductivity, and ductility compared to the as-built state. However, prolonged aging heat treatment (2 h) resulted in a strength-ductility trade-off, whereas TC increased, and aging heat treatment at 550 °C for 1 h exhibited a strength-conductivity trade-off [261]. Another approach to overcome the strength-conductivity trade-off is to modify the alloy composition. For instance, L-PBF LaB_6–doped Cu specimens achieved a remarkable thermal conductivity of 387 W/mK and a YS 3.7 times higher than pure Cu (347 MPa), demonstrating the potential of L/E-PBF Cu alloys for components requiring both mechanical and thermal properties [71]. Furthermore, porosity in L/E-PBF Cu alloys acts as a scattering centre, impairing TC. To address this, TiB_2 additions in Cu–15Ni–8Sn alloys increased processability (with a higher density of 99.4% at a lower energy density), reduced Sn segregation, and resulted in a 12.5% increase in TC over Cu–15Ni–8Sn alloy samples [70].

Future research on L/E-PBF Cu alloys/composites should delve deeper into how process parameters induce the strength-conductivity trade-off and explore strategies to achieve an optimal synergy among strength, ductility, and conductivity. Additionally, there remains a lack of consensus regarding the high-temperature thermal conductivity behaviour of L-E/PBF Cu alloy/composite parts, necessitating a deeper exploration of temperature-dependent variations. Future research should focus on advancing the strength-thermal conductivity synergy in L/E-PBF Cu alloy/composite parts, as current compositions rarely exceed the TC of conventional materials. To enable more effective data comparisons, future research should critically evaluate the discrepancies between direct and indirect thermal conductivity measurement techniques, assessing their suitability for reporting the TC of Cu alloy/composite parts fabricated via L/E-PBF processes.

8.6. *Creep properties*

L-PBF yields a distinctive microstructure, which includes dislocation cells, precipitates, and peculiar grain morphologies, and exhibits a considerable effect on creep performance, in addition to intrinsic properties and operational conditions. Furthermore, the process-induced defects reduce the creep performance of CMMC after L-PBF processing [155]. The creep performance of the L-PBF Cu–CNT composite was location dependent, with a sharp increase in creep stress

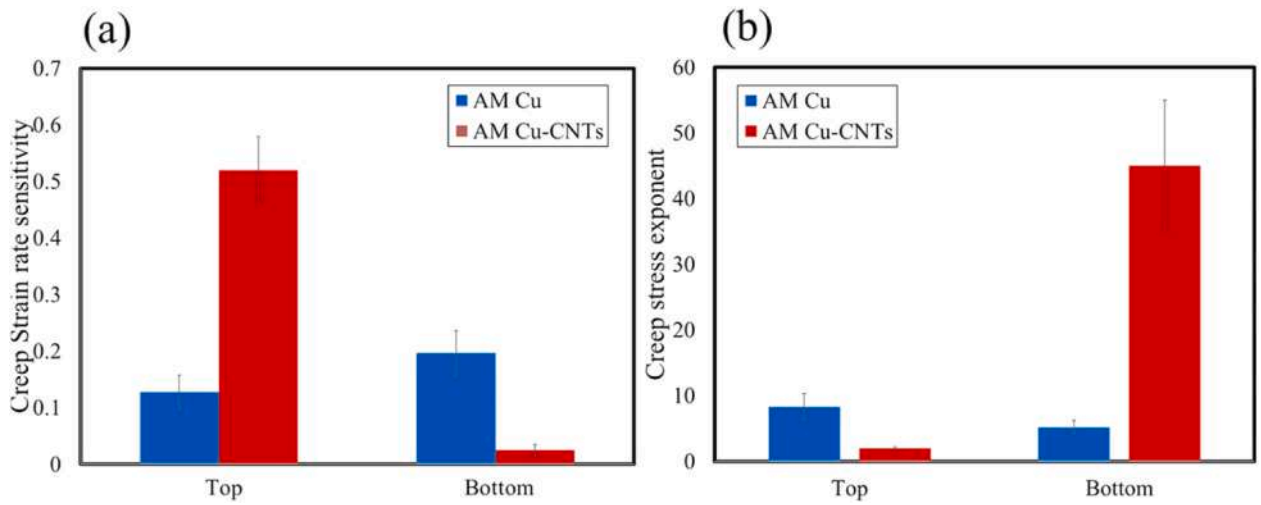


Fig. 67. (a) Variation of creep strain rate sensitivity (m) and (b) Creep stress exponent (n) with position for L-PBF Cu and Cu–CNT composite [155].

exponent value for the bottom surface of Cu–CNTs as a result of increased dislocation generation, as shown in Fig. 67. Moreover, Cu–CNTs exhibited higher creep displacement than copper due to agglomeration and higher porosity during AM [155]. Although creep-resistant Cu alloys are essential for severe environment operations like space exploration and aerospace, an understanding of high-temperature mechanical performance, specifically creep behaviour for PBF (NIR laser, green laser, blue, and electron beam) Cu alloys/composites, are scarce in the literature. Thus, this domain invites ongoing investigation.

Additionally, future research could validate the hypothesis that microstructure modifications, which alter the absolute strengthening contribution in L/E-PBF Cu alloy/composite printed parts through modification of processing parameters, feedstock selection, part geometry, and post-printing heat treatments, could overcome the limitations of conventional copper alloys for creep behaviour, as dispersion and precipitation strongly determine the creep behaviour.

8.7. *Fatigue properties*

L/E-PBF of Cu alloy/composite components is afflicted by internal defects (porosity, unmelted powder, spatter, etc.), poor surface roughness, microstructural inhomogeneity, residual stresses, and orientation-dependent properties, which may serve as stress concentrators. These stress concentrators can initiate fatigue cracks at loads well below the YS of printed parts, leading to premature failure [292]. Therefore, a comprehensive understanding of the fatigue behaviour in AMed Cu alloy/composite parts is essential to optimise their performance and reliability in advanced applications.

Post-printing heat treatments for L-PBF Cu alloy parts are the most prevalent approach to modulating their properties in order to enhance fatigue performance. Process-induced defects, particularly porosity (LoF and pores), act as stress concentrators, which lowers the fatigue strength of AB Cu–Cr–Zr alloys. However, heat treatment can partially mitigate the deleterious effects of LoF at lower strain amplitudes, though this benefit is diminished at higher strains. Regardless of heat treatment, the fatigue resistance of the L-PBF Cu–Cr–Zr alloy is compromised by LoF defects. Overall, at a 0.2% strain amplitude, heat-treated L-PBF Cu–Cr–Zr alloy outperformed the as-printed state for strain-controlled low cycle fatigue (LCF) [293]. Furthermore, with different heat treatments for L-PBF Cu–Cr–Zr alloy, ductility became more significant for fatigue resistance at higher strains, whereas hardness became more relevant at lower strains [293]. Demeneghi et al. [250] found that the fatigue life of AB GRCop–42 specimens was adversely influenced by the size effect because the incidence probability of defects varied. Thinner (1.5 mm) specimens failed faster (98,894 cycles) than thicker (2.1 mm) specimens, which lasted longer (102,312 cycles) due to 70% lower porosity, as illustrated in Fig. 68. However, after post-processing by hot isostatic press (HIP), specimens of both thicknesses surpassed the test limit (10^6 cycles) due to reduced internal porosity. Moreover, tensile samples featured slanted fracture surfaces with distinct shear lips, whereas fatigue specimens (both AB and HIP treated) exhibited flat fractures. Void coalescence (small voids merging into bigger ones) along the gauge section of both fatigued specimens revealed porosity as the limiting factor for L-PBF Cu component fatigue life. Although post-AM heat treatment improved the fatigue resistance of printed parts, its high cost, time, and limited feasibility make it impractical for L/E-PBF printed parts; hence, future studies should focus on the microstructural regulation of as-built components through in-situ treatments, etc., to improve the fatigue resistance of L/E-PBF Cu alloy/composite and determine whether the fatigue enhancement stems from AM microstructures, defect reduction, or modification of surface roughness per se.

So far, there has been a dearth of studies on the fatigue performance of L/E-PBF Cu alloy/composite parts for predicting fatigue life. The statistical estimation of the plastic strain energy method has shown the potential to predict fatigue damage in L-PBF Cu alloy at room and elevated temperatures, as demonstrated by Jirandehi et al. [294]. However, developing as-built components with superior fatigue performance, particularly compared to wrought counterparts, remains a herculean task for researchers. This complexity stems from the presence of process-induced defects, preferred anisotropy, and microstructural heterogeneity in printed parts. To enhance the understanding of fatigue and fracture behaviour in PBF (NIR laser, green, blue and electron beam) Cu alloy/composite parts, future research should focus on investigating the influence of processing parameters-microstructure nexus and the process parameters-defects nexus (pores size and distribution, residual stress, primary surface roughness via melt pool solidification, etc.). For example, how does the CET microstructural transition affect the fatigue performance of L/E-PBF Cu alloy components/lattices or copper-based multi-materials? There are numerous possibilities for investigating the impacts of post-treatment on L/E-PBF Cu alloy/composite components, with an emphasis on how surface and bulk defects affect LCF, HCF and VHCF. Another area that necessitates attention is damage tolerance analysis in the context of L/E-PBF Cu alloys/composites for fatigue crack growth (FCG). Additionally, future research is needed to quantify the corrosion fatigue coupling in L/E-PBF Cu alloy/composite parts to improve the reliability of parts in corrosive environments. Finally, fatigue life prediction for multi-material, new Cu alloy complex components, especially topologically optimised components, using ML algorithms in conjunction with numerical models, where the experimental approach is limited by time and cost, may serve

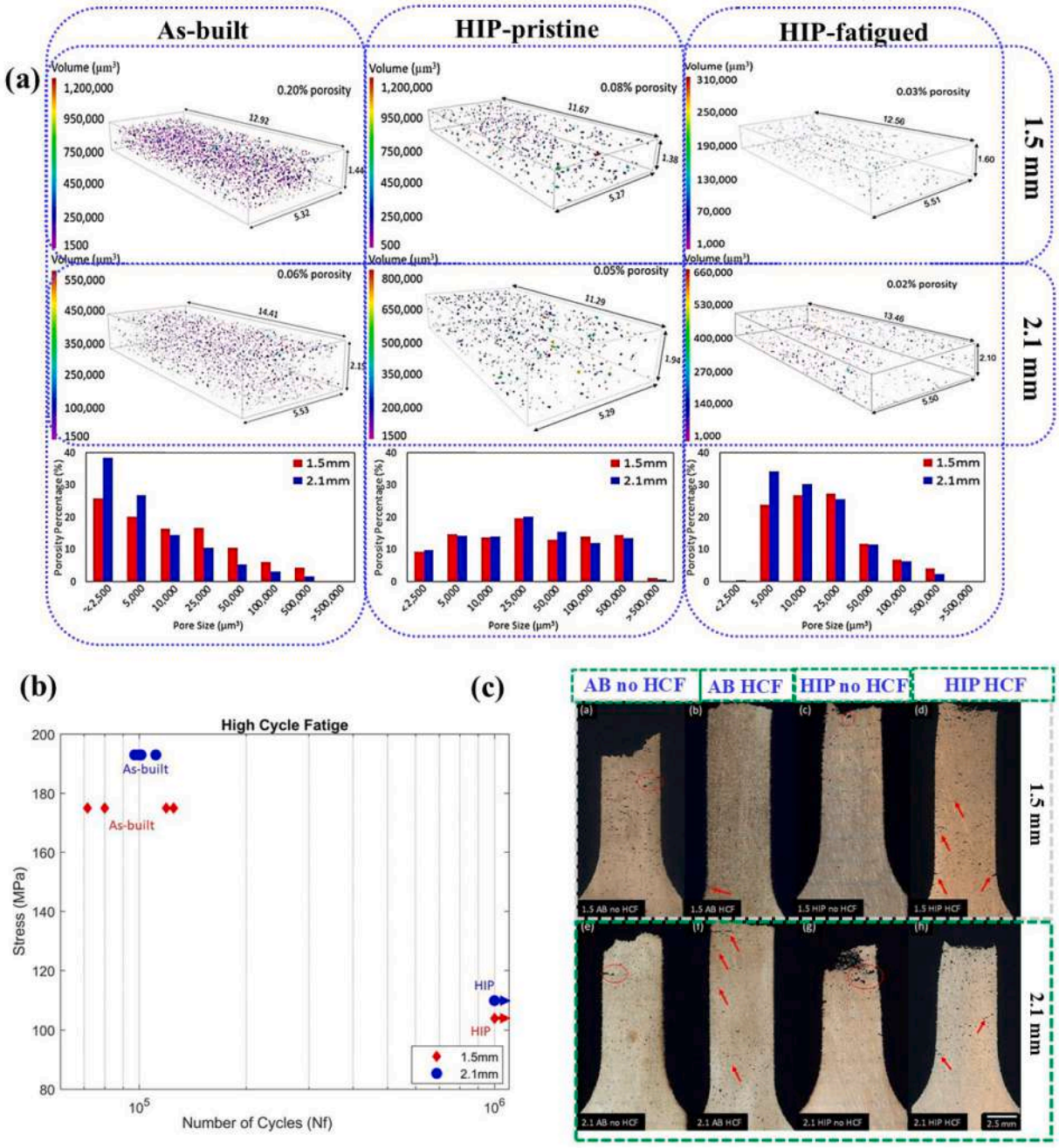


Fig. 68. (a) Porosity percentage; (b) S-N curves; (c) Fracture morphology of 1.5 mm and 2.1 mm samples under AB and heat-treated conditions [250].

as a milestone for the development of the next-generation fatigue resistant L/E-PBF Cu alloy/composite components.

8.8. Corrosion properties

Cu alloy/composite parts are popular for condenser systems, marine and offshore oil/gas devices, etc., where excellent corrosion resistance is important for safety. Typically, AM enables the formation of a peculiar microstructure with no macro-segregation in printed parts, altering the contributions of different phases and, consequently, modifying the galvanic and intergranular corrosion tendencies of Cu alloys [171]. Furthermore, the presence of metallurgical porosities (pores, LoF, etc.) impairs the corrosion resistance of L-PBF or E-PBF Cu alloys (as preferential sites for corrosion) by altering corrosion initiation and propagation, which can be caused by inadequate laser reflectivity, untuned process parameters, printing system variables, and post-printing heat treatments as previously described. Thus, AM technology can yield corrosion-resistant components for specific applications by analysing the microstructure-corrosion link and optimising L/E-PBF process parameters. So far, corrosion research on L-PBF or E-PBF Cu alloys has primarily used immersion tests, electrochemical tests, and passive film characterisation techniques such as Mott-Schottky (M−S) analysis, electrochemical impedance spectroscopy (EIS), and X-ray photoelectron spectroscopy (XPS) to examine the effects of PSD, heat treatment, elemental segregation, and build orientations, etc. Liu et al. [295] noticed anisotropic corrosion in L-PBF Cu–30Ni alloys. After 1200 seconds, the X-Z plane exhibited lower current density (I-t plot shown in Fig. 69) and a higher capacitance arc radius (EIS plot shown in Fig. 69) compared to the X-Y plane, confirming superior corrosion resistance. This noteworthy corrosion behaviour caused by Cu_2O layer formation is

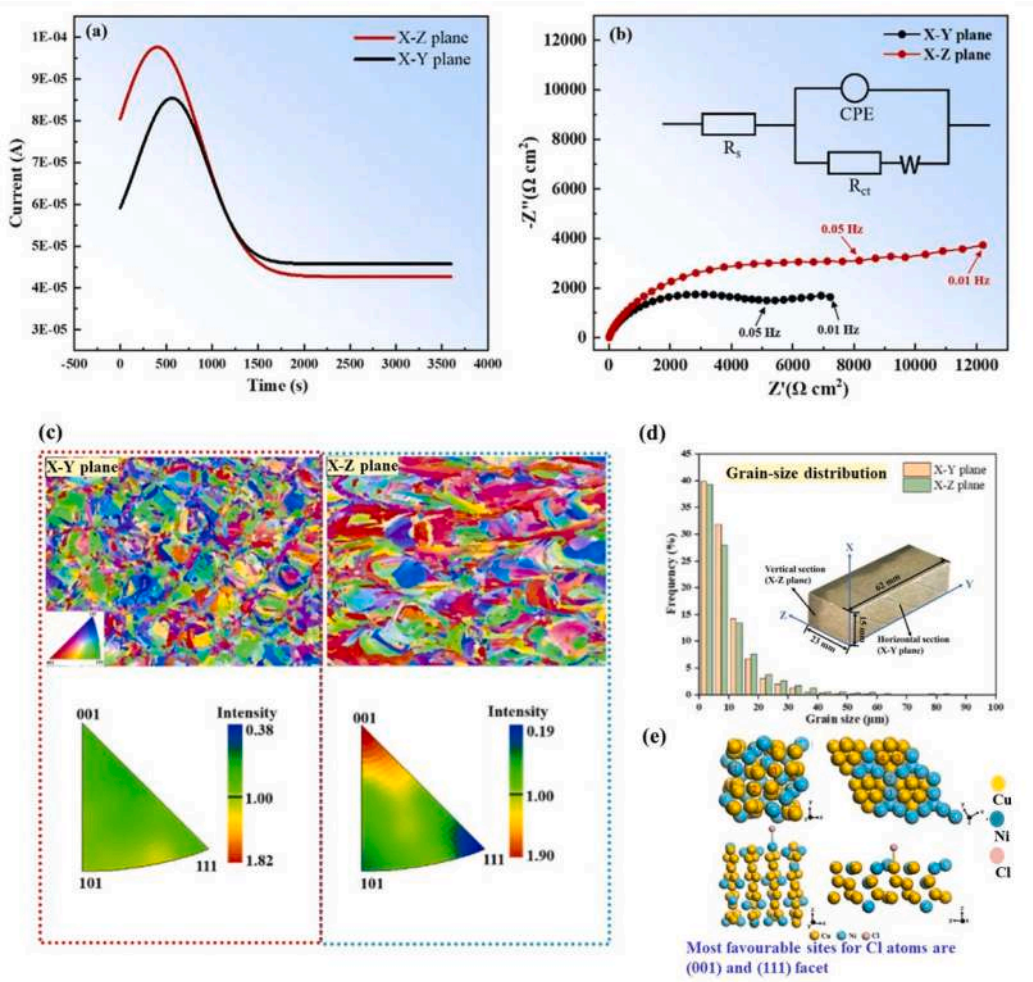


Fig. 69. (a) I-t curve at −0.1 V; (b) Nyquist plots with equivalent circuit model; (c) Inverse pole figure (IPF); (d) Grain size distribution; (e) Mechanistic diagrams of three adsorption sites for L-PBF Cu–30Ni alloy [295].

related to the strong texture of the X-Z plane for (001), which strongly adsorbed Cl^- (essential for Cu_2O formation) due to lower adsorption energy compared to (111). While grain size analysis (refer to Fig. 69) revealed no significant difference between the X-Y and X-Z planes of the L-PBF Cu–30Ni alloy specimens, indicating that anisotropic corrosion behaviour can be adjusted by tweaking the texture during L-PBF and E-PBF. L-PBF Cu–3Ni–1Si samples showed promising corrosion resistance in marine conditions, especially vertical orientations, according to Jóźwik et al. [103]. Although vertical samples showed the lowest current density and maximum potential (favourable trends for corrosion resistance) irrespective of VED, their corrosion rates were not substantially distinct from horizontal samples (4.3 μm/annum). Overall, Cu–3Ni–1Si alloys demonstrated superior corrosion resistance to previously reported L-PBF Cu–10Sn alloys. Zhai et al. [136] utilised two methods to achieve a passive film over E-PBF NAB alloy samples with varying PSD distributions: S-NAB (45–63 μm), M-NAB (63–75 μm), and L-NAB (75–105 μm), as well as for the cast alloy: potential-dynamic polarisation (± 300 mVOCP) and immersion in 3.5 wt.% NaCl. Short-term potential-dynamic polarisation tests (7 days) favoured the M-NAB alloy due to 35% higher resistance (larger Nyquist arc, higher impedance modulus, and higher phase angle as shown in Fig. 70) than as-cast NAB alloys, suggesting superior corrosion behaviour. Similarly, long-term immersion (21 days) revealed better overall corrosion resistance for all E-PBF variants (including M-NAB) compared to as-cast NAB, with M-NAB exhibiting minimal pitting (best performance among E-PBF samples). This superior corrosion behaviour is attributed to less severe selective phase corrosion observed on the E-PBF NAB samples (refer to Fig. 70) and influenced by the presence of distinctive microstructural phases, excluding the β′ phase, which is susceptible to corrosion. PSD variation also altered NiAl phase distribution, while M-NAB precipitate phases are uniform. Interestingly, the homogeneous distribution of phases reduced galvanic corrosion. This underscored the importance of PSD of feedstocks in L/E-PBF for fabricating components with superior corrosion resistance, as well as the critical role of test duration in accurately assessing corrosion resistance in NAB samples through corrosion testing. While short-term tests (below seven days) might indicate lower current density for the as-cast sample, these results can be misleading. An additional benefit of E-PBF is that it is not governed by the reflectivity challenges of Cu-based feedstocks, which results in high component density; otherwise, porosity could accelerate pitting. Zeng et al. [171] observed that heat-treated specimens improved corrosion resistance (lower current densities in the potentiodynamic polarisation test (PP) compared to the AB Cu–Sn alloy). The finer grain size, which causes intergranular corrosion, and the two-phase structure, which promotes galvanic corrosion, render the AB specimen (Cu–Sn alloy) more susceptible to corrosion than the heat-treated specimen. Similarly, heat treatment improved the corrosion resistance of L-PBF silicon brass (higher corrosion potential) in saltwater (3.5% NaCl solution) due to improved microstructure homogeneity, Σ3 grain boundaries, and reduced internal defects (Fig. 71). Specifically, heat treatment increased Σ3 grain boundaries (Fig. 71), which have anti-corrosion properties, interrupting corrosion pathways and being beneficial to enhancing the

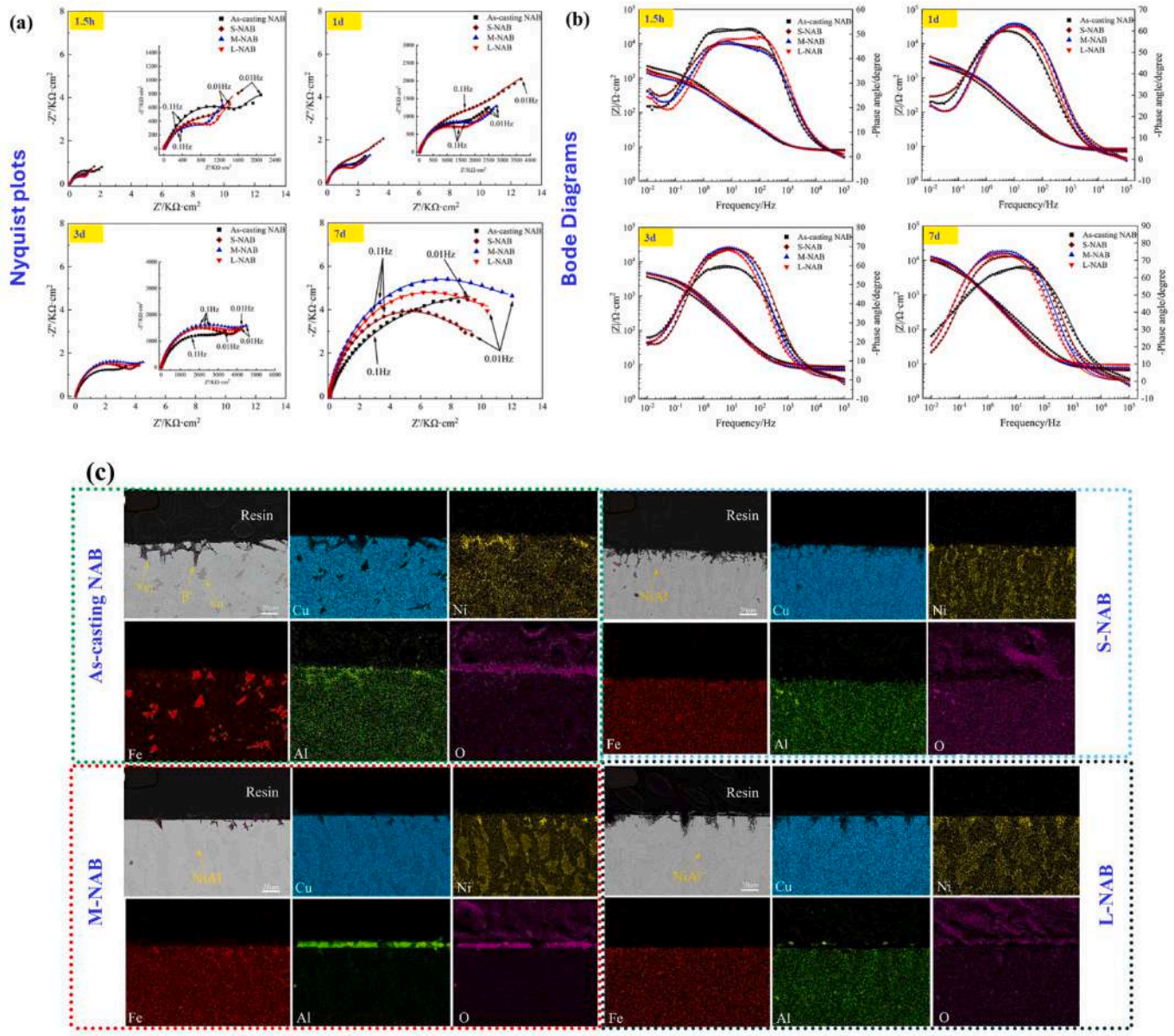


Fig. 70. (a) Nyquist plots; (b) Bode plots of NAB alloy and a cast alloy in 3.5 wt.% NaCl solution for 1.5h, 1 day, 3 days, and 7 days; (c) Cross section after 21 days immersion test [136].

corrosion behaviour of Cu alloys [153]. Contrary to expectation, L-PBF as-built NAB alloy outperformed heat-treated samples in corrosion resistance due to a synergistic effect. Higher Al and Ni contents, homogeneous microstructures, martensite nano-twins, and higher residual stresses all contributed to the formation of a stable corrosion film on the as-built L-PBF NAB alloy samples [234]. This suggested that AMed NAB alloy components for corrosion applications might be usable immediately after printing without the need for the additional time and energy consumption associated with heat treatment. However, the microstructure of the NAB alloy exerted a noticeable effect on localised corrosion. The presence of partially spheroidized κ_{III} impeded microgalvanic attack, thus providing the heat-treated NAB alloy with enhanced resistance to localised corrosion [234]. Thus, the optimisation of the corrosion performance of L-PBF Cu alloy parts is contingent upon the microstructure management of printed parts. The lower negative corrosion potential observed in the L-PBF Cu–15Ni–8Sn alloy specimen during the PP test indicated superior corrosion behaviour compared to the cast alloy and EIS, which further corroborated the PP results. The charge transfer resistance (R_{CT}) increased from 8 kΩ cm^2 (after three days) to 16 kΩ cm^2 (after seven days), indicating the surface of the alloy developing a protective oxide film. The existence of nanoscale tin segregation triggered by L-PBF near melt pool boundaries is responsible for the formation of a protective film that enhances the corrosion resistance of the printed Cu alloy parts [204]. Similar corrosion behaviour was observed in the wrought counterparts of the L-PBF C63000 (Cu–10.2Al–4.8Fe–5.0Ni–0.2Si) and C95800 (Cu–9Al–4Fe–4.6Ni–1.9Mn) NAB alloys [119].

The majority of research on L-PBF Cu alloys has focused on short-term corrosion testing under chloride conditions. However, corrosion is a complex phenomenon influenced by the material and its surrounding environment (system property); thus, testing in a variety of environments could enhance the applicability of the findings. As evidenced by prior studies, short-term tests may be misleading, potentially underestimating the true vulnerability of L/E-PBF Cu alloys/composite parts to corrosion characteristics if performed over a limited timeframe. Furthermore, there is a lack of long-term corrosion studies on L/E-PBF Cu alloy/composite parts. Long-term immersion experiments in diverse environments (altering electrolytes and modifying pH levels)

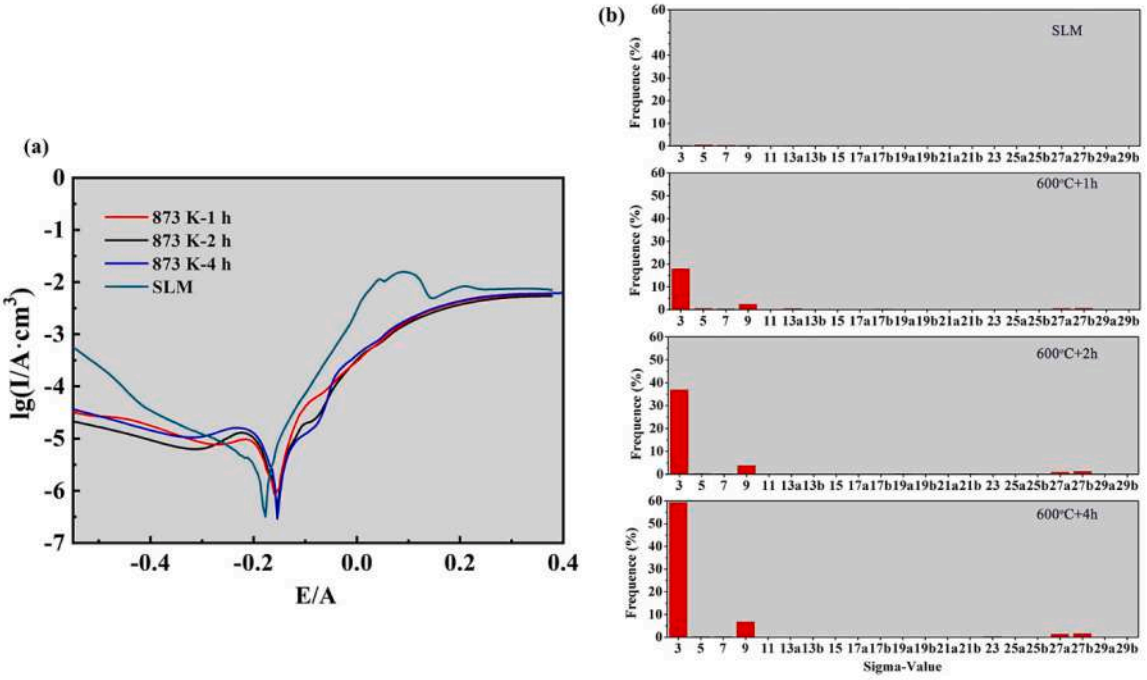


Fig. 71. (a) Potentiodynamic polarisation curves; (b) Distribution of Σ3 grain boundaries for L-PBF silicon brass and heat-treated samples in 3.5% NaCl [153].

present an opportunity for further research. This comprehensive approach will provide a deeper understanding of L/E-PBF Cu alloy corrosion behaviour in real-world conditions. However, only a few corrosion studies have been conducted on L/E-PBF Cu alloys, with most focusing on intergranular corrosion, galvanic corrosion, and pitting. The process-microstructure nexus significantly influences defect susceptibility, multi-scale microstructures, MPB, surface roughness, and part anisotropy, ultimately affecting localised corrosion, pitting, intergranular corrosion (IGC), crevice, etc., and corrosion behaviour. Further research should focus on examining the process-microstructure-corrosion nexus of L/E-PBF Cu alloys/composites/multi-material, as well as exploring modifications to energy sources (green, blue, electron beam, hybrid). Cu alloys are particularly sensitive to crevice corrosion when not cathodically protected, and hot corrosion, fretting corrosion, corrosion fatigue, and erosion corrosion should be studied further to understand the kinetics of corrosion propagation [296]. Additionally, the lack of standardised ASTM guidelines for AMed Cu alloy parts remains a significant barrier to consistent data benchmarking and comparison. Future work should prioritise the development of standardised protocols to address this discrepancy.

8.9. Tribological performance

The durability of an AMed component where failure related to friction and wear, for example, fretting wear, is dominant for NAB alloy propeller hub bearings in marine environments depends on the evaluation of the tribological characteristics of Cu alloy parts produced via L/E-PBF [297]. As previously stated, the microstructure and inherent process-related defects of printed parts are influenced by the L/E-PBF process parameters, post-AM heat treatment, and feedstock characteristics, which consequently regulate the material properties, surface morphology of printed parts and ultimately modulate the tribological behaviour. E-PBF NAB alloy parts demonstrated outstanding wear resistance, outperforming hot-rolled by 60%, while maintaining a constant friction coefficient. Notably, wear increased from 2.1 to 9.8 × 10^7 μm^3 with load (43 to 106 N) [298]. It deduced that the AM method paves the way for the development of Cu-based alloys/composites that exhibit

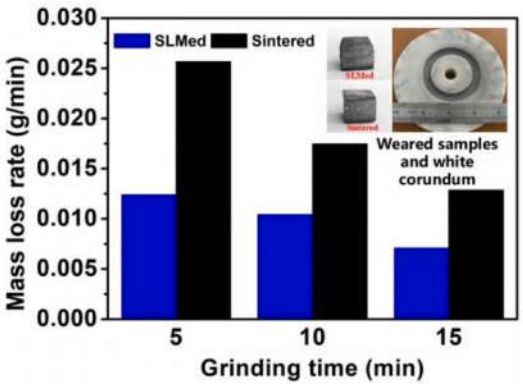


Fig. 72. Comparison of wear resistance between L-PBF Cu–Sn–Ti alloy and sintered alloy [226].

superior mechanical behaviour and high wear resistance. Gan et al. [226] found that grain refinement during rapid solidification increased Vickers hardness (258 ± 24 HV to 302 ± 15 HV) and rendered L-PBF Cu–Sn–Ti alloy samples superior in wear resistance compared to sintered samples, as shown in Fig. 72. Additionally, increased grinding time improves wear resistance through work hardening of metal matrix owing to lattice distortion. Moreover, variable cooling rates produced different grain morphologies (columnar, cellular, equiaxed) in L/E-PBF Cu alloy/composite parts, which influence wear behaviour. Equiaxed grains exhibited high wear resistance (low wear depth) and a high coefficient of friction (CoF), whereas cellular and columnar grains displayed lower wear resistance (higher wear depth) and lower CoF [280]. Also, the coefficient of friction varied by grain morphology and defect presence, with defect-free regions showing higher CoF, suggesting increased resistance to deformation. Fig. 73 shows material fragments are removed rather than nano-sized debris in columnar grains during indenter movement. This implies that the grain morphology and the presence of process defects in L-PBF components have an impact on the wear mechanism and debris formation. In a recent study on the L-PBF

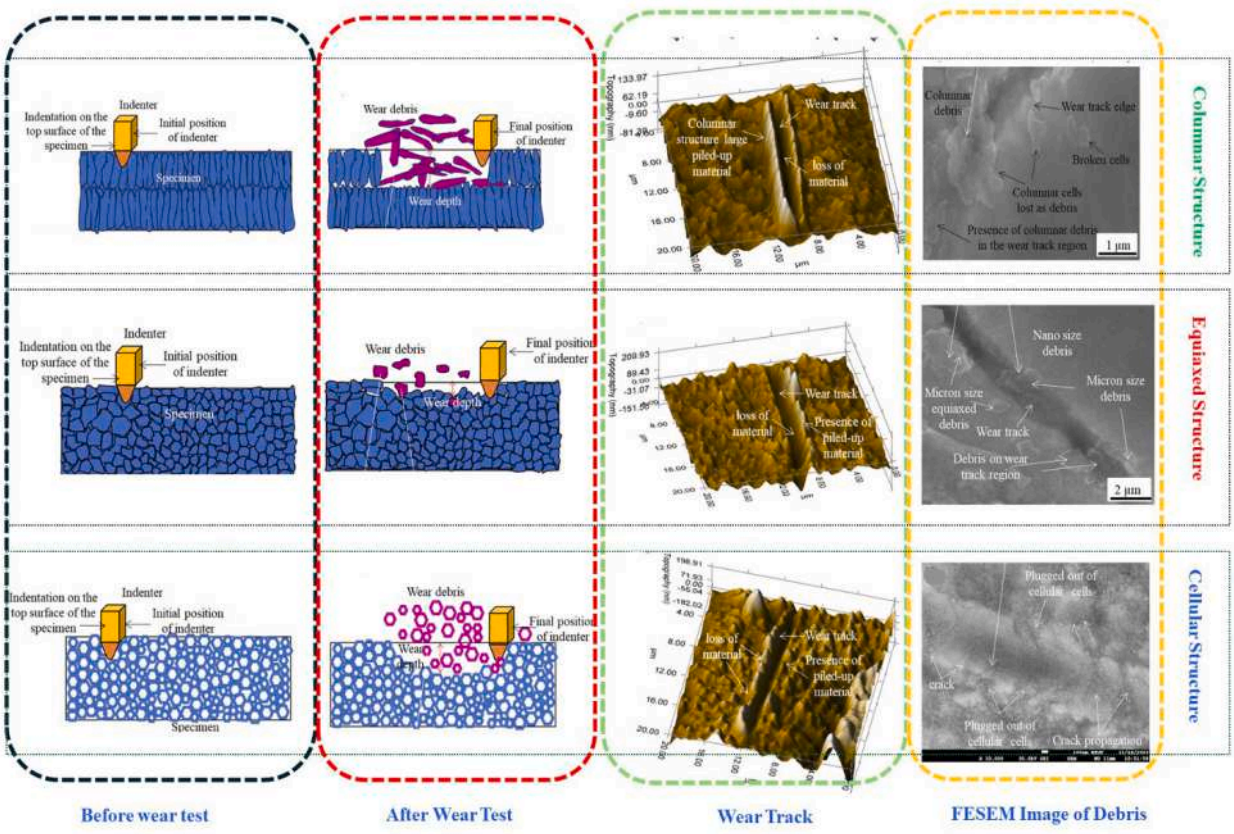


Fig. 73. Variation in wear mechanism from columnar, equiaxed and cellular microstructure under a 500 μN load [280].

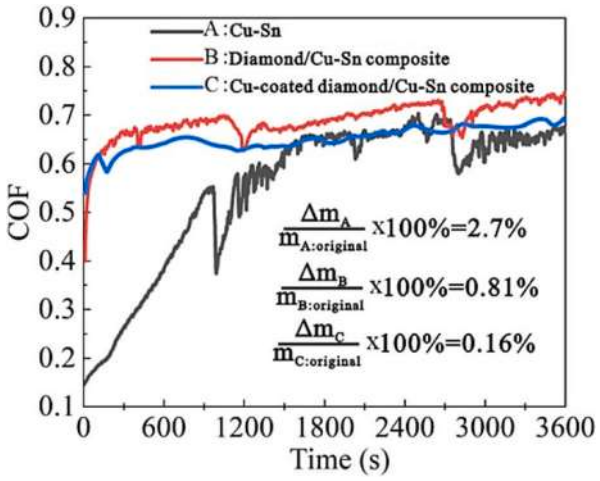


Fig. 74. Variation in friction and wear performance of Cu–Sn alloy, diamond/Cu–Sn composite, and Cu–coated diamond/Cu–Sn composite [299].

diamond/Cu–Sn composite, the presence of Cu–coated diamond particles in the Cu–Sn alloy matrix significantly enhanced wear resistance, as evidenced by lower mass loss and stable friction behaviour (as shown in Fig. 74). Importantly, friction-induced wear mechanisms, including adhesive, abrasive, and fatigue wear, are influenced by bonding strength, defects, and microstructural features, affecting CoF stability and material degradation of the L-PBF Cu–Sn-based composite [299]. Zeng et al. [300] highlighted that the enhanced wear resistance of L-PBF Cu–Fe–P alloys is attributed to Fe-rich phases; however, the tribological behaviour fluctuated with rising current, which altered wear mechanisms from abrasive and adhesive to arc erosion and oxidative wear.

Consideration of tribological parameters, in addition to process parameters and alloy composition, is critical for understanding the wear behaviour of L/E-PBF Cu alloy/composite parts. The inverse trends in the nanoindentation hardness and wear of L-PBF Cu–Cr–Zr alloy indicate that the indexing parameters H/Er and H^3/Er^2, which are typically used for wear resistance in conventional processes, are inappropriate for AMed components with low pitch values [281]. However, systematic investigations are required to establish conclusive findings, as the current literature on the tribological behaviour of L/E-PBF Cu alloys/composite remains scarce. Notably, blue laser-printed Cu parts showed surface roughness variations compared to NIR laser, indicating future research should investigate the impact of energy sources on the tribological performance of L/E-PBF Cu alloys/composites. Moreover, microstructural anisotropy, defect propensity, and distribution in the printed component varied depending on the geometry of the parts. Consequently, it is noteworthy to investigate the correlation between build orientation, geometry (shape, size effect), and tribological performance in L-PBF Cu alloy/composite parts, which remains unclear. Additional research is required to examine the efficacy of friction and wear under various tribological components, with a focus on the system-dependent aspect of tribology (wear and friction) considering normal load, sliding speed temperature (room temperature and high temperature), and different environments (dry and wet etc.). In addition to optimising process parameters and tribological variables, future research should explore post-processing methods to enhance the tribological performance of L/E-PBF Cu alloy/composite parts. This can be accomplished by establishing a correlation between the microstructure, surface roughness, and tribological performance of the L/E-PBF copper matrix composites, Cu-BMGs, Cu–Cr–Zr, Cu–Cr, Cu–Ni–Sn, etc., and the variables of post-AM heat treatment and post-processing methods. Finally, it is essential to comprehend various wear mechanisms in order to design wear-resistant components that are anticipated to be required

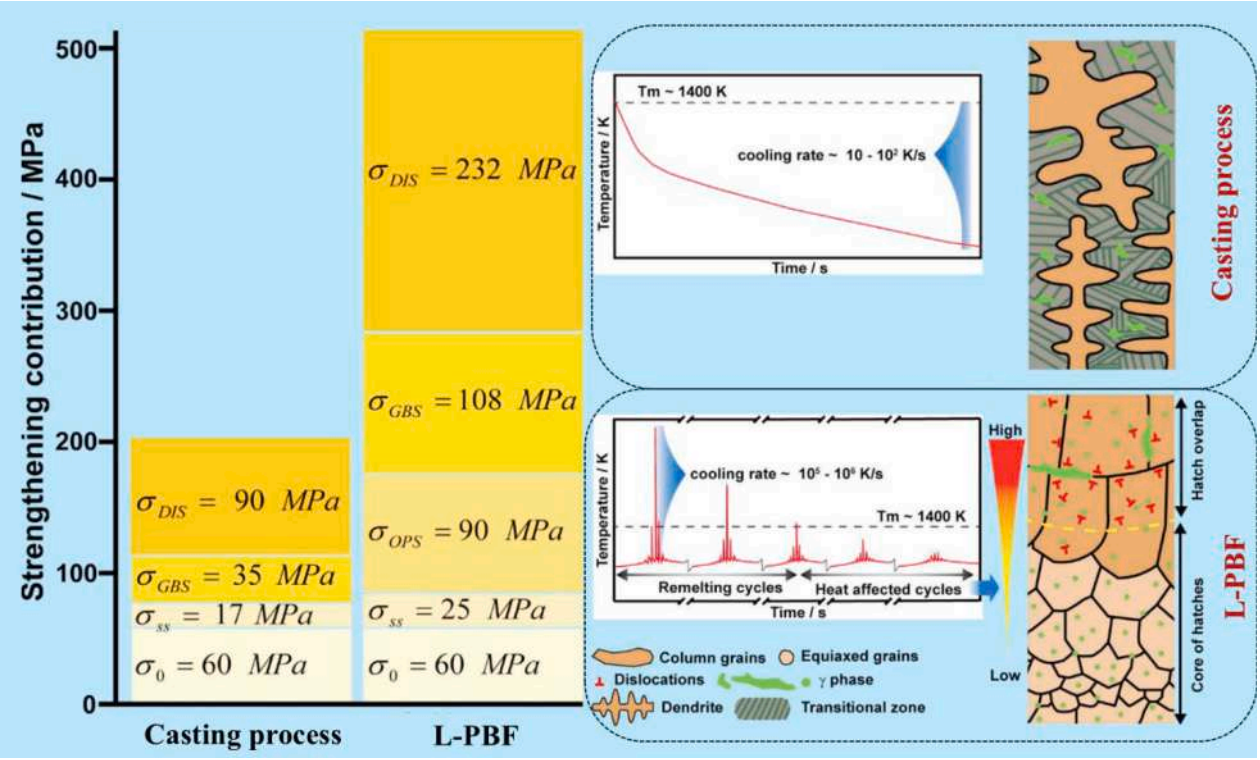


Fig. 75. Comparison of absolute strengthening contributions to the YS during AM and conventional processing [238].

in next-generation applications. Overall, the L/E-PBF of Cu-based alloy/composite shows promise for the development of wear-resistant parts with complex geometries, such as bearings and contacting parts. However, achieving mechanical-tribological performance synergy to improve performance, safety, and reliability requires process parameter optimisation, microstructural control, surface modifications, environmental awareness, and strategic feedstock selection.

9. Strengthening mechanism

Research indicates that solid solution strengthening (SSS), grain boundary strengthening (GBS), Orowan precipitation strengthening (OPS), and dislocation strengthening (DS) are the primary mechanisms contributing to the YS of Cu alloys fabricated using L-PBF and E-PBF [109,112,238,261,262,301]. However, the relative contributions of each mechanism may differ from those produced by conventional methods (casting) owing to the microstructural state, as shown in Fig. 75.

9.1. Grain boundary strengthening

Grain boundaries act as obstacles to dislocation movement. L/E-PBF Cu alloys show finer grains compared to conventional manufacturing due to rapid cooling, resulting in an increased fraction of grain boundaries and a higher contribution to GBS compared to casting (Fig. 75, GBS 208% higher for the printed part compared to the cast counterpart). Aside from the cooling rate, the grain size in L/E-PBF Cu alloys is transformed by alloying elements. For example, in the L-PBF Cu–Cr–Zr–Y_2O_3 alloy, Y_2O_3 doping refines the grains to 13.1 μm (vs 28.9 μm for Cu–Cr–Zr alloys) through Zener pinning, contributing 11% to overall strengthening via GBS [110]. Further, research suggests that pro-peritectic phases (1-2 μm average grain size) are more effective than L/E-PBF (49.7/14.7 μm average grain size) or Zener pinning (13.1 μm average grain size) in providing high-strength L/E-PBF Cu alloys through GBS [26,29,110,120]. Similarly, the Cu–15Ni–8Sn alloy contributed 19%, and the Cu–Cr–Zr alloy contributed 6.67% to YS in AB samples [131,261]. Beyond improving YS/UTS and hardness, the high fraction of grain boundaries resulting from grain refinement also increased ductility by delaying necking for L-PBF Cu–Co, Cu–Cr–Zr doped Y_2O_3 [29,110]. However, the fine grain boundaries in L-PBF Cu alloys moderately reduced conductivity due to electron scattering, though this decrease was less pronounced than the significant drop caused by SSS [45]. Therefore, GBS efficiently balances the strength-ductility synergy (by Hall–Petch effect) in L-PBF Cu alloys, with a negligible influence on electrical conductivity, compared to alternative strengthening strategies (such as SSS). In L-PBF Cu alloys, heat treatment of as-built samples and samples with varying wall thickness showed no significant change in the contribution of GBS (variation mostly below 8% relative to the AB state), as there was no significant variation in grain size (12.03 μm to 11.24 μm for LPBF and heat-treated samples, respectively) [113,199,261,286]. Printing parameters also contributed to the grain refinement of printed Cu alloys; increased laser power during printing resulted in finer grain structures, further contributing to GBS [254]. Overall, the contribution of GBS in L-PBF Cu alloys can be modified through strategic alloy design (pro-peritectic phase-based alloys Cu–Co, Cu–Fe for high nucleation rate), secondary particle reinforcement (Zenner pinning Y_2O_3), and L/E-PBF process parameters (alter thermal gradient (G), solidification rate (R), Δ T) for tailored microstructures. This modification typically enhances the YS of L-PBF Cu alloys/composites by up to 20%, with most cases showing an increase of less than 10% after heat treatments.

The Hall-Petch relation assessed the YS contribution for L/E-PBF Cu alloys/composites using the following equations (Eqn 9.1 and 9.2) [238,302,303].

$$\sigma_{GBS} = \frac{k}{\sqrt{d}} \tag{9-1}$$

$$\sigma_{GBS} = k\left[V_f d_f^{-1/2} + V_c\, d_c^{-1/2}\right] \tag{9-2}$$

where k is the Hall-Petch constant related to the type of alloy, d is the

average grain size, d_f and d_c are fine and columnar average grain sizes, respectively, measured by EBSD/TEM, and V_f and V_C are their volume fractions. However, the literature reported a wide range of values for the Hall-Petch constant (ranging from 110 to 180 MPa $\sqrt{\mu m}$ for Cu–Cr–Zr [113,199,262]), emphasising the absence of a definitive consensus.

9.2. Solid solution strengthening

The solute atoms dissolved (Al, Ni, Mn, etc.) in the Cu matrix form a solid solution. The size mismatch between the matrix and the solute atoms induces localised strain fields and distorts the Cu lattice. This deformation generates a stress field that restricts dislocation mobility, resulting in SSS. The computation is performed using the following equations (Eqn 9.3, 9.4, 9.5, 9.6, 9.7 and 9.8) (Fleischer equation) [304,305].

$$\sigma_{ss} = \sum \frac{M\tau}{700}\varepsilon_{ss}^{3/2}\sqrt{c} \tag{9-3}$$

$$\varepsilon_{ss} = \left|\varepsilon_G^{'} - \beta\varepsilon_b\right| \tag{9-4}$$

$$\varepsilon_G^{'} = \frac{\varepsilon_G}{1 + 0.5|\varepsilon_G|} \tag{9-5}$$

$$\varepsilon_G = \frac{1}{\tau}\frac{d\tau}{dc} \tag{9-6}$$

$$\varepsilon_b = \frac{1}{a}\frac{da}{dc} \tag{9-7}$$

$$\tau = \frac{E}{2(1+\mu)} \tag{9-8}$$

Where M is the Taylor factor (3.06 for FCC materials), τ is the shear resistance of the matrix, E is the Young's modulus, μ is the Poisson's ratio of Cu, ε_{ss} is the strain resulting from the Cu lattice distortion, ε_G and ε_b are the shear modulus and lattice mismatch coefficient, respectively. c represents the solution concentration (atomic fraction), β is a geometric constant (β=3) [304] and a is the lattice parameter of the α-Cu phase in L/E-PBF samples. However, for accurate SSS calculations in L/E-PBF, EBSD-derived Taylor factors should be used due to textural differences (L-PBF Cu–Ni–Sn: 3.10, Cu–Ni–Sn+TiB_2: 3.03 or 2.53) in L/E-PBF Cu alloys [70]. Overall, the solubility limit of alloying elements, their concentration, and atomic radius relative to the Cu matrix govern the SSS contribution.

The SSS contributions to the YS of the cast alloy (8.5% SSS) and L-PBF Cu alloy (5% SSS) are similar, as shown in Fig. 75 [238], though SSS can reach up to 55%, as reported for L-PBF Cu–Ni–Sn alloys [148]. While SSS increases YS/UTS, it impairs the ductility and electrical conductivity of L/E-PBF Cu alloy/composite parts. In L-PBF Cu alloys, SSS contributes more significantly to the reduction of electrical and thermal conductivity than other mechanisms, such as precipitation, dislocations, and grain boundaries, as solute atoms scatter electrons extensively [45]. Li et al. [262] observed a strength-conductivity trade-off in Cu alloys, where a high SSS contribution (~14%) resulted in substantial electron scattering (poor conductivity 19.1% IACS). However, after DA treatment, precipitation significantly reduced electron scattering (<1.5%), leading to increased conductivity (65.1% IACS). Furthermore, rapid solidification in L-PBF Cu alloys inhibits atomic diffusion in both liquid and solid phases, irrespective of element solubility. This leads to solute trapping, causing supersaturation of the α-Cu matrix. Extended solubility (solute trapping) in Cu alloys provides both SSS in as-built parts and precipitation strengthening (nano-precipitates) during post-printing heat treatments. In the L-PBF Cu–13Sn alloy, the high Sn content (6.2 wt%, exceeding the equilibrium solubility of 1.3 wt%) remained in the α-Cu matrix after printing, leading to lattice distortion due to the larger Sn atoms (225 pm vs. 128 pm for Cu). This excess Sn persisted in the α-Cu matrix after heat treatment due to the sluggish precipitation behaviour of the Cu–Sn alloy, potentially impairing its conductivity. To mitigate the solute trapping effect on conductivity, ceramic particles such as LaB_6, Y_2O_3, and TiB_2 have been incorporated in L/E-PBF Cu alloys/composites [70,71]. Therefore, the detrimental effects of solute entrapment on the strength-conductivity nexus can be minimised by using low-solubility alloying elements (such as Zr, Ag, ceramics, and carbon) in optimal quantities or by selecting them based on their propensity to precipitate within the α-Cu matrix. Overall, SSS contributes positively to strength and hardness, but it leads to reduced ductility and conductivity in printed parts. These negative effects can be largely eliminated through appropriate post-printing heat treatments.

9.3. Orowan precipitation strengthening

Orowan precipitation strengthening (OPS) manifests in L/E-PBF Cu alloys due to the impediment of dislocation motion by dispersively distributed precipitates and ex-situ particles (<500 nm). The dominant strengthening mechanism—dislocation shearing or looping—is dictated by the size and strength of these particles. Dislocation shearing typically occurs in the presence of fine, low-strength precipitates, while dislocation looping becomes prevalent when dislocations encounter larger, non-shearable, and incoherent particles, leading to enhanced strengthening [70,262]. The Orowan-Asbhy equations (Eqs. (9.9)–(9.12)) were used to calculate the contribution of OPS to the overall strength using the following set of equations [306,307].

$$\sigma_{OPS} = \mathrm{M}\tau_p \tag{9-9}$$

$$\sigma_{OPS} = \mathrm{M}\tau_p = \frac{0.40M\tau b}{\pi(1-\mu)^{0.5}}\frac{ln\left(\frac{2r_{mp}}{r_c}\right)}{\delta} \tag{9-10}$$

$$\delta = r_p\left(\frac{2\pi}{3f_p}\right)^{0.5} - 2r_p\sqrt{\frac{2}{3}} \tag{9-11}$$

$$r_{mp} = r_p\sqrt{\frac{2}{3}} \tag{9-12}$$

where M is the Taylor factor, τ_p is the precipitate shear stress, τ is the shear modulus of the Cu matrix, b is the magnitude of the Burgers vector of the Cu matrix, μ is the Poisson ratio of Cu, r_{mp} is the mean radius of a circular cross-section in a random plane for a spherical precipitate, r_c is the dislocation core radius (= b: approximating the dislocation core radius to the Burgers vector) [301], r_p is the average radius of the precipitate, δ is the edge-to-edge inter-precipitate spacing, f_p is the volume fraction of the precipitate. The efficiency of OPS is determined by characteristics such as the size, shape, crystal structure, volume fraction, distribution, and strength of the precipitates (are regulated by heat treatment time and temperature, part geometry, etc.) as well as the size and shape, amount, and distribution of ex-situ hard particles.

In L-PBF fabricated Cu–15Ni–8Sn alloys, fine precipitates (80 nm) formed during intrinsic heat treatment (IHT) contribute significantly to OPS contribution (90 MPa), whereas the cast alloy exhibited minimal strength from coarse particles (>10 μm) in the cast alloy, as indicated in Fig. 75 [238]. Notably, in the L-PBF Cu–Ni–Sn alloys, OPS contribution has been reported to reach approximately 83% [148]. Moreover, the literature indicated that in-situ precipitation strengthening depends on feedstock composition, highlighting the importance of careful alloy selection to eliminate the need for additional post-printing heat treatments. For instance, during L-PBF of Cu–1.8Cr–1Nb–2Fe alloys, in-situ Nb(FeCr) core-shell nano-precipitates (~24 nm) served as the dominant strengthening mechanism in the as-built state (>55%) and retained their effectiveness even after heat treatment due to their exceptional coarsening resistance (~29 nm) [113]. Recent research on developing HSHC and HSMC alloys within the L/E-PBF Cu family predominantly explores the integration of precipitation strengthening with complementary

mechanisms to tailor microstructure and achieve an optimal synergy of strength, electrical conductivity, and ductility. Beyond enhancing strength, OPS facilitated the development of Cu alloys with high electrical conductivity (78% vs. 30% IACS) by precipitating elements from the supersaturated matrix (because lattice distortion caused by supersaturation increased electron scattering) [261]. Consequently, OPS served as an effective approach for designing HSHC Cu alloys, addressing the traditional strength-conductivity trade-off. While OPS offered strength-conductivity synergy with minimal plasticity loss, optimising post-printing heat treatments remained essential for achieving the best strength-ductility-conductivity trifecta. For instance, a study by Li et al. [262] demonstrated that switching from ST to DA treatment in L-PBF Cu–Cr–Zr alloys significantly increased the OPS contribution (from 50 to 70% to YS) due to the formation of finer, more uniformly distributed Cr precipitates. Additionally, process parameters influenced OPS: Li et al. [252] identified that increasing scanning speed (from 500 to 1100 mm/s) reduced precipitate size (from 50 to 28 nm) in L-PBF Cu–Cr–Nb–Ti alloys. Conversely, increasing the laser power from 300 to 400 W resulted in larger precipitates (from 30 to 50 nm) due to larger melt pools and heat-affected zones at higher power levels (more time for growth due to different thermal histories) [252]. Furthermore, E-PBF Cu alloys revealed precipitates with core-shell morphology (Fig. 11) that were not present in wrought alloys and showed the potential to disrupt the strength-ductility trade-off as well as an isotropic behaviour [23]. Additionally, part geometry played a key role in determining OPS contribution. Li et al. [286] observed that as wall thickness increased from 0.3 mm to 5 mm, precipitation strengthening weakened due to nano-precipitate coarsening. Overall, in L/E-PBF Cu alloys/composites, the contribution of OPS to YS can be as high as 83%, primarily determined by factors such as feedstock composition, process parameters, processing type (L/E-PBF), part geometry, and post-printing heat treatment conditions.

9.4. Dislocation strengthening

Dislocation strengthening (DS) in L-PBF or E-PBF components of Cu alloys/composites arises from the dislocation forest effect. This dislocation forest, characterised by a high dislocation density (10^{13} – 10^{15} m^{-2}), acts as a formidable barrier to further dislocation motion. In the microstructure of L/E-PBF components, dislocation forests manifest as cellular structures, with their size (300–600 nm) and morphology directly influencing the properties of the printed parts (as shown in Fig. 76) [262]. The high dislocation density, influenced by the mismatch between the coefficients of thermal expansion (CTE) and elastic modulus (EM), results in residual plastic strain, which is further altered by factors such as partial dislocations, stacking fault energy, subgrain structure, printed part size, heat treatments, process parameters, composition, residual stresses, etc. As indicated in Fig. 77, the L-PBF Cu–Ni–Sn alloy showed a long-range misorientation gradient within grains, indicating a higher dislocation density ($1.09 \pm 0.93 \times 10^{14}$ m^{-2}) compared to the cast alloy ($6.83 \pm 3.88 \times 10^{12}$ m^{-2}). The higher dislocation density in L-PBF contributed 152% more to its yield strength (YS, through DS, as shown in Fig. 75) compared to the cast alloy, with an absolute strengthening effect of 46% on the YS of the L-PBF Cu-alloy part [238]. Additionally, the L-PBF Cu–Sn alloy AB sample showed an unusually high dislocation density (~9.49×10^{13} m^{-2}). This dislocation density significantly decreased (74%) with post-printing heat treatment at 420 °C. Further reduction occurred at higher temperatures (500 °C) by 24% and reached its lowest value at 550 °C, like an annealed sample (10^{12} m^{-2}). Consequently, the contribution of DS is significantly reduced in the L-PBF parts after post-printing heat treatments [126]. In the Cu–15Ni–8Sn+TiB_2 alloy, as depicted in Fig. 77, the addition of TiB_2 led to a decline in dislocation density (6.38×10^{14} m^{-2} to 5.61×10^{14} m^{-2}) and, thus, a decrease in the DS contribution [70]. Furthermore, the addition of Y_2O_3 to the Cu–Cr–Zr alloy increased dislocation density due to a higher mismatch in EM and CTE between the matrix and nanoparticles, contributing 56% to YS through DS [110]. When altering composition, alloy design strategies must carefully consider the complex antagonistic and synergistic effects of DS to optimise material properties for future applications. Moreover, Li et al. [286] noticed that as wall thickness increased from 0.3 mm to 5 mm, the absolute contribution of dislocation strengthening decreased due to dislocation dissolution. In the as-built condition, DS contributed as much as 78% to the YS of L-PBF Cu–Cr–Zr alloys, making it the primary strengthening mechanism in certain alloys. However, heat treatment reduced this contribution to below 30% [301]. Additionally, despite this reduction, DS remained a major factor in the strengthening of most printed Cu alloys following precipitation strengthening. Beyond YS, DS also influenced electrical conductivity, though its effect was less significant than SSS and GBS, with DS contributing less than 2%. Therefore, the synergy of strength, ductility, and conductivity in L-PBF-printed parts can be tailored by integrating DS with other strengthening mechanisms.

The Bailey-Hirsch relationship is used to compute the DS contribution using Eq. (9.13) [308]. The dislocation density is computed using EBSD KAM data using the Gao and Kubin Eq. (9.14) and the Williamson-Hall method using Eqs. (9.15) and (9.16), and the Dunn and Koch Eq. (9.17) [309–312]. EBSD analysis utilising the KAM technique gives the GNDs density based on local misorientation, while XRD-based dislocation density computation relies on lattice strain caused by dislocations, vacancies, and solute atoms. However, XRD does not account for dislocations at cells or grain boundaries as it is more sensitive to statistically stored dislocations (SSD) [313]. Therefore, Eq. (9.18) is recommended for improved accuracy in determining the dislocation density of AMed Cu alloy/composite samples, given that dislocation cells are found in the L/E-PBF microstructures.

$$\sigma_{DS} = \varphi \mathrm{M}\, \tau\, \mathrm{b}\left(\sqrt{\rho}\right) \tag{9-13}$$

$$\rho = \text{geometrically necessary dislocation density} = \frac{2KAM_{avg}}{ub} \tag{9-14}$$

$$\delta cos\theta = \frac{\lambda K_{SF}}{D} + 4\varepsilon sin\theta \tag{9-15}$$

$$\rho = k_d \frac{\varepsilon^2}{b^2} \tag{9-16}$$

$$\rho = \frac{\beta_{hkl}^2}{kb^2} \tag{9-17}$$

$$\rho = \frac{(\varepsilon)2\sqrt{3}}{Db} \tag{9-18}$$

where M is the Taylor factor, φ is a geometrical constant, τ is the shear modulus of the Cu matrix, b is the magnitude of the Burger vector, and ρ is the dislocation density, KAM_{avg} is the average misorientation angle, u is the step size used for EBSD (μm), b is the Burger vector (nm), and ε is the internal strain. β_{hkl} is the full width at half maxima (FWHM) of XRD peaks, k_d is a constant (2πln2 for metals), KSF is a dimensionless constant, δ is the physical broadening of FWHM of the diffraction peak, θ is the diffraction angle, λ is the wavelength of radiation, and D is the grain size.

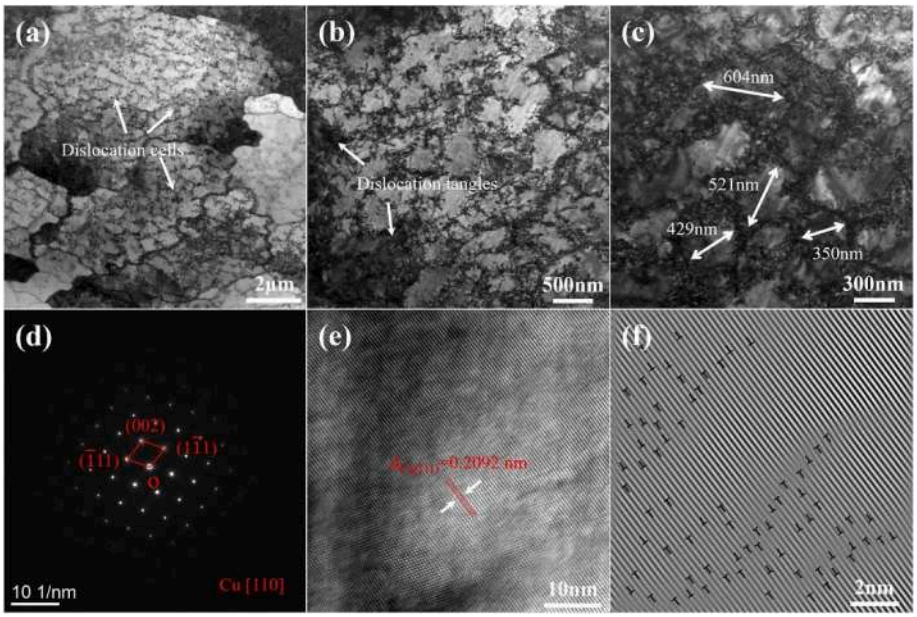


Fig. 76. Dislocation cells, tangles, and high dislocation density in L-PBF Cu–Cr–Zr alloy [262].

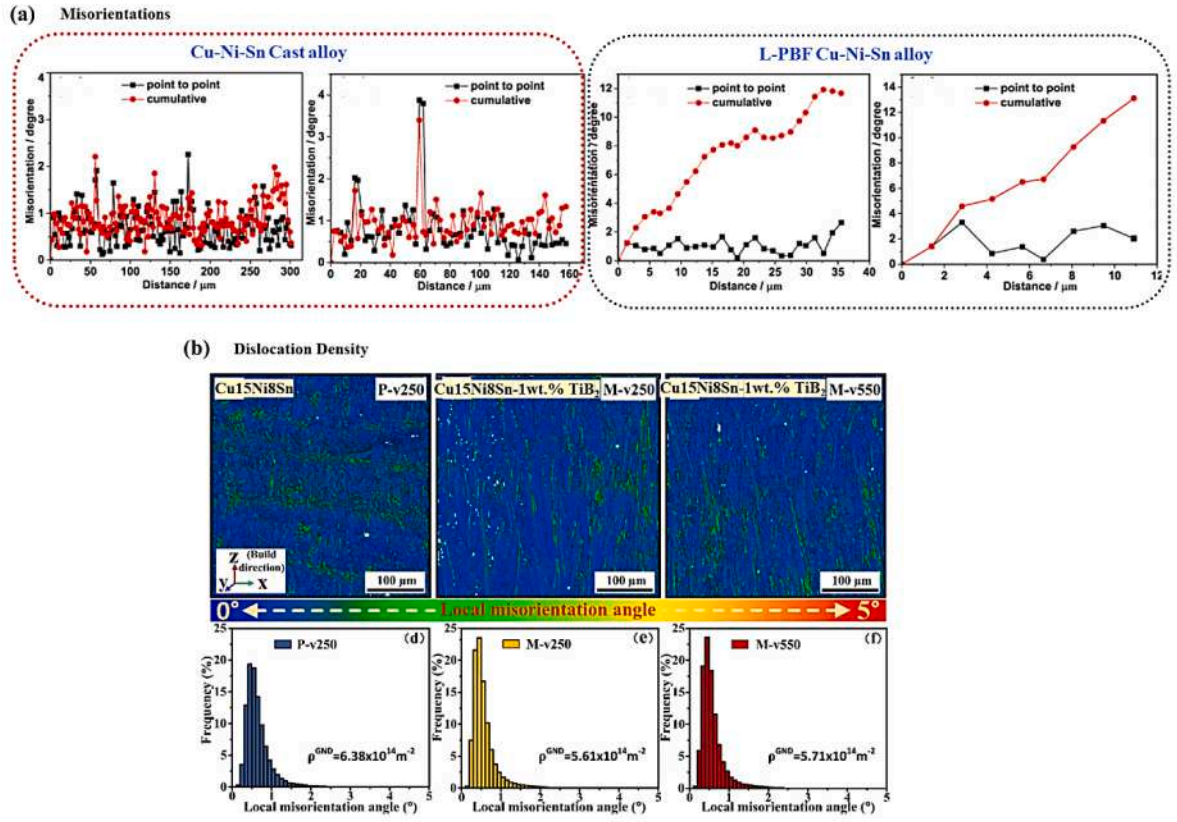


Fig. 77. (a) Variation in misorientation [238]; (b) Variation of dislocation density with the addition of TiB_2 to Cu–15Ni–8Sn [70].

9.5. Load transfer strengthening from soft matrix to hard particles

Stress is transmitted from the Cu matrix to the hard particles/phases, enabling the hard particles/phases to share a portion of the load and enhance the YS of Cu alloys/composites through load transfer strengthening (LTS) and can be computed using Eqs. (9.19) and (9.20) (A=1 for equiaxed or spherical particles) [110,314].

$$\sigma_{load} = f_{vol}\sigma_{cu}\left(\frac{A+1}{4}\right) \tag{9-19}$$

$$\sigma_{load} = \frac{1}{2}f_{vol}\sigma_{cu} \tag{9-20}$$

where A is the aspect ratio, σ_{cu} is the YS of the Cu matrix, and f_{vol} is the

volume fraction of hard particles/phases.

The presence of TiB_2 hard particles in L-PBF Cu–15Ni–8Sn alloys led to LTS; however, their impact on the YS was modest (only 1.6%) [70]. Similarly, L-PBF Cu–Cr–Zr alloys doped with Y_2O_3 contributed 11% to the YS through LTS due to the formation of coherent Cu_2CrZr and $Cu_2CrZr(Y, O)$ precipitates with the Cu matrix [110].

9.6. Hetero-deformation induced strengthening

Previous studies have shown that SSS, GBS, OPS, LTS, and DS can enhance the yield strength of L-PBF Cu alloys by preventing dislocation motion through solute atoms, grain boundaries, and precipitates. However, the absolute contributions of SSS and GBS enhance strength but often compromise ductility and conductivity. Additionally, strength-ductility and strength-conductivity are often antagonistic in L/E-PBF Cu alloy parts. The heterostructured system showed an interesting harmony of strength-ductility-conductivity due to the soft and hard domains within the microstructure, which was enhanced by AM techniques such as L/E-PBF. These techniques produced high dislocation density and nano-precipitates that are not achievable with conventional processes. This resulted in back stress strengthening by strain incompatibility, also known as hetero-deformation induced (HDI) strengthening. The quantification of HDI strengthening is possible using the following Eq. (9.21) based on loading and unloading hysteresis loops [112].

$$\sigma_{HDI} = \frac{\sigma_{UL} + \sigma_{RL}}{2} \tag{9-21}$$

where $\boldsymbol{\sigma_{UL}}$ and $\boldsymbol{\sigma_{RL}}$ represent the unloaded and reloaded yield stresses during loading-unloading-reloading (LUR) tensile testing.

Wang et al. [128] observed that L-PBF Cu–Cr–Nb alloys with HND architecture demonstrated strength-ductility synergy at both ambient and high temperatures, also benefiting from strength-ductility-conductivity synergy. Similarly, L-PBF Cu–Cr–Zr alloys exhibited strength-ductility synergy, with high HDI stress delaying necking with a hierarchical structure [112], a feature also observed in L-PBF Cu–Co alloys [29]. Overall, HDI strengthening offers an effective strategy for designing high-performance L/E-PBF Cu alloy components while addressing the strength-ductility-conductivity paradox.

9.7. Superposition of strengthening mechanisms

The linear addition and square root approaches have been used to predict the YS of L/E-PBF alloys/composites by considering individual strengthening mechanisms [45,70,238]. A linear addition of strengthening mechanisms predicted a YS of 515 MPa for L-PBF Cu–Ni–Sn alloys, 8% higher than the experimental value of 474 MPa using the following Eq. (9.22) (where σ_o is the lattice friction stress) [238].

$$\sigma_{cal} = \sigma_o + \sigma_{ss} + \sigma_{OPS} + \sigma_{GBS} + \sigma_{DS} \tag{9-22}$$

The lattice friction stress, or Peierls-Nabarro stress, can be estimated using the following equation 9–23 [315].

$$\sigma_o = \frac{2\tau}{1-\mu}\exp\left[-\frac{2\pi}{1-\mu}\frac{i_p}{b}\right] \tag{9-23}$$

where τ is the shear modulus, μ is the Poisson's ratio, i_p is the interplanar spacing, and b is the Burgers vector.

Gao et al. [70] estimated the YS of L-PBF Cu–Ni–Sn+TiB_2 using the root mean square (RMS) method with the following Eq. (9.24) (n=2). The estimated values for L-PBF TiB_2–modified Cu–Ni–Sn alloys matched experimental results (0.7-1.5% variation). In contrast, Cu–Ni–Sn alloys deviated by 14% from the experimental results [70].

$$\sigma_{cal} = \sigma_o + \sqrt[n]{\left[\sigma_{ss}^n + \sigma_{OPS}^n + \sigma_{GBS}^n + \sigma_{DS}^n + \sigma_{LOAD}^n\right]} \tag{9-24}$$

Overall, the RMS technique (n=2) yielded a strong correlation with the experimentally measured YS for the AMed Cu alloy/composite parts compared to linear methods (n=1). However, minor discrepancies emerged due to numerous factors: microstructural factors (volume fraction of precipitates, grain size measurement accuracy, texture considerations, and anisotropy), process factors (AM defects), strengthening mechanism (shear hardening may dominate over OPS), and measurement limitations (XRD/TEM/EBSD analysis). In the future, the value of n can be adjusted to improve accuracy, taking into account these factors.

10. Post-processing heat treatments

As previously outlined earlier, the rapid and non-equilibrium solidification during L/E-PBF leads to non-homogeneous microstructures with metastable phases and undesired segregation in the AB state of Cu alloys. These factors hinder the achievement of the optimal combination of mechanical, electrical, thermal, and functional properties for L/E-PBF Cu alloys, thus reducing part reliability. Although certain distinguishing features such as core-shell structures (Nb(FeCr) core-shell) and limited solid solubility resulted in 'in-situ' precipitates that provided a reasonable balance of properties in AB Cu alloy parts, this was typically limited to specific Cu alloys (Cu–1.8Cr–1Nb–2Fe, Cu–Fe) [27,113]. In general, optimising the comprehensive performance of L/E-PBF Cu alloys required precise control over the type, shape, volume fraction, distribution of precipitated phases, as well as microstructure homogenisation. This control was accomplished by carefully selecting heat treatment parameters (temperature, duration, heating and cooling rate) based on the AB microstructures (influenced by process parameters such as laser power, HD, spot size of the laser, machine settings such as platform temperature and layer thickness, type of process L/E-PBF), as well as the elemental compositions of Cu alloy/composite. However, after L/E-PBF, the microstructures of Cu alloys revealed distinctive features, including supersaturated solutions, varied grain structures (including equiaxed, columnar, and cellular grains), crystallographic texture, cellular subgrain structures (coexisting with high dislocation density, internal stresses, etc.), local precipitation, and metastable phases. Therefore, the peculiar microstructure of L/E-PBF Cu alloys necessitated a comprehensive overhaul of thermal treatments to attain uniformity in the microstructure and, ultimately, superior comprehensive performance.

Fig. 78 depicts the progression of grains and precipitate morphologies and melt pool boundaries (MPB) in AB and post-printing heat-treated L-PBF Cu alloy samples. The AB Cu alloy samples exhibited MPB, planar crystals, grains growing toward the centre, a cellular structure, a square-shaped cavity at MPB, and fine chromium precipitates (uniformly distributed). However, the presence of MPB, precipitation, and grain coarsening were altered by heat treatment. Solution treatment (ST) and solution-aging treatments (SAT) revealed no MPB, local precipitates coarsening, and grain coarsening (ST: 27.7 μm, SAT: 30.6 μm). In contrast, direct aging (DA) treatment revealed MPB, precipitates, and coarse grains (35.4 μm). On the other hand, the texture is also influenced by the heat treatment; DA showed <100> orientation was stronger, and ST samples were mainly in the <110> direction, the dominant orientation for Cu alloys (Fig. 78). Further, heat treatment significantly affected HAGBs and LAGBs fraction in the microstructure. For DA treatment, the HAGB fraction was 39%, higher than ST (21%), due to the recrystallisation in the L-PBF Cu–Cr–Zr alloy [316]. The heat treatment transformed the microstructure by not only changing the grain structure from columnar to equiaxed (CET) and erasing the L-PBF microstructure history via the elimination of melt pool boundaries but also by reshaping cellular features such as dislocation distribution and density while altering segregations and phases present. Karthik et al. [126] noticed an interesting transformation in post-printing heat-treated L-PBF Cu–Sn alloy: as temperature and time changed (420 °C for 60 min to 550 °C for 15 min), the microstructure evolved: uniform dislocation distributions became random, the cellular structure with thick cell walls thinned or vanished entirely, dislocation density decreased ($\sim 9.49 \times 10^{13}$ to 10^{12} m^{-2}), and Sn segregation and the δ-ferrite phase (present in the AB Cu–Sn

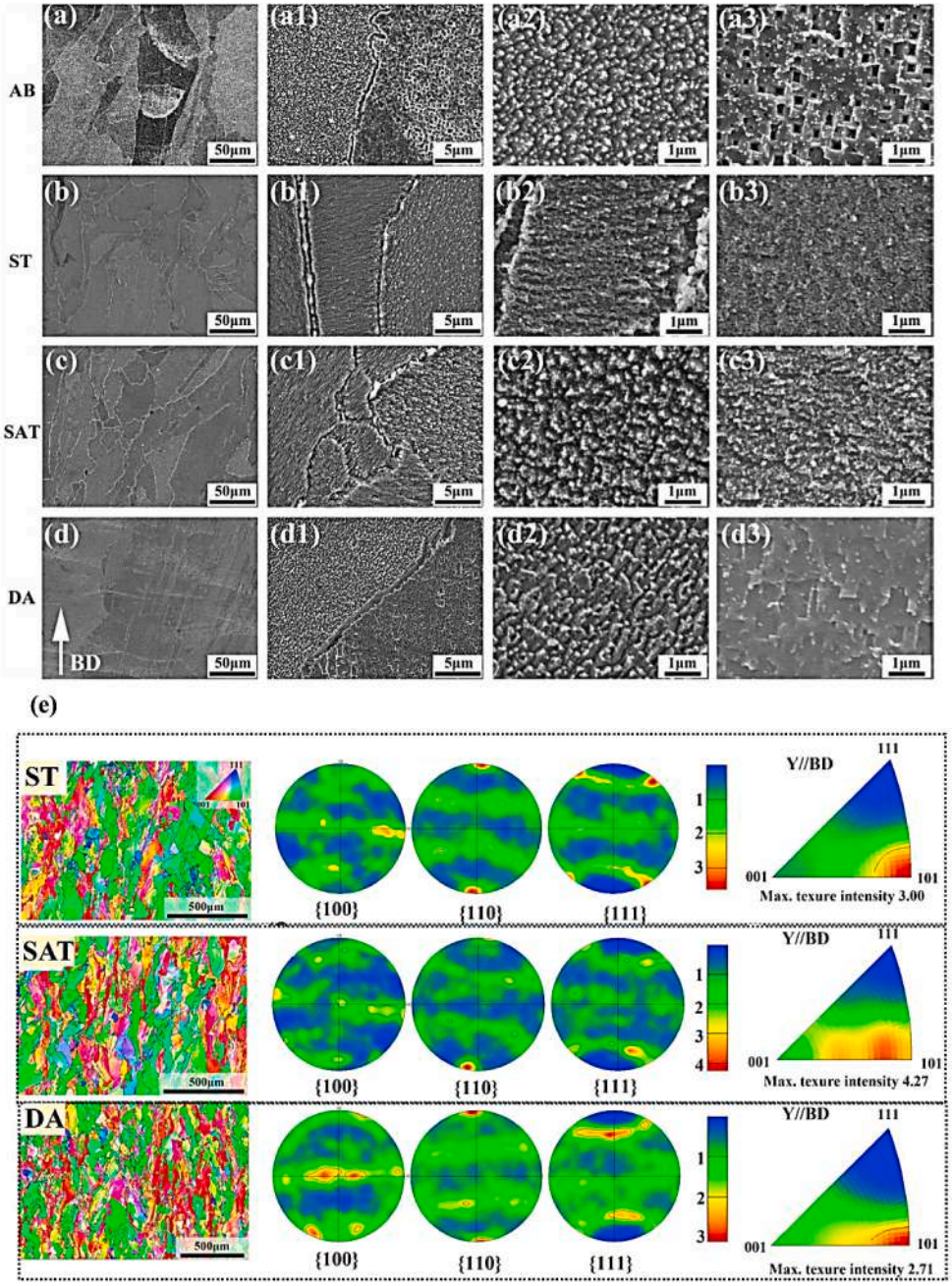


Fig. 78. (a-d) Evolution of grain structure, precipitates, and (e) Crystallographic texture after heat treatment of L-PBF Cu–Cr–Zr alloys [316].

alloy) were eliminated. Also, heat treatment of L-PBF Cu alloys effectively addressed the issue of incomplete alloying dissolution. In the case of L-PBF Cu–Ni–Sn alloys, Ni diffusion resulted in the formation of a (Cu, Ni) solid solution along with distinctive phases, (Cu, Ni)$_3$Sn and (Cu, Ni)$_3$P, which were not present in the as-printed microstructure (Fig. 79 confirmed by EPMA mapping) [270]. Moreover, heat treatment mitigated residual strain (~3%, $\Delta\varepsilon = \alpha\Delta T = 17 \times 10^{-6} \times 1700 \times 100 = 2.9\%$ if Temperature: 2000 K L-PBF) after L-PBF printing in Cu alloys due to thermal expansion and contraction. This is demonstrated by the decreased KAM value for the Cu–Sn alloy after heat treatment, which dropped from 1.7 (AB) to 0.4, indicating relaxed grains due to the reduction of excessive shrinkage and thermal stresses caused by rapid cooling [126].

More interestingly, the integration of heat treatment and the composition of Cu alloy enabled the customisation of precipitation after printing, resulting in reduced anisotropy and enhanced multifunctional properties, ranging from superior mechanical to functional properties. Wang et al. [128] revealed the transition of the heat-treated microstructure in L-PBF Cu alloy. Initially, the microstructure comprised large (~100 nm), oval-shaped Cr_2Nb precipitates with a semi-coherent interface. However, integrating heat treatment with composition modification (varying Cr/Nb ratios (2 to 5) enabled a larger number of nanoscale (5.7×10^{24} m^{-3}), spherical, and elongated Cr–rich uniformly dispersed coherent precipitates within the matrix (confirmed by APT and TEM analyses as shown in Fig. 80). As a result, heat treatment in L-PBF Cu alloy acts as a microstructure sculptor, allowing for customisation of the entire microstructure spectrum. Therefore, selecting the appropriate heat treatment is critical for AMed Cu alloy parts. However, L-PBF Cu alloys require distinct heat treatment parameters to attain the requisite characteristics, which differ from conventional methods.

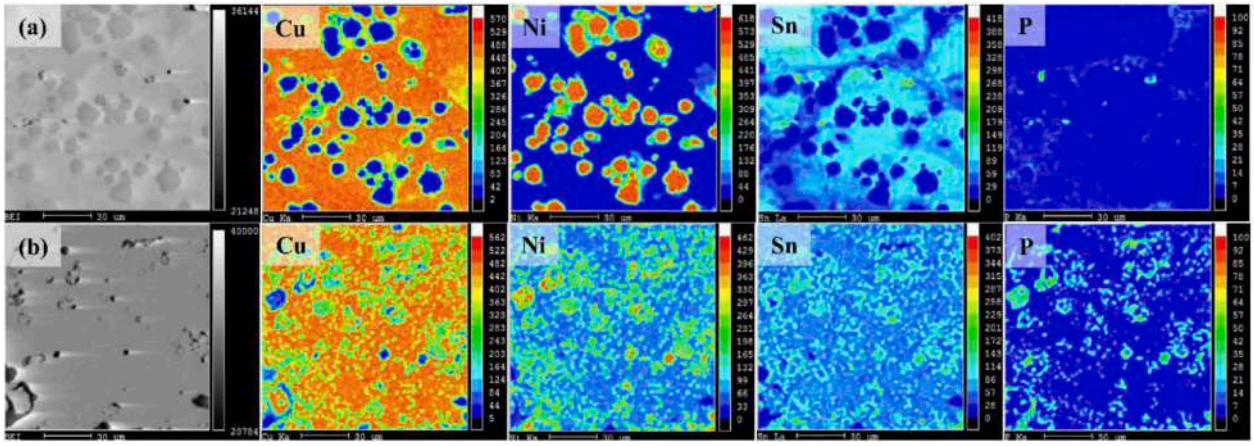


Fig. 79. EPMA maps of L-PBF Cu–16.8Ni–3.6Sn–1.5P alloy: (a) AB state and (b) Heat-treated sample [270].

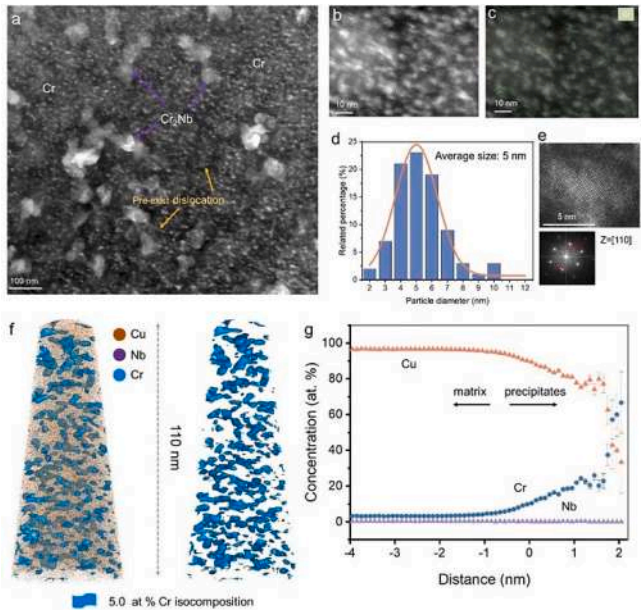


Fig. 80. TEM and APT analyses reveal the shape, size, distribution, and chemical composition of precipitates in L-PBF Cu alloys [128].

Unlike conventional treatments (dissolution at 950 °C), heat-treated L-PBF Cu–Cr alloys revealed that Cr dissolves at temperatures above 1000 °C. Below 1000 °C, precipitation becomes the dominant mode, as confirmed by lower XRD lattice parameters [317].

As already explained, the peculiar microstructure of the AB Cu alloy part is modulated by subsequent heat treatment, which is primarily caused by changes in the morphology of grains and precipitates (shape and size), distribution, % volume fraction, chemical composition, crystallographic texture, dislocation density and distribution, cell structure decomposition, complete dissolution, elimination of segregation, and minimisation of defects (such as strain-free grains, pores, etc.). However, microstructure characteristics have a direct impact on the strength-ductility-conductivity trade-off, as well as corrosion resistance, wear behaviour (tribology), fatigue life, creep resistance, etc. [187,317–320]. Thus, optimising the heat treatment of L/E-PBF Cu alloys by carefully managing temperature and duration (whether single or multi-stage) is crucial to achieving a homogeneous microstructure and superior performance. These heat treatment processes involve single or multi-stage treatments, such as DA, ST, HIP, and SAT, each varying in temperature, cooling rate, and duration. Importantly, the absence of standardised heat treatment protocols for L/E-PBF Cu alloys remains a critical challenge requiring immediate attention. Current research addresses this issue through DSC analysis, identifying DA treatment temperatures ranging from 480-580 °C, associated with exothermic peaks at 155-265 °C and 400-600 °C, alongside conventional heat treatment data from the literature [45]. The reported temperature range for L/E-PBF Cu alloys includes 800-1050 °C for the ST process and 400–700 °C for DA treatment, with treatment durations varying from 0.5-4 hours and 10-420 minutes for ST and DA treatments, respectively [127,148,321]. A combination of optimised DA and ST parameters has been employed in two-stage treatment SAT treatments, as shown in Fig. 81. Table 8 summarises the overall effect of SAT treatment on as-printed Cu alloy parts, including those treated with DA and ST processes. Nevertheless, determining the ideal heat treatment conditions for AMed Cu alloy components is still arduous.

The literature suggests that high-temperature ST after L-PBF of Cu alloys favours electrical conductivity over mechanical properties. The L-PBF Cu–Cr–Zr sample after the ST process (960 °C/60 min) showed improved ductility (from 10 to 40%) and electrical conductivity (30 to 56% IACS), but at the cost of strength and hardness [261]. Interestingly, modifying the ST parameters for Cu–Cr–Zr alloys (950 °C/30 min) resulted in decreased ductility, strength, and hardness while increasing electrical conductivity (28.4 to 52.2% IACS) [127]. DA treatment revealed a trade-off between strength and ductility, as well as a synergy between strength and ductility, which is determined by the characteristics of Cu alloys/composite powder feedstock, the initial microstructural state, and the type of energy source [26,244,261]. Zhou et al. [127] showed that DA treatment of L-PBF Cu–Cr–Zr alloys at 400-620 °C for 2 h resulted in peak UTS followed by a decline (overaging), with an opposing trend in ductility. However, by precipitating from the supersaturated Cu–Cr–Zr alloy, DA treatment developed a microstructure with minimal electron scattering, resulting in continued improvement in electrical conductivity. This demonstrates the inherent challenge in optimising the strength-ductility-electrical conductivity in L-PBF Cu alloys. Similarly, the strength-ductility trade-off following DA treatment was reported for L-PBF Cu–Cr–Zr [262,291,301], Cu–1Cr+CNPs [154], Cu–Cr–Nb–Fe [113], and Cu–Cr–Nb [128]. In contrast to these alloys, Cu–Fe [26], Cu–Co [29], and green laser-printed Cu–Cr–Zr [261] demonstrated a synergistic combination of strength and ductility after DA treatment. Even for hardness, the optimal DA parameters are necessary. According to studies, L/E-PBF Cu alloys initially enhanced hardness with increasing DA temperature over time but then softened (hardness reduced) at even higher temperatures [61,127]. This pattern persisted even with a constant DA treatment temperature (e.g., 500 °C) over time (1 to 3 h) [244,261]. The strength-ductility trade-off is a crucial gauge for assessing the comprehensive mechanical properties of the heat-treated L/E-PBF Cu alloys. Fortunately, DA treatment shows promise in potentially overcoming the strength-ductility trade-off. As a

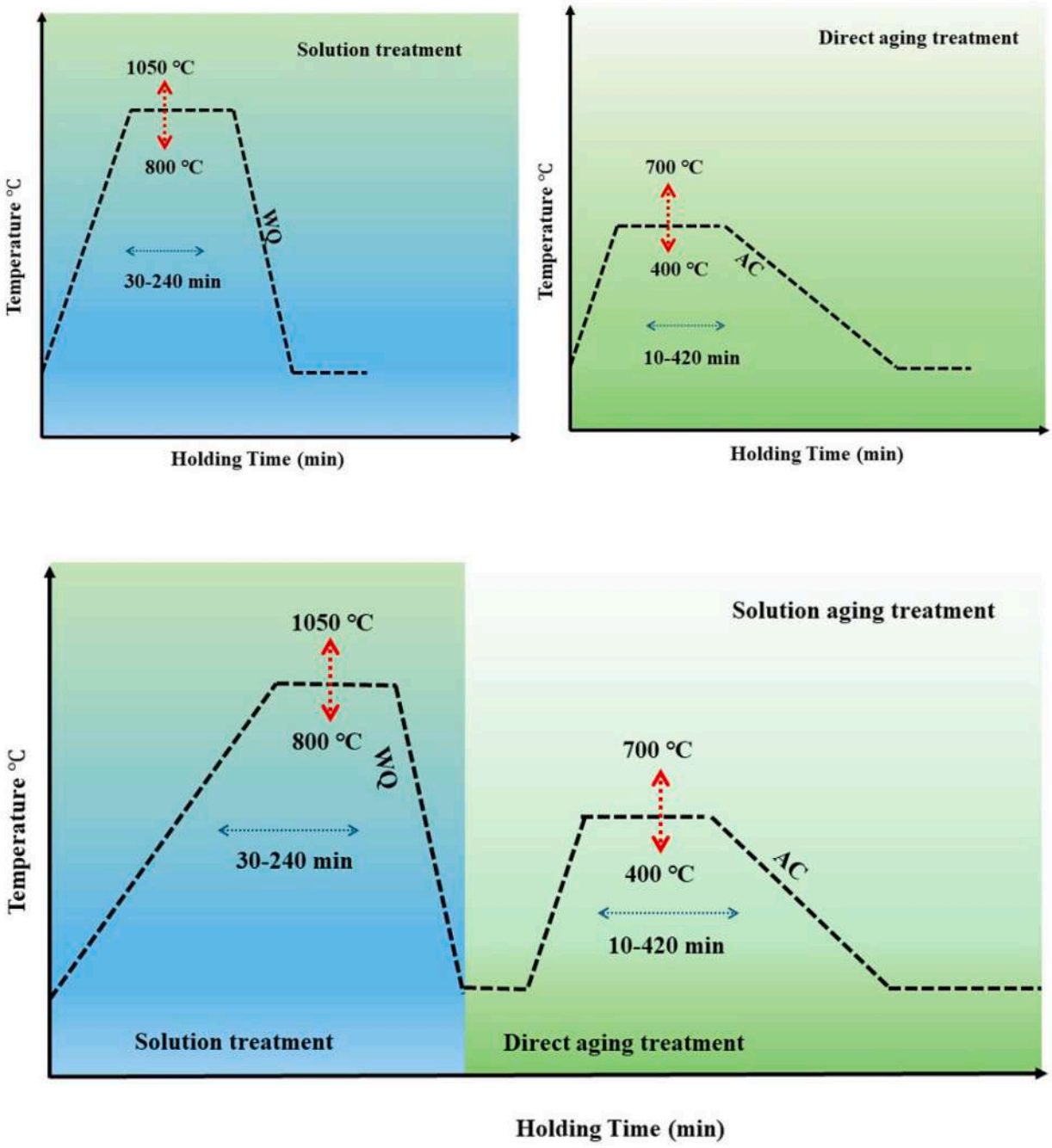


Fig. 81. Temperature ranges and durations for solution treatment, direct aging, solution and aging treatment of L/E-PBF Cu alloys.

result, adopting DA treatment is a superior approach over ST for enhancing the comprehensive mechanical properties such as strength, ductility, and hardness of Cu alloy after L/E-PBF. In addition, the electrical performance of the L-PBF Cu alloys was enhanced by both the ST and DA treatments, irrespective of the particular treatment parameters employed for L-PBF Cu–Ni–Sn, Cu–Cr–Zr, and Cu–Cr–Nb alloys [45,128,150,261], and the DA treatment emerged as a more effective method compared to ST for enhancing electrical conductivity in L-PBF Cu alloys. Both DA and ST treatments initially resulted in a rapid increase in electrical conductivity, notably during the first hour, followed by a slower rise as the treatment time increased [150]. Thus, with an optimised treatment time, DA is the technique most effective for addressing the strength-conductivity trade-off often observed in the as-built microstructure, compared to the ST process. Furthermore, according to the Wiedemann-Franz equation, thermal conductivity is proportional to electrical conductivity. The Cu alloy part showed a similar tendency to thermal conductivity with DA and ST; the treatment increased both strength and thermal conductivity at the same time, resulting in a synergistic effect. Thus, the strength-thermal conductivity trade-off, commonly reported in printed Cu alloys, can be effectively addressed through DA treatment.

As mentioned earlier, executing heat treatment after AM can significantly change the initial microstructure of L/E-PBF Cu alloy, likely influencing their corrosion resistance. Vacuum annealing of the L-PBF Cu–10Sn alloy resulted in a 50% reduction in the corrosion rate compared to the as-built state; this was ascribed to the lower sensitivity of the transformed microstructure to internal galvanic corrosion as well as intergranular corrosion [171]. In contrast, Kremer et al. [322]

Table 8
Overview of the impact of various heat treatments on the microstructure and properties of L/E-PBF Cu alloys.

Properties, Defects	Features	AB	ST	SAT	DA	HIP
			Relative to AB			
Microstructure aspects	Anisotropy	Yes	Yes Orientation-dependent	Yes Orientation-dependent	Yes Orientation-dependent	–
	Cell size (nm)	300-700 Thick cell boundaries	Yes, thin boundaries	Mixed (present/ disappear)	Mixed (present/ disappear)	–
	Lattice constant (Å)	3.800	↓(3.602)	↓(3.618)	↓(3.772)	–
	Segregation	Suppressed (Macro)	Boundary segregation (nano)	Reduced/ disappeared	Disappeared	–
	Grain refinement	LAGBs (45-70%) HAGBs (30-40%)	Low HAGBs (21%)	Medium HAGBs (33%)	High HAGBs (39%)	Low
	Grain morphology	Mixed (C, E)	Mixed (C, E)	Mixed (C, E)	Mixed (C, E)	Mixed (C, E)
	Grain size (μm)	10–300	↓ (15–30)	Mixed (20– 80)	↓ (10–120)	↑
	Dislocation density (m^{-2})	10^{13} –10^{15}	↓ (10^{12} –10^{15})	↓ (10^{13} –10^{15})	↓ (10^{13} –10^{15})	–
	Dislocation distribution	Uniform	–	–	–	–
	Texture	Mixed	Weak	Weak <110>	Weak <110>	Weaken
	MPB	Yes	No	No	Visible	Reduced visibility
Properties	Strength	–	↓	Mixed	Mixed	↓
	Ductility	–	Mixed	Mixed	Mixed	↑
	Hardness	–	↓	Mixed	Mixed	↑
	EC (%IACS)	7-98.4	↑	↑	↑	↑
	TC (W/mK)	50-390	↑(150-260) Medium	↑(350-380) High	↑(170-350) Medium	-
	Creep properties	–	–	–	–	–
	Fatigue properties	–	–	↑	↑	↑
	Corrosion properties	ST > AB > SAT > DA				-
	Tribological properties	–	–	–	–	↑
Defects	Pores, cracks	Present	No role in volumetric defects			↓
	Residual stress	High	Low (Relaxation)			↓
Ref.		[26,29,113,128,154,245,262,263,61,126,127,127,148,198,199,222,250,255,260,268,291,293,316,317,331,332]				

C: Columnar; E: Equiaxed.

reported that both the temperature and stage (single versus two-stage) of heat-treated L-PBF Cu–10Sn alloy affect corrosion resistance. Corrosion susceptibility was slightly reduced in the two-stage process (800 °C and 400 °C) but not in the single-stage treatments (320 °C and 650 °C). Another study found that annealing of L-PBF Cu–Zn–Si at 600 °C for varied times (1, 2, and 4 h) increased its corrosion resistance. This improvement is attributed to the breakdown of the cellular structure and a substantial rise in coherent twin boundaries (from 0.38 in the AB to 60%) [153]. Barr et al. [119] demonstrated that heat treatment induced microstructural changes in L-PBF Cu–Al–Fe–Ni–Si and Cu–Al–Fe–Ni–Mn alloys (C63000 and C95800, respectively), resulting in corrosion resistance comparable to their wrought equivalents. Researchers discovered a trade-off between localised and uniform corrosion resistance in NAB alloys. Notably, heat treatment improved the localised corrosion resistance of the L-PBF NAB alloy but reduced uniform corrosion resistance [234]. Karthik et al. [203] found that full recrystallisation via heat treatment (550 °C/15 min) increased the corrosion resistance of L-PBF Cu–Sn alloys by uniformly distributing dislocations. The key parameters regulating corrosion behaviour are dislocation density and distribution, as opposed to segregation, phases, or residual stress. Overall, the literature on post-printing heat treatments of L-PBF Cu alloys showed mixed results, with NAB alloys [119], Cu–Sn (particular treatments) [203], and Cu–Zn–Si [153] showing improvements, but Cu–Sn (single stage treatments) showing no significant change for corrosion behaviour [322]. However, several questions remain unexplored and could be investigated further in future research.

- Is it possible to design existing or novel Cu alloys/composites with enhanced, homogeneous corrosion resistance across all directions through heat-treated microstructure?
- How do crystallographic texture, HAGBs/LAGBs, elemental segregation, inclusions, second-phase particles, and precipitation during post-printing heat treatments regulate the corrosion behaviour of L/E-PBF Cu alloys?
- Can specific heat treatment regimens be identified that minimise the trade-off between mechanical properties and corrosion resistance for L-PBF Cu alloys in various demanding applications?
- Does heat treatment typically enhance corrosion resistance in L/E-PBF Cu alloys? Despite conflicting results in the literature.
- Can we predict how heat treatment factors govern alloy corrosion mechanisms (uniform, galvanic, crevice, intergranular, pitting, stress corrosion cracking, environmentally assisted cracking, and tribo-corrosion)?

As previously stated, appropriate heat treatment fosters a synergistic enhancement in strength, ductility, and hardness. Archard's wear equation suggests that increasing hardness is one approach to enhancing wear resistance [323]. Consequently, heat treatment of L-PBF Cu alloy paves the way for enhancing the tribological performance of L/E-PBF Cu alloy. However, research on the tribological behaviour of post-printing heat treated L/E-PBF Cu alloys remains limited, despite some L-PBF Cu alloys (Cu–Sn–Ti) demonstrating superior tribological properties compared to their conventional counterparts [226]. This scarcity of data raises uncertainty regarding whether post-printing heat treatments interact synergistically or antagonistically with mechanical properties

and tribological performance in L/E-PBF Cu alloys. One study showed that the cooling rate during post-printing heat treatment of L-PBF Cu–Cr–Zr directly impacts wear/friction [320]. Specifically, water quenching (fastest cooling) produced the highest wear, friction (0.55), and lowest hardness (1.1 GPa), whereas furnace cooling (slowest cooling) produced the least wear, friction (0.53), and maximum hardness (1.5 GPa). Similarly, heat treatment processes (annealing, tempering, quenching, and tempering) of L-PBF NAB alloy influenced the presence and contribution of κ and α phases, thereby affecting tribological behaviour. Notably, annealing improved wear resistance while causing minimal changes in friction coefficients. Additionally, it facilitated a balance between enhanced strength and ductility, albeit with reduced hardness compared to the as-built state [324]. The dearth of knowledge on how post-printing heat treatments alter the microstructure and tribological behaviour in Cu alloys offers numerous opportunities for future studies, as outlined by the following key questions.

- How do heat-treated L/E-PBF Cu alloy parts (such as bronze bearings) compare to conventional bearing alloys in terms of wear resistance and friction coefficient under realistic operating conditions (load, speed, and environment)?
- What impact does heat treatment have on the tribological-corrosion trade-off in L/E-PBF Cu alloys compared to conventional alloys?
- How do post-printing heat treatments influence key wear mechanisms in L/E-PBF Cu alloys, such as adhesion and abrasion, relative to the AB state/conventional alloy?
- How do post-printing heat treatments and operating temperature affect the wear behaviour of L/E-PBF Cu alloys for anti-friction bearings and SMAs, considering the system-dependent aspects of tribology (dependent on surroundings and materials)?
- How can post-printing heat treated L/E-PBF Cu alloy techniques mitigate friction-induced wear—an inherent challenge in contact surfaces—thereby improving component reliability in industrial applications?
- Can post-printing heat treatments reduce fretting wear in L/E-PBF Cu alloy parts, ultimately extending their operational lifespan?

As outlined previously, heat treatment of Cu alloys substantially alters the microstructure, reducing residual stresses and microstructural defects and thereby enhancing fatigue performance after post-AM heat treatments [325]. Although the static mechanical properties of the printed metallic components improved after heat treatment and became comparable to their wrought counterparts, a few post-printing heat-treated metallic parts showed superior fatigue performance [326]. Thus, studying the fatigue behaviour of post-printing heat-treated Cu alloys is essential for unravelling the intricate connections between microstructure and properties. However, fatigue studies on post-printing heat-treated Cu alloys/composites remain scarce. While heat treatment effectively mitigates residual stresses, anisotropy, and microstructural heterogeneity, defect-driven (microstructural and surface defects) failures remain prevalent, particularly in non-HIP-treated components [162]. For heat-treated specimens, excluding HIP-treated parts, fatigue life is primarily dictated by defect characteristics, including size, distribution, orientation, volume fraction, and morphology. These factors become increasingly critical as component size and operational conditions (e.g., type of stress, temperature) change. Wegener et al. [293] showed that the SAT process (950 °C/15 min, 600 °C /480 min) improved low cycle fatigue performance in L-PBF Cu–Cr–Zr alloys compared to DA treatment (500 °C/2 h, 450 °C/2 h) and as-built specimens. Additionally, fracture analysis identified LoF defects as major contributors to crack formation, underscoring the dominant role of process-induced defects in determining the fatigue performance of L-PBF Cu alloys [293]. Moreover, fatigue sensitivity to component size is another crucial factor. Process-induced defects tend to increase with part size, regardless of heat treatment, except in HIP-treated specimens. Thus, future research on fatigue-resistant L/E-PBF Cu alloys/composites should ensure uniform specimen size (gauge diameter), as the interplay between porosity and size effects not only obscures improvements due to the printed/heat-treated microstructure per se or defect minimisation per se but also complicates data comparison. Additionally, fatigue studies for L/E-PBF Cu alloys remain underrepresented in the literature, which may explain why Cu alloys were excluded from a recent review on the fatigue properties of metal AM. Readers seeking further insights into fatigue behaviour and influencing factors in metal AM should refer to [327]. This presents opportunities for future research into tailoring post-printing heat-treated L/E-PBF Cu alloys for specific applications where low, high, and extremely high cycle fatigue are critical, using experimental, theoretical, and numerical methodologies. Moreover, statistical methods for connecting plastic strain energy (PSE) with fatigue life in L/E-PBF Cu alloys need rigorous confirmation. Recently, the hysteresis loop area and statistical estimation of plastic strain energy (SEPSE) approaches were shown to calculate PSE for L-PBF Cu–1.5Cr–0.5Zr alloys, proving the SEPSE method for reliable PSE calculation in AM materials across different temperatures [294]. This demonstrates that plastic strain energy may be used to quantify fatigue damage in L/E-PBF Cu alloys, which can be extended for validation post-treatment. Furthermore, fracture surface analysis of L-PBF GRCop–84 specimens heat-treated at 900 °C for 5 h revealed striations typically associated with fatigue failure [9]. The presence of these striations suggests that the material may be susceptible to fatigue under cyclic stress, although dedicated fatigue investigations are lacking in the literature. Therefore, fracture signature analysis with process-induced defects using machine learning can be used in future studies to estimate fatigue life because fatigue is affected by the presence of process-induced defects [162].

The microstructural characteristics of AMed components are linked to creep behaviour, in addition to the inherent properties of the material (crystal structure, diffusivity, elastic modulus, melting point, etc.) and the operating parameters (time, temperature, stress, environment etc.). Given that heat treatment significantly alters microstructural features such as dislocations, precipitates, grain boundaries, grain and subgrain morphologies, textures, etc., the creep behaviour of post-printing heat treated L/E-PBF Cu alloys may change. However, creep studies on the as-built and post-printing heat-treated L/E-PBF Cu alloys are not available in the literature. Creep should be considered a key factor for long-life component design, particularly for high-temperature applications where safety and reliability are critical in L/E-PBF Cu alloys with coarsening-resistant strengthening phases such as GRCop–84, which can be thoroughly investigated in future research. Furthermore, L-PBF Cu alloys, such as the Cu–Cr–Zr alloy [45], have demonstrated better strength at higher temperatures (500 °C) than in the AB state, which is a positive indicator of creep resistance. Extensive creep research should be conducted post-treatment to validate the creep potential of L/E-PBF Cu alloy/composite parts in future investigations.

The heat treatment of L/E-PBF Cu alloys enhances dynamic and static mechanical characteristics, as well as thermal, electrical, corrosion, and tribological properties, allowing for the modification of functional properties like shape memory. Specifically, post-printing heat treatments, such as isochronous and isothermal quenching of L-PBF Cu–Al–Ni SMAs, resulted in superior shape memory behaviour (3.3-fold shape recoverable strain to as-built and complete shape recovery) as well as improved mechanical properties [25]. Finally, post-printing heat treatments may assess phase stability in AB L/E-PBF microstructures, which could eliminate the need for additional post-processing steps.

As previously mentioned, the presence of porosity, crack susceptibility, segregation, etc., in AMed Cu alloy parts is inherent to L/E-PBF, which is detrimental to their multifunctional properties. HIP mitigates these challenges by minimising pores and healing cracks through compressive stress, reducing residual stresses, and resolving anisotropy by diffusing atoms at high temperatures (80% of $T_{solidus}$) while concurrently applying pressure for an extended period of time. Although HIP has enhanced the reliability and performance of L/E-PBF parts, it is limited by size constraints, high energy consumption for a small number

of parts, ineffectiveness for surface or near-surface pores, etc. [198]. Generally, HIP was tested for L/E-PBF Cu alloys at 750–1030 °C, 200–700 MPa, and 30-180 minutes. These parameters differed from typical Cu alloy HIP treatment, which uses 800–950 °C at 100-200 MPa and holding times below 3 h [328–330]. Jóźwik et al. [103] studied the impact of HIP variables such as temperature (850-1030 °C), isostatic pressure (550-700 bar), and holding time (0-30 minutes) on the porosity, hardness, and electrical conductivity of high- and low-density Cu–Ni–Si alloy samples. HIP-treated samples of Cu–Ni–Si alloy improved density by up to 2.2% and hardness by 24%, significantly boosting conductivity (250-472%), while porosity persisted in low-density samples. In L-PBF GRCop–42, HIP treatment was thickness-sensitive and significantly improved %EL (59% for 2.1 mm, 80% for 1.5 mm) and HCF performance due to reduced porosity (effective in closing smaller pores $< 25{,}000\ \mu m^3$) compared to AB specimens, but significantly reduced YS (42% for 2.1 mm, 39% for 1.5 mm) and UTS (27% for 2.1 mm, 28% for 1.5 mm) due to relieved RS [198]. Similarly, L-PBF GRCop–84 lattices, HIP treatment showed a strong correlation between unit cell size and porosity, where 4 mm cells (40%) exhibited lower porosity than 2 mm cells (28%), which was the key factor in shifting the collapse mechanism from shear banding (AB) to layer-by-layer collapse (HIP-treated) [260]. In an alternative study, Demeneghi et al. [198] found HIP treatment reduced porosity in Cu alloy samples (0.7-2.0 mm thick), with a void volume ratio dropping from 15.9 to 99.9%. Additionally, the HIP treatment appeared to have mixed effects on the surface roughness of the Cu alloys (Sa values for 0.7 mm samples enhanced from 12 to 22 μm, while 1 mm samples declined from 18 to 16 μm) [198]. Minneci et al. [331] noticed a linear relationship between lattice parameter and temperature after HIP treatment in L-PBF GRCop–84, indicating minimal microstructural or compositional changes (stable Cr_2Nb precipitates after HIP). Furthermore, additional features such as increased grain size, the retention of some columnar grains, reduced visibility of melt pool boundaries, and a weakening of the texture were identified following HIP [331]. Additionally, HIP enhanced the functional properties of L-PBF Cu alloys. HIP-treated L-PBF Cu–Ag alloy samples demonstrated superior tribological characteristics (lower wear rate), electrical conductivity (reaching 80-93% IACS compared to 50% for AB state), and hardness (120-150 HV0.5 compared to around 50 HV0.5 for AB) as compared to the AB state [222]. The implementation of the HIP approach as a post-processing method in the AM of Cu alloys remains constrained. Table 8 concludes with a literature review of the impact of HIP on AMed Cu alloy and identifies some major knowledge gaps. First, comprehensive studies are currently lacking in fully elucidating the effects of HIP on the strength-ductility trade-off, the strength-conductivity paradox, and other key functional properties of Cu alloys. Second, there is a notable scarcity of research specifically addressing the influence of HIP when employing alternative beam sources for Cu alloy printing. Third, HIP modifies the microstructural properties of AM components, potentially affecting texture and anisotropy; the nexus between microstructure and properties requires additional investigation for L/E-PBF Cu alloys. Finally, a two-step heat treatment combining HIP (as the limited cooling rate during HIP may induce unintended precipitation in L/E-PBF Cu alloys) with solution treatment or aging can be investigated to ascertain the process scope for superior comprehensive properties.

11. L-PBF and E-PBF Cu alloy physical and data-based modelling

Fig. 8 depicts a material science octahedron with composition as its foundation and modelling at the apex. On top of this, the modelling superimposes information from composition, process, microstructure, post-processing, and performance to further optimise material composition and overall performance through iterative design and trained machine learning (ML) models, etc. Modelling includes data-driven modelling, physical modelling, and hybrid modelling. These modelling concepts helped to understand better the complex process dynamics, which include melting and solidification behaviour, material-specific behaviours, process parameter dependencies, etc., ultimately influencing the overall performance and defect formation of L/E-PBF Cu alloys, as previously discussed. Notably, the multifaceted interactions among composition-properties-process, which frequently vary with composition and process (L/E-PBF), present hurdles for standard optimisation methods based on trial-and-error, which is ultimately costly and time-consuming. Modelling techniques, including empirical, numerical, and hybrid models, facilitate comprehension of the complex material-microstructure-performance link of L/E-PBF Cu alloys through in-depth analysis of heat and mass transfer phenomena. The literature classifies PBF modelling by length scale into macroscopic, mesoscopic, microscale, and nanoscale models [333]. Macroscopic models address heat transfer, fluid dynamics, powder dynamics, process parameters optimisation, etc. Mesoscopic models investigate particle behaviour and interactions, whereas microscale models study melt pool dynamics, solidification, microstructure evolution, etc. Nanoscale models explore the atomic/molecular level, yielding insights into crystallography, phase formation, etc. Currently, numerical models are predominantly employed in the simulation study of L-PBF Cu alloy, accurately capturing complex fluid flow, heat, and mass transfer phenomena due to their precision, flexibility, and ability to manage intricate multi-physics interactions [60,87,211,334–336]. Wang et al. [211] established a 3D multifaceted powder-bed model to simulate the morphology and temperature behaviour of melt pools for highly conductive materials by combining the discrete element method (DEM) and computational fluid dynamics (CFD). The circular melt pool shape observed for Cu alloys, as compared to the comet melt pool shapes and defect-free L-PBF Cu alloy parts requires precise management of bubble dynamics and thermal stability, regulated via energy density tuning, laser power control, and scanning speed adjustment [211]. Ren et al. [60] used the Fresnel and Hagan-Ruben equations in a CFD and DEM framework to explore laser reflection on melt pool dynamics. The Fresnel absorption rule was shown to be less effective for high-reflectivity materials such as Cu alloys, whereas the Hagan-Ruben relation successfully models continuous single tracks. Additionally, heat conduction and melt pool evolution altered global absorptivity, which showed three stages (rise, drop, and stable) and was adversely affected by balling for Cu alloys [60]. Li et al. [87] employed a high-fidelity CFD model based on the volume of fluid method to simulate the melt pool dynamics of the Cu–Cr–Zr alloy, exploiting the ray-tracing (RT) method to address the effect of layer thickness on melt pool dynamics and defect formation since low layer thickness (~30 μm) limits the build rate. Their simulation and experiment results were consistent and indicated that increased layer thickness (30 to 60 μm) demonstrated melt flow instability and defects, which could be mitigated through remelting [87]. Similarly, the top free surface heat source model, which was integrated with CFD and DEM, was utilised to simplify simulations for laser-powder interaction of L-PBF Cu alloys. In this simulation investigation, a scattered heat source (SHS) model was applied, outperforming the concentrated heat source in terms of energy distribution and computational efficiency and accurately predicting track width and depth. Furthermore, scanning speed was critical for producing defect-free tracks, and increased scanning speed reduced effective absorptivity due to melting mode shift [336]. Further, the high reflectivity and thermal conductivity of Cu alloys present challenges for L-PBF because they affect the behaviour of the melt pool, which influences the likelihood of defects and overall performance. Current simulations focus on optimising process parameters for surface roughness and stress distribution to enhance the mechanical performance of L/E-PBF Cu alloy components. Ren et al. [335] employed a mesoscopic CFD model with the RT method to simulate laser-matter interactions and melt pool dynamics in pre- and post-contour scanning. Pre-contour scanning enhanced laser absorption and surface quality, while post-contour scanning led to defects and increased roughness owing to variations in global absorptivity. Interestingly, roughness for vertical surfaces in numerical simulations complemented

experimental results, showing the possibility of altering surface quality through numerical modelling [335]. Kremer et al. [230] utilised finite element modelling to predict the microstructure and residual stresses in L-PBF Cu–10Sn alloys. The model accurately predicted fine-grained microstructure and residual stresses, with minor deviations in surface residual stress values due to measurement limitations and model simplifications. Overall, current models focus on melt pool thermal-fluid dynamics and laser reflection behaviour for defect reduction and process optimisation. Future studies should focus on comprehensive property prediction and alloy design for L/E-PBF Cu components.

Although modelling efficiently captures complicated physics and can aid in designing high-performance Cu alloy parts, current numerical simulation studies of L/E-PBF Cu alloys are limited to three length scales: macroscopic, mesoscopic, and microscopic models, and mostly focus on two aspects. First, a stable melt pool can be obtained by simulating the solidification process to refine process parameters. Second, the results of the thermomechanical analysis of the melt pool improve the processability and performance of the L-PBF Cu alloys. Future simulations could focus on developing models capable of forecasting multi-scale microstructure evolution, such as micro-segregation, precipitation, etc., and correlating them with material performance in L/E-PBF Cu alloys, particularly emphasising nanoscale simulation (processing–property nexus). Furthermore, simulations of mechanical, electrical, functional, etc. properties could be explored for Cu alloy part design in the future to understand the potential to develop site-specific microstructures, a hallmark of L-PBF with multi-scale microstructural variation. Moreover, real-time melt pool monitoring, simulation, and predictive site-specific control of microstructures remain challenges for metal AM that can be addressed in the future.

Despite the numerous benefits of PBF modelling, constructing highly accurate physical models to combine a diversity of processes with multiple physics, scales, and materials is daunting due to data dependency, the need for in-depth knowledge of the process, sensory calibration complications, assumptions introduced in modelling, and significant computational resources. Data-driven modelling, especially machine learning, addresses traditional modelling limitations by effectively handling incomplete data sets and enabling in-situ process monitoring. These models provide in-situ monitoring and closed-loop process control while running quickly and effectively with minimal computational resources. In the future, the nascent understanding of L/E-PBF Cu alloys could be enhanced via a simulation-guided AI active learning approach, predicting the entire process space for AM Cu parts, optimising process parameters, and monitoring melt pool behaviour to print defect-free parts with optimal strength-ductility, strength-conductivity, corrosion resistance, and functional properties. Future research should combine data-driven approaches with numerical simulations for closed-loop control during the L/E-PBF process of Cu alloys to boost the prediction of composition-process performance relationships.

12. Conclusive digest

12.1. Feedstock

The review presented here convincingly established that, particularly for NIR lasers, the printability of Cu alloy/composite hinges on the powder feedstock characteristics (composition, PSD, morphologies, O_2 content, powder rheology, etc.). The literature reveals four primary approaches for improving the processability of Cu feedstock: mechanical mixing, atomization, selective composite approach, and powder surface engineering. Mechanical mixing provides greater flexibility for Cu feedstock design and rapid preliminary investigation but faces challenges with segregation and non-homogeneity. Atomization addresses these challenges, though it is limited by Cu feedstock design freedom and alloy availability in the market. In the selective composite approach, carbon-based and ceramic particles are used, which enhance electrical conductivity in printed parts, while powder surface engineering involves adding elements/particles to the surface of copper/pre-alloyed powder to improve processability. However, scalability, reliance on pre-alloyed powder, and the cost of expensive nanoparticles remain key obstacles for both powder surface engineering and selective composite approaches. Finally, in the pursuit of enhancing functionality, multi-material approaches are being explored, which are constrained in the context of printed Cu alloys.

12.2. Process-induced defects

L/E-PBF Cu alloys/composites are plagued by defects that fall into three categories: microstructural, surface, and geometrical/dimensional. These defects in the printed parts are frequently the consequence of untuned process parameters, which lead to process instabilities. Most defects have an adverse impact on material performance and, in some instances, lead to part failure and recoater blade malfunctions. Overall, the strategies for defect minimisation in L/E-PBF Cu alloys include the optimisation of process parameters and feedstock characteristics combined with simulation and modelling, as well as the implementation of post-processing techniques to achieve unprecedented combinations of corrosion behaviour, mechanical and functional properties, etc.

12.3. Material properties

This review presents a comparative analysis of tensile properties (YS, UTS, and %EL) for various L/E-PBF Cu alloys/composites, with a particular emphasis on the strength-ductility trade-off. Most studies have concentrated on NIR laser-based printing, followed by E-PBF and green laser processes. The strength-ductility trade-off is significantly influenced by process parameter selection and exhibits orientation dependency (anisotropy). It has been demonstrated that the addition of reinforcing particles to the Cu matrix, such as ceramic, metal, and carbon particles, has both antagonistic and synergistic effects on tensile behaviour. Most reported printed Cu alloys/composites exhibit UTS below 600 MPa and %EL below 40% (Fig. 51), yet they show potential for overcoming the conventional strength-ductility trade-off. Collectively, feedstock characteristics, process parameters, microstructural features, defects, build orientation, and part geometry are pivotal in influencing anisotropy and the tensile behaviour of printed Cu alloys/composites. Subsequently, compressive properties were discussed, particularly in the context of SMAs and lattice structures, with L/E-PBF demonstrating superior compressive behaviour. Analogous to tensile behaviour, compressive behaviour is influenced by the same factors discussed earlier. Following the discussion on tensile and compressive properties, hardness (microindentation and nanoindentation) was analysed to assess material performance. Most studies report a significant Vickers hardness gradient along the build direction. Interestingly, the YS and precipitation characteristics of L/E-PBF Cu alloys/composites can be indirectly estimated from hardness measurements. The hardness is influenced by feedstock characteristics, build orientation, process parameters (L-PBF vs. E-PBF), and post-printing heat treatments.

Following that, the electrical conductivity of L/E-PBF Cu alloys/composites was reviewed, emphasising the strength-electrical conductivity trade-off. A classification of four zones (HSMC, HSHC, MSHC, and MSMC; Figs. 60, 62, and 63) based on strength and conductivity was proposed. Most investigated Cu alloys/composites, regardless of process type (green laser, NIR laser, and electron beam powder bed fusion) or process parameters, fall into the MSMC and MSHC zones in the AB state, with few demonstrating electrical conductivity comparable to their wrought counterparts. The highest reported electrical conductivity for the L-PBF Cu–LaB_6 alloy is 98.4% IACS, while the best combination of strength-conductivity was attained by the L-PBF Cu–1.3Cr alloy with a UTS of 640 MPa and an electrical conductivity of 91% IACS. Moreover, printed parts exhibited electrical conductivity anisotropy. The supersaturated state of the AB Cu alloys, along with L/E-PBF defects such as porosity, segregation, etc., reduced electrical conductivity. However,

heat treatment substantially improved the electrical conductivity of the printed heat-treatable Cu alloy. Beyond these factors, Cu alloy/composite powder feedstock characteristics, build orientation, size effects, and process parameters also influence the electrical properties of AMed Cu alloy parts.

The literature indicates that most L/E-PBF Cu alloys in the AB state exhibit lower thermal conductivity than conventional alloys, primarily assessed via the Wiedemann-Franz law, with limited direct measurements. The optimal post-printing heat treatments, composition, and process parameters are critical for achieving the best combination of strength, ductility, and thermal conductivity. In terms of creep behaviour, the literature review revealed that L-PBF Cu alloys exhibited creep anisotropy. Despite the limited study, an in-depth investigation into creep behaviour, considering feedstock characteristics, process parameters, and post-printing heat treatments, is vital for establishing the potential of Cu alloys in high-temperature applications. Subsequently, limited research, mainly focused on LCF, suggested that the fatigue performance of L-PBF Cu alloys was primarily governed by process-induced defects, heat treatment, and size effects.

The corrosion behaviour of the reviewed L/E-PBF Cu alloys was mostly reported for short-term exposures, with limited long-term data for certain Cu alloys (such as Cu–Sn, NAB alloy, and Cu–Ni–Si). The corrosion behaviour of L/E-PBF Cu alloys is strongly influenced by microstructural attributes such as texture and grain structure, as well as subsequent post-printing heat treatments. Notably, heat treatment demonstrated a complex influence on corrosion behaviour, exhibiting both antagonistic and synergistic effects. Lastly, the tribological properties of Cu alloys were reviewed, though limited studies exist, and few L/E-PBF Cu alloys/composites outperformed their counterparts, suggesting the potential of L/E-PBF Cu alloys/composites for tailored tribological performance.

12.4. Strengthening mechanism

The reviewed L/E-PBF Cu alloys demonstrated grain boundary, solid solution, Orowan precipitation, dislocation, and load transfer strengthening mechanisms, along with HDI strengthening, contributing to the yield strength of the L/E-PBF Cu alloy/composite parts before and after heat treatments. The dominance of specific strengthening mechanisms significantly influenced the specific properties (electrical, creep properties, etc.) of L/E-PBF Cu alloys/composites. Notably, electrical conductivity was adversely impacted by the solid solution strengthening mechanism but positively impacted by the Orowan precipitation strengthening mechanism, which specifically addressed the strength-conductivity trade-off. Interestingly, the HDI strengthening mechanism emerged as a promising strategy for resolving the strength-ductility-conductivity paradox.

12.5. Post-processing heat treatments

A comprehensive overview of heat treatment methods for L/E-PBF Cu alloys identified mostly ST, DA, SAT, and HIP as standard techniques for transforming the microstructure. These techniques modified the microstructure, thereby addressing the intrinsic constraints of AM in achieving intended phase transitions and microstructural properties. Temperature, holding duration, and cooling rate are essential parameters for optimum heat treatment, considerably modulating the final microstructure and, ultimately, the properties of Cu alloy printed parts. The L/E-PBF Cu alloy heat treatment significantly altered anisotropy, cell size, grain morphology, texture, segregation, etc. Thus, it is possible to customise the subsequent printed Cu alloy parts to achieve the requisite mechanical and functional performance.

12.6. Modelling

Reviewed modelling studies on limited L/E-PBF Cu alloys mostly used physical modelling to comprehend complex heat, mass, and fluid flow dynamics during powder-laser interactions. These simulations aided process parameter optimisation by revealing the level of defect formation for certain process parameter sets and clarifying complex phenomena at a faster rate and lower cost.

13. Visionary exploration avenue

As indicated in the reviewed studies on L/E-PBF Cu alloys/composites, the Cu–Cr–Zr alloy is a research hotspot for researchers aiming to optimise the material-process-performance nexus; however, there is a considerable scarcity of research on other alloying systems, such as Cu–Fe, Cu–Sn, Cu–Ni, Cu–Ag, Cu–Sc, Cu–La_2O_3, AlN, TiN, Ti_3Si_2, hybrid ceramic particles, Cu-based in-situ alloys, advanced sustainable lean Cu-based alloys, etc. Consequently, alloy design holds significant potential to expand the material palette of Cu alloy/composite systems for L/E-PBF, which is a pressing need in the industry. The stated UTS of all L/E-PBF printed copper alloy/composite was below 800 MPa, with ductility under 40% in the AB state. After post-printing heat treatments, only one composition, L-PBF Cu–Sn alloys, demonstrated a synergistic combination of ductility (~56%) and UTS (~840 MPa). Overcoming the strength-ductility trade-off, as well as the strength-conductivity trade-off remains a challenge for L/E-PBF Cu alloys. No L/E-PBF Cu alloy/composite has reached the HSHC (UTS $>$ 600 MPa, $>$ 60% IACS) zone in the AB state, and only two Cu alloys (Cu–Cr and Cu–Cr–Zr alloy) were found in the HSHC zone even after heat treatment. In this respect, a significant portion of future research is anticipated from the design of L/E-PBF-friendly Cu alloy/composite feedstocks, which not only aim to address reflectivity but also disrupt the strength-ductility (UTS $>$ 600 MPa and %EL $>$ 40%) and strength-conductivity (UTS $>$ 600 MPa, $>$ 60% IACS) trade-offs to achieve tuned synergistic material properties in the L/E-PBF Cu alloy/composite.

Presently, the ex-situ detection approach is the primary focus for identifying inevitable, dynamic, and stochastic process-induced defects, which are the main roadblocks to achieving near-fully dense L/E-PBF Cu alloy/composite parts. However, the in-situ approach is still being developed and may provide a deeper understanding of defect formation and effective mitigation strategies through process optimisation and parameter control in conjunction with modelling/AI/ML for next-generation L/E-PBF Cu alloy/composite parts, which need further exploration to bridge the comprehension gap.

Currently, the primary focus of L/E-PBF Cu alloy/composite research is their static mechanical and electrical properties. Nevertheless, further investigation is required into critical properties such as tribology, corrosion, creep, functional, dynamic, and high-temperature mechanical behaviours to enhance the comprehensive performance of L/E-PBF Cu alloy/composite. In addition, it is imperative to comprehend the process parameters-microstructure nexus for fabricating next-generation L/E-PBF Cu alloy/composite parts free from anisotropy and the strength-conductivity and strength-ductility trade-offs. Future research is expected to focus on site-specific microstructures, the high build rate of printed parts, and multi-material printing using optimised processing parameters.

Cu alloy/composite feedstock characteristics and process parameters significantly influence microstructure, defect susceptibility, and, ultimately, material properties. To achieve fully dense and high-performance parts by resolving potential microstructural anisotropy and defects, an immediate corrective approach should be analysed in contrast to the current reactive approach. Thus, it is crucial to conduct further research in L/E-PBF Cu alloys/composites using AI and ML models to facilitate the modification of real-time parameters for controlling in-situ microstructure and defect identification. Further, considering the challenges posed by intense laser/electron beam interactions coupled with process dynamics, which induce a metastable microstructure in Cu alloys/composites with multi-scale characteristics, leading to variations in local properties that hinder bespoke

performance. This complexity necessitates post-print heat treatment to address the trade-offs among strength, conductivity, ductility, etc., ultimately optimising holistic material performance. Although most L/E-PBF Cu alloys rely on conventional heat treatments, future advancements should aim to eliminate or innovate post-printing treatments (thermal, thermo-mechanical, etc.) for high-performance, fully dense - printed parts. Lastly, research should examine how Cu alloy powder reuse influences feedstock characteristics, printability, and material properties in L/E-PBF, which is crucial for sustainability.

Declaration of competing interest

The authors declare that they have no known competing financial interests or personal relationships that could have appeared to influence the work reported in this paper.

Acknowledgements

The authors express their profound gratitude to all researchers whose pioneering and insightful contributions to the field of laser and electron beam powder bed fusion of copper alloys have significantly enriched the foundational principles upon which this review is built. Special thanks are extended to RAM for guiding me in focusing on absorbing the research articles. This study was conducted as part of the MICS (Made in Italy—Circular and Sustainable) Extended Partnership, receiving generous funding from the European Union's Next-Generation EU initiative (PIANO NAZIONALE DI RIPRESA E RESILIENZA (PNRR)—MISSIONE 4 COMPONENTE 2, INVESTIMENTO 1.3—D.D. 1551.11-10-2022, PE00000004). The content of this manuscript reflects solely the views and opinions of the authors, and neither the European Union nor the European Commission can be held liable for any interpretations or outcomes.

Appendix A. Supplementary data

Supplementary data to this article can be found online at https://doi.org/10.1016/j.matdes.2025.113742.

References

[1] F. Edition, M.F. Ashby, Material Selection in Mechanical Design, (2011).
[2] J.R. Davis, Copper and copper alloys, ASM Int. (2001).
[3] X. Li, B. Ma, C. Wang, Y. Chen, Sustainable recovery and recycling of scrap copper and alloy resources: A review, Sustain. Mater. Technol. (2024) e01026.
[4] D. Zheng, R. Li, J. Kang, M. Luo, T. Yuan, C. Han, Achieving superelastic shape recoverability in smart flexible CuAlMn metamaterials via 3D printing, Int J Mach Tool Manu 195 (2024) 104110.
[5] Z. Kuai, Z. Li, B. Liu, Y. Chen, H. Li, P. Bai, Microstructure and mechanical properties of CuCrZr/316L hybrid components manufactured using selective laser melting, J. Alloy. Compd. 955 (2023) 170103.
[6] L. Zhang, P. Dong, Y. Zeng, H. Yao, J. Chen, Additive manufacturing of Inconel 718/CuCrZr multi-metallic materials fabricated by laser powder bed fusion, Addit. Manuf. 92 (2024) 104377.
[7] A. Marques, A. Cunha, M. Gasik, O. Carvalho, F.S. Silva, F. Bartolomeu, 3D multi-material laser powder bed fusion: Ti6Al4V–CuNi2SiCr parts for aerospace applications, Prog. Addit. Manuf. 9 (2024) 391–400.
[8] P.R. Gradl, C.S. Protz, D.L. Ellis, S.E. Greene, Progress in additively manufactured copper-alloy GRCop-84, GRCop-42, and bimetallic combustion chambers for liquid rocket engines, in: International Astronautical Congress (IAC), 2019.
[9] A.H. Seltzman, S.J. Wukitch, Fracture characteristics and heat treatment of laser powder bed fusion additively manufactured GRCop-84 copper, Mater. Sci. Eng. A 827 (2021) 141690.
[10] C. Wachter, F. Haller, F. Liebetrau, Additive Manufactured Copper Conductors: Impedance Characteristics of Samples with Varying Density and Cross-section profile, in: 2022 12th International Electric Drives Production Conference (EDPC), IEEE, 2022: pp. 1–5.
[11] J. Robinson, A. Arjunan, A. Baroutaji, M. Martí, A.T. Molina, Á. Serrano-Aroca, A. Pollard, Additive manufacturing of anti-SARS-CoV-2 copper-tungsten-silver alloy, Rapid Prototyp. J. 27 (2021) 1831–1849.
[12] H. Xie, X. Tang, X. Chen, F. Sun, L. Dong, Y. Tan, H. Chu, H. Zhou, P. Liu, S. Fu, The effect of build orientations on mechanical and thermal properties on CuCrZr alloys fabricated by laser powder bed fusion, J. Mater. Res. Technol. 23 (2023) 3322–3336.
[13] F. Crescenzi, C. Bachmann, M. Richou, S. Roccella, E. Visca, J.-H. You, Design study of ITER-like divertor target for DEMO, Fusion Eng. Des. 98 (2015) 1263–1266.
[14] S. Sohrabi, J. Fu, L. Li, Y. Zhang, X. Li, F. Sun, J. Ma, W.H. Wang, Manufacturing of metallic glass components: Processes, structures and properties, Prog. Mater Sci. (2024), 101283.
[15] H. Luo, M. Wang, W. Liao, Y. Du, Unraveling the interrelation between process parameters and defects to enhance the strength of laser additively manufactured CuZrAlTi bulk metallic glass, J. Mater. Res. Technol. (2024).
[16] L. Deng, L. Zhang, K. Kosiba, R. Limbach, L. Wondraczek, G. Wang, D. Gu, U. Kühn, S. Pauly, CuZr-based bulk metallic glass and glass matrix composites fabricated by selective laser melting, J. Mater. Sci. Technol. 81 (2021) 139–150.
[17] M. Frey, J. Wegner, E.S. Barreto, L. Ruschel, N. Neuber, B. Adam, S.S. Riegler, H.-R. Jiang, G. Witt, N. Ellendt, Laser powder bed fusion of Cu-Ti-Zr-Ni bulk metallic glasses in the Vit101 alloy system, Addit. Manuf. 66 (2023) 103467.
[18] D. Yanagida, T. Nakamoto, H. Minami, T. Miki, S. Uchida, T. Kimura, K. Watanabe, Electrical discharge machining using copper electrode made by additive manufacturing, Procedia CIRP 95 (2020) 449–453.
[19] Y. Noda, N. Yoshioka, N. Suzuki, T. Fukai, T. Yoshihara, K. Koshiro, Method for forming an electrical contact material, U.S, Patent No. (1996) 5480472.
[20] S. Raghavendra, P. Jayashree, D.A. Rita, G. Piras, D. Scheider, M. Chemello, M. Benedetti, Wear and material characterization of CuSn10 additively manufactured using directed energy deposition, Addit. Manuf. Lett. 6 (2023) 100136.
[21] S. Scudino, C. Unterdörfer, K.G. Prashanth, H. Attar, N. Ellendt, V. Uhlenwinkel, J. Eckert, Additive manufacturing of Cu–10Sn bronze, Mater. Lett. 156 (2015) 202–204.
[22] R. Rahmani, P.R. Resende, R. Couto, S.I. Lopes, R. Kumar, H.S. Maurya, J. Karimi, A.M. Afonso, A. Hussain, J.C.C. Abrantes, Structural analysis of selective laser melted copper-tin alloy, J. Alloys Metallurgical Syst. 7 (2024) 100097.
[23] W. Lu, W. Zhai, J. Wang, X. Liu, L. Zhou, A.M.M. Ibrahim, X. Li, D. Lin, Y. M. Wang, Additive manufacturing of isotropic-grained, high-strength and high-ductility copper alloys, Addit. Manuf. 38 (2021) 101751.
[24] E.M. Mazzer, M.R. Da Silva, P. Gargarella, Revisiting Cu-based shape memory alloys: recent developments and new perspectives, J. Mater. Res. 37 (2022) 162–182.
[25] Y. Zhang, L. Xu, L. Zhao, W. Chen, M. Liu, W. Ren, Y. Han, Simultaneous enhancement of mechanical and functional properties by heat-treatment in CuAlNi shape memory alloys fabricated by laser powder bed fusion, Addit. Manuf. (2024) 104099.
[26] Y. Liu, J. Zhang, Q. Sun, M. Li, M. Yan, X. Cheng, M. Li, M.-X. Zhang, Laser powder bed fusion of copper matrix iron particle reinforced nanocomposite with high strength and high conductivity, J. Mater. Sci. Technol. 134 (2023) 50–59.
[27] Y. Li, X. Yuan, B. Yang, X. Ye, P. Zhang, H. Lang, Q. Lei, J. Liu, Y. Li, Hierarchical microstructure and strengthening mechanism of Cu-36.8 Fe alloy manufactured by selective laser melting, J. Alloy. Compd. 895 (2022) 162701.
[28] C. Wen, Y. Qiu, Z. Zhang, K. Li, C. Deng, L. Hu, D. Chen, Y. Lu, S. Zhou, Deformation behavior of heterogeneous lamellar Cu-Fe-P immiscible alloys with enhanced strength and ductility produced by laser powder bed fusion, J. Alloy. Compd. 971 (2024) 172675.
[29] Y. Liu, J. Zhang, Q. Tan, Y. Yin, S. Liu, M. Li, M. Li, Q. Liu, Y. Zhou, T. Wu, Additive manufacturing of high strength copper alloy with heterogeneous grain structure through laser powder bed fusion, Acta Mater. 220 (2021) 117311.
[30] T.J. Horn, D. Gamzina, Additive manufacturing of copper and copper alloys (2020). https://doi.org/10.31399/asm.hb.v24.a0006579.
[31] R.P. Minneci, E.A. Lass, J.R. Bunn, H. Choo, C.J. Rawn, Copper-based alloys for structural high-heat-flux applications: a review of development, properties, and performance of Cu-rich Cu–Cr–Nb alloys, Int. Mater. Rev. 66 (2021) 394–425.
[32] E. Sharabian, M. Leary, D. Fraser, S. Gulizia, Electron beam powder bed fusion of copper components: A review of mechanical properties and research opportunities, Int. J. Adv. Manuf. Technol. 122 (2022) 513–532.
[33] B. Sankar, C. Vinay, J. Vishnu, K.V. Shankar, G.P. Gokul Krishna, V. Govind, A. J. Jayakrishna, Focused review on Cu–Ni–Sn spinodal alloys: from casting to additive manufacturing, Met. Mater. Int. 29 (2023) 1203–1228.
[34] X. Tang, X. Chen, F. Sun, P. Liu, H. Zhou, S. Fu, The current state of CuCrZr and CuCrNb alloys manufactured by additive manufacturing: A review, Mater. Des. 224 (2022) 111419.
[35] F. Zhou, Y. Zhou, K. Song, Y. Zhang, R. Yang, S. Yang, L. Lu, Y. Yu, L. Liu, J. Chen, The influence of microalloying and preparation process on phase transformation, mechanical properties, and friction/corrosion behavior of Cu–Ni–Sn alloys: A review, J. Mater. Res. Technol. (2023).
[36] K. Morshed-Behbahani, A. Aliyu, D.P. Bishop, A. Nasiri, Additive manufacturing of copper-based alloys for high-temperature aerospace applications: a review, Mater Today Commun (2024) 108395.
[37] E. DIN, ISO/ASTM 52900: 2021 Additive Manufacturing—General Principles—Fundamentals and Vocabulary, (2021).
[38] Y.Y.C. Choong, H.W. Tan, D.C. Patel, W.T.N. Choong, C.-H. Chen, H.Y. Low, M. J. Tan, C.D. Patel, C.K. Chua, The global rise of 3D printing during the COVID-19 pandemic, Nat. Rev. Mater. 5 (2020) 637–639.
[39] R.L. Germscheidt, M.B. Silva, E. Datti, J.A. Bonacin, Materials and challenges of 3D printing for defense applications and humanitarian actions, in 3D Printing, CRC Press, 2023, pp. 471–483.
[40] B. Isaac, White House Convenes to Propel Additive Manufacturing Investments, (2024). https://www.3dnatives.com/en/white-house-am-forward-fund-200220244/ (accessed July 20, 2024).

[41] 3D Printing and Additive Manufacturing 2024-2034: Technology and Market Outlook IDTechEx Research Report, (2024).
[42] H.Y. Jun, E.J. Lee, S.O. Ryu, Synthesis and characterization of copper ink and direct printing of copper patterns by inkjet printing for electronic devices, Curr. Appl Phys. 20 (2020) 853–861.
[43] G. Demeneghi, B. Barnes, P. Gradl, D. Ellis, J.R. Mayeur, K. Hazeli, Directed energy deposition GRCop-42 copper alloy: Characterization and size effects, Mater. Des. 222 (2022) 111035.
[44] E.S. Khoroshko, A.V. Filippov, N.N. Shamarin, E.N. Moskvichev, V. R. Utyaganova, S.Y. Tarasov, N.L. Savchenko, E.A. Kolubaev, V.E. Rubtsov, D. V. Lychagin, Structure and mechanical properties of Cu–Al–Si–Mn system-based copper alloy obtained by additive manufacturing, Russ. Phys. J. 64 (2021) 333–339.
[45] X. Yang, Y. Qi, W. Zhang, Y. Wang, H. Zhu, Laser powder bed fusion of C18150 copper alloy with excellent comprehensive properties, Mater. Sci. Eng. A 862 (2023) 144512.
[46] S.D. Jadhav, S. Dadbakhsh, L. Goossens, J.P. Kruth, J. Van Humbeeck, K. Vanmeensel, Influence of selective laser melting process parameters on texture evolution in pure copper, J. Mater. Process. Technol. 270 (2019) 47–58.
[47] J. Yin, W. Zhang, L. Ke, H. Wei, D. Wang, L. Yang, H. Zhu, P. Dong, G. Wang, X. Zeng, Vaporization of alloying elements and explosion behavior during laser powder bed fusion of Cu–10Zn alloy, Int J Mach Tool Manu 161 (2021) 103686.
[48] S. Zhang, H. Zhu, Z. Hu, X. Zeng, F. Zhong, Selective laser melting of Cu10Zn alloy powder using high laser power, Powder Technol. 342 (2019) 613–620.
[49] J. Liu, P. Wen, Metal vaporization and its influence during laser powder bed fusion process, Mater. Des. 215 (2022) 110505.
[50] J. Helm, A. Schulz, A. Olowinsky, A. Dohrn, R. Poprawe, Laser welding of laser-structured copper connectors for battery applications and power electronics, Weld. World 64 (2020) 611–622.
[51] Z. Hu, Z. Du, Z. Yang, L. Yu, Z. Ma, Preparation of Cu–Cr–Zr alloy by selective laser melting: Role of scanning parameters on densification, microstructure and mechanical properties, Mater. Sci. Eng. A 836 (2022) 142740.
[52] R. Zheng, S.F. Li, R.D.K. Misra, K. Kondoh, Y.F. Yang, Role of W in W-coated Cu powder in enhancing the densification-conductivity synergy of laser powder bed fusion built Cu component, J. Mater. Process. Technol. 322 (2023) 118169.
[53] N. Babacan, S. Pilz, S. Pauly, J. Hufenbach, T. Gustmann, Tailoring the superelastic properties of an additively manufactured Cu–Al–Mn shape memory alloy via adjusting the scanning strategy, Mater. Sci. Eng. A 862 (2023) 144412.
[54] S.D. Jadhav, P.P. Dhekne, S. Dadbakhsh, J.-P. Kruth, J. Van Humbeeck, K. Vanmeensel, Surface modified copper alloy powder for reliable laser-based additive manufacturing, Addit. Manuf. 35 (2020) 101418.
[55] J. Shen, Z. Li, H. Li, B. Yao, B. Teng, Additive manufacturing of high relative density Cu-0.8 Cr alloy by low power 1064 nm Yb-fiber laser powder bed fusion: Role of Nano-TiC modification, Mater. Lett. 308 (2022) 131141.
[56] X. Liu, H. Wang, K. Kaufmann, K. Vecchio, Directed energy deposition of pure copper using blue laser, J. Manuf. Process. 85 (2023) 314–322.
[57] H. von Lintel, E. Evsiutkina, C. Haase, U. Krupp, K. Jahns, Copper alloys for additive manufacturing: Laser powder bed fusion of CuCr1Zr by using a green qcw-laser, Eur. J. Mater. 3 (2023) 2115945.
[58] E. Moskvichev, N. Shamarin, A. Smolin, Structure and mechanical properties of Cu–Al–Mn alloys fabricated by electron beam additive manufacturing, Materials 16 (2022) 123.
[59] D.G. Ovalle, C. Rock, C. Winkler, D. Hartshorn, C. Barr, T. Cullom, P. Tarafder, T. Prost, E. White, I. Anderson, Microstructure development and properties of micro-alloyed copper, Cu-0.3 Zr-0.15 Ag, produced by electron beam additive manufacturing, Mater Charact 197 (2023) 112675.
[60] Z. Ren, D.Z. Zhang, G. Fu, J. Jiang, M. Zhao, High-fidelity modelling of selective laser melting copper alloy: Laser reflection behavior and thermal-fluid dynamics, Mater. Des. 207 (2021) 109857.
[61] N. Ordás, L. Portolés, M. Azpeleta, A. Gómez, J.R. Blasco, M. Martinez, J. Ureña, I. Iturriza, Development of CuCrZr via electron beam powder bed fusion (EB-PBF), J. Nucl. Mater. 548 (2021) 152841.
[62] Z. Kuai, Z. Li, B. Liu, Y. Chen, S. Lu, X. Tang, T. Liu, Selective laser melting of CuCrZr alloy: Processing optimisation, microstructure and mechanical properties, J. Mater. Res. Technol. 19 (2022) 4915–4931.
[63] M. Colopi, L. Caprio, A.G. Demir, B. Previtali, Selective laser melting of pure Cu with a 1 kW single mode fiber laser, Procedia CIRP 74 (2018) 59–63.
[64] A.Y. Kumar, J. Wang, Y. Bai, S.T. Huxtable, C.B. Williams, Impacts of process-induced porosity on material properties of copper made by binder jetting additive manufacturing, Mater. Des. 182 (2019) 108001.
[65] R. Hu, K. Su, Z. Lao, Y. Cai, B. Fu, M.M.F. Yuen, Z. Gao, M. Cao, Y. Wang, Process of pure copper fabricated by selective laser melting (SLM) technology under moderate laser power with re-melting strategy, Materials 16 (2023) 2642.
[66] N. Babacan, S. Pilz, J. Hufenbach, T. Gustmann, Effects of remelting on the properties of a superelastic Cu–Al–Mn shape memory alloy fabricated by laser powder bed fusion, Shape Mem. Superelasticity 9 (2023) 447–459.
[67] L. Gargalis, J. Ye, M. Strantza, A. Rubenchik, J.W. Murray, A.T. Clare, I. A. Ashcroft, R. Hague, M.J. Matthews, Determining processing behaviour of pure Cu in laser powder bed fusion using direct micro-calorimetry, J. Mater. Process. Technol. 294 (2021) 117130.
[68] S.D. Jadhav, D. Fu, M. Deprez, K. Ramharter, D. Willems, B. Van Hooreweder, K. Vanmeensel, Highly conductive and strong CuSn0. 3 alloy processed via laser powder bed fusion starting from a tin-coated copper powder, Addit. Manuf. 36 (2020) 101607.
[69] S.D. Jadhav, S. Dadbakhsh, J. Vleugels, J. Hofkens, P. Van Puyvelde, S. Yang, J.-P. Kruth, J. Van Humbeeck, K. Vanmeensel, Influence of carbon nanoparticle addition (and impurities) on selective laser melting of pure copper, Materials 12 (2019) 2469.
[70] J. Gao, Q. Han, L. Wang, Z. Liu, S. Soe, Z. Zhang, Y. Gu, Laser powder bed fusion of TiB2-modified Cu15Ni8Sn alloy: Processability, microstructure and mechanical performance, Mater. Sci. Eng. A 855 (2022) 143879.
[71] Y. Liu, J. Zhang, R. Niu, M. Bayat, Y. Zhou, Y. Yin, Q. Tan, S. Liu, J.H. Hattel, M. Li, Manufacturing of high strength and high conductivity copper with laser powder bed fusion, Nat. Commun. 15 (2024) 1283.
[72] D. Corona, M. Beatrici, E. Sbardella, G. Di Domenico, F. Lucibello, M. Zarcone, C. Del Gaudio, 3D printing copper–Graphene oxide nanocomposites, in: AIP Conf Proc, AIP Publishing, 2021.https://doi.org/10.1063/5.0070350.
[73] G. Lupi, M. Poulin, F. Gobber, M.A. Grande, R. Casati, Improving laser powder bed fusion processability of pure Cu through powder functionalization with Ag, Powder Technol. 444 (2024) 120044.
[74] R. Gu, X. Yao, D. Wang, H. Wang, M. Yan, K.S. Wong, Selective laser melting of Cu–10Sn–0.4 P: Processing, microstructure, properties, and brief comparison with additively manufactured Cu–10Sn, Adv. Eng. Mater. 24 (2022) 2100716.
[75] 3D printed copper components for industrial use, (2020). https://delva.fi/en/3d-printed-copper-components-for-industrial-use/ (accessed October 29, 2024).
[76] P. Michael, The future of 3D printing – additive manufacturing experts forecast the next decade, (2022). https://3dprintingindustry.com/news/the-future-of-3d-printing-additive-manufacturing-experts-forecast-the-next-decade-202831/ (accessed November 29, 2024).
[77] NASA 3-D Prints First Full-Scale Copper Rocket Engine Part, (2015). https://www.nasa.gov/technology/nasa-3-d-prints-first-full-scale-copper-rocket-engine-part/ (accessed May 29, 2024).
[78] The Complete Guide to Copper 3D Printing, (2023). https://all3dp.com/1/copper-3d-printing-the-ultimate-guide/ (accessed July 29, 2024).
[79] A. Selema, M.N. Ibrahim, P. Sergeant, Metal additive manufacturing for electrical machines: Technology review and latest advancements, Energies (Basel) 15 (2022) 1076.
[80] 3D printed pure copper Pulsating Heat Pipe, (2022). https://www.beamler.com/3d-printed-pure-copper-pulsating-heat-pipe/ (accessed September 5, 2024).
[81] L. Ladani, J. Razmi, M. Sadeghilaridjani, Fabrication of Cu-CNT composite and Cu using laser powder bed fusion additive manufacturing, Powders 1 (2022) 207–220.
[82] Z. Dai, X. Liu, H. Xie, W. Guan, M. Gao, S. Li, Y. Wu, X. Xiao, G. Ling, G. Bao, Laser additive manufacturing of Cu–Cr–Nb alloys by using elemental powder, J. Mater. Sci. (2024) 1–21.
[83] G. Li, X. Li, C. Guo, Y. Zhou, Q. Tan, W. Qu, X. Li, X. Hu, M.-X. Zhang, Q. Zhu, Investigation into the effect of energy density on densification, surface roughness and loss of alloying elements of 7075 aluminium alloy processed by laser powder bed fusion, Opt. Laser Technol. 147 (2022) 107621.
[84] B. Zhang, H. Xiao, W. Zhang, H. Yang, Y. Wang, D. Peng, H. Zhu, B. Chen, Influence of the thermal conductivity of different CuCr0. 8 substrate state on the formability of laser directed energy deposition Inconel718 single track, Mater Charact 202 (2023) 113015.
[85] A. Gatto, M.L. Gatto, R. Groppo, D. Munteanu, P. Mengucci, Influence of laser powder bed fusion process parameters on the properties of CuZn42 components: case study of the laser surface energy density, Prog. Addit. Manuf. 8 (2023) 843–855.
[86] I.H. ZainElabdeen, L. Ismail, O.F. Mohamed, K.A. Khan, A. Schiffer, Recent advancements in hybrid additive manufacturing of similar and dissimilar metals via laser powder bed fusion, Mater. Sci. Eng. A 146833 (2024).
[87] S. Li, G. Fu, H. Li, Z. Ren, S. Li, H. Xiao, Q. Peng, Effect of layer thickness on the melt pool behavior and pore defects evolution of selective laser melting CuCrZr alloy, J. Alloy. Compd. 967 (2023) 171778.
[88] E. Hori, Y. Sato, T. Shibata, K. Tojo, M. Tsukamoto, Development of SLM process using 200 W blue diode laser for pure copper additive manufacturing of high density structure, J. Laser Appl. 33 (2021).
[89] S. Gruber, L. Stepien, L. Gerdt, E. Lopez, J. Kieser, F. Brueckner, C. Leyens, C. Bratt, Process development for laser powder bed fusion of GRCop-42 using a 515 nm laser source, J. Laser Appl. 35 (2023).
[90] Q. Yang, P. Zhang, Q. Lu, H. Yan, H. Shi, Z. Yu, T. Sun, R. Li, Q. Wang, Y. Wu, Application and development of blue and green laser in industrial manufacturing: a review, Opt. Laser Technol. 170 (2024) 110202.
[91] P. Yang, D. He, W. Shao, Z. Tan, X. Guo, S. Lu, K. Anton, Study of the microstructure and mechanical properties of Cu–Sn alloys formed by selective laser melting with different Sn contents, J. Mater. Res. Technol. 24 (2023) 5476–5485.
[92] M. Bonesso, P. Rebesan, C. Gennari, S. Mancin, R. Dima, A. Pepato, I. Calliari, Effect of particle size distribution on laser powder bed fusion manufacturability of copper, BHM. Berg-Und Huttenmannische Monatshefte 166 (2021) 256–262.
[93] Z. Ma, K. Zhang, Z. Ren, D.Z. Zhang, G. Tao, H. Xu, Selective laser melting of Cu–Cr–Zr copper alloy: Parameter optimization, microstructure and mechanical properties, J. Alloy. Compd. 828 (2020) 154350.
[94] C.L.A. Leung, S. Marussi, M. Towrie, R.C. Atwood, P.J. Withers, P.D. Lee, The effect of powder oxidation on defect formation in laser additive manufacturing, Acta Mater. 166 (2019) 294–305.
[95] M. Malý, D. Koutný, L. Pantělejev, L. Pambaguian, D. Paloušek, Effect of high-temperature preheating on pure copper thick-walled samples processed by laser powder bed fusion, J. Manuf. Process. 73 (2022) 924–938.
[96] A. Speidel, L. Gargalis, J. Ye, M.J. Matthews, A. Spierings, R. Hague, A.T. Clare, J. W. Murray, Chemical recovery of spent copper powder in laser powder bed fusion, Addit. Manuf. 52 (2022) 102711.

[97] W. Zhou, T. Kousaka, S. Moriya, T. Kimura, T. Nakamoto, N. Nomura, Fabrication of a strong and ductile CuCrZr alloy using laser powder bed fusion, Addit. Manuf. Lett. 5 (2023) 100121.
[98] Q. Liu, C. Ren, Z. Song, X. Dan, J. Ju, T. Yang, S. Ni, J. Lu, L. Liu, J. Pan, High-strength and high-conductivity additively manufactured Cu-O alloy enabled by cellular microstructure, Addit. Manuf. (2024) 104244.
[99] H. Ellingham, Transactions and communications, J. Soc. Chem. Ind. 63 (1944) 125–160.
[100] D. Corona, O. Giannini, S. Guarino, G.S. Ponticelli, M. Zarcone, Experimental investigation on the electrical, thermal, and mechanical properties of laser powder bed fused copper alloys, J. Manuf. Process. 76 (2022) 320–334.
[101] S. Greco, K. Gutzeit, H. Hotz, B. Kirsch, J.C. Aurich, Selective laser melting (SLM) of AISI 316L—impact of laser power, layer thickness, and hatch spacing on roughness, density, and microhardness at constant input energy density, Int. J. Adv. Manuf. Technol. 108 (2020) 1551–1562.
[102] D. Tiberto, U.E. Klotz, F. Held, G. Wolf, Additive manufacturing of copper alloys: influence of process parameters and alloying elements, Mater. Sci. Technol. 35 (2019) 969–977.
[103] B. Jóźwik, A. Radoń, S. Topolska, J. Kalabis, M. Karpiński, W. Burian, D. Kołacz, M. Polak, A. Brudny, W. Łoński, Influence of SLM printing parameters and hot isostatic pressure treatment on the structure and properties of CuNi3Si1 alloy, J. Alloy. Compd. 947 (2023) 169531.
[104] Z. Hu, Z. Yang, Z. Du, J. Wu, J. Dong, H. Wang, Z. Ma, Effect of scanning strategy on the anisotropy in microstructure and properties of Cu-Cr-Zr alloy manufactured by laser powder bed fusion, J. Alloy. Compd. 920 (2022) 165957.
[105] M. Sabelle, M. Walczak, J. Ramos-Grez, Scanning pattern angle effect on the resulting properties of selective laser sintered monolayers of Cu-Sn-Ni powder, Opt. Lasers Eng. 100 (2018) 1–8.
[106] C.A. Biffi, J. Fiocchi, S. Boldrini, A. Tuissi, CuCrZr alloy manufactured by LPBF process: correlation between microstructure, mechanical and thermal properties, Lasers Manuf. Mater. Process. 11 (2024) 143–153.
[107] F. Calignano, D. Manfredi, S. Marola, M. Lombardi, L. Iuliano, Production of dense Cu-10Sn part by laser powder bed fusion with low surface roughness and high dimensional accuracy, Materials 15 (2022) 3352.
[108] T. Maity, N. Chawake, J.T. Kim, J. Eckert, K.G. Prashanth, Anisotropy in local microstructure–Does it affect the tensile properties of the SLM samples? Manuf. Lett. 15 (2018) 33–37.
[109] A. Mehta, L. Zhou, H. Hyer, T. Huynh, B. Lu, K. Graydon, E.J. Drobner, S.H. Park, Y. Sohn, Microstructural characteristics and mechanical properties of additively manufactured Cu–10Sn alloys by laser powder bed fusion, Mater. Sci. Eng. A 838 (2022) 142775.
[110] Z. Hu, B. Gan, J. Tan, J. Wu, S. Chen, J. Dong, Z. Ma, The enhancement of laser absorptivity and properties in laser powder bed fusion manufactured Cu-Cr-Zr alloy by employing Y2O3 coated powder as precursor, J. Alloy. Compd. 927 (2022) 167111.
[111] Y. Zhang, L. Xu, L. Zhao, D. Lin, M. Liu, X. Qi, Y. Han, Process-microstructure-properties of CuAlNi shape memory alloys fabricated by laser powder bed fusion, J. Mater. Sci. Technol. 152 (2023) 1–15.
[112] W. Ma, F. Cao, L. Gao, Y. Jiang, Z. Chen, H. Shi, Y. Wang, S. Liang, Strength-ductility synergy in a hierarchical Cu-Cr-Zr alloy processed via laser powder bed fusion, J. Mater. Sci. Technol. 191 (2024) 122–133.
[113] X. Yang, Y. Wang, W. Zhang, Y. Qi, B. Zhang, H. Zhang, H. Zhu, Laser powder bed fusion fabricated Cu-1.8 Cr-1.0 Nb-2.0 Fe alloy with in-situ precipitation strengthening, Mater. Sci. Eng. A 878 (2023) 145222.
[114] EBM Anthology, (2024). https://www.colibriumadditive.com/resources (accessed December 10, 2024).
[115] C. Körner, Additive manufacturing of metallic components by selective electron beam melting—a review, Int. Mater. Rev. 61 (2016) 361–377.
[116] A. Filippov, N. Shamarin, E. Moskvichev, N. Savchenko, E. Kolubaev, E. Khoroshko, S. Tarasov, Heat input effect on microstructure and mechanical properties of electron beam additive manufactured (EBAM) Cu-7.5 wt.% al Bronze, Materials 14 (2021) 6948.
[117] L. Varoto, P. Lhuissier, S. Roure, A. Papillon, M. Chosson, C. Pauzon, X. Bataillon, M. Fivel, E. Boller, P. Lapouge, Multi-scale Cu-Cr composites using elemental powder blending in laser powder-bed fusion, Scr. Mater. 242 (2024) 115957.
[118] A.Y. Nikonov, D.V. Lychagin, A.A. Bibko, O.S. Novitskaya, Aluminum bronze crystallization on deformed base during electron beam additive manufacturing, Metals (Basel) 13 (2023) 1012.
[119] C. Barr, A. Pateras, A. Molotnikov, D. Clarke, M. Brandt, Effect of composition on the tensile and corrosion performance of nickel aluminium bronze produced via laser powder bed fusion, Addit. Manuf. 54 (2022) 102771.
[120] Y. Li, S. Liu, Y. Wang, Y. Wei, J. Wang, L. Zhang, P. Yang, W. Wang, Effect of electron beam energy density on the microstructure and properties of CuCrZr alloy prepared by electron beam powder bed fusion (EB-PBF), Mater Charact 114031 (2024).
[121] Y. Wei, X. Li, J. Li, X. Chu, Y. Li, Q. Yan, W. Jia, Z. Du, W. Wang, S. Liu, Refined microstructure and enhanced properties of CuCr50 alloys produced via electron beam powder bed fusion, J. Alloy. Compd. (2025) 178986, https://doi.org/10.1016/j.jallcom.2025.178986.
[122] Z. Fu, C. Körner, Actual state-of-the-art of electron beam powder bed fusion, Eur. J. Mater. 2 (2022) 54–116.
[123] S. Momeni, R. Guschlbauer, F. Osmanlic, C. Körner, Selective electron beam melting of a copper-chrome powder mixture, Mater. Lett. 223 (2018) 250–252.
[124] C. Salvan, E. De Vito, L. Briottet, T. Baffie, Impact of pre-treatments on the surface composition, the optical and flow properties of a CuCrZr powder dedicated to laser powder bed fusion use, Powder Technol. 411 (2022) 117931.
[125] S.D. Jadhav, S. Dadbakhsh, R. Chen, R. Shabadi, J.-P. Kruth, J. Van Humbeeck, K. Vanmeensel, Modification of electrical and mechanical properties of selective laser-melted CuCr0. 3 alloy using carbon nanoparticles, Adv. Eng. Mater. 22 (2020) 1900946.
[126] G.M. Karthik, E.S. Kim, A. Zargaran, P. Sathiyamoorthi, S.G. Jeong, H.S. Kim, Role of cellular structure on deformation twinning and hetero-deformation induced strengthening of laser powder-bed fusion processed CuSn alloy, Addit. Manuf. 54 (2022) 102744.
[127] J. Zhou, Y. Huang, Z. Li, X. Tong, D. You, J. Yang, Q. Zhang, W. Li, X. Wang, Effect of heat treatments on microstructure, mechanical and electrical properties of Cu–Cr–Zr alloy manufactured by laser powder bed fusion, Mater. Chem. Phys. 296 (2023) 127249.
[128] L. Wang, S. Qu, H. Fu, X. Zhou, Z. Hu, Y. Wen, B. Zhang, B. Gan, X. Song, Y. Lu, Additively manufactured copper alloy with heterogeneous nanoprecipitates-dislocation architecture for superior strength-ductility-conductivity synergy, Addit. Manuf. (2024) 104100.
[129] W. Kurz, D. Fisher, M. Rappaz, Fundamentals of solidification, (2023).
[130] S. Qu, S. Gao, L. Wang, J. Ding, Y. Lu, Y. Wen, X. Qu, B. Zhang, X. Song, Full-composition-gradient in-situ alloying of Cu–Ni through laser powder bed fusion, Addit. Manuf. 85 (2024) 104166.
[131] J. Li, T. Cheng, Y. Liu, Y. Yang, W. Li, Q. Wei, Simultaneously enhanced strength and ductility of Cu-15Ni-8Sn alloy with periodic heterogeneous microstructures fabricated by laser powder bed fusion, Addit. Manuf. 54 (2022) 102726.
[132] S. Gorsse, M. Gouné, W.-C. Lin, L. Girard, Dataset of mechanical properties and electrical conductivity of copper-based alloys, Sci. Data 10 (2023) 504.
[133] H. Yang, Z. Ma, C. Lei, L. Meng, Y. Fang, J. Liu, H. Wang, High strength and high conductivity Cu alloys: A review, Sci. China Technol. Sci. 63 (2020) 2505–2517.
[134] C. Zhao, Z. Wang, D. Li, M. Xie, L. Kollo, Z. Luo, W. Zhang, K.G. Prashanth, Comparison of additively manufacturing samples fabricated from pre-alloyed and mechanically mixed powders, J. Alloy. Compd. 830 (2020) 154603.
[135] A. Mussatto, R. Groarke, A. O'Neill, M.A. Obeidi, Y. Delaure, D. Brabazon, Influences of powder morphology and spreading parameters on the powder bed topography uniformity in powder bed fusion metal additive manufacturing, Addit. Manuf. 38 (2021) 101807.
[136] W. Zhai, J. Li, R. Zhou, A. Sun, S. Yan, G. Wang, H. Zhang, Improved corrosion resistance of nickel-aluminum bronze by electron beam powder bed fusion, Mater. Chem. Phys. 296 (2023) 127225.
[137] W. Zhai, Y. Zhao, R. Zhou, W. Lu, W. Zhai, X. Liu, L. Zhou, S. Chang, Additively manufactured (Fe, Ni) Al-reinforced nickel aluminum bronze with nearly-isotropic mechanical properties in build and transverse directions, Mater Charact 184 (2022) 111706.
[138] S. Yu, Y. Zhao, G. Zhao, Q. Liu, B. Yao, H. Liu, Review on preparation technology and properties of spherical powders, Int. J. Adv. Manuf. Technol. (2024) 1–17.
[139] L. Shi, J. Zou, J. Chen, H. Xue, J. Cheng, Y. Wang, L. Sun, D. Song, Z. Zhang, Y. Jiang, Study on segregation solidification and homogenization behavior of Cu–16Sn–0.3 Ti alloy powders, J. Mater. Res. Technol. 23 (2023) 5547–5558.
[140] H. Shi, Y. Zhao, H. Gao, M. Zhang, Y. Jiang, F. Cao, J. Zou, S. Liang, In-situ spherical TiB2/Cu composite powder: A new method of liquid phase reaction coupled with gas atomization, Mater Charact 191 (2022) 112096.
[141] J.H. Tan, W.L.E. Wong, K.W. Dalgarno, An overview of powder granulometry on feedstock and part performance in the selective laser melting process, Addit. Manuf. 18 (2017) 228–255.
[142] K. Chen, C. Wang, Q. Hong, S. Wen, Y. Zhou, C. Yan, Y. Shi, Selective laser melting 316L/CuSn10 multi-materials: Processing optimization, interfacial characterization and mechanical property, J. Mater. Process. Technol. 283 (2020) 116701.
[143] H. Zhang, H. Fu, S. Zhu, W. Yong, J. Xie, Machine learning assisted composition effective design for precipitation strengthened copper alloys, Acta Mater. 215 (2021) 117118.
[144] J. Robinson, A. Arjunan, M. Stanford, I. Lyall, C. Williams, Effect of silver addition in copper-silver alloys fabricated by laser powder bed fusion in situ alloying, J. Alloy. Compd. 857 (2021) 157561.
[145] Y. Chen, S. Ren, Y. Zhao, X. Qu, Microstructure and properties of CuCr alloy manufactured by selective laser melting, J. Alloy. Compd. 786 (2019) 189–197.
[146] M. Xie, S. Zhou, J. Jin, S. Zhao, Y. Zhao, Microstructure and properties of homogeneous Cu90Fe10 immiscible composites with nanotwins by laser powder deposition: effect of spot size, J. Alloy. Compd. 821 (2020) 153231.
[147] M. Dang, H. Xiang, J. Li, C. Cai, Q. Wei, Laser powder bed fusion of full martensite Cu-Al-Mn-Ti alloy with good superelasticity and shape memory effect, Mater. Sci. Eng. A 884 (2023) 145475.
[148] G. Zhang, S. Liu, C. Chen, X. Zhang, X. Gan, Q. Lei, Z. Li, K. Zhou, Effect of heat treatment on microstructure and mechanical properties of a selective laser melted Cu–15Ni–8Sn alloy, Mater. Sci. Eng. A 763 (2019) 138132.
[149] A.R. Kini, D. Maischner, A. Weisheit, D. Ponge, B. Gault, E.A. Jägle, D. Raabe, In-situ synthesis via laser metal deposition of a lean Cu–3.4 Cr–0.6 Nb (at%) conductive alloy hardened by Cr nano-scale precipitates and by Laves phase micro-particles, Acta Mater. 197 (2020) 330–340.
[150] J. Wang, X. Zhou, J. Li, Evolution of microstructures and properties of SLM-manufactured Cu–15Ni–8Sn alloy during heat treatment, Addit. Manuf. 37 (2021) 101599.
[151] D. Palousek, M. Kocica, L. Pantelejev, L. Klakurkova, L. Celko, D. Koutny, J. Kaiser, SLM process parameters development of Cu-alloy Cu7. 2Ni1. 8Si1Cr, Rapid Prototyp J 25 (2019) 266–276, https://doi.org/10.1108/RPJ-06-2017-0116.

[152] K. Jahns, R. Bappert, P. Böhlke, U. Krupp, Additive manufacturing of CuCr1Zr by development of a gas atomization and laser powder bed fusion routine, Int. J. Adv. Manuf. Technol. 107 (2020) 2151–2161.
[153] L.H. Liu, H.W. Ma, S.J. Yang, Y.J. Zhao, W.S. Cai, T. Chen, W.W. Zhang, C. Yang, Decomposition of cellular structure in selective laser melted Cu–Zn–Si silicon brass and its influence on microstructure, mechanical and corrosion properties, Mater. Sci. Eng. A 841 (2022) 143055.
[154] S.D. Jadhav, P.P. Dhekne, E. Brodu, B. Van Hooreweder, S. Dadbakhsh, J.-P. Kruth, J. Van Humbeeck, K. Vanmeensel, Laser powder bed fusion additive manufacturing of highly conductive parts made of optically absorptive carburized CuCr1 powder, Mater. Des. 198 (2021) 109369.
[155] M. Sadeghilaridjani, L. Ladani, Location-dependent deformation behavior of additively manufactured copper and copper-carbon nanotube composite, J. Alloy. Compd. 909 (2022) 164800.
[156] V. Lindström, O. Liashenko, K. Zweiacker, S. Derevianko, V. Morozovych, Y. Lyashenko, C. Leinenbach, Laser powder bed fusion of metal coated copper powders, Materials 13 (2020) 3493.
[157] R. Zheng, J. Cui, Y. Yang, S. Li, R.D.K. Misra, K. Kondoh, Q. Zhu, Y. Lu, X. Li, Enhanced densification of copper during laser powder bed fusion through powder surface alloying, J. Mater. Process. Technol. 305 (2022) 117575.
[158] R. Zheng, S. Li, R.D.K. Misra, K. Kondoh, Y. Yang, Laser powder bed fusion of electrically/thermally conductive component by developing inert Cr2O3-coated Cu powder, Addit. Manuf. 72 (2023) 103617.
[159] T. Herzog, M. Brandt, A. Trinchi, A. Sola, A. Molotnikov, Process monitoring and machine learning for defect detection in laser-based metal additive manufacturing, J. Intell. Manuf. 35 (2024) 1407–1437, https://doi.org/10.1007/s10845-023-02119-y.
[160] W.H. Kan, L.N.S. Chiu, C.V.S. Lim, Y. Zhu, Y. Tian, D. Jiang, A. Huang, A critical review on the effects of process-induced porosity on the mechanical properties of alloys fabricated by laser powder bed fusion, J. Mater. Sci. 57 (2022) 9818–9865.
[161] M. Grasso, B.M. Colosimo, Process defects and in situ monitoring methods in metal powder bed fusion: a review, Meas. Sci. Technol. 28 (2017) 044005.
[162] N. Sanaei, A. Fatemi, Defects in additive manufactured metals and their effect on fatigue performance: A state-of-the-art review, Prog. Mater Sci. 117 (2021) 100724.
[163] T. Mukherjee, J.W. Elmer, H.L. Wei, T.J. Lienert, W. Zhang, S. Kou, T. DebRoy, Control of grain structure, phases, and defects in additive manufacturing of high-performance metallic components, Prog. Mater Sci. 101153 (2023).
[164] B.J. Simonds, J. Tanner, A. Artusio-Glimpse, P.A. Williams, N. Parab, C. Zhao, T. Sun, The causal relationship between melt pool geometry and energy absorption measured in real time during laser-based manufacturing, Appl. Mater. Today 23 (2021) 101049.
[165] C. Du, Y. Zhao, J. Jiang, Q. Wang, H. Wang, N. Li, J. Sun, Pore defects in Laser Powder Bed Fusion: Formation mechanism, control method, and perspectives, J. Alloy. Compd. 944 (2023) 169215.
[166] D. Oropeza, T. Seager, S. Firdosy, J. Guerra, K. Billings, J.-P. Jones, D. C. Hofmann, S. Roberts, Porosity control of copper-based alloys via powder bed fusion additive manufacturing for spacecraft applications, J. Porous Mater. (2024) 1–13.
[167] T. Mukherjee, T. DebRoy, Theory and Practice of Additive Manufacturing, John Wiley & Sons, 2023.
[168] M.S. Kumar, N. Jeyaprakash, C.-H. Yang, Influence of defects formation on the cracking behavior of LPBFed Cu-Cr-Zr alloy: Micro-mechanism and CRITIC-WASPAS approach, Eng. Fail. Anal. 160 (2024) 108206.
[169] S. Singh, I.A. Palani, S. Dehgahi, A.J. Qureshi, A.N. Jinoop, C.P. Paul, K. G. Prashanth, Development of Cu-based shape memory alloy through selective laser melting from elemental powder mixture: Processing and characterization, J. Alloy. Compd. 961 (2023) 171029.
[170] X. Li, T. Saario, T. Ikäläinen, Z. Que, Corrosion behavior of additively manufactured M300-CuCr1Zr by multi-material laser-based powder bed fusion, Electrochim. Acta 507 (2024) 145199.
[171] C. Zeng, B. Zhang, A.H. Ettefagh, H. Wen, H. Yao, W.J. Meng, S. Guo, Mechanical, thermal, and corrosion properties of Cu-10Sn alloy prepared by laser-powder-bed-fusion additive manufacturing, Addit. Manuf. 35 (2020) 101411.
[172] J. Samei, M. Amirmaleki, A.P. Ventura, G.T. Pawlikowski, M. Bayes, W. Z. Misiolek, D.S. Wilkinson, In-situ X-ray tomography analysis of the evolution of pores during deformation of a Cu-Sn alloy fabricated by selective laser melting, Addit. Manuf. 34 (2020) 101196.
[173] J. Liu, B. Wei, H. Chang, J. Li, G. Yang, Review of visual measurement methods for metal vaporization processes in laser powder bed fusion, Micromachines (Basel) 14 (2023) 1351.
[174] C. Yang, Y.J. Zhao, L.M. Kang, D.D. Li, W.W. Zhang, L.C. Zhang, High-strength silicon brass manufactured by selective laser melting, Mater. Lett. 210 (2018) 169–172, https://doi.org/10.1016/j.matlet.2017.09.011.
[175] L. Zhuo, B. Song, R. Li, Q. Wei, C. Yan, Y. Shi, Effect of element evaporation on the microstructure and properties of CuZnAl shape memory alloys prepared by selective laser melting, Opt. Laser Technol. 127 (2020) 106164.
[176] X. Xi, J. Zhang, H. Tang, Y. Cao, Z. Xiao, The ultrahigh functional response of CuAlMnNb shape memory alloy by selective laser melting, J. Mater. Res. Technol. 20 (2022) 671–680.
[177] Y.H. Zhou, Z.H. Zhang, Y.P. Wang, G. Liu, S.Y. Zhou, Y.L. Li, J. Shen, M. Yan, Selective laser melting of typical metallic materials: An effective process prediction model developed by energy absorption and consumption analysis, Addit. Manuf. 25 (2019) 204–217.
[178] Y. Zhao, Y. Cui, Y. Hasebe, H. Bian, K. Yamanaka, K. Aoyagi, T. Hagisawa, A. Chiba, Controlling factors determining flowability of powders for additive manufacturing: A combined experimental and simulation study, Powder Technol. 393 (2021) 482–493.
[179] E. Soares Barreto, J. Wegner, M. Frey, S. Kleszczynski, R. Busch, V. Uhlenwinkel, L. Mädler, N. Ellendt, Influence of oxygen in the production chain of Cu–Ti-based metallic glasses via laser powder bed fusion, Powder Metall. 66 (2023) 343–354.
[180] J. Chen, Y. Yang, Y. Bai, D. Wang, C. Zhao, J.Y.H. Fuh, Single and multiple track formation mechanism of laser powder bed fusion 316L/CuSn10 multi-material, Mater Charact 183 (2022) 111654.
[181] J. Chen, M. Zhang, D. Zhao, G. Bi, Y. Bai, Y. Xiao, D. Wang, The impact of interfacial characteristics on the interfacial properties of 316 L/CuSn10 multi-material manufactured by laser powder bed fusion, Mater Charact 211 (2024) 113862.
[182] S. Mao, D.Z. Zhang, Z. Ren, G. Fu, X. Ma, Effects of process parameters on interfacial characterization and mechanical properties of 316L/CuCrZr functionally graded material by selective laser melting, J. Alloy. Compd. 899 (2022) 163256.
[183] L. Deillon, N.A. Beldarrain, X. Li, M. Bambach, Coupling hot isostatic pressing and laser powder bed fusion: A new strategy to manufacture defect-free CuCrZr-316L steel multi-material structures, Mater. Des. 241 (2024) 112914.
[184] Z. Hu, Z. Ma, L. Yu, Y. Liu, Functionally graded materials with grain-size gradients and heterogeneous microstructures achieved by additive manufacturing, Scr. Mater. 226 (2023) 115197.
[185] X. Li, D. Sukhomlinov, Z. Que, Microstructure and thermal properties of dissimilar M300-CuCr1Zr alloys by multi-material laser-based powder bed fusion, Int. J. Miner. Metall. Mater. 31 (2024) 118–128.
[186] X. Li, Z. Pan, L. Smolej, V.K. Nadimpalli, M. Moshiri, Towards manufacturing intra-layer multi-material mould tools with vertical interfaces using laser-based powder bed fusion, Mater. Des. 113056 (2024).
[187] S. Suwas, R.K. Ray, Crystallographic Texture of Materials, Springer, 2014.
[188] H.L. Wei, J. Mazumder, T. DebRoy, Evolution of solidification texture during additive manufacturing, Sci. Rep. 5 (2015) 16446.
[189] H.L. Wei, J.W. Elmer, T. DebRoy, Origin of grain orientation during solidification of an aluminum alloy, Acta Mater. 115 (2016) 123–131.
[190] S. Kou, Welding metallurgy, New Jersey, USA 431 (2003) 223–225.
[191] B. Song, T. Yu, X. Jiang, W. Xi, X. Lin, Z. Ma, Z. Wang, Development of the molten pool and solidification characterization in single bead multilayer direct energy deposition, Addit. Manuf. 49 (2022) 102479.
[192] P. Köhnen, M. Létang, M. Voshage, J.H. Schleifenbaum, C. Haase, Understanding the process-microstructure correlations for tailoring the mechanical properties of L-PBF produced austenitic advanced high strength steel, Addit. Manuf. 30 (2019) 100914.
[193] S. Ghosh, J. Zollinger, M. Zaloznik, D. Banerjee, C.K. Newman, R. Arroyave, Modeling of hierarchical solidification microstructures in metal additive manufacturing: Challenges and opportunities, Addit. Manuf. 78 (2023) 103845.
[194] A. Thomas, G. Fribourg, J.-J. Blandin, P. Lhuissier, R. Dendievel, G. Martin, Tailoring the crystallographic texture of pure copper through control of the scanning strategy in Electron Powder Bed Fusion, Materialia (Oxf) 24 (2022) 101495.
[195] H. Fan, Y. Xu, H. Li, J. Fang, M. Li, K. Dongfang, P. Liu, A novel study on microstructure and crystallographic characteristics of Cu-Cr-Zr alloy manufactured by laser powder bed fusion, Mater. Today Commun. 37 (2023) 107603.
[196] Y. Zhou, X. Zeng, Z. Yang, H. Wu, Effect of crystallographic textures on thermal anisotropy of selective laser melted Cu-2.4 Ni-0.7 Si alloy, J. Alloy. Compd. 743 (2018) 258–261.
[197] G.M. Karthik, P. Sathiyamoorthi, A. Zargaran, J.M. Park, P. Asghari-Rad, S. Son, S.H. Park, H.S. Kim, Novel precipitation and enhanced tensile properties in selective laser melted Cu-Sn alloy, Materialia (Oxf) 13 (2020) 100861.
[198] G. Demeneghi, B. Barnes, P. Gradl, J.R. Mayeur, K. Hazeli, Size effects on microstructure and mechanical properties of additively manufactured copper–chromium–niobium alloy, Mater. Sci. Eng. A 820 (2021) 141511.
[199] Q. Wang, Y. Zhang, K. Wang, S. Liu, X. Zhang, H. Shao, Effect of process parameters and heat treatment on the microstructure and properties of CuCrZr alloy by selective laser melting, Mater. Sci. Eng. A 857 (2022) 144054.
[200] W.R. Cribb, F.C. Grensing, Spinodal copper alloy C72900–new high strength antifriction alloy system, Can. Metall. Q. 50 (2011) 232–239.
[201] Z. Mao, D.Z. Zhang, P. Wei, K. Zhang, Manufacturing feasibility and forming properties of Cu-4Sn in selective laser melting, Materials 10 (2017) 333.
[202] J. Wang, X.L. Zhou, J. Li, M. Brochu, Y.F. Zhao, Microstructures and properties of SLM-manufactured Cu-15Ni-8Sn alloy, Addit. Manuf. 31 (2020) 100921.
[203] G.M. Karthik, F. Haftlang, J. Kwak, P. Sathiyamoorthi, A. Zargaran, Y.-T. Kim, H. S. Kim, The influence of laser powder-bed fusion microstructures on the corrosion behavior of CuSn alloy, J. Mater. Sci. 57 (2022) 17923–17934.
[204] P. Zuo, Z. Zhang, X. Qi, Z. Liu, J. Xia, J. Wu, X. Li, B. Zhang, Effects of nanoscale Sn segregation on corrosion behavior of laser powder bed fusion Cu-15Ni-8Sn alloy, J. Mater. Sci. Technol. 158 (2023) 96–110.
[205] G. Wang, H. Ouyang, C. Fan, Q. Guo, Z. Li, W. Yan, Z. Li, The origin of high-density dislocations in additively manufactured metals, Mater Res Lett 8 (2020) 283–290.
[206] J. Kwon, G.M. Karthik, Y. Estrin, H.S. Kim, Constitutive modeling of cellular-structured metals produced by additive manufacturing, Acta Mater. 241 (2022) 118421.
[207] H. Chen, W. Yan, Spattering and denudation in laser powder bed fusion process: Multiphase flow modelling, Acta Mater. 196 (2020) 154–167.
[208] D. Gu, Y. Shen, Balling phenomena during direct laser sintering of multi-component Cu-based metal powder, J. Alloy. Compd. 432 (2007) 163–166.

[209] I. Yadroitsev, A. Gusarov, I. Yadroitsava, I. Smurov, Single track formation in selective laser melting of metal powders, J. Mater. Process. Technol. 210 (2010) 1624–1631.
[210] T. Gustmann, A. Neves, U. Kühn, P. Gargarella, C.S. Kiminami, C. Bolfarini, J. Eckert, S. Pauly, Influence of processing parameters on the fabrication of a Cu-Al-Ni-Mn shape-memory alloy by selective laser melting, Addit. Manuf. 11 (2016) 23–31.
[211] Q. Wang, H. Shao, X. Zhang, K. Wang, S. Liu, C. Yang, W. Wang, Study of thermal behavior and microstructure formation mechanism of CuCrZr alloy melted by laser powder bed fusion, Mater Charact 198 (2023) 112721.
[212] B. Vela, S. Mehalic, S. Sheikh, A. Elwany, I. Karaman, R. Arróyave, Evaluating the intrinsic resistance to balling of alloys: A high-throughput physics-informed and data-enabled approach, Addit. Manuf. Lett. 3 (2022) 100085.
[213] Z. Tan, X. Zhang, Z. Zhou, Z. Zhou, Y. Yang, X. Guo, Z. Wang, X. Wu, G. Wang, D. He, Thermal effect on the microstructure of the lattice structure Cu-10Sn alloy fabricated through selective laser melting, J. Alloy. Compd. 787 (2019) 903–908.
[214] P. Lassègue, C. Salvan, E. De Vito, R. Soulas, M. Herbin, A. Hemberg, T. Godfroid, T. Baffie, G. Roux, Laser powder bed fusion (L-PBF) of Cu and CuCrZr parts: Influence of an absorptive physical vapor deposition (PVD) coating on the printing process, Addit. Manuf. 39 (2021) 101888.
[215] V. Lindström, G. Lupo, J. Yang, V. Turlo, C. Leinenbach, A simple scaling model for balling defect formation during laser powder bed fusion, Addit. Manuf. 63 (2023) 103431.
[216] L. Min, S. Xiaojie, L. Peipei, W. Meiping, Forming quality and wettability of surface texture on CuSn10 fabricated by laser powder bed fusion, AIP Adv. 12 (2022).
[217] Z. Ma, D.Z. Zhang, F. Liu, J. Jiang, M. Zhao, T. Zhang, Lattice structures of Cu-Cr-Zr copper alloy by selective laser melting: Microstructures, mechanical properties and energy absorption, Mater. Des. 187 (2020) 108406.
[218] P.V. Cobbinah, S. Matsunaga, Y. Yamabe-Mitarai, Controlled crystallographic texture orientation in structural materials using the laser powder bed fusion process—a review, Adv. Eng. Mater. 25 (2023) 2300819.
[219] S. Rahmati, E. Vahabli, Evaluation of analytical modeling for improvement of surface roughness of FDM test part using measurement results, Int. J. Adv. Manuf. Technol. 79 (2015) 823–829.
[220] T. Maconachie, M. Leary, B. Lozanovski, X. Zhang, M. Qian, O. Faruque, M. Brandt, SLM lattice structures: Properties, performance, applications and challenges, Mater. Des. 183 (2019) 108137.
[221] A.H. Seltzman, S.J. Wukitch, Surface roughness and finishing techniques in selective laser melted GRCop-84 copper for an additive manufactured lower hybrid current drive launcher, Fusion Eng. Des. 160 (2020) 111801.
[222] H.C. Aksa, İ. Hacısalihoğlu, F. Yıldız, T. Varol, O. Güler, G. Kaya, S.B. Akçay, Effects of fabrication parameters and post-processing treatments on the mechanical and tribological behavior of surface-enhanced copper based materials by selective laser melting, J. Mater. Process. Technol. 304 (2022) 117564.
[223] F. Sun, P. Liu, X. Chen, H. Zhou, P. Guan, B. Zhu, Mechanical properties of high-strength Cu–Cr–Zr alloy fabricated by selective laser melting, Materials 13 (2020) 5028.
[224] T. Chen, L. Yang, Y. Huang, S. Zhao, W. Wu, H. Ma, Q. Zhang, S. Fan, J. Sun, The surface morphologies and internal pores evolution of a CuSn10 alloy fabricated by laser powder bed fusion, J. Mater. Res. Technol. (2024).
[225] N. Kraiem, L. Constantin, A. Mao, F. Wang, B. Cui, J.-F. Silvain, Y.F. Lu, Influence of aluminum addition on the laser powder bed fusion of copper-aluminum mixtures, Addit. Manuf. Lett. 3 (2022) 100080.
[226] J. Gan, H. Gao, S. Wen, Y. Zhou, S. Tan, L. Duan, Simulation, forming process and mechanical property of Cu-Sn-Ti/diamond composites fabricated by selective laser melting, Int. J. Refract. Metals Hard. Mater. 87 (2020) 105144.
[227] N. Sanaei, A. Fatemi, Analysis of the effect of surface roughness on fatigue performance of powder bed fusion additive manufactured metals, Theor. Appl. Fract. Mech. 108 (2020) 102638.
[228] S. Chen, H. Gao, Q. Wu, Z. Gao, X. Zhou, Review on residual stresses in metal additive manufacturing: formation mechanisms, parameter dependencies, prediction and control approaches, J. Mater. Res. Technol. 17 (2022) 2950–2974.
[229] P.J. Withers, H. Bhadeshia, Residual stress. Part 2–Nature and origins, Mater. Sci. Technol. 17 (2001) 366–375.
[230] R. Kremer, S. Khani, T. Appel, H. Palkowski, F. Foadian, Selective laser melting of CuSn10: Simulation of mechanical properties, microstructure, and residual stresses, Materials 15 (2022) 3902.
[231] K. Lin, H. Tian, D. Gu, C. Wang, L. Yuan, J. Sun, Laser powder bed fusion of Cu–Al–Ni–Mn shape-memory alloy for the application of active heat sinks: processability, microstructures, and shape-memory effect, Adv. Eng. Mater. 26 (2024) 2301224.
[232] Z. Ma, S. Zhang, C. Gao, X. Gu, X. Xiong, Y. Bi, J.H. Rao, The influence of structural design on the dimensional accuracy of CuCrZr alloy produced by laser powder bed fusion, Sustainability 14 (2022) 14639.
[233] P. Mercelis, J. Kruth, Residual stresses in selective laser sintering and selective laser melting, Rapid Prototyp. J. 12 (2006) 254–265.
[234] K. Morshed-Behbahani, A.J. Rayner, D.P. Bishop, A. Nasiri, Perspectives on the unusual electrochemical corrosion of Nickel Aluminum Bronze (NAB) alloy fabricated through laser-powder bed fusion additive manufacturing, Corros. Sci. 228 (2024) 111846.
[235] J. Chen, Y. Yang, D. Wang, Z. Liu, C. Song, Effect of manufacturing steps on the interfacial defects of laser powder bed fusion 316L/CuSn10, Mater. Lett. 292 (2021) 129377.
[236] T. Iida, R.I.L. Guthrie, The Thermophysical Properties of Metallic Liquids: Volume 1: Fundamentals, Oxford University Press, 2015.
[237] S.K. Murugesan, J. Natarajan, C.-H. Yang, Enhancing the wear resistance by mitigation of defect formations in laser powder bed fusion process of Cu–Cr–Zr alloy, Int. J. Adv. Manuf. Technol. (2024) 1–20.
[238] C. Zhao, Z. Wang, D. Li, L. Kollo, Z. Luo, W. Zhang, K.G. Prashanth, Selective laser melting of Cu–Ni–Sn: A comprehensive study on the microstructure, mechanical properties, and deformation behavior, Int. J. Plast 138 (2021) 102926.
[239] A.H. Seltzman, S.J. Wukitch, Precipitate size in GRCop-42 and GRCop-84 Cu-Cr-Nb alloy Gas atomized powder and L-PBF additive manufactured material, Fusion Sci. Technol. 79 (2023) 503–516.
[240] L. Xu, Y. Zhang, L. Zhao, W. Ren, Y. Han, Performance improvement for the CuCrZr alloy produced by laser powder bed fusion using the remelting process, Materials 17 (2024) 624.
[241] W. Huang, On the selection of shape memory alloys for actuators, Mater. Des. 23 (2002) 11–19.
[242] N. Jeyaprakash, M.S. Kumar, C.-H. Yang, Enhanced nano-level mechanical responses on additively manufactured Cu-Cr-Zr copper alloy containing Cu2O nano precipitates, J. Alloy. Compd. 930 (2023) 167425.
[243] V. Candela, M. Tocci, G. Ischia, F. Valentini, A. Mutanen, S. Candela, H. Lehtonen, J. Hongisto, T. Syvänen, R. Dima, J. Ottelin, M. Nyström, M. Pellizzari, S. Mancin, A. Pepato, P. Sonato, Understanding microstructure and properties evolution in additively manufactured CuCrZr alloy to obtain a high-performance material, Mater. Charact. (2025) 114811, https://doi.org/10.1016/j.matchar.2025.114811.
[244] V. Candela, L. Zanini, M. Tocci, M. Bonesso, C. Scian, M. El Idrissi, G. Favero, M. Ballan, S. Corradetti, R. Dima, Influence of heat treatments on low-power-LPBFed CuCrZr for nuclear fusion applications, J. Nucl. Mater. 155135 (2024).
[245] A. Kulkarni, V.C. Peddiraju, S. Chatterjee, D. Srinivasan, Effect of Build Geometry and Porosity in Additively Manufactured CuCrZr, J. Eng. Mater. Technol. 146 (2024).
[246] D. Kim, N. Takata, J. Umeda, T. Shimizu, M. Kobashi, Anomalous temperature-dependent strength of copper alloy manufactured by laser-beam powder bed fusion, Addit. Manuf. Lett. 11 (2024) 100236.
[247] C. Guerra, J.A. Ramos-Grez, I. La Fé-Perdomo, A. Castillo, M. Walczak, Microstructure and Mechanical Properties of Cu-11Al-5Ni-4Fe wt% Manufactured by LPBF, Metals (Basel) 13 (2023) 459.
[248] S. Uchida, T. Kimura, T. Nakamoto, T. Ozaki, T. Miki, M. Takemura, Y. Oka, R. Tsubota, Microstructures and electrical and mechanical properties of Cu-Cr alloys fabricated by selective laser melting, Mater. Des. 175 (2019) 107815.
[249] C. Zeng, H. Wen, B.C. Bernard, J.R. Raush, P.R. Gradl, M. Khonsari, Effect of temperature history on thermal properties of additively manufactured C-18150 alloy samples, Manuf. Lett. 28 (2021) 25–29.
[250] G. Demeneghi, P. Gradl, J.R. Mayeur, K. Hazeli, Size effect characteristics and influences on fatigue behavior of laser powder bed fusion of thin wall GRCop-42 copper alloy, Heliyon 10 (2024).
[251] B. Zhang, S. Zhang, H. Yang, D. Peng, Y. Wang, H. Zhu, Investigating the influence of the scanning rotation angle on the microstructure and properties of LPBFed CuCr0. 8 alloy, J. Manuf. Process. 84 (2022) 1150–1161.
[252] J. Li, Z. Liu, H. Zhou, S. Ye, Y. Zhang, T. Liu, D. Jiang, L. Chen, R. Zhou, Effect of Process Parameters on the Microstructure and Properties of Cu–Cr–Nb–Ti Alloy Manufactured by Selective Laser Melting, Materials 16 (2023) 2912.
[253] J. Tian, W. Zhu, Q. Wei, S. Wen, S. Li, B. Song, Y. Shi, Process optimization, microstructures and mechanical properties of a Cu-based shape memory alloy fabricated by selective laser melting, J. Alloy. Compd. 785 (2019) 754–764.
[254] J. Li, Z. Kuai, Z. Li, B. Liu, Y. Chen, S. Lu, Y. Nie, Z. Yang, Effects of process parameters on the relative density and properties of CuCrZr alloy produced by selective laser melting, Metals (Basel) 12 (2022) 701.
[255] P. Yang, X. Guo, D. He, W. Shao, Z. Tan, H. Fu, Z. Zhou, X. Zhang, Microstructure twinning and mechanical properties of laser melted Cu-10Sn alloy for high strength and plasticity, J. Mater. Eng. Perform. (2021) 1–9.
[256] Z. Li, Y. Chen, S. Zhang, B. Liu, Z. Kuai, W. Huo, H. Yang, M. Wei, P. Bai, Microstructure and properties in CuCrZr alloy fabricated by selective laser melting with different heat treatment, Results Phys. 54 (2023) 107125.
[257] R.O. Ritchie, The conflicts between strength and toughness, Nat. Mater. 10 (2011) 817–822.
[258] T.H. Becker, P. Kumar, U. Ramamurty, Fracture and fatigue in additively manufactured metals, Acta Mater. 219 (2021) 117240.
[259] M.J. Paul, J.J. Kruzic, U. Ramamurty, B. Gludovatz, The importance of fracture toughness evaluation for additively manufactured metals, Acta Mater. 120061 (2024).
[260] K. Hazeli, D. June, P. Anantwar, B.B. Babamiri, Mechanical behavior of additively manufactured GRCop-84 copper alloy lattice structures, Addit. Manuf. 56 (2022) 102928.
[261] X. Tang, X. Chen, F. Sun, L. Li, P. Liu, H. Zhou, S. Fu, A. Li, A study on the mechanical and electrical properties of high-strength CuCrZr alloy fabricated using laser powder bed fusion, J. Alloy. Compd. 924 (2022) 166627.
[262] L. Li, Q. Wang, K. Wang, W. Wang, Y. Zhang, X. Zhang, Precipitation Behavior of Supersaturated Solid-solubility CuCrZr Alloy by Additive Manufacturing, Mater. Sci. Eng. A 146557 (2024).
[263] S. Zhang, H. Zhu, L. Zhang, W. Zhang, H. Yang, X. Zeng, Microstructure and properties of high strength and high conductivity Cu-Cr alloy components fabricated by high power selective laser melting, Mater. Lett. 237 (2019) 306–309.
[264] A. Popovich, V. Sufiiarov, I. Polozov, E. Borisov, D. Masaylo, A. Orlov, Microstructure and mechanical properties of additive manufactured copper alloy, Mater. Lett. 179 (2016) 38–41.

[265] G. Zhang, C. Chen, X. Wang, P. Wang, X. Zhang, X. Gan, K. Zhou, Additive manufacturing of fine-structured copper alloy by selective laser melting of pre-alloyed Cu-15Ni-8Sn powder, Int. J. Adv. Manuf. Technol. 96 (2018) 4223–4230.
[266] C.J. Barr, D.T. McDonald, K. Xia, Significantly enhanced tensile strength and ductility in nickel aluminium bronze by equal channel angular pressing and subsequent heat treatment, J. Mater. Sci. 48 (2013) 4749–4757.
[267] S.N. Saud, E. Hamzah, T. Abubakar, M. Zamri, M. Tanemura, Influence of Ti additions on the martensitic phase transformation and mechanical properties of Cu–Al–Ni shape memory alloys, J. Therm. Anal. Calorim. 118 (2014) 111–122.
[268] X. Zhang, Q. Lei, M.T. Andani, X. Liu, H. Zhang, W. Wang, Y. Li, Y. Yang, Effects of build orientation and heat treatment on microstructure and properties of Cu–Cr–Zr alloy manufactured by laser powder bed fusion, Mater. Chem. Phys. 298 (2023) 127477.
[269] L. Wang, S. Qu, H. Fu, X. Zhou, J. Ding, H. Yang, Q. Zhao, X. Song, Y. Lu, High-precision Cu alloy microlattices with superior energy absorption capacity enabled by nanoprecipitation engineering, Scr. Mater. 239 (2024) 115801.
[270] Y.-K. Kim, S.-H. Park, K.-A. Lee, Effect of post-heat treatment on the thermophysical and compressive mechanical properties of Cu-Ni-Sn alloy manufactured by selective laser melting, Mater Charact 162 (2020) 110194.
[271] D. Abolhasani, B. Moon, N. Kang, C.J. VanTyne, Y.H. Moon, High-performance Cu-Al shape memory alloy in ternary combination with graphene fabricated by powder bed fusion process, J. Alloy. Compd. 960 (2023) 170707.
[272] X. Xi, H. Tang, J. Zhang, X. Li, Z. Xiao, Unraveling effect of Nb addition on the microstructure, phase transformation behaviour and shape memory effect of CuAlMn alloy fabricated by laser powder bed fusion, J. Mater. Res. Technol. (2024).
[273] Y. Gao, Z. Jian, B. Wang, Effect of laser power on the microstructure, shape memory effect and mechanical properties of Cu–13Al–5Fe high temperature shape memory alloy by laser powder bed fusion, Appl. Phys. A 129 (2023) 836.
[274] T. Gustmann, H. Schwab, U. Kühn, S. Pauly, Selective laser remelting of an additively manufactured Cu-Al-Ni-Mn shape-memory alloy, Mater. Des. 153 (2018) 129–138.
[275] Y. Gao, Z. Jian, Effect of cooling rate on microstructure, shape memory effect and mechanical properties of Cu–13Al–5Fe high-temperature shape memory alloy fabricated by laser powder bed fusion, Trans. Indian Inst. Met. (2024) 1–7.
[276] D.-H. Yang, Y.-K. Kim, S.-H. Park, K.-A. Lee, Improved mechanical and thermophysical properties of additively manufactured Cu-Ni-Sn-P alloy by using aging treatment, J. Alloy. Compd. 875 (2021) 160050.
[277] Y. Zhao, K.B. Lau, W.H. Teh, J.J. Lee, F. Wei, M. Lin, P. Wang, C.C. Tan, U. Ramamurty, Compositionally graded CoCrFeNiTix high-entropy alloys manufactured by laser powder bed fusion: A combinatorial assessment, J. Alloy. Compd. 883 (2021) 160825.
[278] D. Tabor, The Hardness of Metals, Oxford University Press, 2000.
[279] X. Li, X. Xu, X. Hu, H. Shi, X. Li, W. Liu, W. Gan, C. Xu, X. Wang, Microstructure and mechanical properties of Cu-Cr-Zr alloy prepared by electron beam additive manufacturing and laser-MIG hybrid welding, J. Manuf. Process. 117 (2024) 24–39.
[280] G. Prabu, C.-H. Yang, I.A. Alnaser, N. Jeyaprakash, Nanowear characterization of LPBF fabricated CuCrZr alloy, Tribol. Int. 109430 (2024).
[281] G. Prabu, N. Jeyaprakash, C.-H. Yang, I.A. Alnaser, Investigation on deformation of nano-twins of LPBF produced Cu alloy through Triboindenter, Tribol. Int. 191 (2024) 109117.
[282] G. Prabu, N. Jeyaprakash, C.-H. Yang, S. Sivasankaran, Synergetic effect of piled-up material around the nanoindentation cavity on additively manufactured Cu-Cr-Zr alloy, Mater. Today Commun. 38 (2024) 107691.
[283] A. Matthiessen, G. Vogt, The electrical resistivity of alloys, Ann. Phys. Chem. 122 (1864) 19–31.
[284] P.L. Rossiter, The Electrical Resistivity of Metals and Alloys, Cambridge University Press, 1991.
[285] L. Tian, I. Anderson, T. Riedemann, A. Russell, Modeling the electrical resistivity of deformation processed metal–metal composites, Acta Mater. 77 (2014) 151–161.
[286] Y. Li, S. Liu, Y. Wang, J. Wang, L. Zhang, W. Jia, Y. Wei, Effect of wall thickness on the precipitation behavior, microstructure, electrical conductivity and mechanical properties of copper alloy prepared by electron beam powder bed fusion, Mater Charact 218 (2024) 114518.
[287] X. Zhang, J. Gao, J. Zhang, L. Zhang, B. Song, Y. Shi, Mechanism of simultaneous improvement of mechanical performance and conductivity of TiC/Cu composites prepared by laser powder bed fusion, J. Alloy. Compd. 1002 (2024) 175281.
[288] G. Pintsuk, E. Diegele, S.L. Dudarev, M. Gorley, J. Henry, J. Reiser, M. Rieth, European materials development: Results and perspective, Fusion Eng. Des. 146 (2019) 1300–1307.
[289] C.X. Ren, Q. Wang, J.P. Hou, Z.J. Zhang, H.J. Yang, Z.F. Zhang, Exploring the strength and ductility improvement of Cu–Al alloys, Mater. Sci. Eng. A 786 (2020) 139441.
[290] T.M. Tritt, Thermal Conductivity: Theory, Properties, and Applications, Springer Science & Business Media, 2005.
[291] C. Wallis, B. Buchmayr, Effect of heat treatments on microstructure and properties of CuCrZr produced by laser-powder bed fusion, Mater. Sci. Eng. A 744 (2019) 215–223.
[292] F. Ellyin, Fatigue Damage, Crack Growth and Life Prediction, Springer Science & Business Media, 2012.
[293] T. Wegener, J. Koopmann, J. Richter, P. Krooß, T. Niendorf, CuCrZr processed by laser powder bed fusion—Processability and influence of heat treatment on electrical conductivity, microstructure and mechanical properties, Fatigue Fract. Eng. Mater. Struct. 44 (2021) 2570–2590.
[294] A.P. Jirandehi, M.M. Khonsari, S. Guo, P. Gradl, Fatigue assessment of additively-manufactured C-18150 copper alloy at room and elevated temperatures via a microstructure-sensitive algorithm, Int. J. Fatigue 159 (2022) 106777.
[295] Z. Liu, Q. Zhang, B. Zhang, Y. Wang, P. Zuo, Z. Zhang, J. Wu, X. Yan, Y. Huang, X. Li, Investigation on mechanical properties and corrosion behavior of laser powder bed fusion 70/30 copper-nickel alloy, Corros. Sci. 232 (2024) 112040.
[296] J.A. Wharton, K.R. Stokes, The influence of nickel–aluminium bronze microstructure and crevice solution on the initiation of crevice corrosion, Electrochim. Acta 53 (2008) 2463–2473.
[297] G. Lu, Y. Zou, X. Chen, R. Shi, G. Wang, L. Zhu, X. Xie, W. Sun, J. Yang, S. Chang, Micro-morphological analysis, lubricating behaviors, and wear failure characteristics and mechanisms of propeller hub bearings in marine environments, Wear 530 (2023) 205047.
[298] W. Zhai, A. Sun, W. Zeng, W. Lu, X. Liu, L. Zhou, J. Wang, A.M.M. Ibrahim, High wear resistance and mechanical performance of NiAl bronze developed by electron beam powder bed fusion, Tribol. Lett. 69 (2021) 1–10.
[299] Y. Tao, W. Sun, J. Gan, X. Wang, Y. Zhou, L. Duan, S. Wen, Y. Shi, Effect of Cu-coated diamond on the formation of Cu–Sn-based diamond composites fabricated by laser-powder bed fusion, Int. J. Refract. Metals Hard. Mater. 119 (2024) 106526.
[300] D. Zeng, Y. Qiu, Y. Yi, D. Sun, C. Shi, Y. Lu, S. Zhou, Effect of current on the tribological behavior of Cu-Fe-P immiscible alloy produced by laser powder bed fusion, Wear 558 (2024) 205591.
[301] C. Salvan, L. Briottet, T. Baffie, L. Guetaz, C. Flament, CuCrZr alloy produced by laser powder bed fusion: Microstructure, nanoscale strengthening mechanisms, electrical and mechanical properties, Mater. Sci. Eng. A 826 (2021) 141915.
[302] T.W. Clyne, P.J. Withers, An Introduction to Metal Matrix Composites, Cambridge University Press, 1993.
[303] M. Buttard, M.L. Freixes, C. Josserond, P. Donnadieu, B. Chéhab, J.-J. Blandin, B. Gault, F. De Geuser, G. Martin, Ageing response and strengthening mechanisms in a new Al-Mn-Ni-Cu-Zr alloy designed for laser powder bed fusion, Acta Mater. 259 (2023) 119271.
[304] T.H. Courtney, Mechanical Behavior of Materials, Waveland Press, 2005.
[305] R.L. Fleischer, Substitutional solution hardening, Acta Metall. 11 (1963) 203–209.
[306] P.M. Kelly, Progress report on recent advances in physical metallurgy:(C) The quantitative relationship between microstructure and properties in two-phase alloys, Int. Metallurgical Rev. 18 (1973) 31–36.
[307] H. Wen, T.D. Topping, D. Isheim, D.N. Seidman, E.J. Lavernia, Strengthening mechanisms in a high-strength bulk nanostructured Cu–Zn–Al alloy processed via cryomilling and spark plasma sintering, Acta Mater. 61 (2013) 2769–2782.
[308] J.E. Bailey, P.B. Hirsch, The dislocation distribution, flow stress, and stored energy in cold-worked polycrystalline silver, Phil. Mag. 5 (1960) 485–497.
[309] C.G. Dunn, E.F. Kogh, Comparison of dislocation densities of primary and secondary recrystallization grains of Si-Fe, Acta Metall. 5 (1957) 548–554.
[310] G.K. Williamson, W.H. Hall, X-ray line broadening from filed aluminium and wolfram, Acta Metall. 1 (1953) 22–31.
[311] J.Y. He, H. Wang, H.L. Huang, X.D. Xu, M.W. Chen, Y. Wu, X.J. Liu, T.G. Nieh, K. An, Z.P. Lu, A precipitation-hardened high-entropy alloy with outstanding tensile properties, Acta Mater. 102 (2016) 187–196.
[312] S. Fu, P. Liu, X. Chen, H. Zhou, F. Ma, W. Li, K. Zhang, Effect of aging process on the microstructure and properties of Cu–Cr–Ti alloy, Mater. Sci. Eng. A 802 (2021) 140598.
[313] J. Gallet, M. Perez, R. Guillou, C. Ernould, C. Le Bourlot, C. Langlois, B. Beausir, E. Bouzy, T. Chaise, S. Cazottes, Experimental measurement of dislocation density in metallic materials: a quantitative comparison between measurements techniques (XRD, R-ECCI, HR-EBSD, TEM), Mater Charact 199 (2023) 112842.
[314] W.H. Yu, S.L. Sing, C.K. Chua, C.-N. Kuo, X.L. Tian, Particle-reinforced metal matrix nanocomposites fabricated by selective laser melting: A state of the art review, Prog. Mater Sci. 104 (2019) 330–379.
[315] F.R.N. Nabarro, Fifty-year study of the Peierls-Nabarro stress, Mater. Sci. Eng. A 234 (1997) 67–76.
[316] Z. Kuai, Z. Li, B. Liu, Y. Chen, S. Lu, P. Bai, Effect of heat treatment on CuCrZr alloy fabricated by selective laser melting: microstructure evolution, mechanical properties and fracture mechanism, J. Mater. Res. Technol. 23 (2023) 2658–2671.
[317] S. Zhang, H. Zhu, L. Zhang, W. Zhang, H. Yang, X. Zeng, Microstructure and properties in QCr0. 8 alloy produced by selective laser melting with different heat treatment, J. Alloy. Compd. 800 (2019) 286–293.
[318] T. DebRoy, H.L. Wei, J.S. Zuback, T. Mukherjee, J.W. Elmer, J.O. Milewski, A. M. Beese, A. de Wilson-Heid, A. De, W. Zhang, Additive manufacturing of metallic components–process, structure and properties, Prog. Mater Sci. 92 (2018) 112–224.
[319] E. Pei, A. Bernard, D. Gu, C. Klahn, M. Monzón, M. Petersen, T. Sun, Springer Handbook of Additive Manufacturing, Springer Nature, 2023.
[320] N. Jeyaprakash, I.A. Alnaser, Y. Cheng, S.S. Karuppasamy, Effect of heat treatment on microstructure and mechanical characteristics of Laser Powder Bed Fusion (LPBF) produced CuCrZr alloy, Tribol. Int. 109826 (2024).
[321] Q. Wang, J. Song, W. Wang, Y. Zhang, K. Wang, Z. Du, The influence of heat treatment on microstructure and properties of selective laser melting CuCrZr alloy, Adv. Eng. Mater. 26 (2024) 2301680.
[322] R. Kremer, J. Etzkorn, S. Khani, T. Appel, J. Buhl, H. Palkowski, Influence of post-heat treatment on corrosion behaviour of additively manufactured CuSn10 by laser powder bed fusion, Materials 17 (2024) 3525.
[323] I. Hutchings, P. Shipway, Tribology: Friction and Wear of Engineering Materials, Butterworth-Heinemann, 2017.

[324] F. Alkelae, S. Sasaki, Microstructures generated by nickel aluminium bronze alloy L-PBFed and their effect on tribological and mechanical properties, J. Tribol. 29 (2021) 41–56.
[325] R.I. Stephens, A. Fatemi, R.R. Stephens, H.O. Fuchs, Metal Fatigue in Engineering, second ed., John Wiley & Sons, 2000.
[326] D.S. Watring, K.C. Carter, D. Crouse, B. Raeymaekers, A.D. Spear, Mechanisms driving high-cycle fatigue life of as-built Inconel 718 processed by laser powder bed fusion, Mater. Sci. Eng. A 761 (2019) 137993.
[327] M. Yi, W. Tang, Y. Zhu, C. Liang, Z. Tang, Y. Yin, W. He, S. Sun, S. Su, A holistic review on fatigue properties of additively manufactured metals, J. Mater. Process. Technol. 118425 (2024).
[328] M. Ahlfors, Hot isostatic pressing for metal additive manufacturing, additive manufacturing processes, ASM Int. (2020) 316–323, https://doi.org/10.31399/asm.hb.v24.a0006552.
[329] J. Li, Z. Zhang, W. Xu, Y. Yang, P. Xue, Q. Teng, C. Cai, W. Li, Q. Wei, Hot isostatic pressing of Cu–15Ni–8Sn alloy with suppressed Sn macro-segregation and enhanced mechanical properties, Mater. Sci. Eng. A 855 (2022) 143866.
[330] X. Wu, R. Wang, C. Peng, Y. Feng, Z. Cai, Influence of hot isostatic pressing and forging on the microstructure and mechanical properties of Cu-3Ag-1Zr alloys, Mater. Des. 168 (2019) 107676.
[331] R.P. Minneci, M.P. Haines, P.R. Gradl, D.L. Ellis, E.A. Lass, J.R. Bunn, H. Choo, Z. C. Jones, S.S. Babu, C.J. Rawn, Characterization and rationalization of microstructural evolution in grcop-84 processed by laser-powder bed fusion (L-PBF), Metall. Mater. Trans. A 55 (2024) 1377–1396.
[332] X. Chen, P. Dong, Y. Zeng, H. Yao, J. Chen, Effect of heat treatment on the microstructure and properties of CuCrZr prepared by laser powder bed fusion, Mater Charact 114103 (2024).
[333] S.F. Nabavi, A. Farshidianfar, H. Dalir, Comprehensive review: advancements in modeling geometrical and mechanical characteristics of laser powder bed fusion process, Opt. Laser Technol. 180 (2025) 111480.
[334] S. Sahoo, M.M. Keleshteri, J.R. Mayeur, K. Hazeli, Stress localization investigation of additively manufactured GRCop-42 thin-wall structure, Thin-Walled Struct. 201 (2024) 112022.
[335] Z. Ren, D. Wei, S. Wang, D.Z. Zhang, S. Mao, On the role of pre-and post-contour scanning in laser powder bed fusion: Thermal-fluid dynamics and laser reflections, Int. J. Mech. Sci. 226 (2022) 107389.
[336] Z. Ren, G. Fu, D.Z. Zhang, K. Zhang, M. Zhao, Thermal flow characteristics and the evolution of laser absorption in laser powder bed fusion of Cu-Cr-Zr alloy, Int. J. Mech. Sci. 216 (2022) 106957.